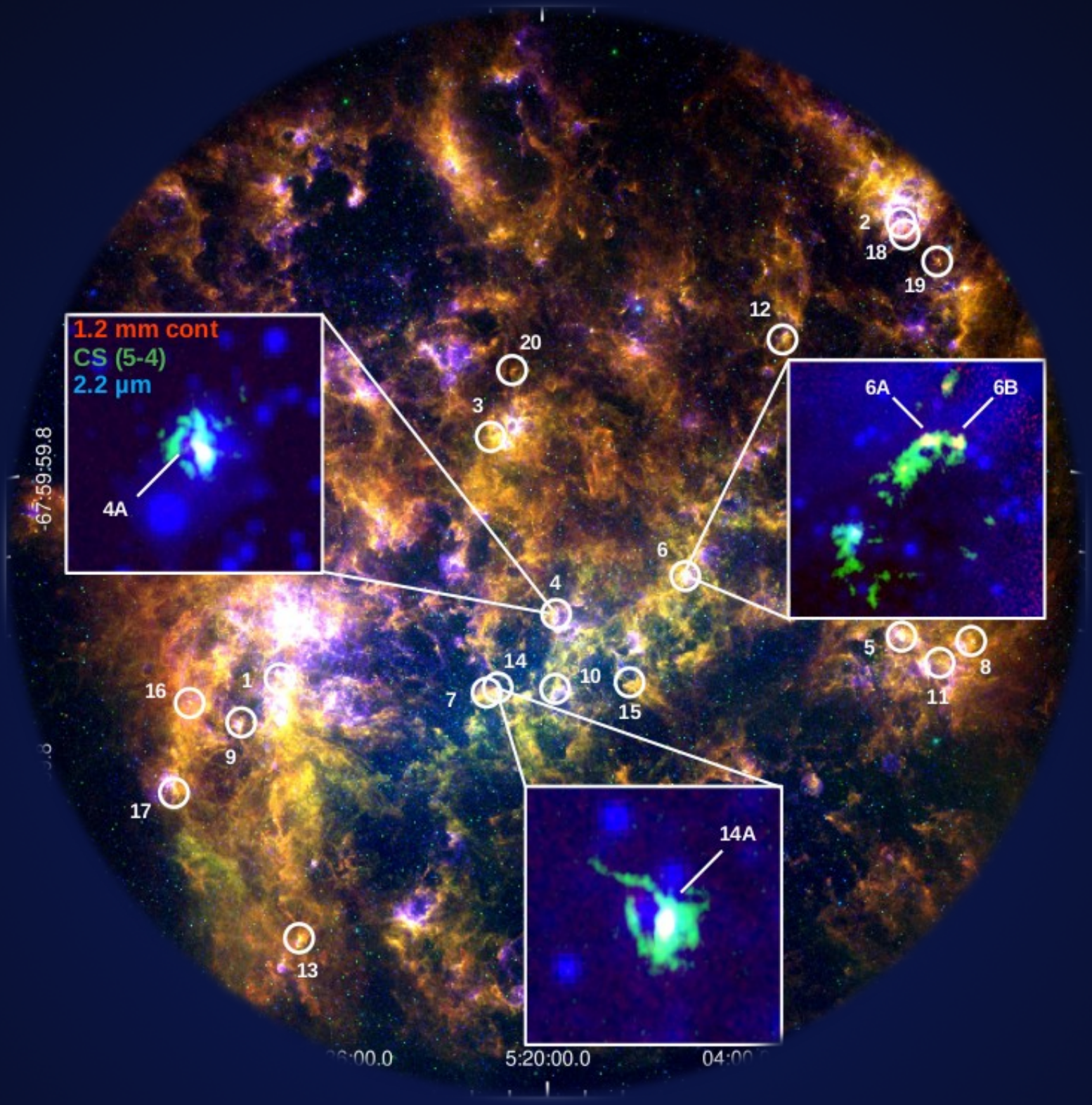
High-mass star formation across the Large Magellanic Cloud

Roya Hamedani Golshan

DISSERTATION



High-mass star formation across the Large Magellanic Cloud

Inaugural-Dissertation

zur
Erlangung des Doktorgrades
der Mathematisch-Naturwissenschaftlichen Fakultät
der Universität zu Köln



vorgelegt von

Roya Hamedani Golshan
aus Esfahan, Iran

Köln, 2025

Supervisor:
Prof. Dr. Peter Schilke
Dr. Álvaro Sánchez-Monge

Berichterstatter (Gutachter):
Prof. Dr. Peter Schilke
Prof. Dr. Andreas Eckart

Vorsitzender der Komission:
Prof. Dr. Ulrich Löhnert

Tag der mündlichen Prüfung: 21. März 2025

Erklärung zur Dissertation

Hiermit versichere ich an Eides statt, dass ich die vorliegende Dissertation selbstständig und ohne die Benutzung anderer als der angegebenen Hilfsmittel und Literatur angefertigt habe. Alle Stellen, die wörtlich oder sinngemäß aus veröffentlichten und nicht veröffentlichten Werken dem Wortlaut oder dem Sinn nach entnommen wurden, sind als solche kenntlich gemacht. Ich versichere an Eides statt, dass diese Dissertation noch keiner anderen Fakultät oder Universität zur Prüfung vorgelegen hat; dass sie - abgesehen von unten angegebenen Teilpublikationen und eingebundenen Artikeln und Manuskripten - noch nicht veröffentlicht worden ist sowie, dass ich eine Veröffentlichung der Dissertation vor Abschluss der Promotion nicht ohne Genehmigung des Promotionsausschusses vornehmen werde. Die Bestimmungen dieser Ordnung sind mir bekannt. Darüber hinaus erkläre ich hiermit, dass ich die Ordnung zur Sicherung guter wissenschaftlicher Praxis und zum Umgang mit wissenschaftlichem Fehlverhalten der Universität zu Köln gelesen und sie bei der Durchführung der Dissertation zugrundeliegenden Arbeiten und der schriftlich verfassten Dissertation beachtet habe und verpflichte mich hiermit, die dort genannten Vorgaben bei allen wissenschaftlichen Tätigkeiten zu beachten und umzusetzen. Ich versichere, dass die eingereichte elektronische Fassung der eingereichten Druckfassung vollständig entspricht.

Teilpublikationen:
1. Hamedani Golshan et al. (2024): *High-mass star formation across the Large Magellanic Cloud I. Chemical properties and hot molecular cores observed with ALMA at 1.2 mm* Hamedani Golshan, R., Sánchez-Monge, Á., Schilke, P., et al. 2024, A&A, 688, A3

Roya Hamedani Golshan

Köln, den 12.01.2025

Abstract

Star formation is a fundamental process that shapes the evolution of galaxies, with high-mass ($(M > 8\ M_{\odot})$) star formation playing a critical role as a major driver of energy input and chemical enrichment. Despite significant progress, the mechanisms governing (high-mass) star formation remain incompletely understood, particularly within the unique extragalactic environments of the Large Magellanic Cloud (LMC).

The LMC provides a rare laboratory for studying high-mass star formation under distinct environmental conditions compared to our Galaxy, the Milky Way, including lower metallicity, enhanced ultraviolet (UV) radiation, reduced cosmic ionization rates, and large-scale dynamical interactions. These factors might influence key star-formation processes such as fragmentation, core mass distribution, clustering, chemical composition, and feedback mechanisms. Thus, studying these processes in the LMC offers critical insights into how environmental factors shape star formation across different galactic contexts.

This thesis presents the first systematic survey of 20 massive young stellar objects in the LMC, selected from *Spitzer* and *Herschel* catalogs. The sample spans diverse physical and chemical conditions, evolutionary stages, and locations across the LMC, where metallicity gradients and varying levels of external feedback provide a statistically significant dataset for understanding star formation.

Using high-resolution observations from ALMA, complemented by ATCA data and ancillary datasets from *Herschel*, *Spitzer*, and VISTA, this study explores the physical and chemical properties of star-forming regions. Among the main findings of this work, the high-angular resolution reveal diverse fragmentation and clustering patterns. Chemical properties exhibit a complex interplay with metallicity, deviating from linear scaling, and signatures of large-scale interactions and metallicity mixing emerge. The detection of filaments, outflows, and HII regions further confirms the dynamic feedback processes shaping gas morphology.

This multiwavelength characterization of 20 star-forming regions advances our understanding of high-mass star formation in low-metallicity environments, emphasizing the influence of environmental diversity. By combining physical, chemical, and kinematic insights, this study provides a statistically robust foundation for future extragalactic star formation research.

Contents

Abstract **v**

1 Introduction **1**
1.1 Star formation . . . 1
1.1.1 From clouds to cores . . . 1
1.1.2 Astrochemistry in star formation . . . 4
1.2 Large Magellanic Cloud and the conditions for star formation . . . 5
1.2.1 Structure and dynamics of the Magellanic System . . . 6
1.2.2 LMC conditions for star formation . . . 9
1.3 About this work . . . 11
1.3.1 Methods and strategies . . . 11
1.3.2 Sample selection . . . 15
1.3.3 Goals and outline . . . 17

2 Dense cores and clusters observed with ALMA at 1.2 mm **19**
2.1 Introduction . . . 20
2.2 Observations . . . 21
2.2.1 Sample selection . . . 21
2.2.2 ALMA observations . . . 21
2.3 Analysis and results . . . 24
2.3.1 Identification and physical properties of the cores . . . 25
2.3.2 Properties of the hosting clouds . . . 29
2.3.3 Cluster analysis of 1.2 mm continuum cores . . . 31
2.4 Discussion . . . 32
2.4.1 Collapse and fragmentation; from clouds to cores and beyond . . . 33
2.4.2 Cluster properties in the sub-solar metallicity . . . 41
2.5 Conclusions . . . 47

3 Chemical properties and hot molecular cores observed with ALMA at 1.2 mm **49**
3.1 Introduction . . . 50
3.2 Observations and sample . . . 53

3.2.1 Sample selection . . . 53
3.2.2 ALMA observations . . . 56
3.3 Results and analysis . . . 57
3.3.1 Spectral analysis of the continuum cores . . . 59
3.3.2 Results from spectral analysis . . . 63
3.4 Discussion . . . 68
3.4.1 Hot cores in our survey . . . 68
3.4.2 Properties of hot cores in the LMC . . . 73
3.4.3 Hot cores in the LMC, SMC, and MW . . . 75
3.4.4 Location of hot cores in the LMC . . . 77
3.5 Conclusions . . . 81

4 Filaments, outflow and radiative feedback 83
4.1 Morphology of the molecular gas . . . 83
4.1.1 Molecular filaments . . . 84
4.1.2 Molecular outflows . . . 87
4.2 Ionized gas: Radiative feedback . . . 89
4.3 Morphology and feedback deriving the star formation evolution . . . 92

5 A multi-wavelength view 95
5.1 Multi-wavelength tracers of star formation . . . 95
5.2 Morphology of the gas and dust in each field across scales . . . 98
5.3 Classifying the target fields . . . 102
5.4 Are we witnessing an evolutionary sequence? . . . 103

6 Conclusion and outlook 107

Appendix A Continuum images and their analysis 111
A.1 Continuum Maps . . . 111
A.2 Physical parameters of 1.2 mm cores . . . 111
A.3 Minimum Spanning Trees . . . 131
A.4 Physical properties in each field . . . 131

Appendix B Observed spectra and XCLASS spectral analysis result 137
B.1 Spectra and XCLASS fits for 1.2 mm continuum cores . . . 137
B.2 XCLASS fits parameters . . . 196

Appendix C Comparisons of molecular abundances in hot cores with chemical models 211

Appendix D Filaments detected in the 20 star-forming regions 215

Appendix E HII regions **219**

Appendix F Multi-wavelength view of the target regions **223**

List of Figures

1.1 Schematic evolutionary sequences for the early phases of massive star formation have been proposed by Motte et al. (2018a). In Section 1.1.1, a detailed description of each phase, identified by assigned numbers, is provided. 2

1.2 Elements of the interactions within the Magellanic System and with the MW. For a detailed description, see Section 1.2.1. Credit: NASA, ESA, and L. Hustak (STScI). 7

1.3 Color-composite image of the LMC combining the HERITAGE/SPIRE 350 μm (red, Meixner et al., 2013), SAGE/IRAC 8 μm (green, Meixner et al., 2006), and Hα (blue, Smith et al., 2000) images. The positions of the 20 ALMA fields are marked with white circles 15 times larger than the field of view of our ALMA observations and the field number (see Section 1.3.2) 12

1.4 Artist's rendering of the Atacama Large Millimeter Array (ALMA) in an extended configuration. ALMA (ESO/NAOJ/NRAO)/L. Calçada (ESO) – (Not referred to in the text) 13

1.5 Five of the six antennas of the Australian Telescope Compact Array (ATCA) arranged on the main East-West track and the North spur (the latter is the horizontal track shown in this image). Credit: ATNF/CSIRO – (Not referred to in the text) 14

1.6 Spitzer spectra of our target YSOs grouped with the classification from Jones et al. 2017. From top to bottom are the YSO1 and YSO2, YSO3, YSO3-HII, and HII (for more details see the text) 16

2.1 Color-composite image of the LMC combining the HERITAGE/SPIRE 350 μm (red, Meixner et al., 2013), SAGE/IRAC 8 μm (green, Meixner et al., 2006), and Hα (blue, Smith et al., 2000) images. The positions of the 20 ALMA fields are marked with white circles 15 times larger than the field of view of our ALMA observations and the field number. . . . 22

2.2 The 1.2 mm pb-corrected continuum maps for Field 1 and 2: *left* an overview to the field, *right* a detailed view to the region inside the black rectangle on the left side panel. The contours show the 3, 6, and 9 times the $\sigma_{\rm rms}$. The identified cores are highlighted with white contours at 50% of the peak emission. The position of the YSOs is marked with a yellow star. The synthesized beam of the images and a scale bar are shown in the bottom-left and -right corners of each panel. 24

2.3 KDE distribution of physical properties of continuum sources. *Top* Source radiia, flux density, and luminosity. The minimum detectable flux density is calculated for a circular source, with a size equal to the average beam size and a Gaussian intensity profile with a peak intensity of five times the typical $\sigma_{\rm rms}$ level of the continuum images. *Bottom* mass, number density, and surface density of molecular hydrogen. The mass sensitivity is based on the minimum detectable flux at a temperature of 27 K. 28

2.4 KDE distribution of mass, number density, and column density for the target clouds. 30

2.5 Minimum spanning tree (MST) for the ALMA continuum cores in the most populated fields: *left* field 6 and *right* field 13. The positions of the dense cores are indicated with circles, scaled with the mass of the cores, while the lines mark the tree. 32

2.6 KDE of the projected separation between nearest neighbors for the 12 fields with more than two dense cores. 33

2.7 *Top*: Total core mass versus cloud mass in each field. *Middle*: Maximum core mass vs. cloud mass in each field. The dashed lines indicate CFE of 2%, 5%, 10%, and 20%. *Bottom*: Maximum core mass vs. total core mass in each field. The lines indicate the ratio of total core mass in the most massive core. 35

2.8 *Left*: $T_{\rm core}$ vs. $T_{\rm cloud}$. The iso-thermal line signaling the same temperate within the cores and hosting clouds is depicted with dashed line. *Right*: $M_{\rm core}$ vs. $M_{\rm cloud,\ th-J}$. The dashed line represents the thermal Jeans fragmentation, where $M_{\rm core} = M_{\rm cloud,\ th-J}$. The cores with minimum and maximum value in each field are indicated with magenta triangle and indigo circle. 37

2.9 Virial mass vs. the $M_{\rm core}$. The dashed lines representing virial parameters $\alpha = 0.1$, 1, and 2. 38

2.10 Comparisons of total Jeans mass and core masses. The inserted lines show the possible number of fragments form. *Left*: Assuming a fragmentation efficiency of 100%. *Right*: Assuming a self-similar frag mention across the scales as suggested by Xu et al. (2024) and adapting a fragmentation efficiency of 5%, obtained from CFE from clouds to cores in our sample. 40

2.11 Cumulative core mass function (CMF), *Left panels* for all the cores and *Right panels* excluding cores with ATCA detection. The observed CMF is fitted with *Top panels* Kroupa mass function scaled to core masses and *Bottom panels* double power-law. The best fit curve, and free parameters for fitting is indicated in each panel. The Salpeter IMF and mass sensitivity are depicted for reference. 43

2.12 Correlation of mass and radius of the cores. Colored symbols represent the cores in the LMC from our sample, as well as Sewiło et al. (2022) and Brunetti & Wilson (2019). Gray symbols indicate Galactic structures from Xu et al. (2024). The two lines, along with their respective uncertainties (indicated by the shaded regions), show the fits to the Galactic and the LMC data points. 46

2.13 Spatial distribution of cores in the cluster with respect to their mass. The dashed-dotted lines represent the mass sensitivity limit and the average synthetic beam size for our sample. The two gray lines divide the parameter space into four quadrants. The vertical gray line separates cores with separation sizes smaller than the median separation (from Fig. 2.6) from those with larger separations. The horizontal gray line is positioned just above the most massive cores with separations larger than the median separation. The percentage of cores in each quadrant is indicated within the plot. 46

3.1 Color-composite image of the LMC combining the Hα (blue, Smith et al., 2000), SAGE/IRAC 8 μm (green, Meixner et al., 2006), and HERITAGE/SPIRE 350 μm (red, Meixner et al., 2013) images. The positions of the 20 ALMA fields are marked with white circles 15 times larger than the field of view of our ALMA observations and the field number. The color-composite images of the fields with hot core detection combining the VMC K-band (blue, Cioni et al., 2011), ALMA CS (5–4) peak intensity (green, this work), and 1.2 mm ALMA continuum (red, this work and Paper II) images are shown as insets. The hot cores reported in this paper, 4A (ST16; Shimonishi et al., 2020), 6A (N105-2 B; Sewiło et al., 2022), 6B (N105-2 A; Sewiło et al., 2022), and 14A are highlighted in the insets images. 54

3.2 Examples of the 1.2 mm continuum emission toward four regions of the LMC sample. The contours show the three, six, and nine times the σ_{rms}. The identified compact cores are highlighted with white contours at 50% of the peak emission. The synthesized beam of the images and a scale bar are shown in the bottom-left and bottom-right corners of each panel, respectively. See Paper II for more details on the 20 fields observed across the LMC (see Table 3.1). 57

3.3 ALMA Band 6 observed spectra toward source 14A overlaid with the best-fit XCLASS model. Molecular transitions with definite detections (S/N $>$ 5) are represented by solid black lines, while those with tentative detections (3 $<$ S/N $<$ 5) are denoted by dotted gray lines. Dotted red lines indicate transitions of molecules for which abundance upper limits are provided. 58

3.4 Best-fit XCLASS temperature for different molecular tracers. In case of definite detection in more than two transitions, CH_3OH, SO_2, and CH_3CN were free for fitting (for more details, see Section 3.3.1). There is an uncertainty of 40%–60% for the temperatures. The sources are ordered by increasing mass (from Paper II), calculated with the temperature of the CH_3OH (cold) component to account for the total mass in the core. The hot cores are highlighted with yellow bars. 62

3.5 Best-fit XCLASS line width (full width at half maximum, FWHM) for different molecular species. The line width of 5 km/s is marked with a dashed line as a reference. There is an uncertainty of 10%–30% for the line widths. The sources are ordered by increasing mass (from Paper II) with the temperature of CH_3OH (cold) component to account for the whole mass in the core. The hot cores are highlighted with yellow bars. 63

3.6 Abundances of molecular species with a high detection rate in our sample. There is an uncertainty of 20%–40% on the column densities. The sources are ordered by increasing mass (from Paper II) with the temperature of CH_3OH (cold) component to account for the whole mass in the core. The hot cores are highlighted with yellow bars. The arrows show an upper-limit estimation. 65

3.7 The same as Fig. 3.6 but for S-bearing species, H_2CS, SO_2, and SiO. . . 65

3.8 Same as Fig. 3.6 but for N-bearing species, $H^{13}CN$, $HC^{15}N$, and HNCO. 66

3.9 Same as Fig. 3.6 but for N-bearing species, HC_3N, CH_3CN, and NH_2CHO. 66

3.10 Same as Fig. 3.6 but for O-bearing species, CH_3OCH_3, CH_3OCHO, and HDCO. 67

3.11 Peak-intensity images of the molecular species detected toward hot core 14A. The maps are ordered based on the frequency of the transition from left to right, top to bottom. The 1.2 mm continuum contours with contour levels of three, six, and nine times the σ_{rms} and the 50% 1.2 mm continuum contour are overlaid in each image for reference. Top is north and right is west. 70

3.12 Comparisons of the derived temperatures (left) and abundances (right) from the current study and the literature. The top panels show a comparison of 4A and ST16 (Shimonishi et al., 2020), the middle panels show 6A and N105-2B, and the bottom panels show 6B and N105-2A (Sewiło et al., 2022). An error range of 40% is depicted for the temperatures and column densities from the current paper. 72

3.13 Abundances of different molecular species for all the known hot cores in the LMC after scaling to the gas-to-dust mass ratio. The LMC hot cores are ST11 (Shimonishi et al., 2016a), 4A, 6A, 6B and 14A (this work), and N113 A1 and N113 B (Sewiło et al., 2022). Black arrows show an upper limit estimation. An error range of 40% is shown on the abundances from the current paper. 74

3.14 Comparisons of abundances for SO_2, CH_3OH, and CH_3CN from observations of the seven hot cores detected in this galaxy and the LMC hot core models for the final hot core temperature of 100 K (*top*) and 200 K (*bottom*). The black curves show abundances over time for an initial dust temperature of 10 (dotted curve), 15 (dashed curve), 20 (larger dashed curve), and 25 K (the solid curve). The horizontal colored line shows the single abundance value for each hot core and follows the same color code as Fig. 3.13 (see the text for more details). 75

3.15 Abundances of CH_3OH, CH_3CN, SO_2, and SiO for all known hot cores in the SMC and LMC and for a selection of Galactic hot cores. The SMC hot cores are included, S07 and S09 (Shimonishi et al., 2023). The LMC hot cores are ST11 (Shimonishi et al., 2016a), 4A, 6A, 6B and 14A (this work), and N113 A1 and N113 B (Sewiło et al., 2022). We selected four Galactic hot cores: an outer Galaxy hot core (Shimonishi et al., 2020), Orion Hot Core (HC) (Sutton et al., 1995), Sgr B2(N) (Nummelin et al., 2000), and W3(H_2O) (Helmich & van Dishoeck, 1997). The extent of each bar with a dotted pattern represents the abundances scaled to the Galactic metallicity. 78

3.16 Comparisons of the abundances of CH_3OH and CH_3CN and SO_2 and SO for the hot cores in the SMC (open green circles), LMC (red rectangles), and MW (black triangles for inner Galactic hot cores and gray triangle for outer Galactic hot core). Dashed lines show abundance relations of 1:1 for the top-right panel and 1:100 for the other panels. The dotted lines show a variation of a factor of ten above and below the relations described by the dashed lines. 78

3.17 Three color composite image of the LMC combining 3.6 μm (blue), 4.5 μm (green), and 5.8 μm (red Meixner et al., 2006) images to highlight the position of the stellar bar. The dashed ellipse marks the bar region. The 20 ALMA fields from the current study are overlaid with white circles 15 times larger than the field of view of our ALMA observations. The fields accommodating hot cores are highlighted in yellow, including the YSO ST16 and N105 star-forming region. The field marked with a star shows the position of the new hot core detected in our survey. The location of the hot cores in N105 (Sewiło et al., 2022) and N113 (Sewiło et al., 2018) are marked with yellow rectangles. The hot cores ST11 (Shimonishi et al., 2016b) and ST16 (Shimonishi et al., 2020) are shown with yellow plus signs. The hot core ST11 with no COMs is the only hot core detected out of the LMC bar. 79

4.1 Filaments detected in the CS peak-intensity maps for Fields 1 and 2. . 84

4.2 KDE of filaments properties. 87

4.3 Outflows detected toward continuum cores 4A (top panel), 6A (middle panel), and 14A (bottom panel). The left panel in each row shows the CS peak intensity map overlaid with continuum contours at 5, 15, 30, and 45 $\sigma_{\rm rms}$, as well as red- and blue-shifted outflow lobes at 0.6 and 0.75 of the maximum value from the integrated intensity maps over the velocity range highlighted in the right panel. The right panel displays the SiO spectra averaged over the source polygon, with red- and blue-shifted lobes marked using the corresponding color spans. 88

4.4 Rotation detected toward continuum cores 4A (top panel) and 14A (bottom panel) in a direction approximately perpendicular to the outflow direction. The left panel in each row shows the CS peak intensity map overlaid with continuum contours at 5, 15, 30, and 45 $\sigma_{\rm rms}$, along with the outflow direction and a position-velocity (PV) slice. The right panel displays the PV diagram along the PV slice depicted in the left panel. . 90

4.5 ATCA 4 cm maps, tracing the free-free continuum emission for Fields 3 and 4. ALMA 1.2 mm continuum contours are overlaid at 4, 8, 12 times the $\sigma_{\rm rms}$. 91

4.6 Proposed evolutionary sequence of star formation in the LMC. Based on the study of gas morphology and the detection of filaments, outflows, and HII regions in the 20 target fields, I propose an evolutionary sequence for star-forming regions in the LMC. Arrow indicates the direction of evolution. The number of fields at each stage is shown, and a legend explains the symbols used for different object types. For a detailed explanation, see Section 4.3. 94

5.1 Multi-wavelength view of Field 1. For caption details see Appendix F. . 96

5.2 Proposed evolutionary sequence of star formation in the LMC. Based on the study of gas morphology and the detection of filaments, outflows, and HII regions within the 20 target fields, as well as the morphology of gas and dust on larger scales surrounding these regions, I expand the evolutionary sequence presented in Figure 4.6 for star-forming regions in the LMC. Arrow indicates the direction of evolution. Internal stages of star formation (as defined in the text and Table 5.1) are shown. Two categories of star formation, based on the nature of the large-scale ambient gas and dust, are shown to highlight a correlation between early-stage star formation and externally active environments, and later stages with more quiescent surroundings. A legend explains the symbols used for different object types. For a detailed explanation, see Section 5.4. . . . 106

A.1 The 1.2 mm pb-corrected continuum maps for Field 3: *left* an overview to the field, *right* a detailed view to the region inside the black rectangle(s) on the left side panel. The contours show the 3, 6, and 9 times the $\sigma_{\rm rms}$. The identified cores are highlighted with white contours at 50% of the peak emission. The position of the YSOs is marked with a yellow star. The position of H_2O, and OH and H_2O masers are also marked with a pentagon and triangle, respectively, where there is a detection (only in Fields 6 and 17). The synthesized beam of the images and a scale bar are shown in the bottom-left and -right corners of each panel. 112
A.2 Same as Fig. A.1 for Field 4. 112
A.3 Continued. 113
A.4 Continued. 114
A.5 Continued. 115
A.6 Continued. 116
A.7 Continued. 116
A.8 Continued. 117
A.9 Continued. 118
A.10 Continued. 118
A.11 Continued. 119
A.12 Continued. 120
A.13 Continued. 121
A.14 Continued. 121
A.15 Continued. 122
A.16 Continued. 122
A.17 Continued. 123
A.18 Continued. 123
A.19 Minimum spanning tree (MST) for the ALMA continuum cores in Fields 2, 3, 7, 8, 10, 11. The positions of the dense cores are indicated with circles, scaled with the mass of the cores, while the lines mark the tree. 132
A.20 Same as Fig. A.19 but for Fields 12, 15, 18 and 19. 133
A.21 $M_{\rm core}$ from all the cores in each field. The median core mass in each field is shown with a star mark. 134
A.22 Like Fig. A.21 for $L_{\rm core}$ 134
A.23 Core formation efficiency in each field 134
A.24 Luminosity ratio in each field 134
A.25 Estimated Virial parameter ($\alpha_{\rm vir}$) 135
A.26 Estimated magnetic field strength to support the cores from collapse . . 135

B.1 ALMA Band 6 observed spectra toward source 1A overlaid with the best-fit XCLASS model. Molecular transitions with definite detections (S/N > 5) are represented by solid black lines, while those with tentative detections (3 < S/N < 5) are denoted by dotted gray lines. Dotted red lines indicate transitions of molecules for which abundance upper limits are provided. (See Section 3.3.1 for more details.) 138
B.2 Same as Fig. B.1 but for source 2A. 139
B.2 Same as Fig. B.1 but for source 2B. 140
B.2 Same as Fig. B.1 but for source 2C. 141
B.2 Same as Fig. B.1 but for source 2D. 142
B.2 Same as Fig. B.1 but for source 2E. 143
B.2 Same as Fig. B.1 but for source 2F. 144
B.3 Same as Fig. B.1 but for source 3A. 145
B.3 Same as Fig. B.1 but for source 3B. 146
B.3 Same as Fig. B.1 but for source 3C. 147
B.3 Same as Fig. B.1 but for source 3D. 148
B.4 Same as Fig. B.1 but for source 4A. 149
B.5 Same as Fig. B.1 but for source 5A. 150
B.5 Same as Fig. B.1 but for source 5B. 151
B.6 Same as Fig. B.1 but for source 6A. 152
B.6 Same as Fig. B.1 but for source 6B. 153
B.6 Same as Fig. B.1 but for source 6C. 154
B.6 Same as Fig. B.1 but for source 6D. 155
B.6 Same as Fig. B.1 but for source 6E. 156
B.6 Same as Fig. B.1 but for source 6F. 157
B.7 Same as Fig. B.1 but for source 7A. 158
B.7 Same as Fig. B.1 but for source 7B. 159
B.7 Same as Fig. B.1 but for source 7C. 160
B.8 Same as Fig. B.1 but for source 8A. 161
B.8 Same as Fig. B.1 but for source 8C. 162
B.9 Same as Fig. B.1 but for source 9A. 163
B.10 Same as Fig. B.1 but for source 10A. 164
B.10 Same as Fig. B.1 but for source 10B. 165
B.10 Same as Fig. B.1 but for source 10C. 166
B.10 Same as Fig. B.1 but for source 10D. 167
B.11 Same as Fig. B.1 but for source 11B. 168
B.11 Same as Fig. B.1 but for source 11C. 169
B.11 Same as Fig. B.1 but for source 11D. 170
B.12 Same as Fig. B.1 but for source 12A. 171

B.12 Same as Fig. B.1 but for source 12B. 172
B.12 Same as Fig. B.1 but for source 12C. 173
B.12 Same as Fig. B.1 but for source 12D. 174
B.13 Same as Fig. B.1 but for source 13A. 175
B.13 Same as Fig. B.1 but for source 13C. 176
B.13 Same as Fig. B.1 but for source 13D. 177
B.13 Same as Fig. B.1 but for source 13E. 178
B.13 Same as Fig. B.1 but for source 13F. 179
B.13 Same as Fig. B.1 but for source 13G. 180
B.13 Same as Fig. B.1 but for source 13H. 181
B.13 Same as Fig. B.1 but for source 13K. 182
B.14 ALMA Band 6 observed spectra toward source 14B with no emission line detections. (See Section 3.3.1 for more details.) 183
B.15 Same as Fig. B.1 but for source 15A. 184
B.15 Same as Fig. B.1 but for source 15B. 185
B.15 Same as Fig. B.1 but for source 15C. 186
B.16 Same as Fig. B.1 but for source 16B. 187
B.17 Same as Fig. B.1 but for source 17A. 188
B.18 Same as Fig. B.1 but for source 18A. 189
B.18 Same as Fig. B.1 but for source 18B. 190
B.18 Same as Fig. B.1 but for source 18C. 191
B.19 Same as Fig. B.1 but for source 19A. 192
B.19 Same as Fig. B.1 but for source 19C. 193
B.19 Same as Fig. B.1 but for source 19D. 194
B.20 Same as Fig. B.1 but for source 20A. 195
B.21 Comparisons of the LTE and non-LTE fit for two CH_3OH lines at 241.767 and 241.791 GHz. 196

C.1 Comparisons of abundances for CS, SO, SiO, H_2CS, HNCO, and NH_2CHO from observations of the seven hot cores detected in the LMC and the LMC hot core models for the final hot core temperature of 100 K. The black curves show abundances over time for initial dust temperatures of 10 (dotted line), 15 (dashed curve), 20 (larger dashed curve), and 25 K (solid curve; this curve does not necessarily appear in the range of abundances in the plot). The horizontal colored line shows the single abundance value for each hot core and follows the same color code as Fig. 3.13 (see the text for more details). 212
C.2 Same as Fig. C.1 but for the LMC hot core models for the final hot core temperature of 200 K. 213

D.1 Filaments detected in the CS peak-intensity maps for Fields 3 to 11. . . 216
D.2 Same as Fig. D.1 but for Fields 12 to 19. 217

E.1 ATCA 4 cm maps, tracing the free-free continuum emission for Fields 5, 7, 8, 12, 13, 15, 16 and 17. ALMA 1.2 mm continuum contours are overlaid at 4, 8, 12 times the $\sigma_{\rm rms}$. 220
E.2 Same as Fig. E.1 for Fields 19 and 20. 221

F.1 Multi-wavelength view of Field 2. For caption details see the Appendix text. 224
F.2 Same as Fig F.1 but for Field 3. 225
F.3 Same as Fig F.1 but for Field 4. 226
F.4 Same as Fig F.1 but for Field 5. 227
F.5 Same as Fig F.1 but for Field 6. 228
F.6 Same as Fig F.1 but for Field 7. 229
F.7 Same as Fig F.1 but for Field 8. 230
F.8 Same as Fig F.1 but for Field 9. 231
F.9 Same as Fig F.1 but for Field 10. 232
F.10 Same as Fig F.1 but for Field 11. 233
F.11 Same as Fig F.1 but for Field 12. 234
F.12 Same as Fig F.1 but for Field 13. 235
F.13 Same as Fig F.1 but for Field 14. 236
F.14 Same as Fig F.1 but for Field 15. 237
F.15 Same as Fig F.1 but for Field 16. 238
F.16 Same as Fig F.1 but for Field 17. 239
F.17 Same as Fig F.1 but for Field 18. 240
F.18 Same as Fig F.1 but for Field 19. 241
F.19 Same as Fig F.1 but for Field 20. 242

List of Tables

1.1 Target coordinates and type. 15

2.1 Field coordinates and the continuum image parameters observed with the ALMA. 23
2.2 Physical properties of the clouds derived from SED fitting on the Herschel bands observations. 30
2.3 Core separations in each field from MST analysis 31

3.1 Coordinates and names of our target fields. 55
3.2 Spectral cube parameters for primary beam corrected images. 55
3.3 Definite and tentative detections of molecular species along with the corresponding number of sources exhibiting these emissions. 59

4.1 Properties of the filaments derived from `Filfinder` analysis of the CS peak intensity maps. 86
4.2 Physical properties of the HII regions derived from ATCA 4 cm maps. . 92
4.3 Summary of internal gas morphology and feedback in the 20 star-forming regions. 93

5.1 Summary of internal and external gas and dust morphology and feedback in the 20 star-forming regions. 104

A.1 Physical properties of 1.2 mm continuum cores. 124
A.2 Inferred properties of the cores. 127

B.1 Parameters of the LTE fits for CH_3OH. 197
B.2 Parameters of the best-fit model for all detected molecules and their abundances. 199

Chapter 1

Introduction

1.1 Star formation

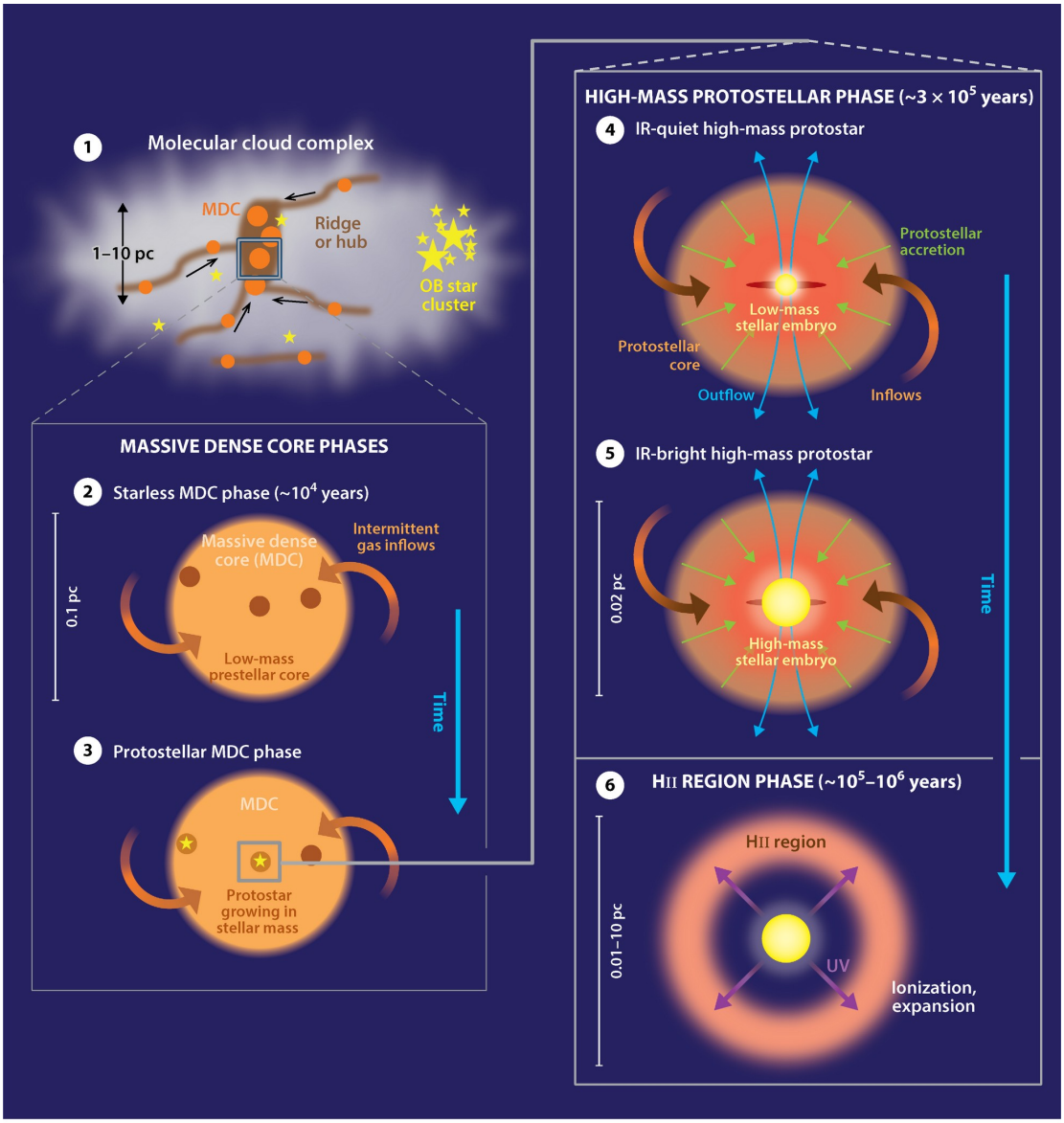
Stars glow in our night sky, some brighter and some dimmer. The difference in their luminosity is a function of their mass, age and their distance to earth. Astronomers differentiate between low to intermediate mass and high mass stars, as their evolutionary paths from formation to death vary significantly. This section focuses on the formation of high mass stars, highlighting their importance and relevance to the research conducted.

High mass stars ($M > 8\ M_{\odot}$) are vital for the cosmic ecosystem. From their birth to the death, they are contributing significantly to the structural evolution, energy dynamics and chemical complexity of the galaxies. These stars are essential for producing the heavy elements necessary for the formation of complex species and the emergence of life. This section presents an overview of the high mass star formation process (Section 1.1.1) and the chemical development within star-forming regions (Section 1.1.2).

1.1.1 From clouds to cores

Stars are born in vast, cold, and dense regions of interstellar space known as molecular clouds. These clouds, primarily composed of molecular hydrogen (H_2) along with other molecules and dust, serve as the cradles of star formation. Spanning tens to hundreds of parsecs (pc), molecular clouds exhibit a turbulent and clumpy structure, often organized into complex networks of elongated filaments and dense ridges. Filaments act as conduits for mass transport, channeling material into hubs and ridges—regions of enhanced density where gravitational forces begin to dominate over internal pressure. These dense regions serve as the sites of intense star formation, particularly for high-mass stars.

In the context of high-mass star formation, these molecular clouds must satisfy specific conditions, such as sufficient mass and density, to overcome the challenges



Motte F, et al. 2018.
Annu. Rev. Astron. Astrophys. 56:41–82

Figure 1.1: Schematic evolutionary sequences for the early phases of massive star formation have been proposed by Motte et al. (2018a). In Section 1.1.1, a detailed description of each phase, identified by assigned numbers, is provided.

posed by their energetic feedback and rapid evolution. Understanding how these clouds transition into protostars and eventually high-mass stars involves dissecting a sequence of stages, each characterized by distinct physical and chemical phenomena.

The empirical scenario proposed by Motte et al. (2018a) breaks down the early phases of high-mass star formation into several key stages. This is a qualitative replication of global hierarchical collapse and clump-fed accretion scenarios (e.g., Smith et al., 2009; Vázquez-Semadeni et al., 2017). The stages described below are shown in Fig. 1.1 with the assigned numbers.

1. Molecular cloud complex: High-mass stars preferentially form in regions known as hubs and ridges, which are massive clumps and filaments with sizes on the parsec scale. These hubs and ridges are embedded within molecular cloud com-

plexes, and their velocity and density structures suggest they undergo a globally controlled collapse. The initial conditions in these environments set the stage for subsequent fragmentation and star formation.

2. Starless Massive Dense Cores (MDCs): As the hubs and ridges experience global collapse, they fragment into MDCs approximately 0.1 parsec in scale. Initially, these fragments are referred to as IR-quiet MDCs, meaning they lack significant infrared emission indicative of active protostellar heating. At this stage, the cores are starless but developing low-mass prestellar cores in their interior. This phase is transient, lasting for about 10^5 years, and represents the earliest phase of core formation in high-mass star-forming regions.

3. Protostellar MDCs: As the gas stream developed by global collapse of along the filament or throughout the clump flow into the even smaller scales of 0.02 pc, the mass of starless MDCs increases and they evolve to protostellar objects. This evolution marks the transition from a starless core to one that harbors a protostar, signaling the beginning of significant mass accumulation.

4. IR-quiet high-mass protostar: This phase occurs when inflowing gas streams efficiently reach and feed low-mass protostellar cores, allowing them to grow into high-mass protostars. During this phase, the protostars still contain low-mass (< 8 $M_\odot$) stellar embryos, but their strong accretion rates drive outflows and raise the surrounding temperatures to 100-200 K, creating regions known as hot molecular cores. These cores are characterized by rich chemistry and play a crucial role in the development of the protostar's internal structure and its immediate environment.

5. IR-bright high-mass protostar: As the mass of stellar embryos crosses the 8 $M_\odot$ threshold, their luminosity increases significantly, transitioning them into IR-bright high-mass protostars. At this stage, the surrounding hot molecular core expands, and hyper-compact HII regions -zones of ionized hydrogen formed by the high-energy photons emitted by the protostar- begin to develop. These regions are confined to the accretion disk within the infalling envelope. This phase marks a critical transition, where increasing radiation from the the protostar exerts a growing influence on its immediate environment.

6. HII Regions: The increasing UV field radiation from the stellar embryos results in the development of HII regions. These regions, along with other processes including outflows and winds, slow down and ultimately halt gas accretion toward the newborn star, leading to the termination of the main accretion phase. The formation of HII regions signifies the star's transition to a phase, where it begins to influence its broader environment more significantly.

This simplified picture of high-mass star formation is highly dynamic and involves multi-scale evolution of the interstellar medium (ISM). Following this description of the high-mass star formation evolutionary sequence, the next section will focus on the chemical development of the interstellar gas and dust.

1.1.2 Astrochemistry in star formation

Astrochemistry is the study of the chemical interactions, processes, and compositions of astronomical objects. It combines principles of astronomy and chemistry to understand the formation, destruction, evolution, and distribution of chemical compounds in the universe. In this section, I focus particularly on the molecular chemistry initiated in star forming regions, tracing the formation of simple molecules to complex organic molecules (COMs; molecules with more that six atoms including carbon Herbst & van Dishoeck, 2009). The formation of very complex compounds, such as polycyclic aromatic hydrocarbons (PAHs)[1], fullerenes, and other large molecules, is beyond the scope of this dissertation.

Molecular hydrogen (H_2) is the simplest and most abundant molecule in the ISM. H_2 does not form efficiently in the gas phase to the extent required to explain its abundance. Since the early 1940s, it has been thought that dust grains play a catalytic role in H_2 formation by increasing the cross section of interaction for atomic hydrogen. Essentially, hydrogen atoms stick to dust grains, diffuse across the grain surface, and react in the so-called diffuse molecular clouds phase (where the density, n_H, is $\sim$ 100 cm^{-3}). The efficiency of H_2 formation varies in different phases of the ISM, influenced by physical conditions and sources of radiation. Wakelam et al. (2017) presents an in-depth view of H_2 formation across different regions.

The second most abundant molecule in the ISM is carbon monoxide (CO). In regions of the cloud where ionized carbon (C^+) is shielded from interstellar Far-Ultra-Violet (FUV) radiation, it transitions to neutral C or CO. In the cold (10-100 K) and moderately dense ($n_H \sim 10^2$-10^4 cm^{-3}) parts of the molecular cloud, ion-neutral reactions dominate the chemical processes. Under these conditions, reactions with barriers, endothermic reactions, and multi-body collisions are unlikely. Cosmic rays play a crucial role by ionizing H_2 to form $H_3{}^+$, which drives the interstellar chemistry. A series of ion-neutral reactions lead to the formation of simple molecules such as H_2O, HCO^+, and HCN^+.

As molecular clouds become colder and denser, gas-phase molecules freeze onto dust grain surfaces, forming ices. Different molecules have varying sticking efficiencies, resulting in layered ice structures. As the cloud continues to condense (as detailed in

[1]Large, carbon-based molecules found in space, composed of multiple aromatic rings. They emit strongly in the infrared, particularly around 3–12 μm, when excited by UV radiation from young, massive stars.

Section 1.1.1), it fragments and enters the prestellar phase. At this stage the grain surface chemistry plays a crucial role in the development of the chemistry. The Hydrogenation (adhering H atoms that are the most mobile species on the grain surface) of simple molecules and reactions with CO are fundamental. With the impact of UV radiation or cosmic rays, radicals form from the molecules in the ice layers.

During the protostellar phase, mass accretion creates an inward temperature gradient. This gradient drives the evolution of surface chemistry, leading to ice sublimation as dust particles approach the hotter inner regions. As the temperature rises, radicals become more mobile on the grain surface and combine to form more complex species, including COMs. When temperatures reach approximately 100-200 K (in the hot molecular phase), the sublimation of ices releases the chemically enriched material into the gas phase. The most chemically rich phase occurs in the hot molecular cores (Bisschop et al. 2007; Belloche et al. 2013; Manna & Pal 2022a,b; Manna et al. 2023).

The protostar also generates jets and molecular outflows at various velocities, resulting in shocks that enable shock and hot-gas chemistry. High-velocity shocks can sputter or fragment dust grains, promoting silicon and sulfur-bearing chemistry, leading to the formation of species such as SiO, SO, and SO_2 (e.g., Schilke et al., 1997). In contrast, lower-velocity shocks contribute to the sublimation of ice layers and the release of molecules formed in the ices. The formation of molecules, including COMs, continues in the gas phase in the dense regions of hot molecular cores ($n_{H_2} \sim 10^6$ cm^{-3} Taquet et al., 2016).

The advent of new-generation receivers aboard radio observatories, equipped with broader frequency coverage, has facilitated numerous molecular line surveys in recent years at millimeter and sub-millimeter wavelengths (e.g., Belloche et al., 2013; Liu et al., 2020; Motte et al., 2022). These surveys focus on sources at various stages of star formation, offering critical insights into the intricate chemistry and physical processes that drive star formation and the evolution of molecular environments.

1.2 Large Magellanic Cloud and the conditions for star formation

Star formation requires continuous cooling to facilitate the contraction of gas. Metals, which are elements heavier than helium, serve as the main coolants in the interstellar medium (ISM). These heavier elements are produced through fusion processes within stars. Consequently, the metallicity, or the abundance of metals in the ISM, increases with cosmic age as stars evolve and new generations of stars are born and evolve again.

A fundamental question remains: how did star formation occur in the much warmer or even hotter ISM of the early universe, which had very low metallicity? Understanding the impact of metallicity on star formation is therefore of great importance. By

studying environments with varying metallicity, we can gain insights into the processes that governed star formation in the early universe and across cosmic time.

Metallicity typically shows a decreasing profile from the center of galaxies outward, and the Milky Way (MW) exhibits the same trend. The MW offers a wide range of metallicity in star-forming regions, from high metallicity in the central molecular zone to lower metallicity in the outskirts of the Galaxy (Rolleston et al., 2000). However, low-metallicity regions of the MW appear to be quiescent in terms of star formation, based on their radiation field strength, which is a tracer of star formation. Additionally, because of our position within the MW plane, Galactic observations often suffer from line-of-sight confusion.

Therefore, we considered local star-forming templates with low metallicity to investigate star formation under such conditions. The Magellanic System, a complex of the MW's satellite galaxies and their interacting gas streams, offers an excellent template for this study. The metallicity of the gas throughout the Magellanic System ranges from half solar metallicity to very low metal abundances ($\sim$ 0.1 solar metallicity). In this section, first we discuss the structure and dynamics of the Magellanic System (Section 1.2.1). Then we focus on the Large Magellanic Cloud (LMC) and the conditions it offers for star formation (Section 1.2.2).

1.2.1 Structure and dynamics of the Magellanic System

The Magellanic System refers to the two most luminous and massive satellite galaxies of the MW: the LMC and Small Magellanic Cloud (SMC), with three gaseous structures around them. These galaxies are located at a distance of $D_{LMC} \approx 49.59 \pm 0.09$ (statistical) $\pm$ 0.54 (systematic) kpc (Pietrzyński et al., 2019) and $D_{SMC} \approx 62.1 \pm 1.9$ (Graczyk et al., 2014) from the MW, respectively. They appear to be physically connected by a bridging gas, known as the Magellanic Bridge. The system includes both the mass flow leading their orbit, known as the Leading Arm and the trailing filaments left in their wake, known as the Magellanic or Trailing Stream.

The Magellanic System may be part of Magellanic Group, a collection of dwarf galaxies that fell into the MW's halo some time in the past (e.g., D'Onghia & Fox, 2016, and the refrences therein). This area of study is an active field of research, focusing on the observational detection of faint and ultra-faint dwarf galaxies with in the local group of the galaxies. Researchers aim to track the orbits of these galaxies to reconstruct their past trajectories through simulations and modeling. In the following, we only focus on the main known members of the System. We discuss the structure and dynamics of the Magellanic System in the context of interactions between the LMC and the SMC, as well as the interactions between the System and the MW.

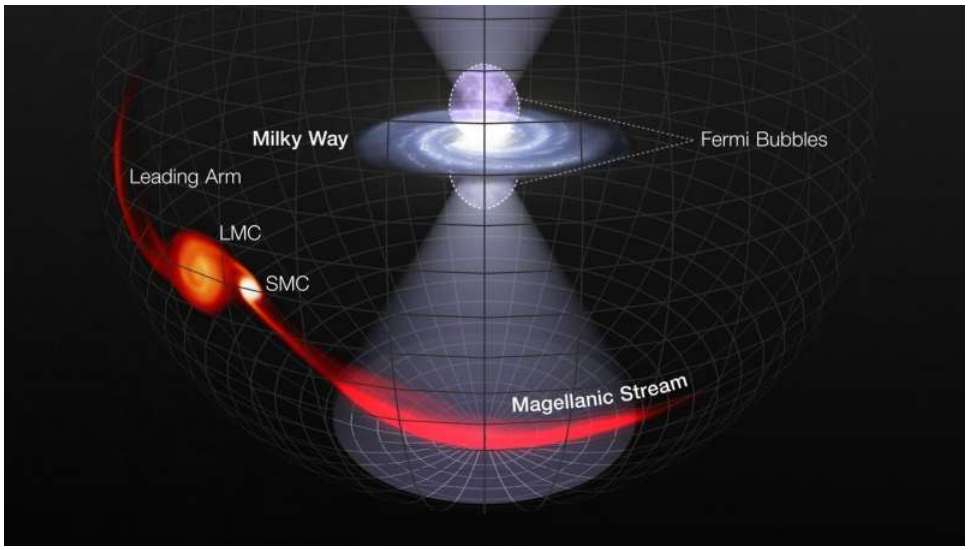


Figure 1.2: Elements of the interactions within the Magellanic System and with the MW. For a detailed description, see Section 1.2.1. Credit: NASA, ESA, and L. Hustak (STScI).

LMC and SMC interactions

LMC and SMC are interacting; the stretching of gas between the two galaxies is strong evidence of their physical connection, possibly from their encounter as recent as 100 Myrs ago (Besla et al., 2012). The Magellanic Bridge exhibits very low metal abundances ($\sim$ 0.1 $Z_\odot$), which is lower than the average metallicity of the LMC (Z_{LMC} $\sim$ 0.3-0.5 $Z_\odot$) and the SMC (Z_{SMC} $\sim$ 0.2 $Z_\odot$), complicating conclusions about its origin. Another piece of evidence for the interaction between the LMC and SMC is their morphological type. While the classification of the SMC remains uncertain, the LMC is a typical Magellanic Spiral galaxy. Magellanic Spirals are characterized by an asymmetry with the presence of a single arm, indicating that the galaxy is in a binary system and has an interacting companion.

Traditionally, the interaction between the two galaxies has been explained by their tidal interactions. However, measuring the proper motion of the stars in the Bridge from *Gaia* data suggested that the interaction was not merely a grazing event; instead, the SMC has passed through the LMC (Zivick et al., 2019). This event has undoubtedly impacted the composition of the ISM, and shaped the gas with high-velocity interactions (for details on the impact of this interaction on the distribution and morphology of gas in the LMC, see Section 1.2.2.).

Magellanic System and MW

Magellanic Clouds are also in interactions with the MW. Figure 1.2 illustrates the main elements of the Magellanic System in relation with the MW's components. A significant signature of this interaction is the extension of a gas network spanning

200° across the sky in the Magellanic Stream and the Leading Arm. As depicted in Fig. 1.2, the Leading Arm is leading the Clouds orbit toward the MW's disk, while the Magellanic Stream extends as a trailing filament.

The Leading Arm is primarily formed through tidal interactions. Analysis of the gas velocity along the Leading Arm suggests that the net velocity is directed towards the MW's disk, ruling out ram pressure stripping as the origin of formation. Instead, it suggests that tidal interaction with the MW is the formation origin.

The Magellanic Stream, with an atomic neutral and ionized gas mass of 2.7×10^8 and $\sim 10^9$ $M_\odot$ (see Table 1 from D'Onghia & Fox, 2016), respectively, consists of a double-helix filaments of clumpy gas. Analysis of metallicity and velocity structure along the two filaments suggests that each originates from one of the Clouds. Substantial effort has been made to simulate and model the formation of the Magellanic Stream since its discovery in the 1960s. Its formation is strongly rooted in the interactions of the LMC and SMC with the MW, leading to models that incorporate tidal interactions and the ram pressure striping exerting on the gas as the Clouds move through the MW's halo.

The latest Hubble Space Telescope (HST) proper motion measurements of the Clouds indicate that the LMC and SMC are on their path to pass through the MW's disk. However, whether this is their first passage or if they are completing their orbit with a second passage remains unclear. Simulations considered the first- and multi-passage scenarios. The first-passage scenario suggests that the LMC and SMC fall together into the MW's gravitational potential, whereas the multi-passage scenario proposes that they were initially unbound and found each other within the MW's halo. The first-passage model successfully reproduces many observed features, while the multi-passage scenario better explains the helix structure of the two filaments of the Magellanic Stream.

Recently, the HST ultraviolet (UV) spectroscopy of background quasars in multiple line-of-sights revolutionized our understanding. Fox et al. (2020) detected the signature of photo-ionized gas in the Stream that can be explained by the Seyfert-flare model of the MW. The Seyfert-flare model proposes the burst of ionized radiation from the Galactic Center, the same event also creating the Fermi Bubbles[2] two to four million years ago. This intense flash from the MW's black hole illuminated the gas in the trailing Stream.

The discovery of the Magellanic Corona (Krishnarao et al., 2022) is another outstanding finding. The Magellanic Corona is a warm-hot gaseous halo at the virial temperature of $10^{5.3-5.5}$ K, which is ionized collisionally (Fox et al., 2023). Its presence

[2]Fermi Bubbles are $\approx$ 6 kpc large, balloon-like structures of high-energy gas extending above and below the plane of the MW's center. They are discovered in by the Fermi Gamma-ray Space Telescope and are thought to be the result of either a burst of star formation or an outburst from the supermassive black hole at the Galactic Center.

was foreseen in hydrodynamic simulations of the Magellanic Clouds, falling onto the Milky Way (Lucchini et al., 2020), and HST UV spectroscopy of background quasars confirmed it (Krishnarao et al., 2022). Including the Magellanic Corona in the simulations has helped reproduce the neutral and ionized mass of the Magellanic Stream, a problem that had remained unresolved (Lucchini et al., 2024). The authors emphasize the integral role of the Magellanic Corona in the survival, morphology, and composition of the Clouds and the Stream.

Understanding the Magellanic System is crucial for insights into galactic formation and evolution, as well as the dynamics of satellite galaxies within a larger galactic halo. Of particular interest to this research, however, is the broad range of metallicities within the System, which mirrors the conditions in the universe during the peak of star formation, corresponding to redshifts between one and three. This project focuses on the LMC, a prominent member of the Magellanic System. Discovered over half a millennium ago, the LMC has been extensively studied through multiple large observational programs in recent decades.

1.2.2 LMC conditions for star formation

The LMC is a dwarf galaxy with Baryonic mass[3] of $M = 1.7 \pm 0.7 \times 10^{10}$ $M_\odot$ at the radius of 8.7 kpc and tidal radius[4] of 22.3 $\pm$ 5.2 kpc (van der Marel & Kallivayalil, 2014). The relatively face-on view of the LMC makes it ideal for detailed observational investigations. In the remainder of this section, we discuss the star formation history, the evolution of the ISM, and the unique conditions the LMC offers for star formation.

The LMC consists of an off-center Bar embedded within its flat disk component (Bekki & Chiba, 2007a). The disk contains young, massive stars, star clusters, and star-forming regions, which contribute significantly to the galaxy's overall luminosity. As mentioned earlier, a single spiral arm extends outward from the Bar. The LMC hosts several active star-forming regions, among which 30 Doradus is highly recognized as the largest star-forming region in the LMC and the most active starburst region in the Local Group of galaxies. The LMC also contains multiple Globular Clusters (GCs; groups of old stars), providing valuable information about the early history of the galaxy.

The star formation in the LMC and the SMC is proposed to have passed through four epochs: dawn, hibernation, restoration, and inferno[5]. While we do not delve into

[3]The total mass of baryonic matter in a galaxy, including stars, interstellar gas and dust, as well as planets and other solid objects.

[4]The tidal radius is the distance from the center of a galaxy within which the galaxy's self-gravity is the dominant force, maintaining its structure. Beyond this radius, the tidal interactions with neighboring bodies, such as other galaxies or galaxy clusters, become significant and can strongly influence the dynamics and distribution of the galaxy's mass.

[5]Kenji Bekki's slides at https://slideplayer.com/slide/5072554/

the details of each era, the key concepts are informative. This classification begins with the dawn of star formation more than 10 billion years ago, based on observations of globular clusters (GCs; group of old stars), followed by a hibernation period lasting approximately 6 to 7 Gyrs. Star formation was reactivated around 3 to 4 Gyrs ago with the formation of new GCs, possibly due to interactions between the LMC, the SMC, and the MW. The formation of prominent star-forming regions such as 30 Doradus is proposed to be related to the close interaction of the Clouds, as recent as 200 million years ago.

The metallicity of the LMC (ZLMC) has been measured to have a mean value of approximately 0.4 times that of the ISM in the solar neighborhood ($Z_\odot$; [Fe/H] = -0.42 $\pm$ 0.04 dex[6]) with a decreasing gradient from the central to the outer region (Choudhury et al., 2021). The close encounter between the LMC and SMC about 200 Myrs ago allowed for the gas mixing that might have altered the chemical composition of the LMC (e.g., Bekki & Chiba, 2007a).

An LMC metallicity map, derived from the Red Giants' optical photometric data and calibrated using spectroscopic data (Choudhury et al., 2016), revealed significant deviations from the mean metallicity in some areas of the LMC. The maximum value, exceeding 0.7 $Z_\odot$, is mostly found in the Bar region, while a minimum of less than 0.2 $Z_\odot$ is observed in the outer regions. Additionally, a recent optical emission line spectroscopic study of 59 sight lines showed that metallicity varies by approximately 0.5 dex across the LMC (Lah et al., 2024). Furthermore, an investigation into metal depletion from gas to dust in the ISM using HST UV spectroscopy of 32 sight lines found variations of up to 0.8 dex (Roman-Duval et al., 2021). These variations relative to the radial gradients are large compared to those observed in other nearby galaxies (e.g., Groves et al., 2023).

In addition to sub-solar metallicity with large variations, the ISM of the LMC exhibits a high UV radiation field strength, ranging from 10 to 100 times that of the solar neighborhood (Welty et al., 2006). Another prominent feature is the lower cosmic ray density, which is about four times less than that of Galactic star-forming regions (Abdo et al., 2010). All these factors play a crucial role in regulating the star formation and the chemistry in star forming regions.

Lower metallicity implies a lower dust-to-gas ratio (or a higher gas-to-dust ratio). This reduced metal and dust content has at least two significant effects. First, metal-driven cooling is less efficient, leading to warmer dust temperatures (e.g. van Loon et al., 2010). Second, decreased dust content reduces the shielding effect, allowing UV radiation to penetrate deeper into the clouds. The enhanced dust temperature

[6]Decimal exponent; in this context, this is a way to compare the metallicity of an object to a reference object, most commonly the Sun, on a logarithmic scale. For example, [Fe/H] = 0 dex means the object has the same iron abundance as the Sun, and [Fe/H] = +1 dex means the object has an iron abundance 10 times that of the Sun.

results in faster evaporation of grain ice mantles, while increased UV exposure leads to photodesorption and photodissociation of chemical compounds in the gas phase. Moreover, the high temperature of the ISM can alter the masses of forming cores, favoring more massive cores and fragments.

To investigate the unique environmental conditions of the LMC, extensive observational efforts have been undertaken over the years. Key large-scale survey programs include Spitzer Agents of the Galaxy Evolution (SAGE), Herschel Agents of the Galaxy Evolution (HERITAGE), Magellanic Clouds Emission-Line Survey (MCELS), and more recently the VISTA survey for Magellanic Clouds (VMC), alongside the long-running Optical Gravitational Lensing Experiment (OGLE). These programs represent just a fraction of numerous small and large-scale initiatives spanning various wavelengths. This extensive effort underscores the LMC's significance in advancing our understanding of the local and distant universe, particularly in studying star formation under low metallicity within an interacting galaxy system.

1.3 About this work

In this section, I introduce the methodology to study star formation in the sub-solar metallicity of the LMC (see Section 1.3.1), followed by details of the selected sample for observation (see Section 1.3.2). Section 1.3.3 highlights the main goals in this research endeavor.

1.3.1 Methods and strategies

As presented in the previous sections, to investigate the impact of environmental conditions, specifically metallicity, on high-mass star formation, the LMC is an excellent target. The LMC has been extensively studied over the past decades and is close enough to observe sub-parsec scales within molecular clouds where the early phases of star formation occur. These early phases are highly embedded in dense, cold regions with temperatures ranging from 20 to 100 K. Consequently, the emission from such regions is predominantly observable in the millimeter regime. Depending on the phase of star formation and the nature of the dense cores and clumps, it is also possible to detect emissions in infrared and centimeter wavelengths.

There are different emission mechanisms in the millimeter to centimeter wavelengths, including both continuum and spectral line emissions. While the continuum emission in millimeter wavelengths arises predominantly from the dust, in centimeter wavelengths, the interaction of free electrons generates the so-called free-free emission. Spectral line emissions result from the rotational transitions of neutral and ionized molecular species or high-order recombination lines. As discussed in Section 1.1.2,

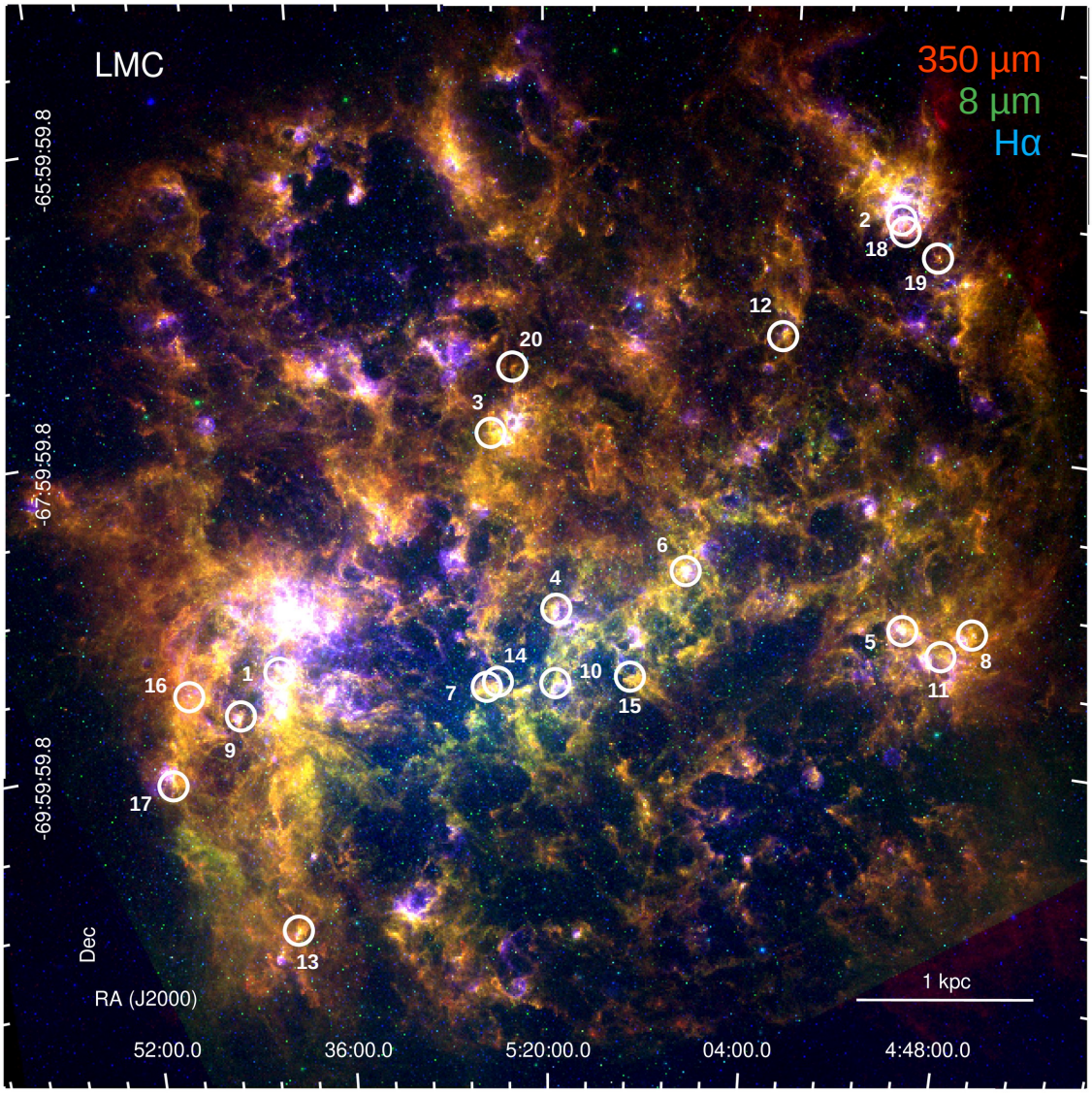


Figure 1.3: Color-composite image of the LMC combining the HERITAGE/SPIRE 350 μm (red, Meixner et al., 2013), SAGE/IRAC 8 μm (green, Meixner et al., 2006), and Hα (blue, Smith et al., 2000) images. The positions of the 20 ALMA fields are marked with white circles 15 times larger than the field of view of our ALMA observations and the field number (see Section 1.3.2)



Figure 1.4: Artist's rendering of the Atacama Large Millimeter Array (ALMA) in an extended configuration. ALMA (ESO/NAOJ/NRAO)/L. Calçada (ESO) – (Not referred to in the text)

various molecular species are present in the gas phase throughout the star formation process, serving as excellent tracers of the physics and kinematics of the region under study.

We adopt an observational approach. To observe star-forming regions at the distance of the LMC, specific requirements must be met. First, the LMC's celestial coordinates are approximately 5h and -70°; thus, it is best observed from the southern hemisphere. Additionally, an angular resolution of less than 0.5 arcseconds is required to detect star-forming cores at spatial resolutions of around 0.1 parsecs. The Atacama Large Millimeter/submillimeter Array (ALMA)[7] and the Australian Telescope Compact Array (ATCA)[8] offer great potential to meet these needs for our project.

In the following, I provide a general overview of the capabilities of these two observatories. Detailed descriptions of our observational setups will be presented in the next chapters, when we use the data for further analysis.

ALMA

The ALMA, located at the Chajnantor Plateau in the Atacama Desert in Chile, is an interferometer composed of high-precision antennas that act as a single telescope. ALMA features two arrays that can be configured in different ways by varying the distance between antennas, "baseline", ranging from a maximum of 150 meters to 16

[7]ALMA is a partnership of the European Southern Observatory (ESO), the U.S. National Science Foundation (NSF), and the National Institutes of Natural Sciences (NINS) of Japan in cooperation with the Republic of Chile.

[8]ATCA is operated by Astronomy and Space Science division as part of the Australia's National Science Agency



Figure 1.5: Five of the six antennas of the Australian Telescope Compact Array (ATCA) arranged on the main East-West track and the North spur (the latter is the horizontal track shown in this image). Credit: ATNF/CSIRO – (Not referred to in the text)

kilometers. The main array consists of fifty 12-meter diameter antennas, while the ALMA Compact Array (ACA) includes four 12-meter and twelve 7-meter antennas.

Interferometry is achieved by combining data from each single dish with the other antennas as a pair. A simple calculation shows that for the main array with 50 antennas, there are 1225 possible pairs. The correlation of each pair is performed by the ALMA Correlators, which are differentiated for the main array and the ACA. These two arrays complement each other, and with their different configurations, ALMA is capable of achieving a wide range of angular resolutions, from 0.0048" to 8.5" on the main array.

ALMA antennas can be equipped with radio receivers that are sensitive to specific frequency ranges, referred to as "bands". Currently, ALMA is capable of observing in 10 different bands, covering a frequency range from 35 to 950 GHz (corresponding to wavelengths from 8.8 to 0.3 mm). Each frequency band is very broad, and when proposing observations, researchers can request four different spectral windows. This wide bandwidth allows for the detection of a plethora of molecular transitions, facilitating the study of ongoing chemical processes and the discovery of new molecules. Additionally, detecting multiple transitions from the same molecular species is essential for tracing the temperature of the astronomical target.

ATCA

The ATCA, located at the Paul Wild Observatory located at Narrabri desert in Australia, consists of six 22-meter antennas. The array includes a 3 km east-west track and a 214-meter north-south track. Five of the antennas are movable along these tracks, while one antenna is fixed 3 km west of the east-west track. This configuration allows for the longest possible baseline of 6 km. The antennae can be arranged in various con-

figurations. The movable antennas can be positioned at different distances along the east-west and north-south tracks. The ATCA supports observations in five frequency bands, ranging from 1.1 GHz to 105 GHz, covering wavelengths from approximately 27 cm to 3 mm.

1.3.2 Sample selection

We compiled a catalog of massive Young Stellar Objects (YSOs) in the LMC from Seale et al. (2009), selecting young, highly embedded YSOs. From this subset, we chose YSOs without ice features and with Herschel/HERITAGE counterparts Seale et al. (2014). Applying a cutoff on the pixel values in the MCELS Hα maps (Smith et al., 2000) at the positions of the YSOs, we excluded those showing strong emission. This step was crucial to omit YSOs exposed to intense radiation feedback that could disrupt the complex chemistry used to study star formation. The 18 selected YSOs are ordered then by their Herschel 160 μm fluxes. Additionally, we included two YSOs with clear ice features in the Spitzer spectra from Shimonishi et al. (2016a).

Table 1.1: Target coordinates and type.

Field Number	Target ID Gruendl & Chu (2009)	Target type Jones et al. (2017)
1	053941.12-692916.8	YSO1
2	045640.79-663230.5	YSO1
3	052343.48-680033.9	YSO3-HII
4	051912.27-690907.3	YSO2
5	045358.57-691106.7	HII
6	050953.89-685336.7	HII
7	052423.39-693904.7	YSO3
8	044854.41-690948.3	HII
9	054248.90-694446.3	YSO3
10	051916.87-693757.5	YSO3
11	045100.16-691934.4	HII
12	050355.87-672045.1	YSO3-HII
13	053952.11-710930.7	YSO3-HII
14	052333.40-693712.2	YSO1
15	051344.99-693510.6	YSO3
16	054629.32-693514.2	HII
17	054826.21-700850.2	YSO3-HII
18	045622.61-663656.9	YSO3
19	045406.43-664601.4	YSO3
20	052210.08-673459.6	YSO3

Figure 1.6 displays the Spitzer spectra from all the 20 YSOs in our sample (Jones et al., 2017, and the references therein). Jones et al. (2017) suggests a careful classifica-

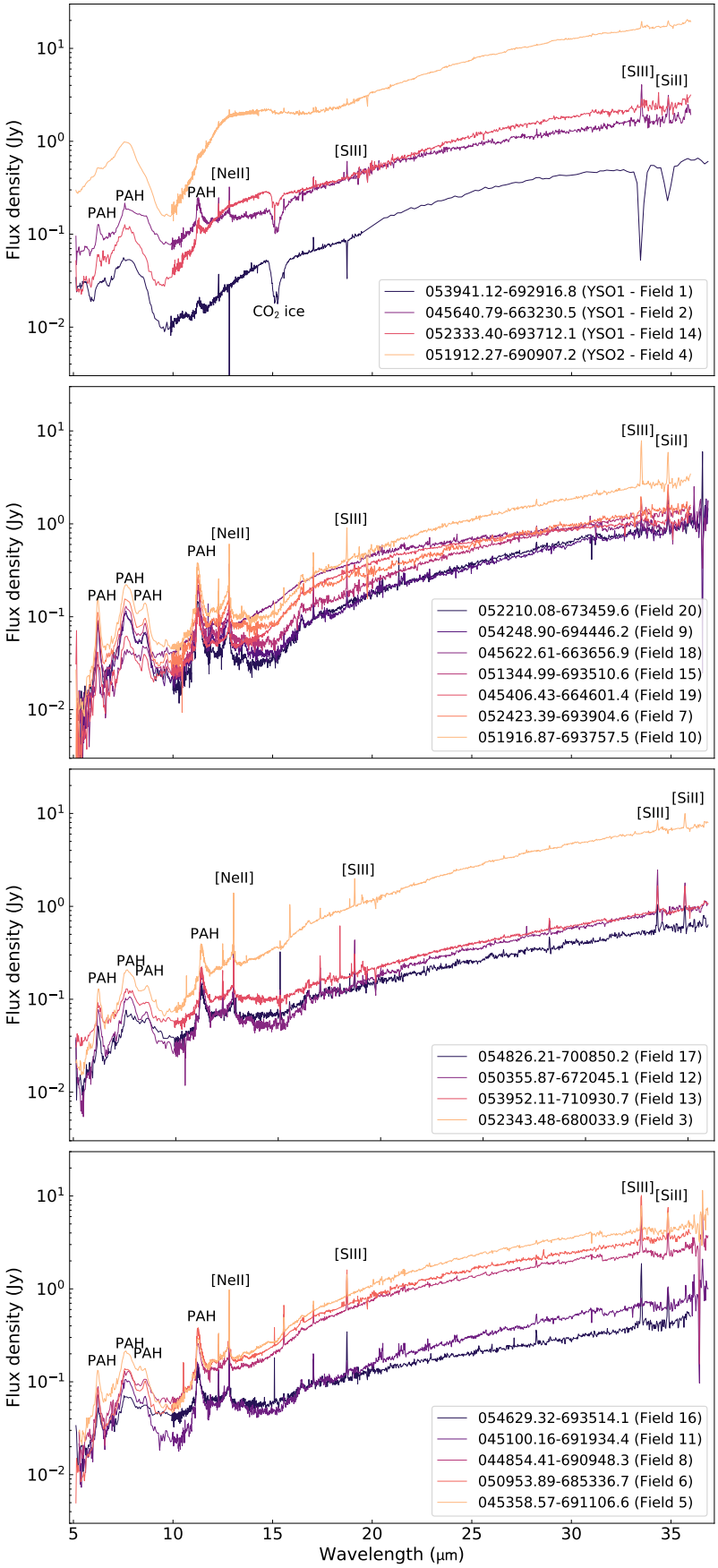


Figure 1.6: Spitzer spectra of our target YSOs grouped with the classification from Jones et al. 2017. From top to bottom are the YSO1 and YSO2, YSO3, YSO3-HII, and HII (for more details see the text)

tion of the point sources' spectra from the Infrared Spectrograph (IRS) on the Spitzer Space Telescope using a decision tree format. This classification primarily relies on spectral features but also incorporates Spectral Energy Distribution (SED) information and Bolometric Luminosity when necessary. The distinction between the five different classes of sources in our sample can be summarized as follows, reflecting the evolutionary stages of YSOs from less evolved to more evolved: YSO1, YSO2, YSO3, and HII.

YSO1: These are highly embedded YSOs. The main spectral feature is ice absorption of molecular species locked in the ice mantles on the dust grains, such as the CO_2 ice absorption at 15.2 μm, highlighting the existence of a dense, cold envelope around the YSO.

YSO2: This class is characterized by the broad silicate absorption dip at 10 μm, indicative of a more evolved YSO that has heated its envelope, evaporated the ice mantles, and partially destroyed the dust particles.

YSO3: At this stage, the young star emits a copious UV field that reaches further out as the circumstellar envelope is pushed out and gradually dispersed. The UV radiation excites PAHs, making PAH emission the main characteristic of this class. Additionally, photodissociation and photoionization at this stage ignite emission from atomic and ionized gas.

HII: At this stage, the surrounding gas is completely ionized, and an ultra-compact or classical HII region is developed. The main characteristic, compared to the YSO3, is diminished PAH emission and enhanced ionized emission lines.

YSO3-HII: There can be ambiguity in the classification of YSO3 and HII regions, especially when the HII region is in the ultra-compact phase. Therefore, there is another group in between to contain sources that cannot be clearly classified into either of these sub-classes.

The overall spectral profile of the early stages of star formation shows a rise toward the red end of the spectra due to the cold dust temperature, with peak emission at 100 μm in the very early stages (van Dishoeck, 2004). However, in later stages, free-free emission might also contribute to the overall continuum emission in the red end, maintaining its intensity.

1.3.3 Goals and outline

This thesis investigates high-mass star formation under the sub-solar metallicity conditions of the Large Magellanic Cloud (LMC). The study focuses on 20 massive young stellar objects (YSOs) selected based on Spitzer and Herschel data (see Section 1.3.2). These YSOs were observed with ALMA, complemented by additional data from ATCA. The thesis is organized into six chapters. This introductory chapter, Chapter 1, high-

lights the significance of studying star formation in the LMC's unique environment, characterized by lower metallicity, enhanced UV radiation, and reduced cosmic ionization. It also provides an overview of the observational strategy, including the selection of targets and the use of ALMA and ATCA interferometry. The overarching goal is to deepen our understanding of star formation processes at parsec and sub-parsec scales in the LMC.

Chapter 2 and Chapter 3 present the publications derived from this work. Chapter 2 investigates the physical properties, and Chapter 3 delves into the chemical characteristics of the 1.2 mm continuum cores from ALMA. Chapter4 explores gas kinematics by identifying filaments and outflows in the ALMA molecular line maps and examines radiative feedback processes through the detection of HII regions from ATCA observations. Chapter 5 presents a multi-wavelength view to the environments of our target fields from large scales of $\sim$ 150 pc to smaller scales, with an effort to classify these regions. Finally, Chapter 6 offers a comprehensive conclusion and outlook of this research, with several appendices included to clarify key concepts and developments utilized throughout the project.

Chapter 2

Dense cores and clusters observed with ALMA at 1.2 mm

This chapter presents the work of Hamedani Golshan et al. that is going to be submitted soon to the Astronomy and Astrophysics Journal, a project that I have led and accomplished from the data reduction through the analysis to the final publication. The other authors (Álvaro Sánchez-Monge, V. S. Veena, Peter Schilke, Marta Sewiło, Fengwei Xu, Thomas Möller, Gary A. Fuller and Anna F. Mcleod) have participated in discussions and provided comments. The paper has been seamlessly incorporated into the thesis text, with the title and author list omitted. Additionally, the appendices from the paper have been relocated to the end of the thesis.

Abstract

Context. The physical properties of dust continuum cores in the Large Magellanic Cloud (LMC) provide insights into star formation in low-metallicity environments and allow comparisons with Galactic studies.

Aims. We aim to characterize the fragmentation, mass distribution, and spatial arrangement of dust continuum cores in the LMC and explore how environmental factors, such as metallicity and feedback, influence these properties.

Methods. Using ALMA 1.2 mm continuum observations of 20 massive Young Stellar Object (YSO) fields in the LMC, we identify and analyze compact continuum cores, focusing on their spatial distribution, fragmentation, and physical properties.

Results. A total of 65 compact continuum cores are detected, with an average separation of $\sim$ 0.5 pc. Fragmentation is observed in 80% of the fields, with non-thermal Jeans fragmentation providing a better explanation for the observed fragmentation at scales from 10 pc down to 0.1 pc. The core formation efficiency (CFE) is $\sim$5%, and the core mass function (CMF) resembles that of Galactic regions, despite the LMC's lower metallicity. Evidence of mass segregation is observed, with massive cores preferentially located at cluster centers. The mass-radius relation is consistent with Galactic cores

but shows a tendency for more massive cores in the LMC, likely due to environmental effects.
Conclusions. LMC cores exhibit similarities to Galactic cores in their mass distribution and fragmentation processes, but environmental factors such as metallicity and feedback may drive the formation of more massive cores.

2.1 Introduction

Star formation begins with the collapse and fragmentation of molecular clouds, the stellar nurseries of the universe. Fragmentation occurs on various physical scales, from clouds to clumps to cores, and even within prestellar cores (e.g., McKee & Ostriker, 2007; Motte et al., 2018a). The resulting structures range from dense clusters, which dominate star formation, to isolated single star-forming cores, which are comparatively rare (e.g., McKee & Ostriker, 2007; Pillai et al., 2011). The mechanisms driving fragmentation are scale-dependent and vary between different environments. On larger scales (1–10 pc), turbulence is often the dominant factor, driving and sustaining fragmentation (e.g., Pillai et al., 2011; Sadaghiani et al., 2020). On smaller scales, such as within cores, gravitational forces play an increasingly significant role, often overpowering turbulence and shaping the final stages of fragmentation and collapse (e.g., McKee & Ostriker, 2007; Sadaghiani et al., 2020).

Metallicity, defined as the abundance of elements heavier than hydrogen and helium, plays a crucial role in star formation and fragmentation processes. It is often viewed as a byproduct of stellar evolution, but its impact on the physical processes of star formation is profound. In metal-rich environments, higher interstellar medium (ISM) opacity leads to increased cooling efficiency because of metals such as carbon, which act as primary coolants in cold, dense regions. This enhanced cooling promotes greater fragmentation rates. Furthermore, metallicity affects light extinction, UV penetration, and radiation pressure, which can influence accretion and collapse dynamics.

To fully understand star formation, it is vital to investigate environments with diverse metallicities. Nearby low-metallicity regions, such as the Large Magellanic Cloud (LMC), serve as excellent laboratories for studying star formation under conditions analogous to high-redshift, metal-poor galaxies (e.g., Wolfire et al., 2022). The LMC, located at a distance of $D \approx 49.59 \pm 0.09$ (statistical) ± 0.54 (systematic) kpc (Pietrzyński et al., 2019), has a metallicity of approximately 0.3–0.5 $Z_\odot$. This, combined with its proximity, face-on orientation, and reduced line-of-sight dilution, makes it an ideal target for detailed observations. The advent of the Atacama Large Millimeter/submillimeter Array (ALMA) allows us to probe spatial scales comparable to Galactic cores and protostellar clusters, enabling high-resolution studies of star formation in this unique environment.

The LMC's distinct properties, such as its reduced metallicity, higher UV radiation field (e.g. Browning et al., 2003), and lower cosmic ray ionization rates (e.g. Abdo et al., 2010), provide a compelling backdrop for understanding star formation under subsolar metallicity conditions. This paper is part of an ongoing effort to systematically study these processes on different scales in the LMC.

In this second paper in the series, we focus on compact and dense sources (or cores, typically $\sim$ 0.1pc in size) within molecular clouds. We characterize their physical properties and those of their parent clouds, as well as their clustering properties, in Section2.3. In Section 2.4, we discuss the conditions driving collapse and fragmentation, the stability of the cores, and construct their mass function. The chemical properties of these regions were explored in the first article of this series (Hamedani Golshan et al., 2024, hereafter PaperI). Finally, in Section2.5, we summarize our findings and discuss their broader implications.

2.2 Observations

2.2.1 Sample selection

We selected 20 massive Yong Stellar Objects (YSOs) in the LMC for the cycle 5 ALMA observation to study massive star formation across the galaxy. The sample includes 18 very young YSOs, typically lacking ice features and fine structure lines in their Spitzer IRS spectra (Gruendl & Chu, 2009), and having Herschel counterparts (Seale et al., 2014) at far-IR frequencies. These YSOs are located away from massive star forming sites, as indicated by the absence of strong Hα in the MCELS[1] images (Smith et al., 2000).

The selected YSOs are all bright at 160 μm , indicating substantial dust and high column densities, which favor the detection of molecular lines. Additionally, we include two regions centered on YSOs ST6 and ST10, where Shimonishi et al. (2016b) detected methanol ice. The selected target YSOs (referred to as fields) are well distributed throughout the LMC (see Fig. 2.1). Table 2.1 lists the target YSOs, and their names (from the Henize, 1956, catalogue of emission nebulai).

2.2.2 ALMA observations

The ALMA observation of all fields were conducted during Cycle 5, between November 11 and December 3, 2018 (2017.1.00696.S). Each YSO was observed as a single pointing, with a total integration time of 19.3 minutes across eight different execution blocks. The observations utilized the main array with 12-M antennas in two configurations, C43-4 and C43-5, with baselines ranging from 15 to 1400 meters. This setup

[1]Magellanic Cloud Emission-line Survey

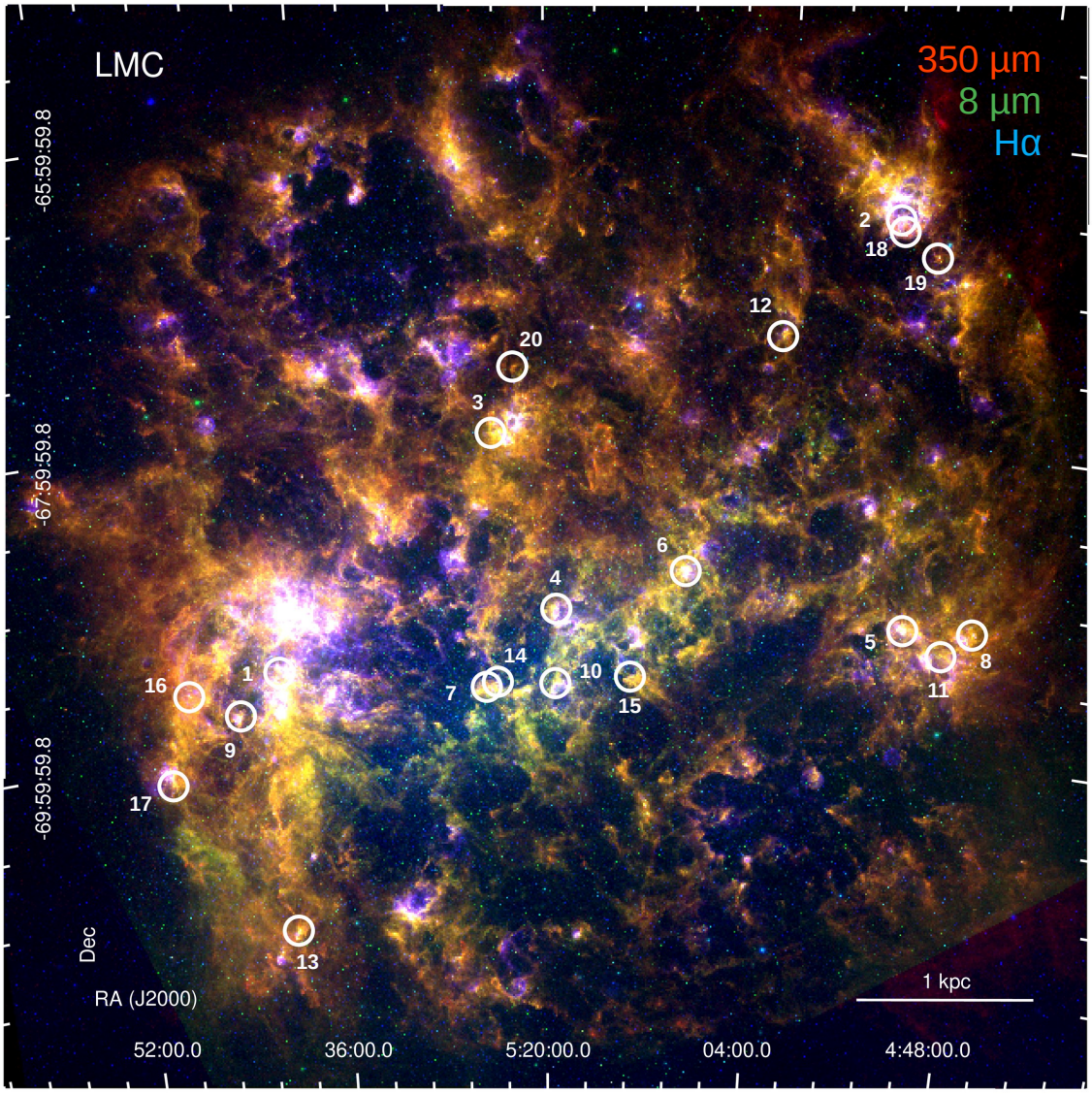


Figure 2.1: Color-composite image of the LMC combining the HERITAGE/SPIRE 350 μm (red, Meixner et al., 2013), SAGE/IRAC 8 μm (green, Meixner et al., 2006), and Hα (blue, Smith et al., 2000) images. The positions of the 20 ALMA fields are marked with white circles 15 times larger than the field of view of our ALMA observations and the field number.

provided an angular resolution of approximately 0.4″ (corresponding to 0.09 pc) and a maximum recoverable angular scale of about 5″ (corresponding to 1.2 pc). This maximum recoverable scale enabled the detection of dense cores and clumps with typical sizes $\leq$ 0.5 pc. The total field of view (or primary beam) for the ALMA observations is approximately 44″ (corresponding to 10 pc). The spectral setup included four windows, with bandwidth of 469 MHz wide centering at 241.6 and 1875 MHz wide centering at 244.6, 257.6, and 259.5 GHz.

Table 2.1: Field coordinates and the continuum image parameters observed with the ALMA.

Field	Target ID	Target Name	Synth. beam (Θ_B, PA)	Image rms	
Number	Gruendl & Chu (2009)	(" × ", °)		(μJy/beam)	(mK)
1	053941.12-692916.8	ST6 [a]	0.383 × 0.329, −9.3	57.4	8.9
2	045640.79-663230.5	ST10 [a]	0.370 × 0.330, +18.7	59.4	9.5
3	052343.48-680033.9		0.373 × 0.331, +0.5	67.3	10.7
4	051912.27-690907.3	ST16 [a, b]	0.379 × 0.330, +8.6	62.4	9.8
5	045358.57-691106.7		0.384 × 0.330, +16.9	62.5	9.7
6	050953.89-685336.7	N105-2 E [c]	0.378 × 0.329, +13.6	70.9	11.1
7	052423.39-693904.7		0.385 × 0.329, +7.1	60.3	9.3
8	044854.41-690948.3		0.386 × 0.330, +20.3	59.9	9.2
9	054248.90-694446.3		0.385 × 0.329, −8.2	59.0	9.1
10	051916.87-693757.5		0.382 × 0.328, +8.5	60.2	9.4
11	045100.16-691934.4		0.386 × 0.329, +20.1	59.2	9.1
12	050355.87-672045.1		0.374 × 0.330, +17.5	59.4	9.4
13	053952.11-710930.7		0.393 × 0.330, −0.7	61.5	9.3
14	052333.40-693712.2		0.383 × 0.329, +9.9	59.6	9.2
15	051344.99-693510.6		0.383 × 0.328, +14.5	59.4	9.2
16	054629.32-693514.2		0.385 × 0.329, −7.9	57.5	8.9
17	054826.21-700850.2		0.383 × 0.327, −2.1	56.4	8.8
18	045622.61-663656.9		0.374 × 0.331, +24.5	58.4	9.2
19	045406.43-664601.4		0.375 × 0.330, +25.7	58.2	9.2
20	052210.08-673459.6		0.375 × 0.331, +13.4	58.1	9.2

Notes.
[a] Shimonishi et al. (2016a)
[b] Shimonishi et al. (2020)
[c] Sewiło et al. (2022)

Data calibration was performed using the ALMA pipeline version 42030M (Pipeline-CASA54-P1-B) in CASA (Common Astronomy Software Applications; McMullin et al., 2007) version 5.4.0-68. The amplitude and bandpass calibrators were J0635-7516 or J0519-4546, and the phase calibrators J0529-7245 or J0601-7036 depending on the execution block. Continuum subtraction, determined from the line-free channels, was performed in the UV domain using CASA `uvcontsub` task. Imaging was then carried out using the CASA tclean task to produce spectral cubes for each spectral window and a single continuum image for each field. The `tclean` parameters included standard gridding with "briggs" weighting and a robust parameter of 0.5. The final images are primary beam corrected using `impbcor` task in CASA.

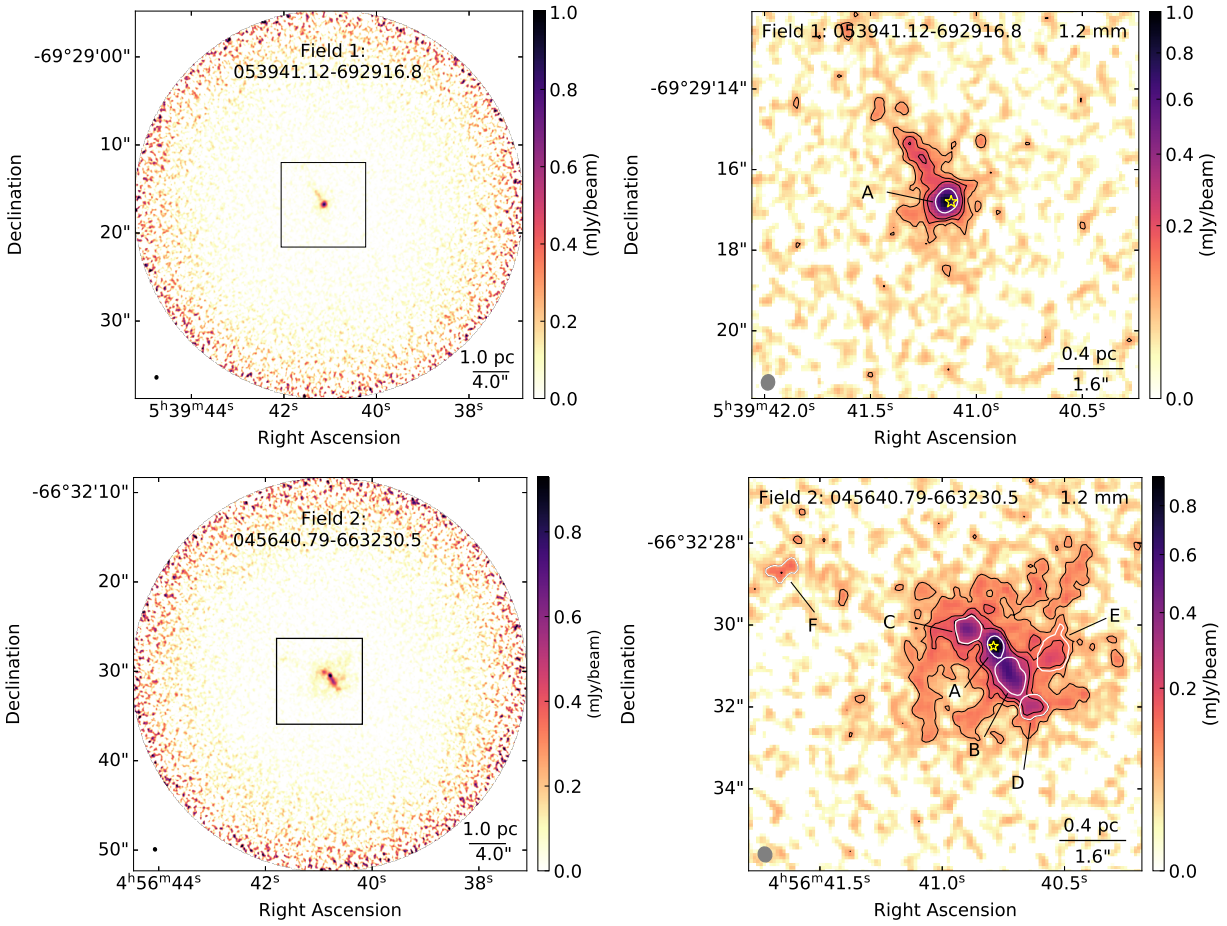


Figure 2.2: The 1.2 mm pb-corrected continuum maps for Field 1 and 2: *left* an overview to the field, *right* a detailed view to the region inside the black rectangle on the left side panel. The contours show the 3, 6, and 9 times the $\sigma_{\rm rms}$. The identified cores are highlighted with white contours at 50% of the peak emission. The position of the YSOs is marked with a yellow star. The synthesized beam of the images and a scale bar are shown in the bottom-left and -right corners of each panel.

Typical errors for the continuum images are about 60 μJy beam^{-1} (10 mK) and about 1.92 mJy beam^{-1} (0.23 K) for the cubes (see Table 2.1 for continuum images and Table 2 in Paper II for cube images). Figure 2.2 shows the 1.2 mm ALMA continuum emission toward the first two fields, ST6 and ST10, with the full field view on the left and a zoomed-in view on the right.

2.3 Analysis and results

The ALMA 1.2 mm continuum images show emission in all the 20 target fields. The intensity of the emission varies across the field of view, enabling the detection of single or multiple high intensity compact structures. To characterize these structures, we performed a series of analyses. We identify and calculate the physical properties of the 1.2 mm continuum sources (see Section 2.3.1) and their hosting clouds (see Sec-

tion 2.3.2). Additionally, we analyze the clustering properties within these regions (see Section 2.3.3).

2.3.1 Identification and physical properties of the cores

The 1.2 mm continuum emission of each LMC field is shown in Fig. 2.2 and Figures. A.1 to A.18. The left panels display the complete field of view, with boxes highlighting the regions around the detected continuum sources, and the right panels presenting more detailed zoomed-in views of these regions. To identify cores, we focused on emission peaks, manually identified as local maxima in the intensity. The extent of each core was later defined as the contour at the 50% level of the peak intensity. For this process, we used the continuum images prior to applying the primary beam correction, ensuring a uniform noise distribution. In a few cases (five sources) where the 50% contour level enclosed two intensity peaks, we manually adjusted the contours to define them as distinct sources.

As a result, we identified a total of 65 continuum cores with peak intensities above $5\sigma_{\rm rms}$ in the non-primary beam corrected images. The core IDs and their peak coordinates are listed in columns (1) to (3) of Table A.1. Once the polygons delineating the sources at the 50% contour level were defined (see the white contours in Fig. 2.2 and Figures. A.1 to A.18), we used them to extract flux from the primary-beam corrected images.

To estimate physical properties of the identified cores, we calculated the mean intensity ($\overline{I}$) and the size of the cores from the continuum primary-beam corrected images. The mean intensity, derived from all the pixels within the 50% contour that defines each core (see white contours in Fig. 2.2 and Figs. A.1 to A.18), was used to compute the flux density (F_ν) as:

$$F_\nu = \overline{I}\ \frac{\Omega_{\rm obs}}{\Omega_{\rm beam}} \tag{2.1}$$

where $\Omega_{\rm obs}$ and $\Omega_{\rm beam}$ are the observed source and beam solid angles, respectively. Since the source area (or solid angle) is defined at half of the peak emission, we calculated the beam area also at the half-power beam width from $\frac{\pi}{4}\theta_{\rm min}\theta_{\rm maj}$, with $\theta_{\rm min}$ and $\theta_{\rm maj}$ being the beam minor and major axis (Table 2.1).

The size of each source is defined by both the observed ($\theta_{\rm obs}$) and deconvolved ($\theta_{\rm deconv}$) angular diameter, calculated as $\theta = 2\sqrt{\Omega/\pi}$, with Ω being the solid angle. Assuming Gaussian source shapes, the deconvolved solid angle is determined using:

$$\Omega_{\rm deconv} = \sqrt{\Omega_{\rm obs}^2 - \Omega_{\rm beam}^2} \tag{2.2}$$

Column (4) of Table A.1 lists the observed and deconvolved angular diameters for each

source. The linear sizes were derived using the distance to the LMC, yielding values in the range 0.1 to 0.3 pc (see Fig. 2.3). The calculated flux densities are listed in column (6) of Table A.1, and range from approximately 0.3 mJy to 15 mJy.

Assuming that the continuum emission at 1.2 mm is primarily due to thermal dust emission, the dust mass ($M_{\rm dust}$) for each core is calculated as:

$$M_{\rm dust} = \frac{F_\nu D^2}{\kappa_\nu B_\nu(T_{\rm dust})} \tag{2.3}$$

where D is the distance to the source, assumed to be the LMC distance of 49.59±0.09 kpc (Pietrzyński et al., 2019) and κ_ν is the dust opacity (or mass absorption coefficient). We adopt a value of $\kappa_\nu = 1.04$ cm^2 g^{-1} from Ossenkopf & Henning (1994) for dust grains with thin ice mantels after 10^5 yr of coagulation in a hydrogen density of 10^6 cm^{-3}. $B_\nu(T_{\rm dust})$ is the black body radiation at a frequency ν (set to 250 GHz) and at a dust temperature $T_{\rm dust}$.

For the dust temperature, we assume effective mixing and good coupling between gas and dust, and rely on spectral line analysis results. Paper I provides the detailed analysis of spectral lines, where three species — SO_2, CH_3OH, and CH_3CN — could trace the gas temperature at the location of the cores through their multiple transitions within the observed spectral windows. However, only four cores have reliable temperature estimates from all three tracers. These cores are identified as hot molecular cores in Paper I. Among the temperature tracers, CH_3OH was detected in 72% (47/65) of the cores. Based on this high detection rate, we use the CH_3OH temperature estimates from the XCLASS[2] line fitting tool (eXtended CASA Line Analysis Software Suite; Möller et al., 2017, 2023, with additional extensions, T. Möller, priv. comm.), which range 10–60 K (see Fig. 2.3 and column (7) of Table A.1). For cores without temperature data, we assign a temperature of 27 K, the median of the best-fit values for CH_3OH-derived temperatures.

The total mass ($M_{\rm core}$) is then derived from the dust mass and the gas-to-dust ratio ($R_{\rm g/d}$) as:

$$M_{\rm core} = (R_{\rm g/d} + 1)\ M_{\rm dust}. \tag{2.4}$$

We assume a gas-to-dust ratio of 316 (Sewiło et al., 2022) for all the cores. $M_{\rm core}$ is listed in column (8) of Table A.1. Assuming spherical geometry we calculate the gas number density $n_{\rm core}(H_2)$ as:

$$n_{\rm core}(H_2) = \frac{1}{\mu_{H_2} m_{\rm H}} \frac{M_{\rm core}}{\frac{4}{3}\pi {R_{\rm core}}^3} \tag{2.5}$$

where μ_{H_2} is the mean molecular weight (2.8) and $m_{\rm H}$ is the atomic hydrogen mass (1.674×10^{-24} g). The linear radius $R_{\rm core}$ is half of the linear source size. The column

[2] `https://xclass.astro.uni-koeln.de/`

density of molecular gas $N_{\rm core}(H_2)$ is calculated as:

$$N_{\rm core}(H_2) = \frac{1}{\mu_{H_2} m_H} \frac{M_{\rm core}}{4\pi R_{\rm core^2}} \tag{2.6}$$

Similarly, the gas surface density $\Sigma_{\rm core}(H_2)$ is:

$$\Sigma_{\rm core}(H_2) = \frac{M_{\rm core}}{4\pi R_{\rm core}^2} \tag{2.7}$$

The gas number, column and surface densities are listed in column (9), (10) and (11) of Table A.1.

Finally, assuming the emission is thermal blackbody radiation, the luminosity ($L_{\rm core}$) of each core is estimated using the Stefan-Boltzmann law:

$$L_{\rm core} = 4\pi R_{\rm core}^2 \sigma_{\rm SB} T_{\rm core}^4 \tag{2.8}$$

where $\sigma_{\rm SB}$ denotes the Stefan-Boltzmann constant. The uncertainties in the parameters are calculated through error propagation using the Python package `uncertainties`, accounting for the uncertainty on the LMC distance, a 20% error on temperature values ($T_{\rm core}$) and one $\sigma_{\rm rms}$ on the mean intensity ($\overline{I}$).

The distributions of the physical parameters are shown in Fig. 2.3. The top panels display the source radiia, flux densities, and luminosities. The minimum detectable flux density is calculated for a circular source, with a size equal to the average beam size and a Gaussian intensity profile with a peak intensity of five times the typical $\sigma_{\rm rms}$ level of the continuum images. The bottom panels show the core masses, the H_2 number, and column densities. The mass sensitivity is based on the minimum detectable flux at a temperature of 27 K.

The source radius range from 0.05 to 0.15 pc, with cores 11A and 11C representing the extremes. The Kernel Density Estimate (KDE) curve peaks at 0.06 pc, suggesting this as the typical source size within the sample. The 1.2 mm flux densities vary between 0.27 ± 0.09 mJy for source 12B to 15.39 ± 0.41 mJy for source 3A, with the latter exhibiting a flux roughly twice as high as the other sources. The median flux density of the sample is 0.96 mJy.

The core masses range from 17.73 ± 9.62 $M_\odot$ for core 12D to 991 ± 235.77 $M_\odot$ for core 3A. Furthermore, core 4A exhibits the highest hydrogen volume density, at $(10.56 \pm 2.56) \times 10^6$ cm^{-3}, and highest column density, at $(25.06 \pm 6.41) \times 10^{23}$ cm^{-2}. The median volume and column densities in the sample are 7.25×10^5 cm^{-3} and 1.89×10^{23} cm^{-2}, respectively.

The tentative detection of hydrogen recombination lines in the spectra toward source 3A suggests that the 1.2mm emission from this source may be contaminated by

free-free emission. Furthermore, in separate study (ATCA observation, PI: Hamedani Golshan), we identified cm-wave emission slightly offset from nine sources in our sample (3A, 4A, 5A, 8A, 12A, 15C, 16A, 19C, 20A). This indicates that the 1.2mm emission from these sources may also be affected by contamination from cm-band emission. While investigating this impact lies beyond the scope of this paper and warrants a future publication, we note that the masses of the affected sources could be overestimated.

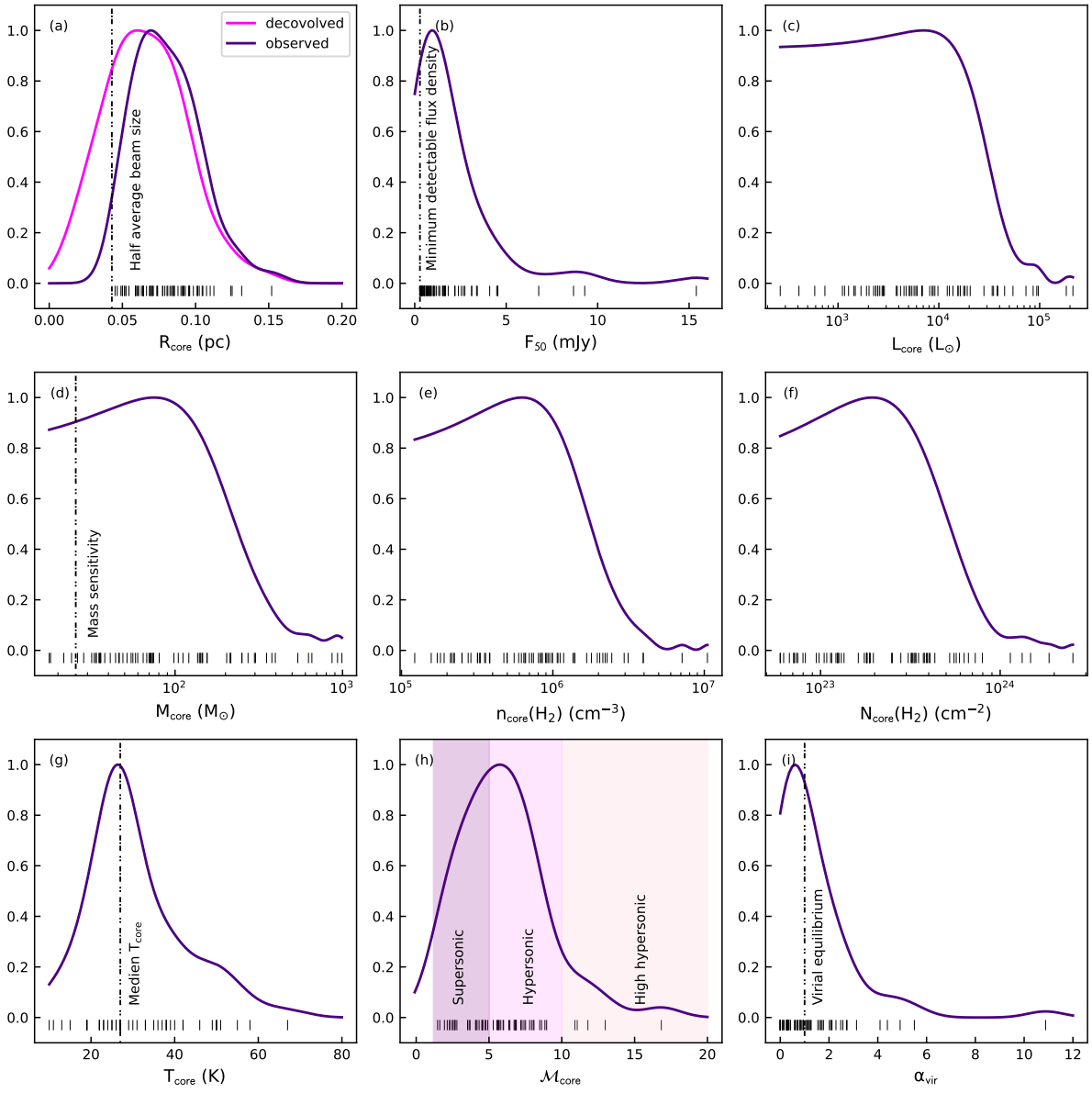


Figure 2.3: KDE distribution of physical properties of continuum sources. *Top* Source radiia, flux density, and luminosity. The minimum detectable flux density is calculated for a circular source, with a size equal to the average beam size and a Gaussian intensity profile with a peak intensity of five times the typical $\sigma_{\rm rms}$ level of the continuum images. *Bottom* mass, number density, and surface density of molecular hydrogen. The mass sensitivity is based on the minimum detectable flux at a temperature of 27 K.

2.3.2 Properties of the hosting clouds

The 20 target fields of our survey are centered at the position of YSOs detected with *Spitzer* (e.g. Meixner et al., 2006; Gruendl & Chu, 2009), and associated with bright *Herschel* emission from 70 to 500 μm (e.g. Meixner et al., 2013; Seale et al., 2014) tracing molecular clouds that host the cores detected with ALMA. To characterize the physical properties of these clouds, we constructed the SED (spectral energy distribution) within the wavelength range from 160 μm to 500 μm for all the 20 fields. We performed this analysis by integrating the flux density over an aperture that matches the ALMA field of view (with a radius 22″, or $\sim$ 5.3 pc at the distance of the LMC). The obtained flux density data were subsequently fitted with a modified blackbody function, described by:

$$F_\nu = \Omega B_\nu(T_\mathrm{d})(1 - e^{-\tau_\nu}) \tag{2.9}$$

where:

$$\tau_\nu = \mu_{\mathrm{H}_2} m_\mathrm{H} \kappa_\nu N_\mathrm{cloud}(\mathrm{H}_2) \tag{2.10}$$

Here, Ω represents the solid angle subtended by the cloud, assuming a circular shape with a radius of 22″. B_ν (T_d) denotes the black body function at the dust temperature T_d. κ_ν corresponds to the dust opacity, and $N_\mathrm{cloud}(\mathrm{H}_2)$ is the column density of molecular hydrogen. The dust opacity is described by:

$$\kappa_\nu = 0.1 \left(\frac{\nu}{1000\mathrm{GHz}}\right)^\beta \tag{2.11}$$

where κ_ν is in cm^{-2} g, ν the frequency, and β the dust emissivity index, assumed to be 2 in our analysis (e.g. Anderson et al., 2012). We obtained the best-fit parameters using a non-linear least squares Marquardt-Levenberg algorithm, with T_d and $N_\mathrm{cloud}(\mathrm{H}_2)$ as free parameters. A 15% uncertainty in flux density was assumed for all observed bands (e.g. Launhardt et al., 2013). We do not use data at 70 μm in our analysis. This is due to the anticipated influence of contributions from transiently heated very small grains (VSGs) to the 70μm data (e.g. Shetty et al., 2009; Russeil et al., 2013).

The molecular hydrogen volume density (n_cloud (H_2)) and gas surface brightness (Σ_cloud (H_2)) were calculated from the mass and radius of the cloud, assuming a spherical geometry. Finally, we integrated the flux density (F_ν) over frequency to calculate the luminosity of the cloud as:

$$L_\mathrm{cloud} = 4\pi D^2 \int F_\nu d\nu \tag{2.12}$$

where D is the distance to the LMC.

Figure 2.4 shows the distribution of masses, number densities and column densities of the hosting clouds. While the temperatures vary slightly between 20 to 28 K, the

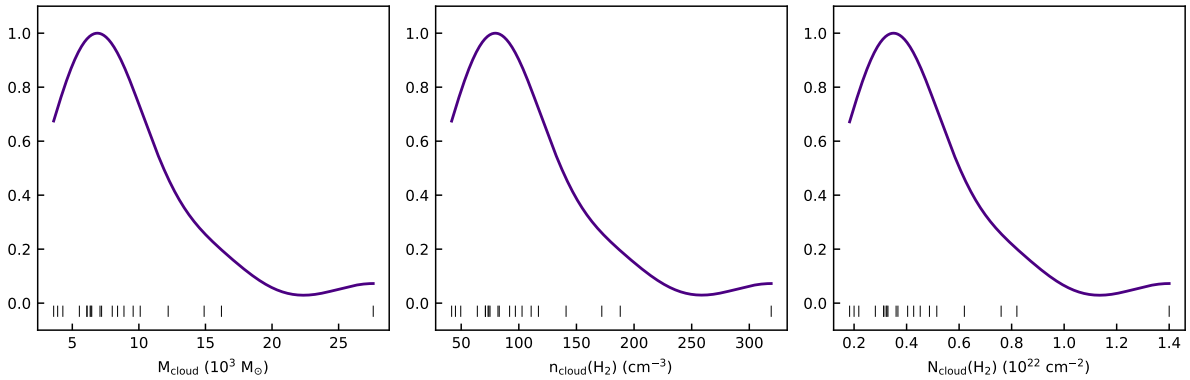


Figure 2.4: KDE distribution of mass, number density, and column density for the target clouds.

masses range from $(3.60 \pm 0.25) \times 10^3$ $M_\odot$ for field 20 to $(27.58 \pm 0.87) \times 10^3$ $M_\odot$ for field 6. Luminosities range from 3.37×10^5 $L_\odot$ for field 18 to 84.90×10^5 $L_\odot$ for field 6. All the derived parameters are listed in Table 2.2. The uncertainties are estimated through error propagation, accounting for the uncertainties derived from SED fitting, on $T_{\rm cloud}$ and $N_{\rm cloud}(H_2)$. Finally, we also estimate the local standard of rest velocity ($v_{\rm LSR}$) for each field (i.e., each cloud) based on the frequency shift of the CS emission line (at 244.935 GHz) as observed with ALMA.

Table 2.2: Physical properties of the clouds derived from SED fitting on the Herschel bands observations.

Field	$v_{\rm lsr}$ [a] (km s^{-1})	$T_{\rm cloud}$ [b] (K)	$M_{\rm cloud}$ (10^3 M$_\odot$)	$n_{\rm cloud}$ (H$_2$) (cm^{-3})	$N_{\rm cloud}$ (H$_2$) (10^{21} cm^{-2})	$L_{\rm cloud}$ (10^5 L$_\odot$)	$l_{\rm cloud,\ th-J}$ (pc)	$M_{\rm cloud,\ th-J}$ (M$_\odot$)
1	225	23.06±0.60	6.40±0.56	74.01±6.47	3.25±0.28	8.71	2.18±0.10	10.12±0.59
2	268	22.58±0.51	7.95±0.68	91.98±7.90	4.04±0.35	9.42	1.94±0.09	8.80±0.48
3	284	24.66±0.25	10.13±0.37	117.13±4.31	5.15±0.19	19.57	1.80±0.03	8.90±0.21
4	263	27.55±0.34	6.34±0.25	73.30±2.87	3.22±0.13	24.42	2.40±0.05	13.28±0.36
5	245	24.54±0.48	16.21±1.12	187.55±12.93	8.25±0.57	28.54	1.42±0.05	6.98±0.32
6	240	27.74±0.28	27.58±0.87	319.05±10.06	14.03±0.44	84.90	1.15±0.02	6.43±0.14
7	252	25.90±0.19	9.57±0.25	110.66±2.87	4.87±0.13	24.70	1.89±0.03	9.85±0.17
8	240	22.82±0.38	8.39±0.56	97.01±6.47	4.27±0.28	10.53	1.90±0.07	8.70±0.36
9	241	23.06±0.70	6.15±0.68	71.14±7.90	3.13±0.35	8.40	2.23±0.13	10.32±0.74
10	239	25.02±0.46	12.17±0.81	140.84±9.34	6.19±0.41	24.99	1.65±0.06	8.29±0.36
11	235	23.12±0.31	5.53±0.25	63.95±2.87	2.81±0.13	7.72	2.35±0.06	10.93±0.33
12	268	23.37±0.30	6.46±0.31	74.73±3.59	3.29±0.16	9.51	2.19±0.05	10.28±0.32
13	227	22.26±0.49	14.91±1.24	172.46±14.37	7.58±0.63	15.24	1.41±0.06	6.29±0.33
14	248	23.58±1.49	3.85±0.87	44.55±10.06	1.96±0.44	6.15	2.85±0.33	13.49±1.99
15	236	24.99±0.07	8.88±0.06	102.76±0.72	4.52±0.03	18.80	1.93±0.01	9.69±0.05
16	236	22.93±0.44	7.21±0.50	83.36±5.75	3.67±0.25	9.42	2.05±0.07	9.46±0.42
17	221	22.46±0.13	7.08±0.19	81.92±2.16	3.60±0.09	8.21	2.05±0.03	9.25±0.15
18	279	19.75±0.34	6.15±0.43	71.14±5.03	3.13±0.22	3.37	2.06±0.08	8.18±0.36
19	273	22.59±0.37	4.29±0.25	49.58±2.87	2.18±0.13	5.29	2.64±0.08	11.99±0.46
20	284	22.48±0.41	3.60±0.25	41.68±2.87	1.83±0.13	4.35	2.87±0.10	12.98±0.57

Notes. The field of view's radii is 22″ (5.3 pc) for all the fields.
[a] $v_{\rm lsr}$ is defined from the shift in frequency of CS emission line in the spectra of the ALMA observations for the most line-rich core in each field.
[b] $T_{\rm cloud}$ is the temperature achieved from the SED fitting.
[c] Sewiło et al. (2022)
[d] Henize (1956)

Table 2.3: Core separations in each field from MST analysis

Field	number of cores	Min. sep (pc)	Max. sep (pc)	Med. sep (pc)	Mean sep (pc)
2	6	0.17	1.15	0.25	0.40
3	4	0.35	0.70	0.38	0.48
6	6	0.25	1.96	0.88	0.99
7	3	0.41	2.62	1.51	1.51
8	3	1.53	2.24	1.89	1.89
10	4	0.36	1.94	0.49	0.93
11	4	0.27	3.73	0.31	1.44
12	4	0.17	1.38	0.17	0.57
13	9	0.14	3.74	0.48	1.03
15	3	1.44	2.50	1.97	1.97
18	3	0.29	0.96	0.63	0.63
19	4	0.50	1.20	1.16	0.96

2.3.3 Cluster analysis of 1.2 mm continuum cores

The emission distribution observed in the continuum images reveals varying levels of fragmentation across our target fields. Some regions exhibit a single dense core, while others display more complex fragmentation patterns. In this section, we focus on regions with more than two cores to explore the properties of star-forming clusters in the LMC.

The number of fragments (cores) per target field varies from one to nine in this sample. To study the spatial distribution of these fragments, we calculated the typical separation between the cores. For this, we apply a minimum spanning tree (MST) algorithm using the Python package `networkx`[3] (version 2.8.6). The MST connects the core positions without creating loops, minimizing the total path length between them. We performed the MST analysis on the 12 fields of our sample that contain at least three cores.

Figure 2.5 shows the MST for the most densely populated fields (the plots of the remaining fields are available in Appendix A.3). The circles represent the positions of the cores, scaled by their masses, while the lines indicate the connection between the cores. Table 2.3 provides a summary of the core separations for each field. The mean separation of the cores in a field ranges from 0.4 to 1.97 pc, while the median separation varies between 0.25 and 1.97 pc.

Due to the limited number of cores in each field, a detailed cluster analysis is not feasible for individual fields. Assuming that all the targets in the observed sample correspond to star-forming clusters with comparable properties, we combined the core

[3]https://github.com/networkx/networkx

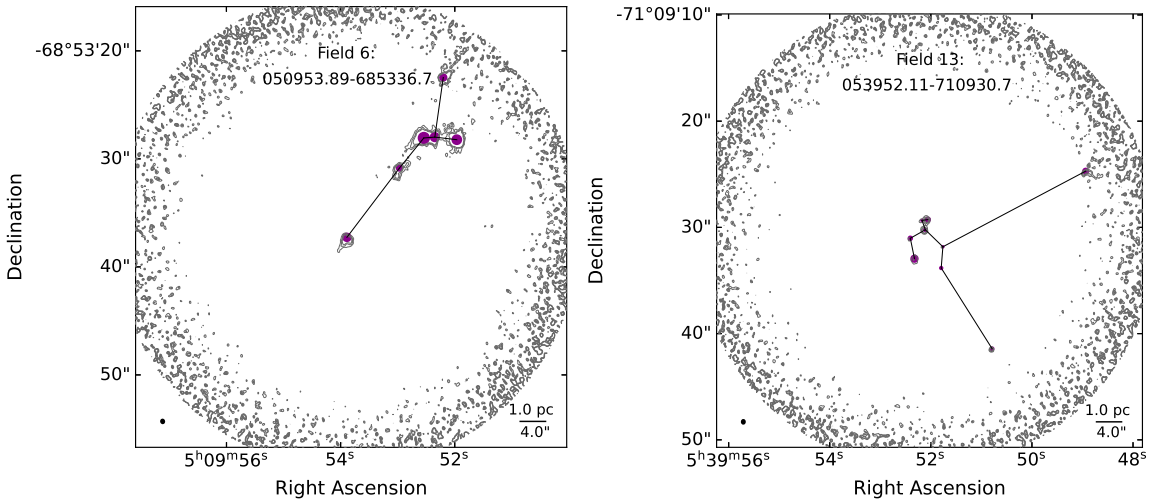


Figure 2.5: Minimum spanning tree (MST) for the ALMA continuum cores in the most populated fields: *left* field 6 and *right* field 13. The positions of the dense cores are indicated with circles, scaled with the mass of the cores, while the lines mark the tree.

separation data from all 12 fields. The separation distribution of the cores is shown in Fig. 2.6, where the distribution peaks at a separation of 0.35 pc, with a median and average value of 0.50 pc and 0.98 pc, respectively. The minimum resolvable spatial scale is 0.09 pc, and core sizes ($2R_{\rm core,deconv}$) range from 0.1 to 0.3 pc. Given the typical core size of 0.12 pc, the cores are separated by a length of a factor of 2.9.

2.4 Discussion

Based on the distribution of our target fields across the whole LMC, we consider our sample to be representative of the star formation occurring in this galaxy. With this in mind, we now discuss the results from Section 2.3, in light of the environmental conditions that the LMC offers for star formation. In particular, we assess the potential impact of the LMC's lower metallicity on star formation by comparing our findings with other theoretical and observational studies from the Milky Way (MW) and the LMC.

In our survey of 20 fields, we detected 65 continuum cores at 1.2 mm. These cores reflect various levels of fragmentation in the fields. In the following, we investigate the conditions for collapse and fragmentation from the cloud to the core scales and beyond (see Section 2.4.1). Additionally, we explore the star-forming clusters representative of the LMC (see Section 2.4.2).

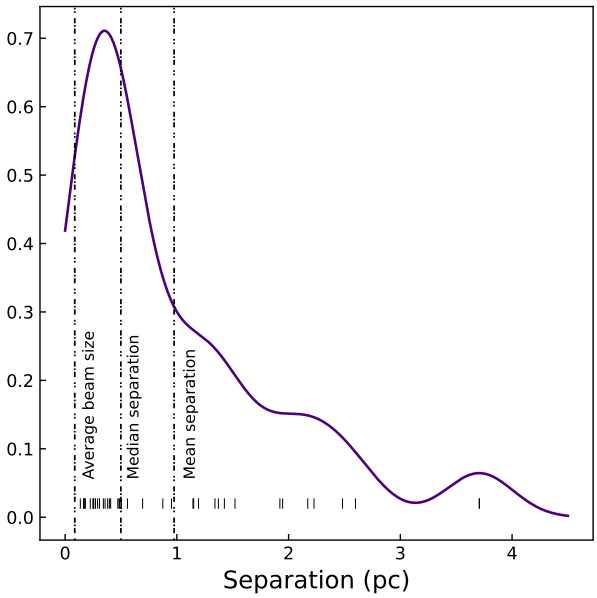


Figure 2.6: KDE of the projected separation between nearest neighbors for the 12 fields with more than two dense cores.

2.4.1 Collapse and fragmentation; from clouds to cores and beyond

In this section, we discuss the conditions for collapse and fragmentation across different spatial scales, from clouds (10 pc) to cores (0.1 pc). We begin by exploring these processes at cloud-to-core scales (Section 2.4.1), followed by an investigation into the stability of the cores (Section 2.4.1). Finally, we assess the potential for further fragmentation into structures smaller than the size of the cores seen with ALMA (Section 2.4.1).

From clouds to cores

The detection of single and multiple cores in our ALMA data confirms that the target clouds must have undergone collapse and fragmentation. The size and mass of the fragments (cores; $2R_{\rm core,deconv}$ and $M_{\rm core}$) range from 0.1 to 0.3 pc and 17.73 ± 9.62 $M_\odot$ to 991 ± 235.77 $M_\odot$, respectively. In Fig. 2.7 (top panel), we assess the core formation efficiency (CFE) by comparing the total mass contained in the cores with the mass of each hosting cloud. The CFE in our sample varies between approximately 1% and 20%, with a median of (4.7 ± 0.8)%.

The QUARKS[4] survey observed 139 massive star-forming clumps in the MW with ALMA Band 6 (Xu et al., 2024). The massive clumps span a wide range of sizes, from 0.2 to 4 pc, while the fragments within them (a total of 207) range in size from 0.015

[4]Querying Underlying mechanisms of massive star formation with ALMA-Resolved gas Kinematics and Structures

to 0.5 pc. A comparison of clump and fragment masses suggests a CFE (or Dense Gas Fragments) of 6% (Xu et al., 2024). The CFE derived in our current study of the LMC is slightly lower.

Figure 2.7 (top panel) compares the correlation between the total core mass and the hosting cloud mass from the current study and Xu et al. (2024). It is evident that the current work traces the high-mass end of the clouds, while still following similar trends. The luminosity-to-mass ratio (L/M) as an indicator of evolutionary sequence has been shown to correlate with the CFE in the Galactic star-forming regions (e.g., Traficante et al., 2023; Xu et al., 2024). We have also looked for any correlation between the CFE and L/M in our LMC regions. In the plots, presented in Appendix A.4, we do not identify any clear trend likely due to the large scatter of the data and the relatively narrow range of the L/M across the 20 fields from 1.67×10^2 to 3.85×10^2 $M_\odot/L_\odot$.

In the middle panel of Fig. 2.7, we examine the relationship between the most massive core mass and the respective host cloud mass. Our findings reveal a trend indicating that more massive clouds tend to form more massive cores. To quantify how much mass is concentrated in the most massive cores, we construct a relation between the maximum core mass in a field and the total core mass. From this plot, two key observations emerge. First, while the general trend is similar between the LMC and the MW, the data from this study show that a higher percentage of the total mass is concentrated in the most massive cores in the LMC, with a minimum ratio of 27%. Second, in the Xu et al. (2024) dataset, a significant fraction of fields (67%) exhibit the detection of a single core, resulting in 100% of the total mass being concentrated in the most massive core. In contrast, only 20% of the fields in our sample are single-core fields, suggesting a lower level of fragmentation in the Xu et al. (2024) dataset compared to our study.

A commonly used approach to characterize fragmentation is through Jeans fragmentation. According to this theory, a cloud with initially uniform density may collapse under its own gravity, forming fragments that can further collapse and fragment over time. The general expression for calculating the Jeans mass is:

$$M_{\rm J} = \frac{\pi^{5/2}}{6G^{3/2}} \frac{c_{\rm eff}^3}{\rho^{1/2}} \tag{2.13}$$

where G is gravitational constant, $c_{\rm eff}$ is the effective sound speed and ρ is the density. Assuming thermal pressure as the primary counteracting force against gravity, we consider the thermal Jeans fragmentation of a cloud, composed of molecular hydrogen. In this context, $c_{\rm eff}$ is expressed as:

$$c_{\rm eff} = \sqrt{\frac{k_{\rm b}\ T_{\rm cloud}}{\mu_{\rm H_2}\ m_{\rm H}}} \tag{2.14}$$

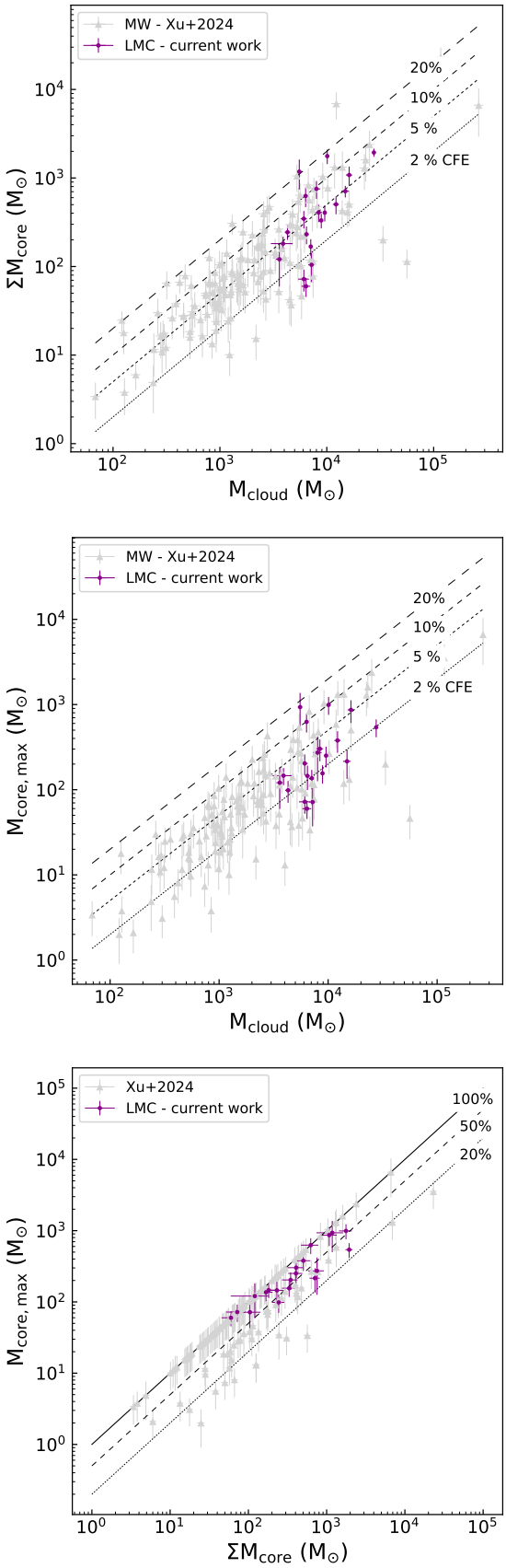


Figure 2.7: *Top*: Total core mass versus cloud mass in each field. *Middle*: Maximum core mass vs. cloud mass in each field. The dashed lines indicate CFE of 2%, 5%, 10%, and 20%. *Bottom*: Maximum core mass vs. total core mass in each field. The lines indicate the ratio of total core mass in the most massive core.

and ρ as:

$$\rho = n_{\rm cloud}({\rm H_2})\ \mu_{\rm H_2}\ m_{\rm H}. \tag{2.15}$$

The last column of Table 2.2 lists the derived thermal Jeans mass of the clouds ($M_{\rm cloud,th-J}$), providing an estimate of the expected core masses if the clouds underwent thermal Jeans fragmentation. Figure 2.8 compares $T_{\rm core}$ versus $T_{\rm cloud}$, as well as $M_{\rm core}$ with $M_{\rm cloud,\ th-J}$. The dashed lines mark the isothermal condition and one-to-one mass relation, respectively. The median $T_{\rm core}$ in 90% of the fields equals or exceeds $T_{\rm cloud}$. This results suggests the presence of internal heating inside the cores, as has been found towards star-forming clouds in the MW (Xu et al., 2024), which is a signature of ongoing star formation.

Comparisons between the observed 1.2 mm continuum core masses and the cloud thermal Jeans mass reveal that all cores have significantly higher masses than thermal Jeans mass. This implies that non-thermal (dynamical) gas motions, likely driven by turbulence, play a crucial role in the collapse and fragmentation at scales of 10 pc, greater mass accumulation in fragments. Accounting for turbulence, the $c_{\rm eff}$ in Equation 2.13 includes both thermal and non-thermal contributions. This results in a total line width of 1.40 ± 0.05 km/s with a non-thermal contribution of 1.156 ± 0.022 km/s. These values are consistent with the typical line widths observed in molecular clouds in the MW (e.g., Neralwar et al., 2022) and the LMC (e.g., Grishunin et al., 2024).

This cascading process, from cloud scales ($\sim$ 10 pc) to core scales ($\sim$ 0.1 pc) is consistent with observations in the Galactic environments. For example, Sadaghiani et al. (2020) identify two regimes of fragmentation in the NGC 6334 star-forming region: turbulence-dominated fragmentation at scales of 1–12 pc and thermal-support fragmentation at smaller scales. Similarly, Xu et al. (2024) also report turbulence-supported fragmentation at spatial scales of $\sim$ 3–5 pc.

Stability of the cores

To assess the stability of the observed ALMA continuum cores, we estimate their virial masses. Following Pillai et al. (2011), the general expression to estimate the virial mass ($M_{\rm vir}$) is:

$$M_{\rm vir} = \frac{5 r \sigma^2}{G} \tag{2.16}$$

where r represents the source radius (in this case $R_{\rm core}$), σ is the velocity dispersion, and G is the gravitational constant. The velocity dispersion (σ) is related to the line width (Δv) through the relation:

$$\sigma = \frac{\Delta v}{\sqrt{2 \ln 2}} \tag{2.17}$$

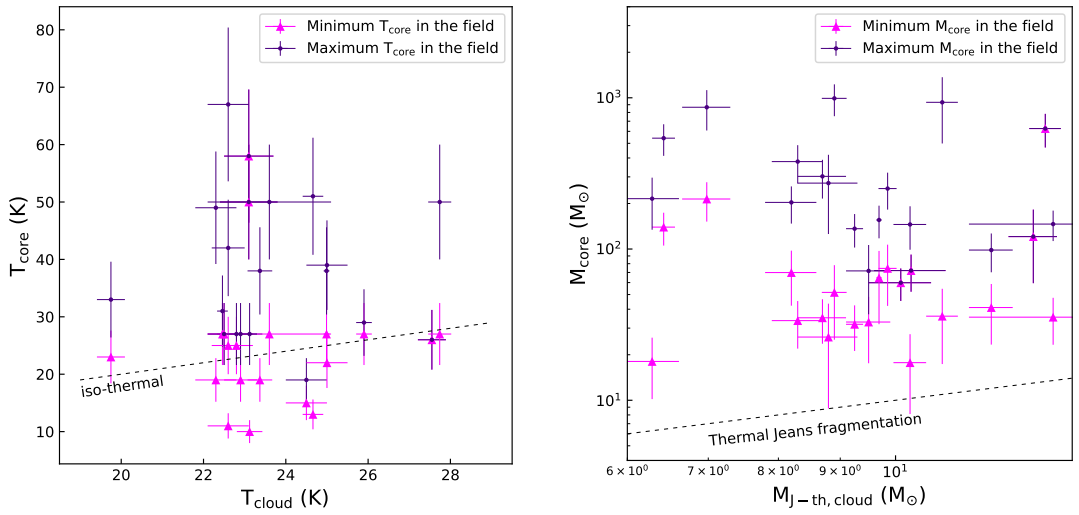


Figure 2.8: *Left*: $T_{\rm core}$ vs. $T_{\rm cloud}$. The iso-thermal line signaling the same temperate within the cores and hosting clouds is depicted with dashed line. *Right*: $M_{\rm core}$ vs. $M_{\rm cloud,\ th-J}$. The dashed line represents the thermal Jeans fragmentation, where $M_{\rm core}$ = $M_{\rm cloud,\ th-J}$. The cores with minimum and maximum value in each field are indicated with magenta triangle and indigo circle.

This allows us to drive σ from the Δv. For this purpose, we use the line-width measured at the position of each core from the spectral line analysis of CH_3OH presented in Paper I. Cores without spectral lines are excluded from this analysis, leaving a total of 58 cores for which virial masses are calculated. The observed line width ($\Delta v_{\rm obs}$) is a combination of thermal and non-thermal (or dynamic) broadening and the channel width. Assuming Gaussian spectral line profiles, $\Delta v_{\rm obs}$ can be expressed as:

$$\Delta v^2_{\rm obs} = \Delta v^2_{\rm th} + \Delta v^2_{\rm nonth} + \Delta v^2_{\rm chan} \tag{2.18}$$

Here $\Delta v_{\rm th}$ accounts for the thermal broadening, while $\Delta v_{\rm nonth}$ captures the contribution from dynamic motions such as turbulence and $\Delta v_{\rm chan}$ represents the channel width of the observations. The resulting values for $\Delta v_{\rm obs}$, $\Delta v_{\rm th}$ and $\Delta v_{\rm nonth}$ are listed in columns (2), (3) and (4) of Table A.2. The role of turbulence in supporting the cores against collapse can also be evaluated through the Mach number ($\mathcal{M}_{\rm core}$), defined as the ratio of the non-thermal velocity dispersion to the thermal sound speed. Our results show a range of values from 1.5 ± 1.0 to 16.8 ± 3.8 for $\mathcal{M}_{\rm core}$. This result suggests that all the cores are supersonic and hypersonic with turbulence speed being the dominant component in the cores (see Fig. 2.3 panel h).

The combined thermal and non-thermal velocity dispersion $\sigma_{\rm th+nonth}$ is calculated as:

$$\sigma_{\rm th+nonth} = \sqrt{\frac{\Delta v^2_{\rm obs} - \Delta v^2_{\rm chan}}{2{\rm ln}2}} \tag{2.19}$$

The thermal velocity dispersion ($\sigma_{\rm th}$) is derived using Equation 2.14 with the core

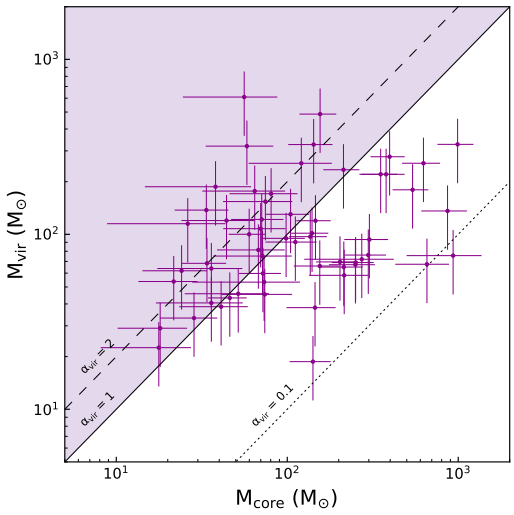


Figure 2.9: Virial mass vs. the $M_{\rm core}$. The dashed lines representing virial parameters α = 0.1, 1, and 2.

temperature ($T_{\rm core}$). This allows us to decompose the observed velocity dispersion into thermal and nonthermal components.

The virial mass for each core is then calculated as:

$$M_{\rm core,vir} = \frac{5R_{\rm core}\sigma^2_{\rm th+nonth}}{G} \tag{2.20}$$

The virial parameter $\alpha_{\rm vir}$, defined as the ratio of the virial mass to the observed core mass is:

$$\alpha_{\rm vir} = \frac{M_{\rm vir}}{M_{\rm core}}. \tag{2.21}$$

The parameter serves as an indicator of core stability. In the classical interpretation, if $\alpha_{\rm vir} < 1$, the core is gravitationally bound and may collapse, whereas $\alpha_{\rm vir} > 1$ suggests the core is not gravitationally bound and could eventually disperse (see Fig. 2.3 panel i). The $M_{\rm core,vir}$ and $\alpha_{\rm vir}$ are listed in column (5) and (6) of Table A.2.

Figure 2.9 illustrates the relation between virial masses and core masses. Approximately 50% of the cores exhibit $\alpha_{\rm vir} < 1$, indicating that these cores may collapse in the absence of additional supporting mechanisms. To explore whether these cores are indeed collapsing or if any forces are contracting gravity, we consider the case of $\alpha_{\rm vir}$ = 1, which implies virial equilibrium.

Following Pillai et al. (2011), we assess the role of magnetic fields in stabilizing the cores against gravitational collapse. Incorporating the effect of magnetic fields, the virial mass equation is modified as:

$$M_{\rm B,vir} = \frac{5R}{G}(\sigma^2_{\rm th+nonth} + \frac{1}{6}\sigma^2_{\rm A}) \tag{2.22}$$

where $\sigma_{\rm A}$ is the Alfvén speed, defined as:

$$\sigma_A = \frac{B}{4\pi\rho}. \tag{2.23}$$

The magnetic field strength ($B_{\rm core}$) required to support the core against collapse is then given by:

$$B_{\rm core} = \sqrt{24\pi\rho_{\rm core}(\frac{GM_{\rm core}}{5R_{\rm core}} - \sigma^2_{\rm th+nonth})}. \tag{2.24}$$

For the cores in our sample, the magnetic field strengths needed to counteract collapse range from 10 to 100 μG (see Fig. 2.9 right panel). These values are consistent with typical magnetic field strengths observed in star-forming regions in the MW (e.g. Pillai et al., 2011).

Further fragmentation

We next investigate whether the ALMA cores are likely to undergo further fragmentation. This analysis provides insight into the potential for the cores to form multiple stars or systems, thereby enhancing our understanding of the star formation process. To this end, we calculate the thermal and non-thermal Jeans masses of the cores using the modified Jeans mass equation (Equation 2.13):

$$M_{\rm core,th+nonthJ} = \frac{\pi^{5/2}}{6G^{3/2}} \frac{\sigma^3_{\rm th+nonth}}{\rho^{1/2}} \tag{2.25}$$

By substituting the thermal and non-thermal velocity dispersions into this equation, we derive their respective contributions. The thermal Jeans masses and combined Jeans masses are presented in columns (7) and (8) of Table A.2.

Figure 2.10 compares the total Jeans mass of the cores to their actual masses. Cores within the shaded region are presumed to remain as single fragments, while those below the x=y line (where core mass equals the Jeans mass) are likely to undergo further fragmentation. To estimate the number of fragments each core may produce, we consider two limiting cases. First, we assume that all the mass in the core fragments into smaller structures (fragmentation efficiency of 100%). Our analysis suggests that approximately 70% of the cores may experience further fragmentation. Under this scenario, around 15% of the cores have the potential to fragment into up to 20 smaller fragments (Fig. 2.10 left panel).

To estimate the lower limit of fragmentation efficiency, we adopt a value of 5%, derived from the cloud-to-core conversion efficiency. Previous studies, specifically, Xu et al. (2024) observed a size-independent dense gas fraction and suggested self-similar fragmentation of 6% across spatial scales ranging from 0.2–4pc down to 0.015–0.5pc. Similarly, studies such as Sanhueza et al. (2019) and Traficante et al. (2023) reported a

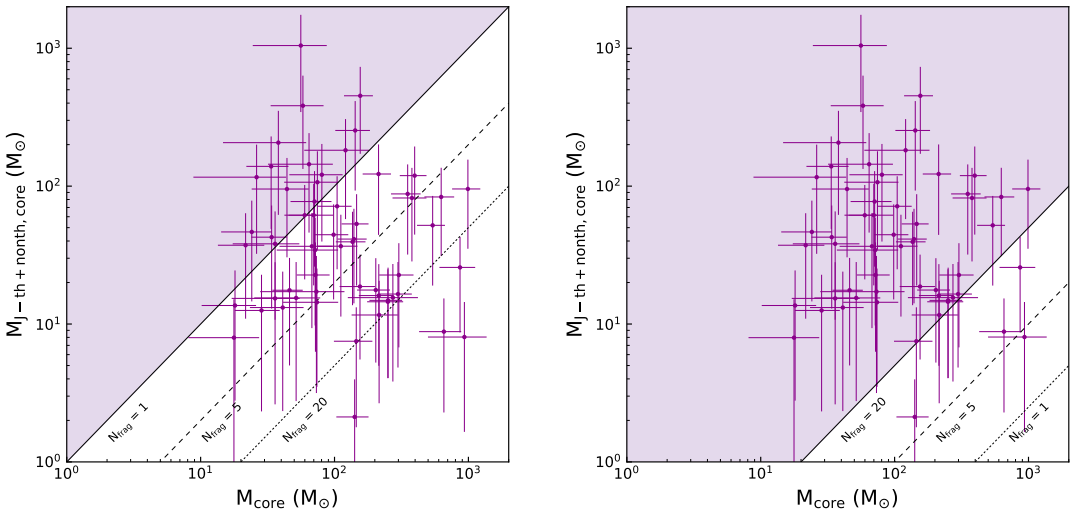


Figure 2.10: Comparisons of total Jeans mass and core masses. The inserted lines show the possible number of fragments form. *Left*: Assuming a fragmentation efficiency of 100%. *Right*: Assuming a self-similar frag mention across the scales as suggested by Xu et al. (2024) and adapting a fragmentation efficiency of 5%, obtained from CFE from clouds to cores in our sample.

fragmentation efficiency of approximately 6% at smaller scales of 0.015–0.15 pc. Adapting this self-similar fragmentation efficiency across scales, we use 5% as a conservative estimate for the fragmentation efficiency in our analysis.

These two scenarios highlight the need for deeper, high-resolution observations to compare the fragmentation levels in the LMC and the MW. Observations from the ALMAGAL survey (Molinari et al. submitted, Sanchez-Monge et al. submitted, Coletta et al. submitted), which cover a field of view of $\sim$ 0.1 pc (comparable to the typical size of the cores in our sample), frequently reveal multiple fragments within cores. This suggests that the cores in our sample could plausibly host clusters of smaller fragments.

Following the approach in Xu et al. (2024), we estimate the potential for massive star formation. Assuming monolithic collapse, where only a single star forms per core, 60 cores in our sample (92%) are massive enough to form a massive star ($>$ 8 $M_\odot$) with a core-to-star efficiency $\sim$ 30%. Alternatively, if each core forms a cluster, we use the empirical relation in Equation 9 of Xu et al. (2024) and Larson 2003, to estimate the formation of 39 (60%) massive stars within the ALMA cores. This result suggests a higher fraction of massive stars compared to the Galaxy, with 59% cores forming massive stars under monolithic collapse and 34% forming massive stars in the cluster forming state in Xu et al. (2024).

2.4.2 Cluster properties in the sub-solar metallicity

As discussed in the introduction, environments with lower metallicity are expected to influence the collapse and fragmentation processes in star-forming clusters. Reduced metallicity leads to higher temperatures within molecular clouds due to a weaken shielding effect. This increase in temperature results in larger Jeans masses, which in turn enhances the formation of more massive stars within a cluster. Consequently, we expect an excess of mass at the high-mass end of the mass function, often referred to as a top-heavy mass function. Moreover, lower metallicity affects the impact of the surrounding radiation field. On one hand, the increased population of massive stars due to lower metallicity leads to enhanced radiative feedback. On the other hand, the reduced dust content in these environments diminishes the radiation pressure. Therefore, the combined effects of metallicity on the mass function and core sizes, driven by mutual feedback and accretion processes, warrant a thorough investigation. In this section, we examine three key aspects of the cores: the mass function (Section 2.4.2), the radius-mass correlation (Section 2.4.2), and the spatial distribution of cores within clusters (Section 2.4.2).

Core Mass Function

Observations of massive star-forming regions in the MW suggest that the core mass function (CMF), which represents the mass distribution of prestellar and protostellar cores, may resemble the stellar initial mass function (IMF), linking it to the process of cloud fragmentation (see e.g., Liu et al., 2018). However, deviations, such as an excess of massive cores, have been reported (see e.g., Zhang et al., 2015; Sánchez-Monge et al., 2017; Motte et al., 2018b). The relationship between the CMF and the IMF remains a critical area of study in understanding star formation processes. The evolution of the CMF from the cloud mass function and its subsequent transition to the IMF involves factors such as filaments, magnetic fields, feedback, and star formation paradigms (e. g., André et al., 2019; Krumholz et al., 2019; Pelkonen et al., 2021).

Evidence suggests that the mass function of star clusters varies over time (e.g., Cheng et al., 2024). Nonetheless, the mass function is typically characterized by a differential power-law form as:

$$\frac{dN}{dM} \propto M_{\rm core}^{\alpha-1} \tag{2.26}$$

or

$$N(\geq M) \propto M_{\rm core}^{\alpha} \tag{2.27}$$

where $\alpha = -1.35$ corresponds to the Salpeter stellar IMF slope (Salpeter, 1955). Studies of evolved regions, such as G012.80 within the ALMA-IMF sample, indicate CMF slopes closer to the Salpeter IMF. This suggests that the CMF steepens as regions

evolve, consistent with the longer timescales required for low-mass star formation, which results in a CMF increasingly dominated by lower-mass cores over time (Louvet et al., submitted).

The IMF of the LMC has been studied through observations of OB-associations and field star populations. (Massey, 2003, and the references therein) compared the IMF slopes of the Small Magellanic Cloud (SMC), LMC, and MW, finding that the slope of the high-mass IMF in the LMC is broadly consistent with the Salpeter IMF. However, the LMC's sub-solar metallicity has led to speculation about a top-heavy IMF, favoring massive star formation (e. g., Li et al., 2023; Tanvir & Krumholz, 2024). In the 30 Doradus region, Bestenlehner et al. (2020) identified evidence of a top-heavy IMF in the R136 massive star-forming region.

In this study, we constructed the cumulative CMF for the 1.2 mm cores detected in the LMC sample (see Fig. 2.11). Core masses were estimated using CH_3OH temperatures, assuming gas and dust coupling in high-density regions to ensure well-mixed conditions (Tang et al., 2017). For cores lacking temperature measurements, a median temperature of 27 K was adopted. We fit the cumulative CMF using two models. First we scaled the Kroupa IMF (Kroupa, 2001) to higher core masses, using the form of Equation 2.27 with α value as:

$$N(\geq M) = Scaling\ Factor\ . \begin{cases} M_{\rm core}^{\alpha_1} & M_{\rm core} < 0.08 \\ M_{\rm core}^{\alpha_2} & 0.08 < M_{\rm core} < 0.5 \\ M_{\rm core}^{\alpha_3} & M_{\rm core} > 0.5 \end{cases} \tag{2.28}$$

The scaling factor and the α values were treated as free parameters for fitting. The scaling factor proportional to the inverse of star formation efficiency, which we estimate to be $\sim 0.3\%$.

Then we used a double power-law function:

$$N(\geq M) \propto \begin{cases} M_{\rm Break}^{(\alpha_{\rm h}-\alpha_{\rm l})}\ M_{\rm core}^{\alpha_{\rm l}} & M_{\rm core} < M_{\rm Break} \\ M_{\rm core}^{\alpha_{\rm h}} & M_{\rm core} \geq M_{\rm Break} \end{cases} \tag{2.29}$$

Here, $M_{\rm Break}$, $\alpha_{\rm l}$ and $\alpha_{\rm h}$ were free parameters. Using a Monte Carlo Markov Chain (MCMC) algorithm implemented in the Python package `emcee`, we derived the best-fit parameters for the cumulative CMF, excluding the data points below the mass sensitivity limit. Figure 2.11 shows the best-fit curves and parameters for the Kroupa mass function (top panels) and double power-law (bottom panels). The left panels include all the cores, while the right panels exclude cores with ATCA detections.

Comparison of the high-mass slops indicates that the Kroupa function is slightly shallower than the Salpeter IMF, while the double power-law fit aligns more closely

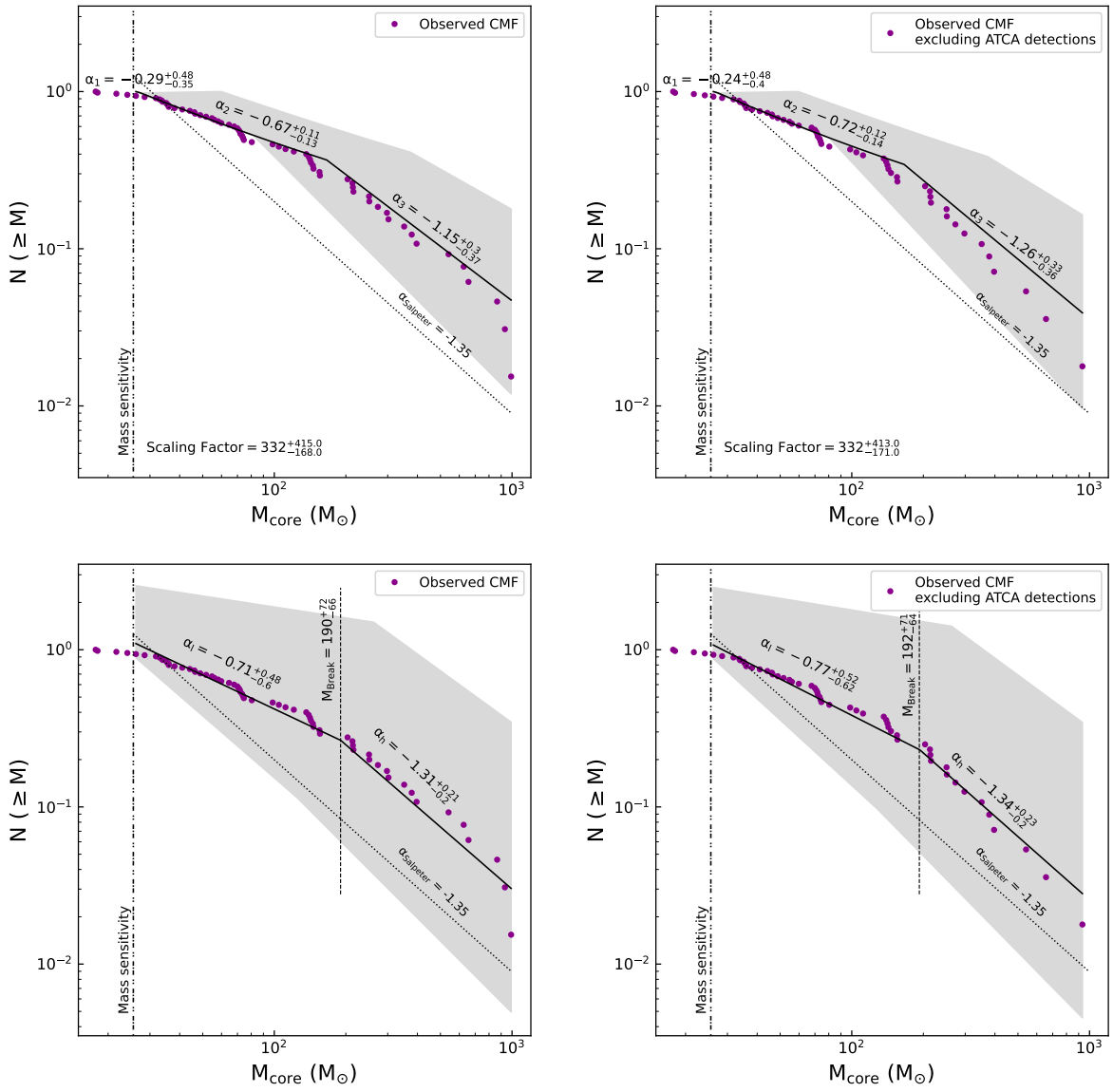


Figure 2.11: Cumulative core mass function (CMF), *Left panels* for all the cores and *Right panels* excluding cores with ATCA detection. The observed CMF is fitted with *Top panels* Kroupa mass function scaled to core masses and *Bottom panels* double power-law. The best fit curve, and free parameters for fitting is indicated in each panel. The Salpeter IMF and mass sensitivity are depicted for reference.

with the Salpeter slope. For intermediate masses, all fits yield comparable slopes, , albeit with varying uncertainties. Due to the mass sensitivity of our sample, we do not discuss the low-mass regime further. The break mass for the double power-law function is approximately 190 $M_\odot$.

Brunetti & Wilson (2019) constructed the mass function of 32 molecular clumps with the total dust mass between 200 and 5700 $M_\odot$ in the LMC. Using a double power-law function they derived an $\alpha_{\rm l} = 0.76^{+0.04}_{-0.05}$ and $\alpha_{\rm h} = -2.3 \pm 0.2$ with a break mass of 2500^{+300}_{-200} $M_\odot$. When comparing their results to our study, their lower mass range overlaps with the higher mass end of our sample. Our derived average $\alpha_{\rm h} \simeq -1.26$ is steeper than their $\alpha_{\rm l} = 0.76$. Considering that the 32 clumps analyzed by Brunetti & Wilson (2019) are located in the massive star-forming regions of 30 Dor and N159, the shallower slope observed in their study, which reflects an excess of higher-mass clumps, is understandable.

Comparing the core/clump mass function and the double power-law indices from their study with thoes from MW(e.g., Reid & Wilson, 2006), Brunetti & Wilson (2019) found consistent α values, suggesting that the mass function for the LMC represents an extension of the Galactic core/clump mass function. Additionally, they compared their dust-driven mass function with the CO-driven mass function from Indebetouw et al. (2013) for the 30 Dor region in the LMC. Incorporating results from the hydrodynamic simulation of Fujii & Portegies Zwart (2015), which includes radiative feedback and yield $\alpha = -0.99 \pm 0.14$ for clusters with masses 10 and 2000 $M_\odot$ after 5Myr evolution, Brunetti & Wilson (2019) emphasized that their clump mass function is broadly consistence with previous studies.

The power-law index derived from our study does not indicate a top-heavy CMF, which might have been expected under low-metallicity conditions. However, the variations in slope compared to other clump-scale studies in the LMC (Indebetouw et al., 2013; Brunetti & Wilson, 2019; Wong et al., 2019) could reflect differing levels of feedback within our sample. To explore this further, we construct the Radius-Mass relation in the next section.

Several uncertainties influence the construction and interpretation of the CMF:

- Spatial Resolution: The spatial resolution of ALMA limits the detection of smaller fragments and core multiplicity.
- Mass Sensitivity: Observational sensitivity and beam size restrict the detection of lower-mass cores, potentially biasing the CMF's low-mass end.
- Temperature Estimation: Core masses derived from CH_3OH temperatures or assumed median temperatures introduce variability.
- Dust Emission Assumption: Assuming that all 1.2 mm emission arises from dust

may overestimate core masses, particularly for massive cores where free-free emission could contribute.

- Evolutionary Stages: The cores' evolutionary stages, spanning prestellar to protostellar phases, add complexity to CMF interpretation.

- Gas-to-Dust Ratio Variability: Spatial variations in the gas-to-dust ratio across the LMC challenge the use of a uniform value for all cores.

Despite these limitations, comparing our CMF with the Salpeter, and Kroupa IMF and other CMFs from the MW and Magellanic Clouds provides valuable insights into star formation processes in low-metallicity environments.

Mass-Radius relation

From statistical perspective, alongside the mass function of a population, the Radius-Mass relation provides valuable insight. Figure 2.12 presents the deconvolved source radii ($R_{\rm core,deconv}$) plotted against $M_{\rm core}$ for a sample of LMC from this work, Sewiło et al. (2022) and Brunetti & Wilson (2019), spanning a spatial range of 0.01 to approximately 1 pc. Additionally, we include the data from Xu et al. (2024), which covers a similar spatial range but extends up to 4 pc. The plot clearly shows that LMC fragments are shifted toward the higher-mass end. This shift could be attributed to a lack of sensitivity or the influence of metallicity.

If we fit a curve to the LMC data points (shown in purple in Fig. 2.12) and MW data points (shown in gray in Fig. 2.12) the β index in $R \propto M^{\beta}$ is found to be 0.53 ± 0.05 and 0.49 ± 0.01 respectively. The slightly higher β value for the LMC may indicate a higher level of feedback. Our comparison suggests that the Galactic and LMC results are consistence within the spatial scales of 0.01 to 4 pc and mass range of 10 to 10000 $M_{\odot}$. However, it appears that the α and β power-law indices evolve from lager scales of clouds and clumps to the smaller scales of cores.

Spatial distribution in the clusters

Figure 2.13 illustrates the distance to the nearest neighbor as a function of core mass. The plot reveals a clear trend: more massive cores are generally located closer to their nearest neighbors, while cores with larger separations tend to have lower masses. This trend likely reflects clustering around massive cores. However, it is crucial to emphasize that this observation should not be interpreted as evidence of mass segregation, which specifically refers to the most massive cores being centrally concentrated within a cluster (e.g., Sadaghiani et al., 2020).

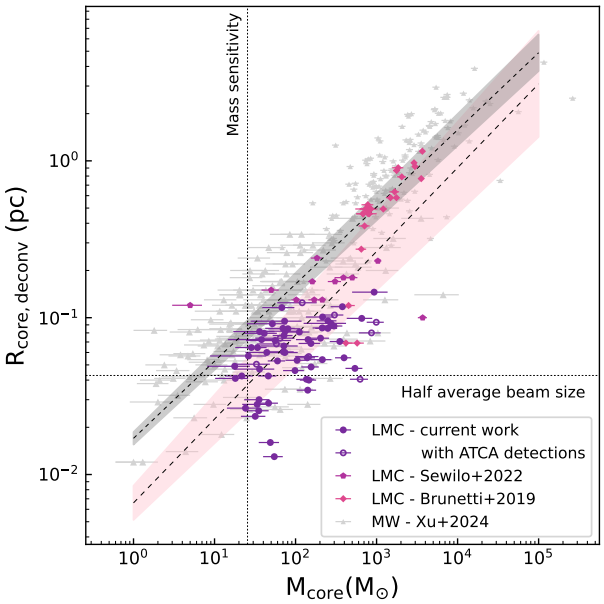


Figure 2.12: Correlation of mass and radius of the cores. Colored symbols represent the cores in the LMC from our sample, as well as Sewiło et al. (2022) and Brunetti & Wilson (2019). Gray symbols indicate Galactic structures from Xu et al. (2024). The two lines, along with their respective uncertainties (indicated by the shaded regions), show the fits to the Galactic and the LMC data points.

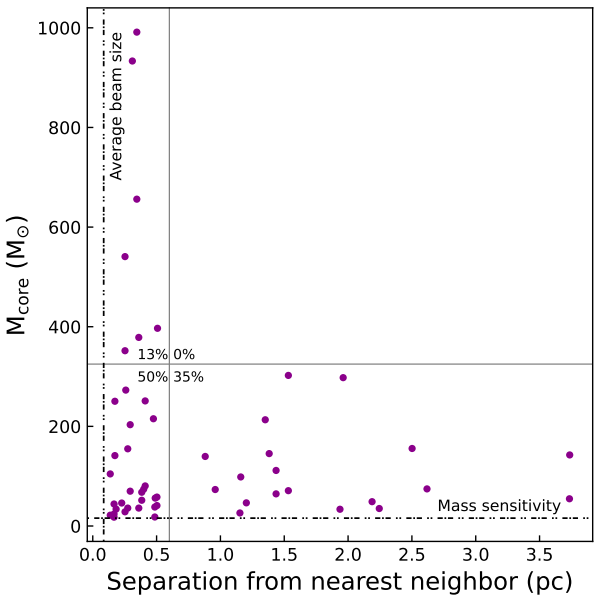


Figure 2.13: Spatial distribution of cores in the cluster with respect to their mass. The dashed-dotted lines represent the mass sensitivity limit and the average synthetic beam size for our sample. The two gray lines divide the parameter space into four quadrants. The vertical gray line separates cores with separation sizes smaller than the median separation (from Fig. 2.6) from those with larger separations. The horizontal gray line is positioned just above the most massive cores with separations larger than the median separation. The percentage of cores in each quadrant is indicated within the plot.

2.5 Conclusions

We conducted observations of 20 star-forming regions across the LMC using ALMA in Band 6 ($\sim$ 250 GHz) with an angular resolution of $0.4''$, corresponding to a physical scale of approximately 0.09 pc. A total of 65 continuum cores were identified. This work focuses on exploring their physical properties, while the chemical characteristics are addressed in Paper I. The main conclusions of this study are outlined below:

1. The 65 1.2 mm compact continuum sources, ranging from 0.1 to 0.3 pc in size, are representative of core-scale structures in the LMC. Their masses range from 17.73 ± 9.62 to 991 ± 235.77 $M_\odot$ and the number and column densities vary from $(1.2 \pm 0.5) \times 10^5$ to $(1.1 \pm 0.3) \times 10^7$ cm^{-3} and $(6.0 \pm 3.2) \times 10^{22}$ to $(2.5 \pm 0.6) \times 10^{24}$ cm^{-2}, respectively.

2. In the collapse and fragmentation of clouds approximately 10 pc in diameter into cores around 0.1 pc, nonthermal components such as turbulence play a crucial role. The CFE is approximately 5%, and more massive clouds are observed to preferentially form more massive cores.

3. All the cores are supersonic and hypersonic. Half of the 65 continuum cores are sub-virial, indicating that they are unstable against collapse in the absence of any other supporting mechanism.

4. While this study can not infer how many fragments and massive stars may form in each core, it is evident that furthur fragmentation of the cores is plausible. In addition, compared to higher metallicity Galactic regions, it seems more massive stars may form in the LMC.

5. The core mass function (CMF) we construct is consistent with the Salpeter IMF on the high-mass end (200 to 1000 $M_\odot$). We build up the Radius-Mass relation that suggests a correlation between the two parameters with the power-law index comparable to the Galactic clumps, though slightly shifted to the more massive side. This can be due to lack of mass sensitivity, or an impact of lower metallicity in the LMC.

6. Our cluster analysis reveals that more massive cores tend to be closer to their neighboring cores, with an average separation of 1.0 pc between cores within clusters in the LMC.

These findings do not indicate a significant difference in star formation between the sub-solar metallicity of the LMC and the MW. However, our study highlights the need for further research to determine at what spatial scale and metallicity the

impact of metallicity becomes evident. It raises the question of whether the variation with metallicity is gradual and continuous or abrupt and discrete. Future studies should explore star formation across a range of metallicities and spatial scales to better understand these processes.

Chapter 3

Chemical properties and hot molecular cores observed with ALMA at 1.2 mm

This chapter presents the work of Hamedani Golshan et al. (2024), a project that I have led and accomplished from the data reduction through the analysis to the final publication. The other authors (Álvaro Sánchez-Monge, Peter Schilke, Marta Sewiło, Thomas Möller, V. S. Veena and Gary A. Fuller) have participated in discussions and provided comments. The paper has been seamlessly incorporated into the thesis text, with the title and author list omitted. Additionally, the appendices from the paper have been relocated to the end of the thesis.

Abstract

Context. The formation of massive stars passes through a so-called hot molecular core phase, where the temperature of molecular gas and dust rises to above 100 K within a size scale of approximately 0.1 pc. The hot molecular cores are rich in chemical compounds found in the gas phase, which are a great probe of ongoing star formation.

Aims. To study the impact of the initial effects of metallicity (i.e., the abundance of elements heavier than helium) on star formation and the formation of different molecular species, we searched for hot molecular cores in the sub-solar metallicity environment of the Large Magellanic Cloud (LMC).

Methods. We conducted Atacama Large Millimeter/submillimeter Array (ALMA) Band 6 observations of 20 fields centered on young stellar objects (YSOs) distributed over the LMC in order to search for hot molecular cores in this galaxy.

Results. We detected a total of 65 compact 1.2 mm continuum cores in the 20 ALMA fields and analyzed their spectra with XCLASS software. The main temperature tracers are CH_3OH and SO_2, with more than two transitions detected in the observed frequency ranges. Other molecular lines with high detection rates in our sample are CS, SO, $H^{13}CO^+$, $H^{13}CN$, $HC^{15}N$, and SiO. More complex molecules, such as HNCO, HDCO,

HC_3N, CH_3CN, and NH_2CHO, and multiple transitions of SO and SO_2 isotopologues showed tentative or definite detection toward a small subset of the cores. According to the chemical richness of the cores and high temperatures from the XCLASS fitting, we report the detection of four hot cores and one hot core candidate. With one new hot core detection in this study, the number of detected hot cores in the LMC increases to seven.

Conclusions. Six out of seven hot cores detected in the LMC to date are located in the stellar bar region of this galaxy. These six hot cores show emission from complex organic molecules (COMs), such as CH_3OH, CH_3CN, CH_3OCHO, and CH_3OCH_3. The only known hot core in the LMC with no detection of COMs is located outside the bar region. The metallicity in the LMC presents a shallow gradient increasing from outer regions toward the bar. Various studies emphasize the interaction between the LMC and the Small Magellanic Cloud, which resulted in the mixing and inhomogeneity of the interstellar medium of the two galaxies. These interactions triggered a new generation of star formation in the LMC. We suggest that the formation of hot molecular cores containing COMs ensues from the new generation of stars forming in the more metal-rich environment of the LMC bar.

3.1 Introduction

Hot molecular cores are compact ($d \leq 0.1$ pc) and dense ($\geq 10^6$ cm^{-3}) regions that are heated up to temperatures above 100 K, either internally or externally, in the immediate surroundings of formation sites of massive stars (e.g. Qin et al., 2022). At these temperatures, the molecules that are formed and developed in the ice mantles on the surfaces of dust grains are released into the gas due to thermal evaporation or sputtering with shock waves, UV photons, or cosmic rays. Once in the gas phase, more complex chemical compounds can be formed (e.g., Garrod et al., 2008). This results in the formation and development of complex organic molecules (COMs, molecules with six or more atoms including carbon; Herbst & van Dishoeck, 2009). Eventually, most complex molecules are dissociated by strong UV radiation from the newly formed massive stellar object(s) and the associated HII region. In the time between the evaporation of the ice mantels to the destruction of the complex molecular species in the gas phase, the rich molecular gas chemistry is accompanied by the excitation of a plethora of rotational transitions observable at (sub)millimeter wavelengths (e.g., Belloche et al., 2013; Möller et al., 2023).

The development, chemical richness, and molecular composition of hot molecular cores may be affected by environmental conditions. One important environmental factor is the metallicity of the gas where stars are forming. Metallicity is the abundance of elements heavier than helium, and it is known to increase over cosmic time with every

new generation of stars due to the nucleosynthesis processes in the stellar interiors, supernova explosions, and neutron star mergers. This triggers a fundamental question in astrochemistry regarding how the difference in the elemental abundances influences the formation, survival, and destruction of molecular species. To answer this question, searching for the sites of rich chemistry in different (e.g., sub-solar) metallicity conditions is a crucial step, and hot molecular cores are prominent candidates for providing a complete molecular inventory in the gas phase. Thanks to the high sensitivity and resolving power of the Atacama Large Millimeter/submillimeter Array (ALMA), detecting and pinpointing massive star-forming regions and hot molecular cores down to sub-parsec scales at 1 mm is feasible for relatively short integration times in our Galaxy and the immediate galactic neighborhood (i.e., the Magellanic Clouds). In this work, we aim to search for and characterize hot molecular cores in the lower metallicity gas of the Large Magellanic Cloud (LMC).

The LMC is a nearby dwarf galaxy at a distance of $D \approx 49.59 \pm 0.09$ (statistical) ± 0.54 (systematic) kpc (Pietrzyński et al., 2019). This galaxy, with an average metallicity[1] of $Z_{LMC} \sim 0.38\ Z_{\odot}$ is one of the closest laboratories to study the physics and chemistry of a low-metallicity environment. Low metallicity means less dust and hence diminished shielding effects, allowing UV radiation to penetrate deeper into clouds. The UV field strength in the LMC is ten to 100 times larger than in the Milky Way (MW, e.g., Welty et al., 2006). As a result, the dust temperature is expected to be higher, likely affecting the development of the more complex molecular species. Moreover, the metallicity has been found to vary across the LMC, showing a moderate gradient that increases toward the bar region in this galaxy (e.g., Choudhury et al., 2021).

The development of ALMA enabled the detection of the first hot molecular cores in the LMC in recent years. The six hot cores detected so far (see Shimonishi et al., 2016b; Sewiło et al., 2018; Shimonishi et al., 2020; Sewiło et al., 2022) present a picture of a diverse chemistry. While metallicity-scaled abundances for detected COMs in four hot cores are comparable to those observed in the Galaxy, COMs are either absent or underabundant in the remaining two hot cores. Hot cores in the N 113 star-forming region show emission from molecules containing up to nine atoms, with abundances that match the lower end of Galactic values after scaling for metallicity (Sewiło et al., 2018). The two bona fide hot cores in the N 105 star-forming region (Sewiło et al., 2022) also exhibit a rich chemistry, with abundances that follow the trend of the ones in N 113, although with lower values. On the COM-poor side, a hot core with CH_3OH and

[1]Different works have estimated the metallicity of the LMC to be between 0.3 and 0.5 of the metallicity in the Solar neighborhood interstellar gas ($Z_{\odot}$). In this work, we use the recent estimate by Choudhury et al. (2021), who derives [Fe/H] $= -0.42$ dex, with [Fe/H] $= \log\left(\frac{Z_{\rm gal}}{Z_{\odot}}\right)$), and results in $Z_{LMC} \sim 0.38\ Z_{\odot}$.

CH_3CN molecular lines but no larger molecules has been detected by Shimonishi et al. (2020). This hot core, which shows an underabundance of complex species compared to Galactic hot cores, is associated with the massive young stellar object (YSO) ST16. Even more extreme is the hot core associated with the YSO ST11 (Shimonishi et al., 2016b). There are no emission lines from COMs in this source, and the temperature above 100 K is obtained from SO_2 and its isotopologues. Shimonishi et al. (2016b) have suggested high dust temperatures that prohibit effective freeze-out and subsequent hydrogenation of CO on the dust surface to be the likely cause of the suppression of CH_3OH formation, the building block for more complex COMs (e.g. Garrod et al., 2008). The existence of hot cores with metallicity-scaled COM abundances similar to the Galactic values shows that higher dust temperatures in the cold collapse phase are not ubiquitous in the LMC and may exist only in specific regions. Based on these results, a statistically significant sample needs to be analyzed to better characterize the hot cores in the LMC and their relation to environmental conditions (e.g., proximity to star-forming regions having higher UV radiation levels or variations in metallicity).

To expand the search for hot molecular cores from the LMC to other sub-solar metallicity environments, recent works have studied objects in the outer regions of the MW (e.g. Shimonishi et al., 2021; Fontani et al., 2022) as well as in the Small Magellanic Cloud (SMC Shimonishi et al., 2023). The Galaxy's outer regions harbor an interstellar medium with a diminished metallicity compared to the inner Galactic regions (e.g., **?**) as well as more quiescent radiation fields. Studies in the outer Galaxy are crucial, as they can bridge our knowledge of the higher metallicity (and more active) star-forming environment of the inner Galaxy to the low metallicities of the LMC and SMC. Recently, a hot molecular core has been discovered in the outskirts of the MW in the WB 89−789 star-forming region at a distance of 10.7 kpc (galactocentric distance of 19 kpc) (Shimonishi et al., 2021). The metallicity at this position is estimated to be $Z \sim 0.25\ Z_\odot$. Interestingly, the chemical composition of the hot core in WB 89−789 resembles that of hot cores in the inner Galactic regions and not of those in the LMC. On the other hand, the SMC is a star-forming dwarf galaxy at a distance of 62.1 ± 1.9 kpc (Graczyk et al., 2014) and has the lowest metallicity in the nearby universe where we are able to search for hot cores with currently available facilities. The metallicity is $Z \sim 0.2\ Z_\odot$, with a shallow but significant gradient (Choudhury et al., 2018). Shimonishi et al. (2023) have reported the detection of two hot cores in the SMC, S07 and S09, coinciding with the position of two massive YSOs. Notably, SO_2 traces the hot compact (~ 0.1 pc) component with temperatures higher than 100 K in these two hot cores, while CH_3OH is extended ($\sim$ 0.2–0.3 pc) and much cooler (≤ 40 K for S07).

In summary, the detection of hot cores in the LMC, the SMC, and the outskirts of the MW, added to the multiple Galactic examples, suggests that the development of

hot molecular cores is common during the formation of stars in the Z = 0.2–1 $Z_\odot$ metallicity range (Shimonishi et al., 2023). Despite this, the first studies in low-metallicity environments have found a diverse population of objects with molecular abundances sometimes consistent with Galactic-like metallicity environments and others with lower abundances. Furthermore, some hot cores appear to be poor in COMs abundance, while others have abundances similar to those in the MW disk. All in all, it is noticeable that a larger sample of sources observed and analyzed with a common methodology is still necessary to provide insight into the formation and properties of hot cores in low-metallicity regions. With this in mind, we studied 20 different fields in the LMC, the largest sample to date, in order to search for hot cores and improve our current understanding of the physics and chemistry of high-mass star-forming cores in this nearby dwarf galaxy.

This is the first paper of a series that is accompanied by a publication by Hamedani Golshan et al. (in prep., hereafter Paper II). Paper II presents the observed sample and studies the dense cores and star-forming clusters identified in the observed regions. In the current paper, we focus on the chemical content of the identified cores and their connection to the LMC's global metallicity trend and large-scale properties. In Section 3.2 we introduce the sample and the observations. In Section 3.3, we present the results and main analysis procedures. We discuss the results in the context of our knowledge about the hot cores in the LMC, SMC, and MW in Section 3.4. Several appendixes show our dataset or elaborate on specific concepts or methodologies.

3.2 Observations and sample

3.2.1 Sample selection

We selected 20 massive YSOs identified with Spitzer (e.g., Gruendl & Chu, 2009) distributed throughout the LMC to be observed with ALMA (see Table 3.1 for their names and coordinates and see Fig. 3.1 for their distribution across the LMC). We selected YSOs without ice features or strong fine-structure lines in their Spitzer IRS spectra (Seale et al., 2009) and with *Herschel* counterparts at submillimeter wavelengths (Seale et al., 2014) to maximize the chance of selecting the evolutionary stage of hot cores and not earlier or later evolutionary stages. These sources are located away from prominent massive star-forming sites (based on the absence of strong Hα emission in the Hα image from the MCELS survey, Smith et al., 2000), making the cold initial conditions (which favor methanol formation) more likely. The selected sources are all bright at 160 μm to ensure the presence of large amounts of dust and large column densities, favoring the detection of molecular lines. We also added two regions centered on the YSOs ST6 and ST10, for which Shimonishi et al. (2016a) detected methanol ice. A more detailed

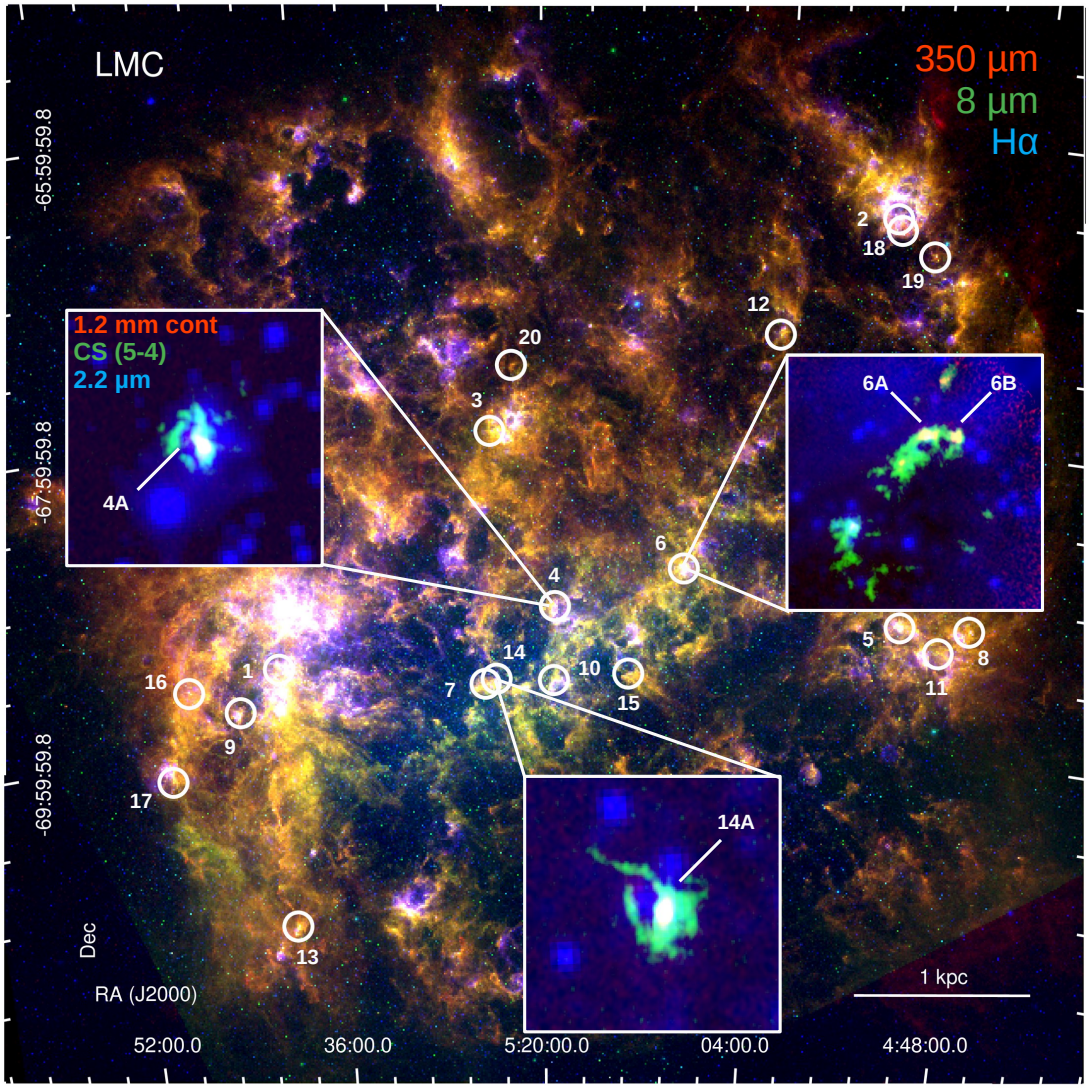


Figure 3.1: Color-composite image of the LMC combining the Hα (blue, Smith et al., 2000), SAGE/IRAC 8 μm (green, Meixner et al., 2006), and HERITAGE/SPIRE 350 μm (red, Meixner et al., 2013) images. The positions of the 20 ALMA fields are marked with white circles 15 times larger than the field of view of our ALMA observations and the field number. The color-composite images of the fields with hot core detection combining the VMC K-band (blue, Cioni et al., 2011), ALMA CS (5–4) peak intensity (green, this work), and 1.2 mm ALMA continuum (red, this work and Paper II) images are shown as insets. The hot cores reported in this paper, 4A (ST16; Shimonishi et al., 2020), 6A (N105-2 B; Sewiło et al., 2022), 6B (N105-2 A; Sewiło et al., 2022), and 14A are highlighted in the insets images.

Table 3.1: Coordinates and names of our target fields.

Field Number	Target ID (Gruendl & Chu, 2009)	Alternative name
1	053941.12-692916.8	ST6 [a]
2	045640.79-663230.5	ST10 [a]
3	052343.48-680033.9	
4	051912.27-690907.3	ST16 [a,b]
5	045358.57-691106.7	
6	050953.89-685336.7	N105-2 E [c, d]
7	052423.39-693904.7	
8	044854.41-690948.3	
9	054248.90-694446.3	
10	051916.87-693757.5	
11	045100.16-691934.4	
12	050355.87-672045.1	
13	053952.11-710930.7	
14	052333.40-693712.2	
15	051344.99-693510.6	
16	054629.32-693514.2	
17	054826.21-700850.2	
18	045622.61-663656.9	
19	045406.43-664601.4	
20	052210.08-673459.6	

Notes.
[a] Shimonishi et al. (2016a)
[b] Shimonishi et al. (2020)
[c] Sewiło et al. (2022)
[d] Henize (1956)

Table 3.2: Spectral cube parameters for primary beam corrected images.

Spectral window	Frequency range[a] (GHz)	Synthesized beam (Θ_B)[a] (" × ")	Channel width (MHz / kms^{-1})	Cube rms[a, b] (mJy beam^{-1} / K)
241 GHz	241.37–241.84	0.497 × 0.436	0.122 / 0.15	2.58 / 0.28
244 GHz	243.67–245.54	0.421 × 0.362	0.488 / 0.6	1.50 / 0.21
257 GHz	256.72–258.59	0.405 × 0.347	0.488 / 0.6	1.61 / 0.22
259 GHz	258.76–260.63	0.405 × 0.360	0.488 / 0.6	2.01 / 0.25

Notes.
[a] The average value for the 20 fields.
[b] The rms noise per channel width is estimated in a line-free channel.

description of the sample and its properties, including the continuum images and the compact sources detected with ALMA can be found in Paper II.

3.2.2 ALMA observations

The sample of 20 regions (see Fig. 3.1) in the LMC was observed with the ALMA 12-m Array during its Cycle 5 between November 11 and December 3, 2018 (project number 2017.1.00696.S). The observations were carried out as single pointings centered at the coordinates listed in Table 3.1 with a duration of about 19 minutes on-source per field. The observations were executed during eight different execution blocks that were later merged to reach the requested sensitivity. We used the main array of ALMA with the 12-m antennas in two configurations (C43-4 and C43-5) and baselines ranging from 15 to 1400 m, which resulted in an angular resolution of $\approx 0.4''$ (corresponding to $\sim$ 0.09 pc at the distance of the LMC) and a maximum recoverable angular scale of $\approx 5''$ (corresponding to $\sim$ 1.2 pc at the distance of the LMC). This maximum recoverable scale, although not enough to map large extended structures, allowed us to detect dense cores and clumps with typical sizes $\leq$ 0.5 pc. The total field of view (or primary beam) of the ALMA observations is $\sim 44''$ (corresponding to $\sim$ 10 pc). The spectral setup (see Table 3.2) covered four spectral windows, including a 469 MHz-wide band centered at 241.6 GHz and three 1875 MHz-broad bands centered at 244.6, 257.6, and 259.5 GHz. All four spectral windows have 3840 channels, resulting in channel widths of 0.122 MHz and 0.488 MHz, respectively. Throughout the paper, we refer to these four spectral windows as 241, 244, 257, and 259 GHz.

The data were calibrated using the ALMA pipeline in CASA (Common Astronomy Software Applications; McMullin et al., 2007) version 5.4.0-68. The amplitude-bandpass calibrator was chosen to be J0635−7516 or J0519-4546 in different execution blocks, with the complex gains being corrected with the calibrators J0529−7245 or J0601−7036. Continuum subtraction, determined from line-free channels, was done in the u,v-domain using the CASA task `uvcontsub`. The images were produced with the CASA task `tclean`, using a standard gridding and the *Briggs* weighting with the robust parameter set to 0.5 as a compromise between sensitivity and resolution. The final images, both continuum and spectral data cubes, have been primary beam corrected using the `impbcor` task in CASA. Typical errors for the continuum images are about 65 μJy beam^{-1} (10 mK) and about 1.92 mJy beam^{-1} (0.23 K) for the cubes (see Table 3.2). More details on the observations and the continuum images can be found in Paper II. As an example, Fig. 3.2 shows the 1.2 mm ALMA continuum emission toward four fields.

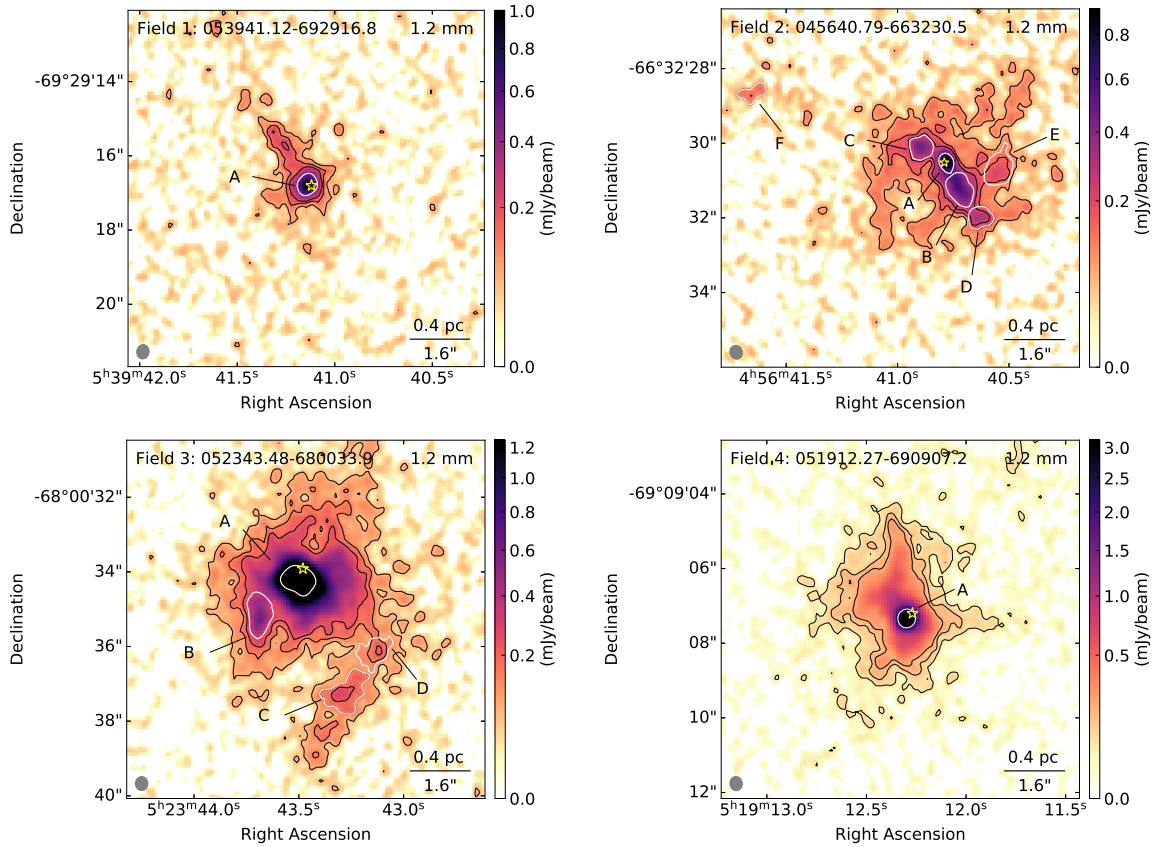


Figure 3.2: Examples of the 1.2 mm continuum emission toward four regions of the LMC sample. The contours show the three, six, and nine times the σ_{rms}. The identified compact cores are highlighted with white contours at 50% of the peak emission. The synthesized beam of the images and a scale bar are shown in the bottom-left and bottom-right corners of each panel, respectively. See Paper II for more details on the 20 fields observed across the LMC (see Table 3.1).

3.3 Results and analysis

A total of 65 compact sources were identified in the continuum images of the 20 fields in the LMC, defined by the 50% intensity contour level around well-defined intensity peaks (see Paper II). These objects have peak continuum fluxes above five times the image rms noise and constitute clear detections of compact sources. We used the temperatures estimated in the current paper to calculate the dust and gas mass of each core, assuming that the 1.2 mm continuum emission originates in optically thin dust with an opacity of 1.04 cm^2 g^{-1} (for dust grains coated by thin ice mantels after 1×10^5 yr of coagulation in a hydrogen density of 1×10^6 cm^{-3}, Ossenkopf & Henning, 1994) and a gas-to-dust mass ratio of 316 (Sewiło et al., 2022). The cores have masses[2]

[2]According to the tentative detection of radio recombination lines toward one of the cores (see Section 3.3.1), we note that there might be a certain level of contamination from thermal free-free emission in the 1.2 mm continuum fluxes for at least the most massive core. Therefore, the higher-end value of the masses, H_2 column, and volume densities may be overestimated.

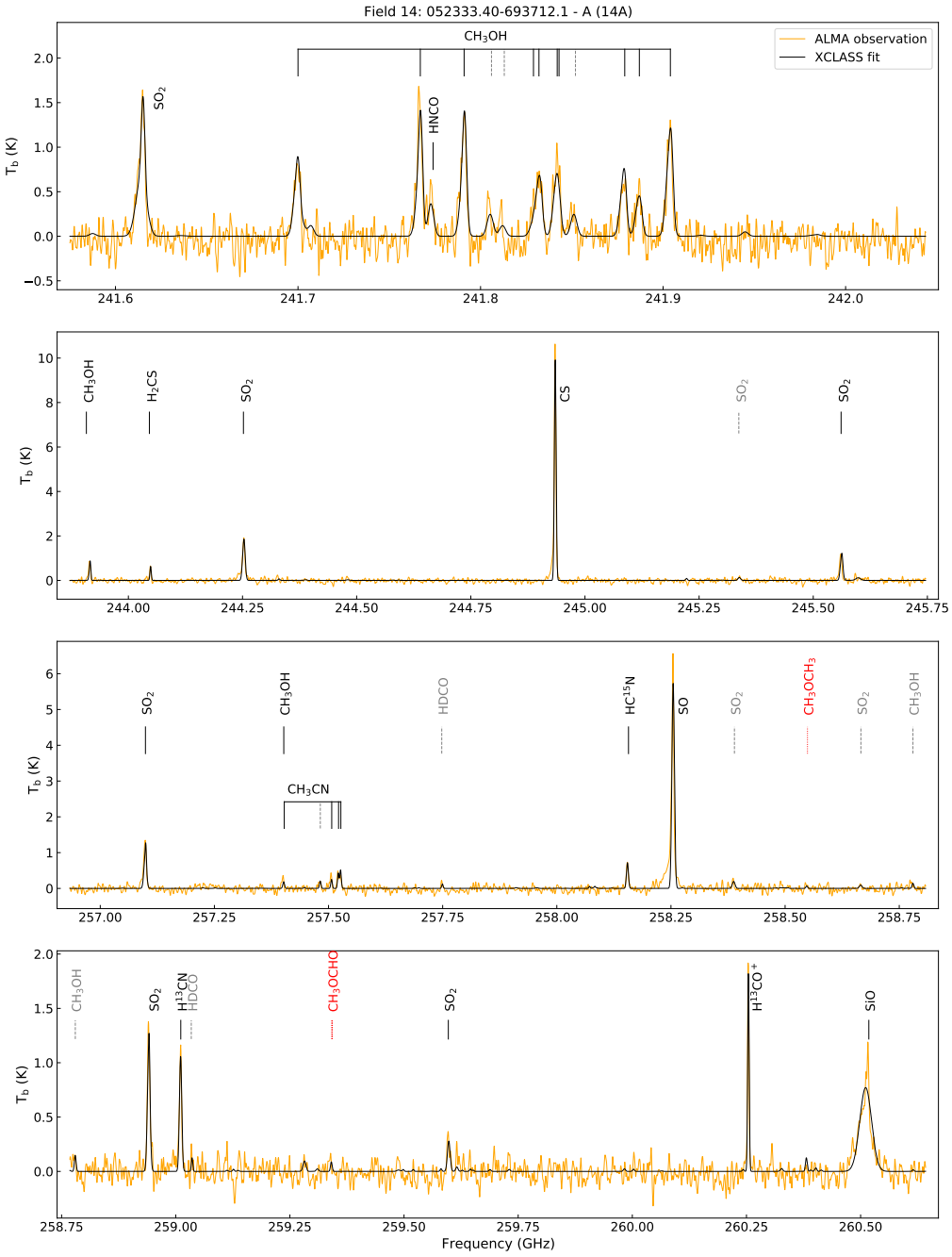


Figure 3.3: ALMA Band 6 observed spectra toward source 14A overlaid with the best-fit XCLASS model. Molecular transitions with definite detections (S/N > 5) are represented by solid black lines, while those with tentative detections (3 < S/N < 5) are denoted by dotted gray lines. Dotted red lines indicate transitions of molecules for which abundance upper limits are provided.

in the range of 20–1000 $M_\odot$, H_2 densities in the range 1.2×10^5–4.0×10^6 cm^{-3}, and H_2 column densities ranging from 6.0×10^{22}–1.5×10^{24} cm^{-2}. In this paper, we focus on the chemical properties of these 65 compact objects. In Section 3.3.1, we describe the spectral analysis performed toward these sources, while in Section 3.3.2 we analyze their spectral properties, such as temperature, line width, and chemical content.

Table 3.3: Definite and tentative detections of molecular species along with the corresponding number of sources exhibiting these emissions.

Molecular species	Number of sources	Molecular species	Number of sources
CS	58 / –	$HC^{15}N$	6 / 3
SO	43 / 2	H_2CS	23 / 7
^{33}SO	3 / –	HNCO	3 / 1
SiO	8 / 12	HDCO	– / 1
SO_2	16 / 11	HC_3N	– / 3
$^{33}SO_2$	1 / 1	CH_3OH	45 / 2
$^{34}SO_2$	1 / 2	CH_3CN	4 / 1
$H^{13}CO^+$	32 / 3	NH_2CHO	– / 1
$H^{13}CN$	15 / 8		

Notes.
Definite / tentative detection(s)

3.3.1 Spectral analysis of the continuum cores

In this section, we present the steps to analyzing the extracted spectra from the 65 compact sources identified in the ALMA 1.2 mm continuum images (see Paper II). The spectra of each source were extracted from the primary beam corrected cube images of the four spectral windows (see Table 3.2). The average spectra were computed using the `spectral-cube` python package (Robitaille et al., 2016) with the pixels enclosed within the 50% peak-intensity contour of the 1.2 mm continuum emission maps. Figure 3.3 shows an example spectrum (see Appendix B for the rest of the spectra).

As a first step in the analysis of the extracted spectra, we identified the molecular lines toward the most chemically rich sources (i.e., spectra with the largest number of line detections; see Fig. 3.3 for an example) using the CDMS catalog (Cologne Database for Molecular Spectroscopy; Müller et al., 2005). For this, we estimated the noise level ($\sigma_{\rm rms}$) in each spectrum (i.e., for each source and spectral window) by performing a sigma clipping analysis. Based on this noise-level determination and the intensity of each spectral line feature, we sorted the detected lines. We considered the lines as a definite detection if their peak value exceeded $5\sigma_{\rm rms}$ and as tentative features if the line strength is between 3 and $5\sigma_{\rm rms}$. The definite and tentative detections are respectively labeled with black and gray in Fig. 3.3 and Figures B.1 to B.20. With a complete set of molecules presented in Table 3.3, including definite and tentative detections, we fit the spectra using the XCLASS toolbox[3] (eXtended CASA Line Analysis Software Suite; Möller et al., 2017, 2023, with additional extensions, T. Möller, priv. comm.). XCLASS solves the radiative transfer equation in one dimension in local thermodynamic equilibrium (LTE) or non-LTE based on the request. It can solve the radiative

[3] `https://xclass.astro.uni-koeln.de/`

transfer equation for an unlimited number of molecules simultaneously, taking line blending into account and producing modeled spectra. XCLASS provides the basis for finding the best-fit model to the observed spectra by encompassing a large set of fitting algorithms available within the MAGIX interface (Möller et al., 2013). The fitting procedure works with the χ^2 minimization. The contribution of a certain molecule can be described by more than one component. This is useful when the detected molecular emission line may come from different unresolved structures with different sizes, temperatures, or even distances to the observer. Each component is described by source size, temperature, column density, line width, and velocity offset. These can be fixed or free to vary to get the best-fit spectra and the best set of parameters.

Using XCLASS, we analyzed the spectra assuming that all the considered molecular species are located within a core layer at the position of the source (i.e., we did not consider foreground clouds located between the source and the observer). In the absence of optically thick transitions, column density and source size are degenerate and cannot be determined separately. Therefore, we fixed the source size for all the molecules to a very large value to impose a beam-filling factor of one.[4] The temperature, column density, line width, and velocity shift are in general free parameters to fit. While parameters such as line width and velocity shift can be determined from Gaussian fits to the detected spectral lines, a good determination of the temperature requires the detection of several transitions from the same molecular species. Based on this, we grouped the molecules into two different categories: molecules with more than two transitions detected within the four spectral windows and molecules with only one or two transitions. The first group includes CH_3OH, SO_2, and CH_3CN, and we fit the temperature for them using XCLASS when multiple transitions were detected.

Out of 65 sources, CH_3OH was detected in 48, while 37 sources show clear detections of three or more transitions. One or two transitions were detected toward the other 11 sources. Seventeen sources have no CH_3OH features with line intensities higher than $3\sigma_{rms}$. In the first iteration, we fit CH_3OH using an LTE approximation, which resulted in low temperatures (5–17 K; see Table B.1) and some line features to be underfit or overfit (see Fig. B.21). Based on these inaccuracies, we switched to non-LTE for fitting CH_3OH, which resulted in better fits. In the non-LTE description, we have two additional parameters to consider: the ratio of A and E CH_3OH and the collision partner[5] volume density. We fixed the A to E CH_3OH ratio to one and fit the collision partner density in the cores with more than two CH_3OH lines. The fit collision partner densities are $\approx 1 \times 10^6$ cm^{-3} for most of the cores and about $\approx 1 \times 10^7$ cm^{-3} for those cores with bright CH_3OH lines. For the sources with one or two CH_3OH

[4]We note that a smaller source size results in higher column densities.

[5]XCLASS uses a similar prescription as RADEX (van der Tak et al., 2007) for its non-LTE fitting. The collision parameters are from the Leiden Atomic and Molecular Database (LAMDA, Schöier et al., 2005).

lines, we fixed the density of collision partners to the median value of the rest of the cores: 2.0×10^6 cm^{-3}. With this, we then fit the temperature, column density, line width, and velocity offset. The derived gas kinetic temperatures for CH_3OH with the non-LTE description are generally in the range of 20–60 K (see Table B.2). Finally, for those sources with no CH_3OH detection, we fixed the temperature to the median value of the other cores and the line width and velocity offset to values derived for CS, if this was detected, and we derived an upper limit for the CH_3OH column density.

We found SO_2 to be present in 12 sources with enough lines for temperature determination under LTE conditions. However, only in five sources were there enough SO_2 lines to fit the spectra using non-LTE. For these sources, we compared the LTE and non-LTE fits, finding no major differences in the output temperatures and fit quality. Therefore, we fit SO_2 for all the fields using an LTE approach. For the rest of the molecular species, we fixed the temperature to the best-fit value for CH_3OH. If CH_3OH was not detected or properly fit in the spectra of a source, we fixed the temperature of other molecules to the median of the best-fit value for CH_3OH from other sources.

For four sources (4A, 6A, 6B, and 14A), a one-component model for CH_3OH and SO_2 did not give satisfactory results. A two-layered morphology with a hot central component and a colder envelope as the foreground provided the most convincing results. The core component's source size was fixed to a sub-beam size (not beam filling), while the foreground component was set to fill the beam. In these sources, we detected several transitions of CH_3CN with a high enough S/N, which provided an additional temperature estimate. As done for the other sources in the sample, for the rest of the molecules, we fixed the temperature to what was derived from the hot component of CH_3OH. Moreover, some isotopologues were also detected in these sources. We used the flexibility of XCLASS to link the isotopologues to the main species, giving them the same temperature and velocity profile to fit the isotopologue ratio from the ratio of column densities. We also detected HNCO and tentatively detected HDCO, HC_3N, and NH_2CHO in one or more cores among these four cores. Furthermore, we estimated an upper limit for HDCO, NH_2CO, CH_3CHO, and CH_3OCH_3 in these four cores when they appeared in the spectra, but they were not fit properly due to having a low S/N (S/N < 3). To this purpose, we fixed the temperature and line width and velocity shift to the hot component of CH_3OH. These transitions are marked with red in the figures of the corresponding spectra.

In addition, we searched for hydrogen recombination lines (RLs) in all sources. Within the four observed spectral ranges, there are two potentially detectable RLs (H36β and H41γ). However, we only found one tentative detection of H36β toward source 3A (see Fig. B.3). We used XCLASS to fit the RL emission. For the fit, we fixed the electron temperature to 1×10^4 K (e.g. Selier & Heydari-Malayeri, 2012; Jin et al., 2023) and fit the other three parameters, obtaining an emission measure estimate of

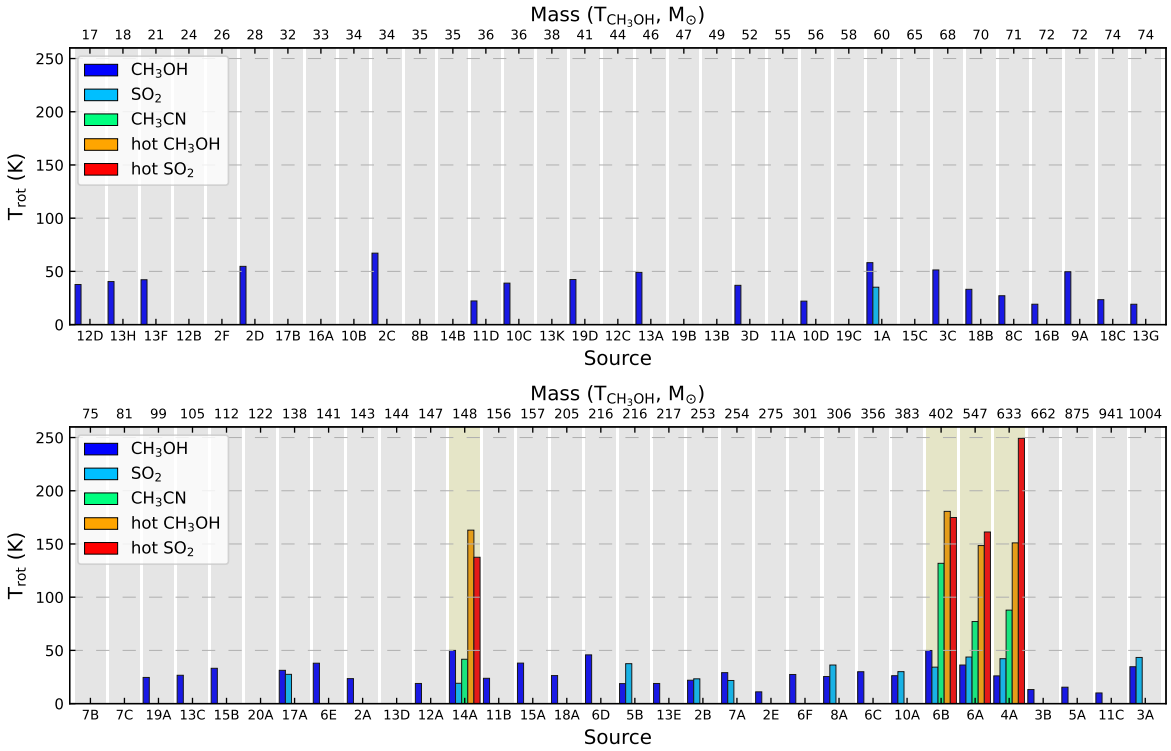


Figure 3.4: Best-fit XCLASS temperature for different molecular tracers. In case of definite detection in more than two transitions, CH_3OH, SO_2, and CH_3CN were free for fitting (for more details, see Section 3.3.1). There is an uncertainty of 40%–60% for the temperatures. The sources are ordered by increasing mass (from Paper II), calculated with the temperature of the CH_3OH (cold) component to account for the total mass in the core. The hot cores are highlighted with yellow bars.

2.5×10^6 pc cm^{-6}, a line width of 18.2 km s^{-1}, and a velocity offset of 284.4 km s^{-1}, consistent with the velocity derived for the molecular species.

The fitting procedure in XCLASS uses an algorithm chain from the MAGIX interface, including the genetic algorithm as a global minimizer and the Levenberg-Marquart algorithm as a local minimizer. We also ran XCLASS with a Markov chain Monte Carlo (MCMC) algorithm on a few spectra to estimate typical errors on the different fitting parameters. The error values range from 40%-60% for the temperatures, 20%-40% for the column densities, and 10%-30% for the line widths and velocity shifts. In the non-LTE solution, there is a degeneracy in defining the temperature, column density, and collision partner density that makes it hard to agree on an error value. The outcome of the fitting procedure is shown as modeled spectra (in black) overlaid on observed spectra (in colors) in Fig. 3.3 and Figures. B.1 to B.20. The best-fit parameters are listed in Table B.2, and the upper-limit estimations are marked with a less than (<) sign.

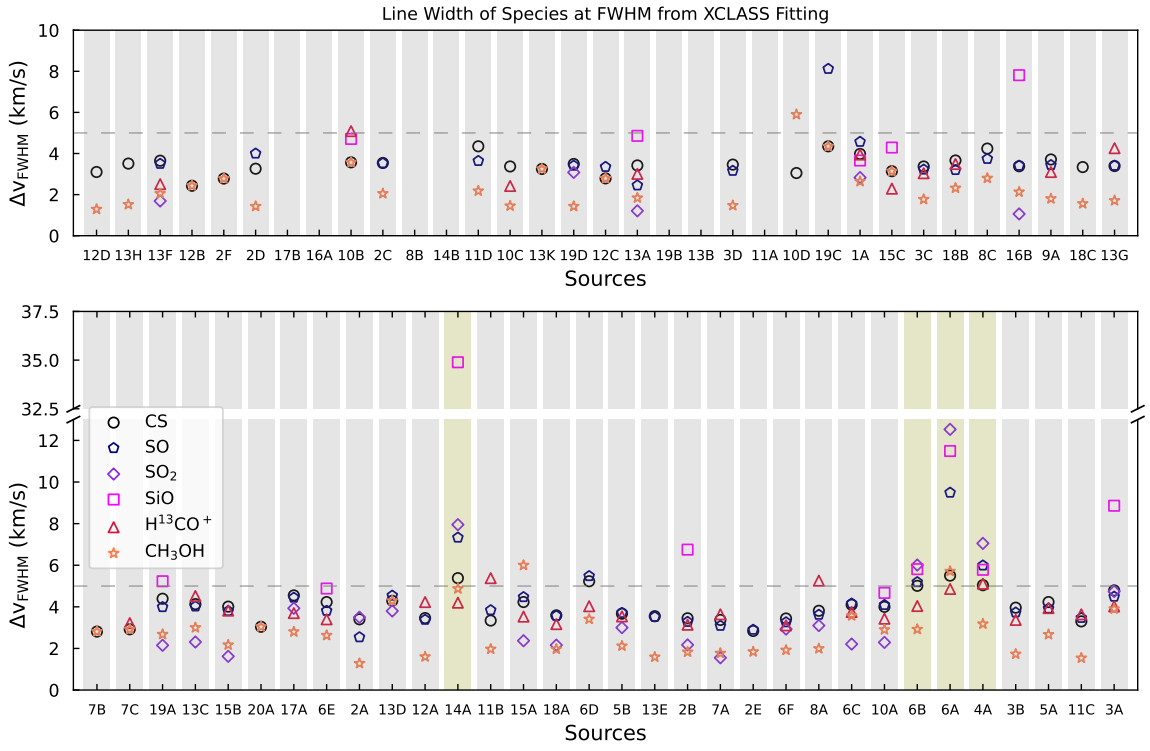


Figure 3.5: Best-fit XCLASS line width (full width at half maximum, FWHM) for different molecular species. The line width of 5 km/s is marked with a dashed line as a reference. There is an uncertainty of 10%–30% for the line widths. The sources are ordered by increasing mass (from Paper II) with the temperature of CH_3OH (cold) component to account for the whole mass in the core. The hot cores are highlighted with yellow bars.

3.3.2 Results from spectral analysis

Temperature of compact cores

As discussed in Section 3.3.1, we fit the temperature for three molecular tracers, CH_3OH, SO_2, and CH_3CN, when there were firm detections. This resulted in 47 sources with a temperature determination using CH_3OH, 12 sources with SO_2, and only four sources with CH_3CN-derived temperatures. Figure 3.4 shows the derived temperatures for the different molecular tracers for all 65 compact cores. The cores are ordered based on their mass (as determined in Paper II).

As stated earlier, out of the 65 cores, only four have a reliable temperature determined using CH_3CN, and it is only for these four cores that we needed more than one component to fit SO_2 and CH_3OH (see Table B.2). Furthermore, we only obtained temperatures above 100 K for the hottest component of these four sources, with the temperature remaining consistently below 60 K for the rest of the sources. Based on the definition of a hot molecular core to have a temperature higher than 100 K, we can classify these four sources (4A, 6A, 6B, and 14A) as such. These hot cores are

likely embedded in a colder envelope with temperatures about 30–40 K, similar to the temperatures derived for the other cores in the sample.

Line-width of different molecules

The line width of a molecular species provides useful information about the kinematics of the gas. Figure 3.5 compares the line widths derived for different molecular species from fitting the Gaussian line profile with XCLASS (see Section 3.3.1). Six molecules, including the ubiquitous ones, CS, SO, CH_3OH, and two other abundant species, SO_2 and $H^{13}CO^+$, together with the shock tracer SiO were utilized. The line widths vary between 1 and 35 km s^{-1}, with methanol having the lowest value in 49% of the cores. In this plot, we present the line width value for the hot component of SO_2 and CH_3OH when there are two temperature components. A value of 5 km s^{-1} is shown with a dashed line as a reference. The number of cores with line-width values larger than 5 km/s for at least one of the molecular species is 16. In nine of these sources, SiO is one of the molecules with a large line width suggesting the presence of molecular outflows, which will be studied in a forthcoming paper. Among them, we can identify the four cores (4A, 6A, 6B, and 14A) with temperatures higher than 100 K (see Section 3.3.2 and Fig. 3.4).

Chemical contents of the cores

Several molecular lines were detected in the spectra of each core. Among all the species, methanol was detected toward 74% of the cores (48/65). Among 17 cores with no-CH_3OH line detection, seven cores showed no emission lines at all (8B, 11A, 13B, 14B, 16A, 17B, and 19B). Other molecular species with high detection rates include CS, SO, SO_2, $H^{13}CO^+$, $H^{13}CN$, $HC^{15}N$, H_2CS, and SiO, while more complex molecules, such as HDCO, HNCO, HC_3N, and CH_3CN or isotopologues of SO and SO_2, were detected only toward a small subset of objects (about 8% of the sample). We also report a tentative detection of NH_2CHO in one of the cores (6A). Moreover, CH_3OCHO or CH_3OCH_3 emerged in the modeled spectra after fitting an upper limit column density for them toward the cores 4A, 6B, and 14A. In addition, a hydrogen RL, H36β, was detected tentatively toward the most massive core in our sample (3A). In addition, H41γ is also in the observed bands, and we mark it with red on the spectra of this core, as it was detected with an S/N less than three. The detection of this RL suggests the presence of HII regions that likely contribute to the 1.2 mm continuum emission. Preliminary data at 6 GHz obtained with ATCA (Hamedani Golshan, priv. communication) favors this interpretation. The mass derived for this source is likely overestimated in the current analysis. Interestingly, we have a tentative detection of CH_3CN towards the source 3A. The detection of CH_3CN, which is only clearly detected toward the four cores 4A, 6A,

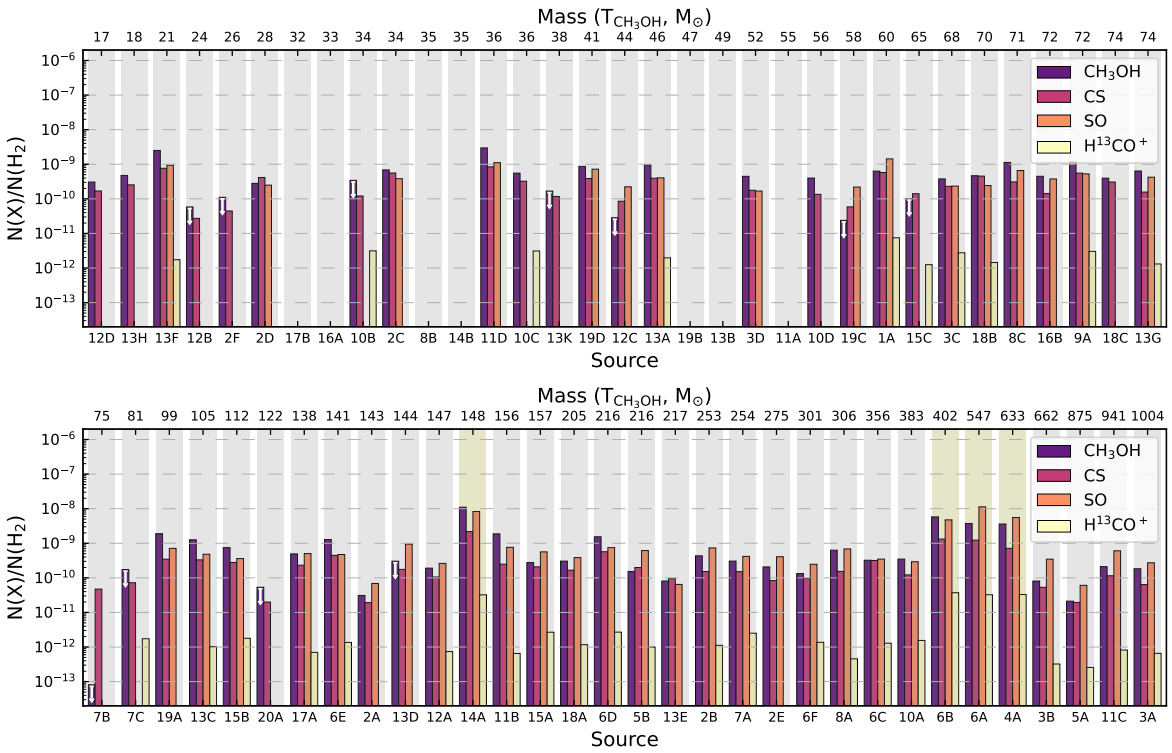


Figure 3.6: Abundances of molecular species with a high detection rate in our sample. There is an uncertainty of 20%–40% on the column densities. The sources are ordered by increasing mass (from Paper II) with the temperature of CH_3OH (cold) component to account for the whole mass in the core. The hot cores are highlighted with yellow bars. The arrows show an upper-limit estimation.

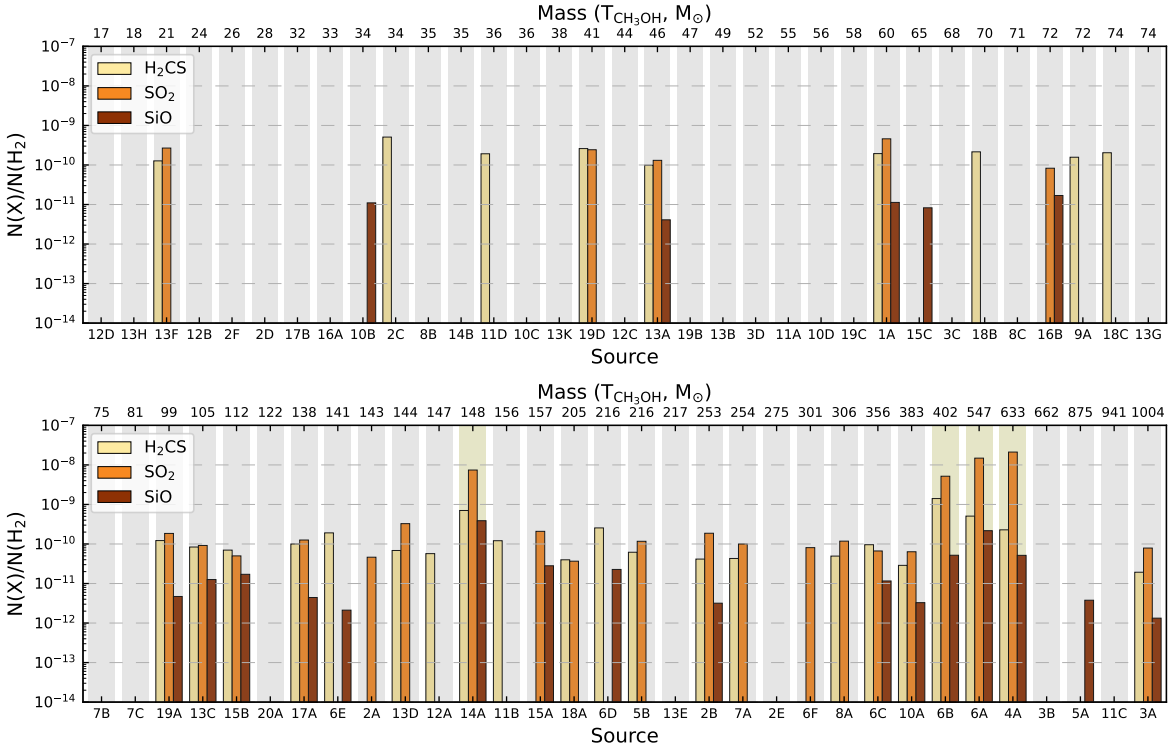


Figure 3.7: The same as Fig. 3.6 but for S-bearing species, H_2CS, SO_2, and SiO.

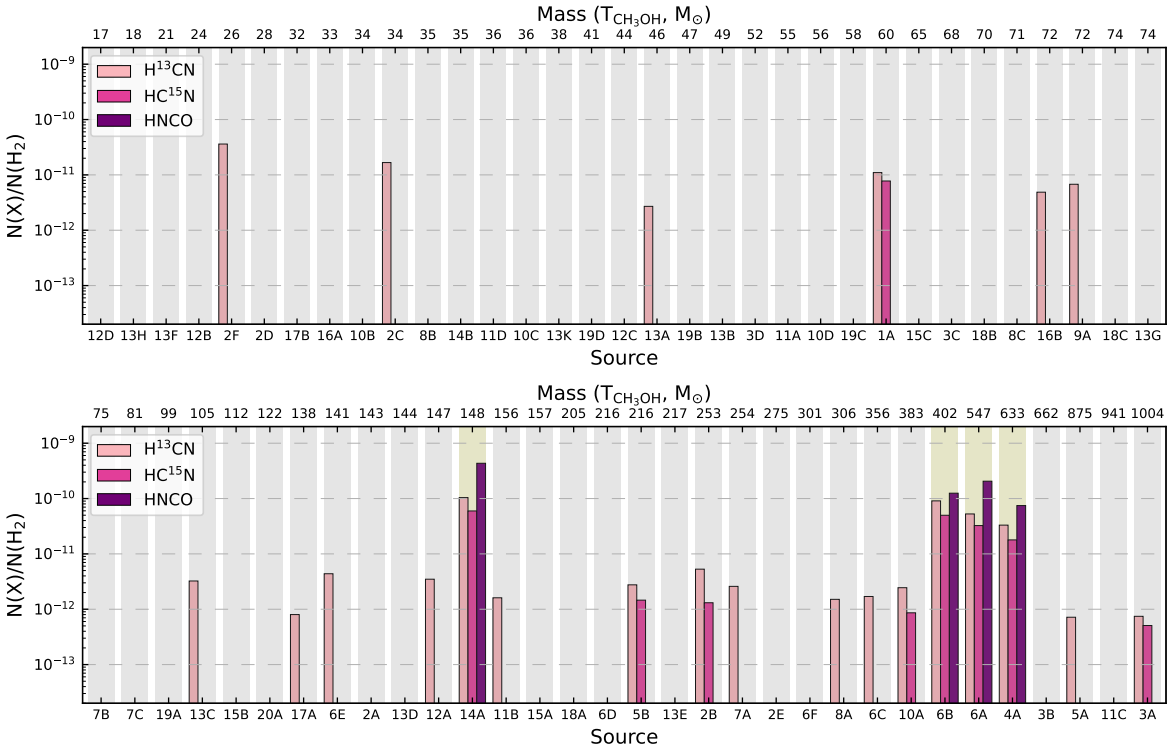


Figure 3.8: Same as Fig. 3.6 but for N-bearing species, $H^{13}CN$, $HC^{15}N$, and HNCO.

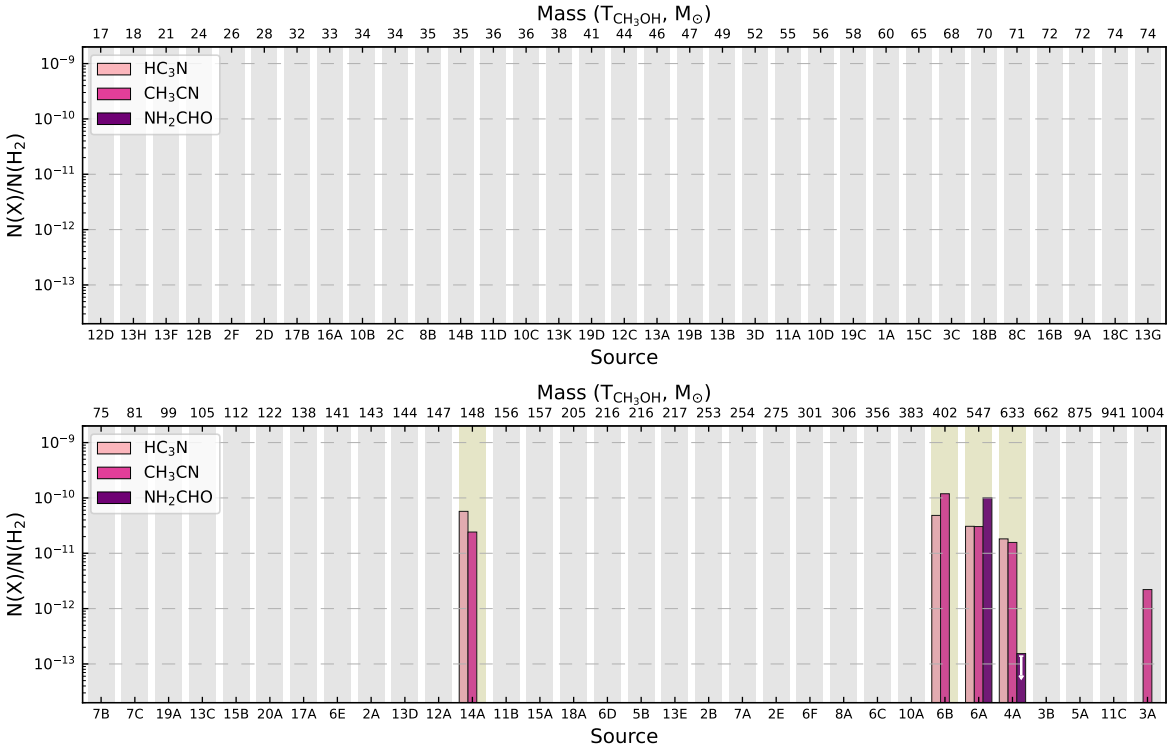


Figure 3.9: Same as Fig. 3.6 but for N-bearing species, HC_3N, CH_3CN, and NH_2CHO.

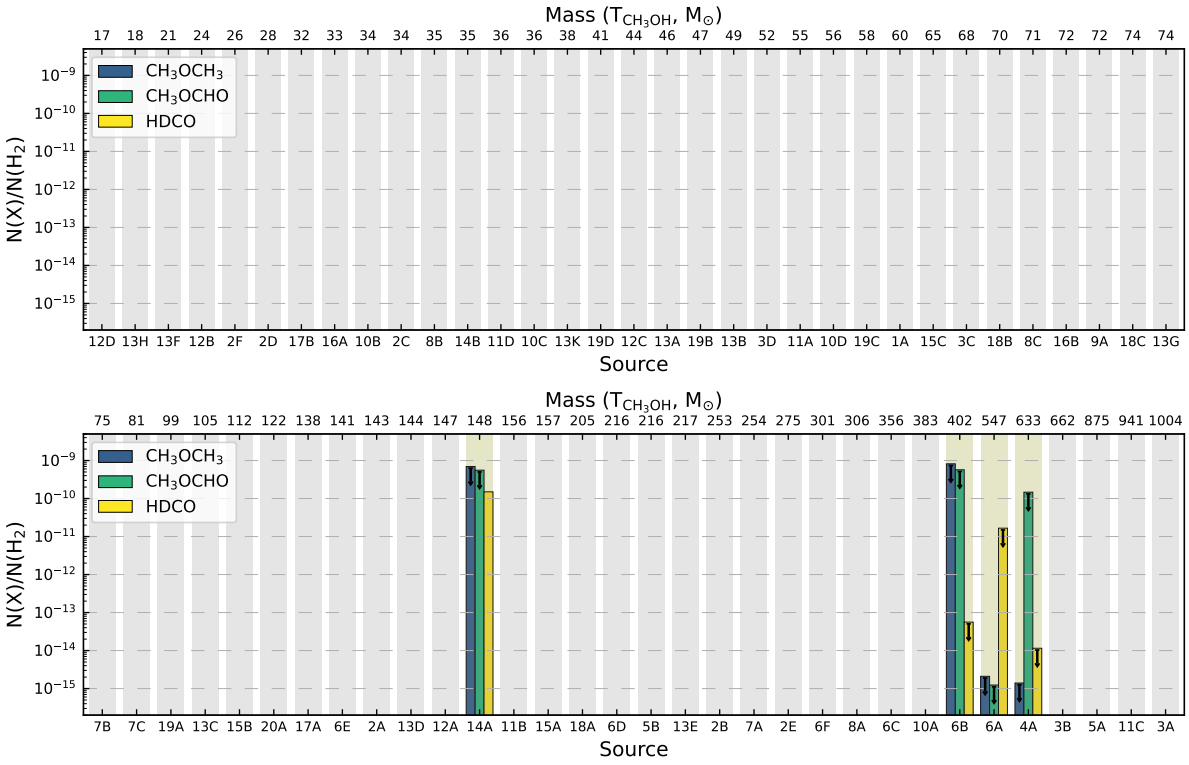


Figure 3.10: Same as Fig. 3.6 but for O-bearing species, CH_3OCH_3, CH_3OCHO, and HDCO.

6B, and 14A in the sample (see Section 3.4), together with the detection of RLs (likely related to an HII region) in 3A suggests the presence of a hot core near an expanding HII region, a scenario that is commonly found in several hot cores of the MW (e.g., Kurtz et al., 2000; Sánchez-Monge et al., 2013b; Cesaroni et al., 2017).

We compared the abundances of different molecules in all the sources. The abundances were derived by dividing the column density of every molecule by the molecular hydrogen column density ($N(H_2)$, derived in Paper II). For this purpose, we assumed that the dust and gas at the position of the source are well mixed and have the same temperature as derived from the XCLASS fits (see Table B.2). Figure 3.6 shows the abundance of the molecules with the highest detection rate for all the cores, whereas in Figures 3.7 to 3.10, the molecules are grouped into three different groups: S-bearing species (SO, SO_2) and SiO; N-bearing species ($H^{13}CN$, $HC^{15}N$, and HNCO) and (HC_3N, CH_3CN, and NH_2CHO); and O-bearing species (HDCO, CH_3OCHO, CH_3OCH_3). We ordered the cores based on their mass, but we did not see any clear correlation between mass and abundance for any of the species. When comparing the different groups of molecules, we observed that S-bearing species are, on average, more abundant than N- and O-bearing species.

Finally, comparing all the abundance plots, it was evident that four sources show a rich chemistry with the presence of various molecular species. These sources would

classify as hot molecular cores based on their chemistry, as well as their temperatures, since these objects are the only cores with temperatures above 100 K and average line widths above 5 km s^{-1}. Interestingly, these four sources are those with the largest SO_2 abundances, thus supporting the interpretation by Shimonishi et al. (2023) that bright SO_2 lines are a good tracer of hot molecular cores in the low-metallicity environment of the LMC and SMC.

3.4 Discussion

3.4.1 Hot cores in our survey

Based on the spectral analysis of the 65 continuum sources, we report the detection of four hot molecular cores and one hot core candidate from the ALMA observations of 20 fields hosting YSOs in the LMC. As highlighted in Section 3.3, four cores (4A, 6A, 6B, and 14A) have temperatures above 100 K, large line widths, and the highest chemical richness among all the cores in the sample. This, together with the fact that the spatial size of these cores where the emission reaches half of the peak value in the continuum map, $\Omega_{\rm obs}$ ($\Omega_{\rm deconv}$), is between 0.12 (0.08) and 0.14 (0.11) pc (see Paper II) suggest that they are in the hot molecular core phase. This result confirms the previous detection of hot cores in ST16 YSO (Shimonishi et al., 2020) and two hot cores N105-2 A and N105-2 B in the N105 star-forming region (Sewiło et al., 2022). In addition, we present a new hot core detection in field 14: 0523333.40−693712.1, 14A. With this new detection, the number of known hot cores in the LMC increases to seven.

Isotopologues of SO and SO_2 were detected toward the hot cores in our sample. The hot cores 4A and 6A show emission lines from ^{33}SO, $^{33}SO_2$, and $^{34}SO_2$. Hot core 6B contains ^{33}SO and $^{34}SO_2$ but no $^{33}SO_2$, and the core 14A shows no reliable detection of these isotopologues. We derived the isotopic ratios of $^{32}S/^{33}S$ and $^{32}S/^{34}S$ toward hot cores 4A and 6A and found them to vary between 12 and 21 and 9 and 19. These values can be compared with previous estimates in the LMC and other galaxies. Gong et al. (2023) used the APEX 12-m telescope to measure sulfur isotopic ratios in the LMC and compiled a set of measurements toward the LMC, different regions of the MW, and starburst galaxies (see their Table 2). For the LMC, Gong et al. (2023) found the ratios of $^{32}SO/^{33}SO$ and $^{32}SO/^{34}SO$ to range between 27 and 53 and 15 and 19, respectively. Combined with our results, which are similar to or slightly lower than previous estimates, the range for these isotopic ratios increases to 12 to 53 for $^{32}SO/^{33}SO$ and 9 to 19 for $^{32}SO/^{34}SO$. The sulfur isotopic ratios in the LMC are lower than in different regions throughout the MW but more consistent with measurements in starburst galaxies. Gong et al. (2023) suggest that the low values in the LMC might be attributed to a combination of age, low metallicity, and star-formation history.

Source 3A may be a potential hot core candidate based on the presence of COMs in the analyzed spectra. This source is associated with a common hot core tracer, CH_3CN. However, the temperatures that we derived for this source are below 100 K. We note that source 3A is also associated with RLs in addition to CH_3CN, suggesting a scenario where a compact hot core may be located in the near vicinity of an HII region. Future observations of these objects at higher resolution as well as covering additional frequency ranges may help in unambiguously determining the presence of hot cores in this region.

New hot core in the LMC

The newly identified hot core 14A is located at the position of the YSO 0523333.40−693712.1. The color composite image from the 1.2 mm continuum (dust emission, in red), CS (dense gas tracer, in green), and K-band (tracer of stellar population and possible H_2 emission, in blue) in the lower insert panel of Fig. 3.1 shows the peak emission toward the position of the hot core. Figure 3.11 shows the integrated intensity maps of different molecular species toward the hot core 14A, with the 1.2 mm continuum emission shown in contours as reference. Apart from the bright emission toward the hot core position, the CS map also reveals prominent filamentary structures. The emission from CH_3OH, SO, $H^{13}CO^+$, and H_2CS show faint elongation in the north-south direction. Moreover, HNCO and HDCO show a very faint emission, offset from the hot core, and H_2CS emission also peaks offset to the hot core, where the HNCO emission peaks.

Comparison of hot cores common to other studies

In addition to 14A, which is detected for the first time in this work, the other three hot cores (4A, 6A, and 6B) have previously been identified in other studies based on independent observational datasets. In the following, we compare our results with those in the literature for the temperatures and abundances of species detected toward all the cores, including CH_3OH, CH_3CN, HNCO, $H^{13}CO^+$, SO_2, SO, and SiO.

Shimonishi et al. (2020) reported the detection of a hot molecular core based on ALMA Band 6 and 7 observations of the embedded high-mass infrared source ST16. Our study results in the detection of the same hot core that we name 4A following the adopted nomenclature. The hot components of CH_3OH and SO_2 have the same temperatures in both studies considering uncertainties (see Fig. 3.12, top-left panel). However, the cold component of both species has slightly lower temperatures in our study, and the derived temperature from CH_3CN is larger by a factor of 1.5. The top-right panel of Fig. 3.12 compares the abundances from the two studies, after accounting for the difference in the gas-to-dust mass ratio assumed in our study and that of

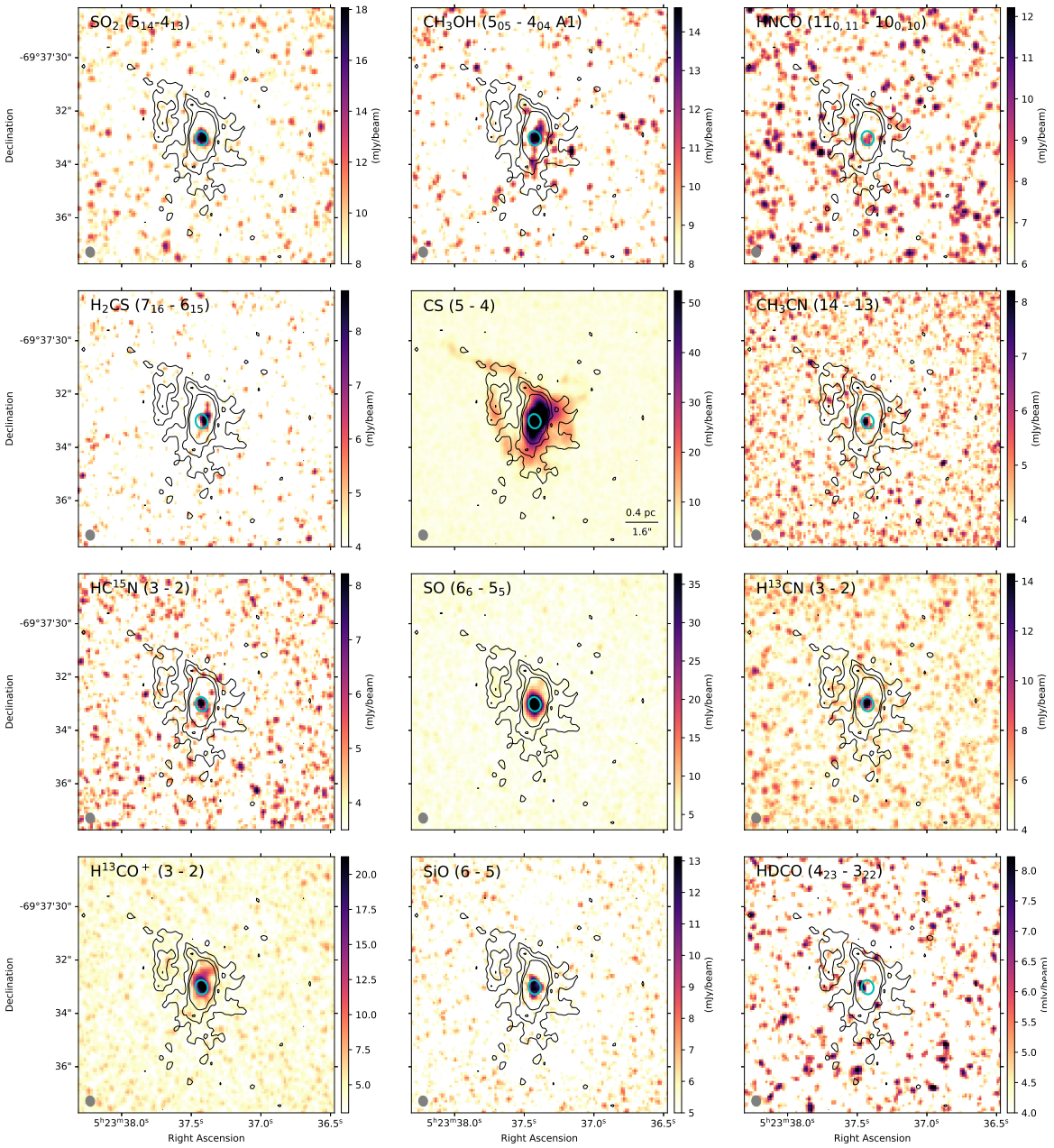


Figure 3.11: Peak-intensity images of the molecular species detected toward hot core 14A. The maps are ordered based on the frequency of the transition from left to right, top to bottom. The 1.2 mm continuum contours with contour levels of three, six, and nine times the σ_{rms} and the 50% 1.2 mm continuum contour are overlaid in each image for reference. Top is north and right is west.

Shimonishi et al. (2020).[6] While the abundances for SO_2, and SiO are slightly higher in the current work, CH_3OH, CH_3CN and SO show lower abundances. The higher temperature and lower abundance for CH_3CN in the current work could be due to a possible degeneracy between these two parameters when fitting the spectral data, suggesting that these two sets of parameters can reproduce the observed lines. Further observations can help in better constraining both the temperature and density for this hot core. Sewiło et al. (2022) found two hot cores, N105-2 A and N105-2 B, from Cycle 7 Band 6 observations of three fields in the N105 star-forming region. We note that the hot cores 6B and 6A in the current study correspond to the objects N105-2 A and N105-2 B, respectively. The temperature estimations are in good agreement for each pair of sources (see Fig. 3.12, middle- and bottom-left panels), with larger variations happening for the cold components of CH_3OH and SO_2 in 6B compared to N105-2 A. The middle- and bottom-right panels of Fig. 3.12 compare the abundances from the two studies. Sewiło et al. (2022) assumed a gas-to-dust mass ratio of 316, very close to the value we use, 320. The abundances of nearly all the molecules in 6A compared to N105-2 B fall in the same range except CH_3OH and CH_3CN, which are slightly higher in N105-2 B. Similar results were obtained for 6B and N105-2 A, with abundances falling in the same range. However CH_3OH, HNCO and $H^{13}CO^+$ show abundances approximately two to five times lower in 6B (this work). The observed differences are likely due to the slightly different temperatures used to calculate the column densities in both studies. Finally, we searched for detections of other species, such as HDCO, CH_2CO, and NH_2CHO, that had been previously detected by Sewiło et al. (2022). We could not confirm their detection because the expected brightness of the species is less than the sensitivity of the current dataset. Only a tentative feature was seen for NH_2CHO toward source 6A (see Fig. B.6).

Overall, the differences in the molecular abundances between the different works are within a factor of less than five. This factor is acceptable considering all possible errors and uncertainties in the analysis process. For example, different interferometric filtering during the observations as well as weather conditions or calibration effects, procedures followed to extract the spectra, or methodology used for fitting the lines may affect the derived temperatures and abundances by factors commonly in the range of two to ten. Therefore, we consider that our derived abundances are in agreement with previous studies, and we used them in the following discussion.

[6]Shimonishi et al. (2020) assumed a dust-to-gas mass ratio of 0.0027 for ST16, which corresponds to a factor 1.15 lower compared to the value we use. In order to compare the abundances, we applied this factor to the molecular abundances reported by Shimonishi et al. (2020).

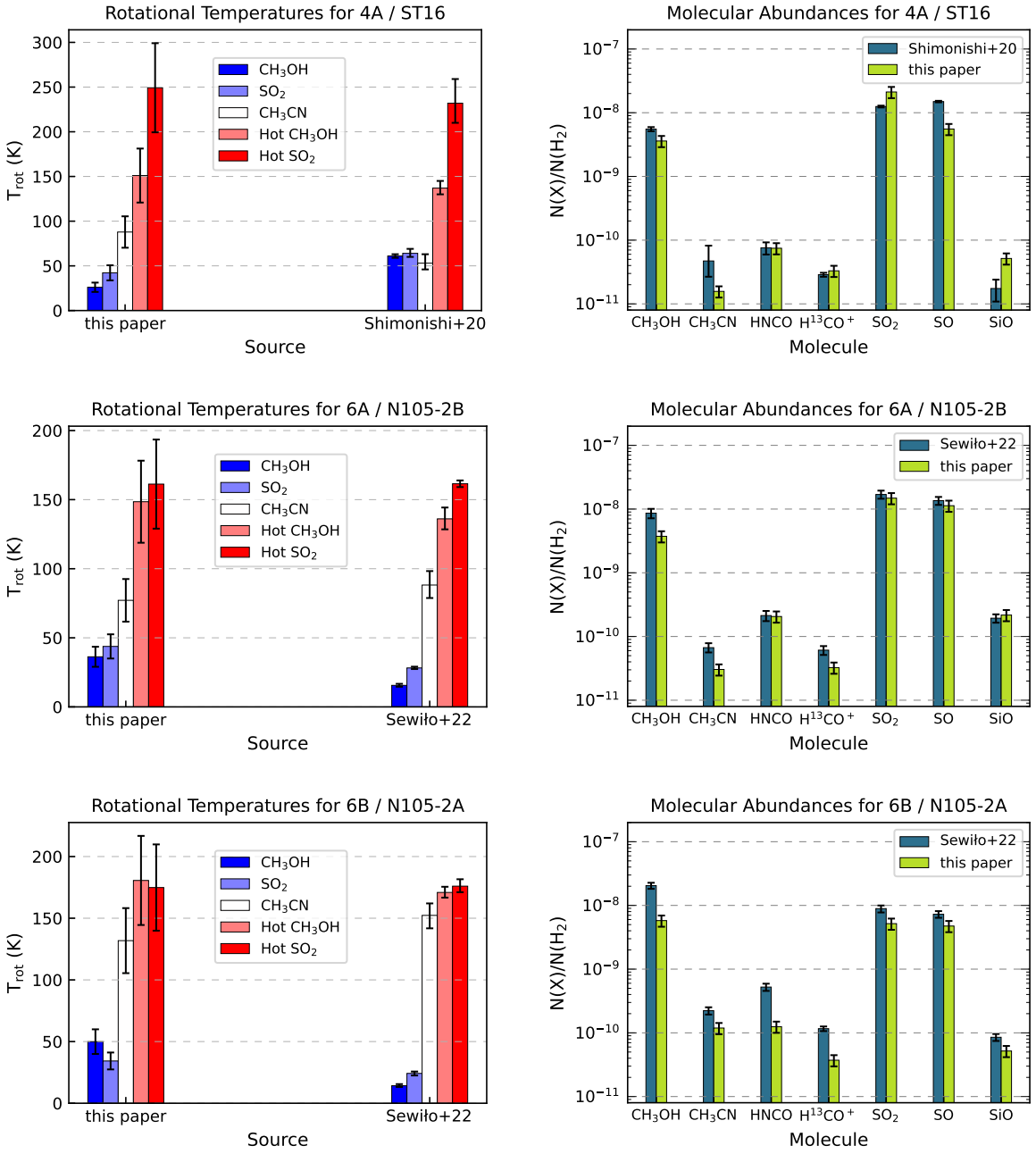


Figure 3.12: Comparisons of the derived temperatures (left) and abundances (right) from the current study and the literature. The top panels show a comparison of 4A and ST16 (Shimonishi et al., 2020), the middle panels show 6A and N105-2B, and the bottom panels show 6B and N105-2A (Sewiło et al., 2022). An error range of 40% is depicted for the temperatures and column densities from the current paper.

3.4.2 Properties of hot cores in the LMC

Comparison of the hot cores in the LMC

Apart from the four hot cores discussed in the previous section, three more have been reported in the LMC. Sewiło et al. (2018) discovered the first two chemically rich hot cores in the N113 star-forming region, N113 A1 and N113 B3, with COMs with up to nine atoms being detected in extra-galactic hot cores for the first time. The abundance of the molecular species for these objects, after scaling for metallicity, falls on the lower end of the Galactic values. In contrast, the hot core ST11 reported by Shimonishi et al. (2016b) was detected based on the presence of hot SO_2, although no reliable COMs were detected. The absence of COMs in this hot core was explained by a hot dust temperature resulting in inefficient CO hydrogenation to form CH_3OH (Shimonishi et al., 2016b).

Figure 3.13 shows a comparison of the molecular abundances in the seven hot molecular cores detected to date in the LMC after scaling to the gas-to-dust mass ratio used in the current paper (see Section 3.4.1). Each bar stands for one hot core, with error bars and upper limits also depicted in the plot. The non-detections of CH_3CN, HNCO, $H^{13}CO^+$, and SO toward N113 A and N113 B are due to a lack of bright transitions of these species in the observational setup, whereas the upper limits for ST11 show the absence or underabundance of this species, which was in the observed frequency ranges but not detected. The methanol abundance varies between 3.6×10^{-9} for 4A and 6A and 5.3×10^{-8} for N113 A1, where it is detected. The abundance of SO_2 varies between 5.0×10^{-9} for 6B and 2.1×10^{-8} for 4A and ST11.

The abundances shown in Fig. 3.13 reveal some trends for the hot cores in the LMC. We found an ascending pattern of an order of magnitude in the abundance of CH_3OH from the ST11 to N113 region, while the abundance of SO_2 shows small variations among the hot cores. At a second level, there seems to exist a correlation between CH_3OH and SiO. If SiO is produced in shocks, likely associated with molecular outflows (e.g. Schilke et al., 1997; Sánchez-Monge et al., 2013c), this correlation may suggest that the higher abundance of CH_3OH for some sources may have a shock origin. These correlations will be explored in a forthcoming work evaluating the spatial correlation of multiple molecular species.

Comparison with chemical models

The presence of hot SO_2 in ST11 has been taken as a signature of a hot core, with the absence of COMs in this source strengthening the idea of a warm dust chemistry in the LMC (see e.g. Shimonishi et al., 2016b). Although only one hot core of this kind has been detected in the LMC, we took advantage of the hot core models by Acharyya

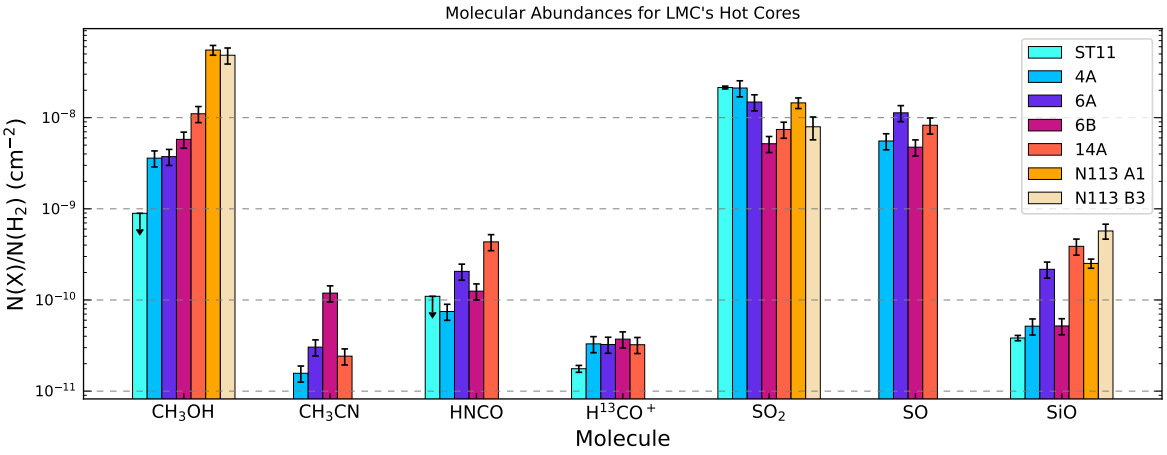


Figure 3.13: Abundances of different molecular species for all the known hot cores in the LMC after scaling to the gas-to-dust mass ratio. The LMC hot cores are ST11 (Shimonishi et al., 2016a), 4A, 6A, 6B and 14A (this work), and N113 A1 and N113 B (Sewiło et al., 2022). Black arrows show an upper limit estimation. An error range of 40% is shown on the abundances from the current paper.

& Herbst (2018) to investigate how the warm dust hypothesis for low-metallicity environments compares to the current observations of hot cores in the LMC.

Acharyya & Herbst (2018) simulated the stages of star formation leading to hot cores and their lower-mass counterparts, hot corinos, under the conditions of the LMC (and the SMC). They used a gas-to-dust mass ratio of 175, a cosmic-ray ionization rate of 1.3×10^{-17} s^{-1}, and a radiation field strength similar to the Galactic values. The star formation was modeled in three stages. The first stage is an isothermal cloud collapse under free fall with fixed gas and dust temperatures of 10, 15, 20, and 25 K and a visual extinction A_v of 1.64 mag. The collapse is stopped when the density reaches 10^7 cm^{-3}, a process that lasts 9.3×10^5 yr, during which A_v increases up to ≈ 450 mag. In the second stage, the density is fixed at 1×10^7 cm^{-3}, while the temperature increases linearly with time up to 100 or 200 K, resembling the temperature of hot cores. Two different times for the heating process are considered, reproducing expected conditions for high-mass (5×10^4 yr) and low-mass (1×10^6 yr) star formation. Once 100 or 200 K is reached, the warm-up ceases, and the newly formed hot core is allowed to evolve until a final total time of 1×10^7 yr. This model does not include the effects of shocks in the chemical evolution.

Figure 3.14 shows the time evolution of SO_2, CH_3OH, and CH_3CN abundances for the hot core model described above for the 100 and 200 K final temperatures (for other molecules see Figures C.1 and C.2). The observed abundances for the seven hot cores in the LMC are overlaid as horizontal lines in each panel following the same color scheme as in Fig. 3.14. Interestingly, only the models where the initial dust temperature is assumed to be between 10 and 20 K reproduce the observed molecular

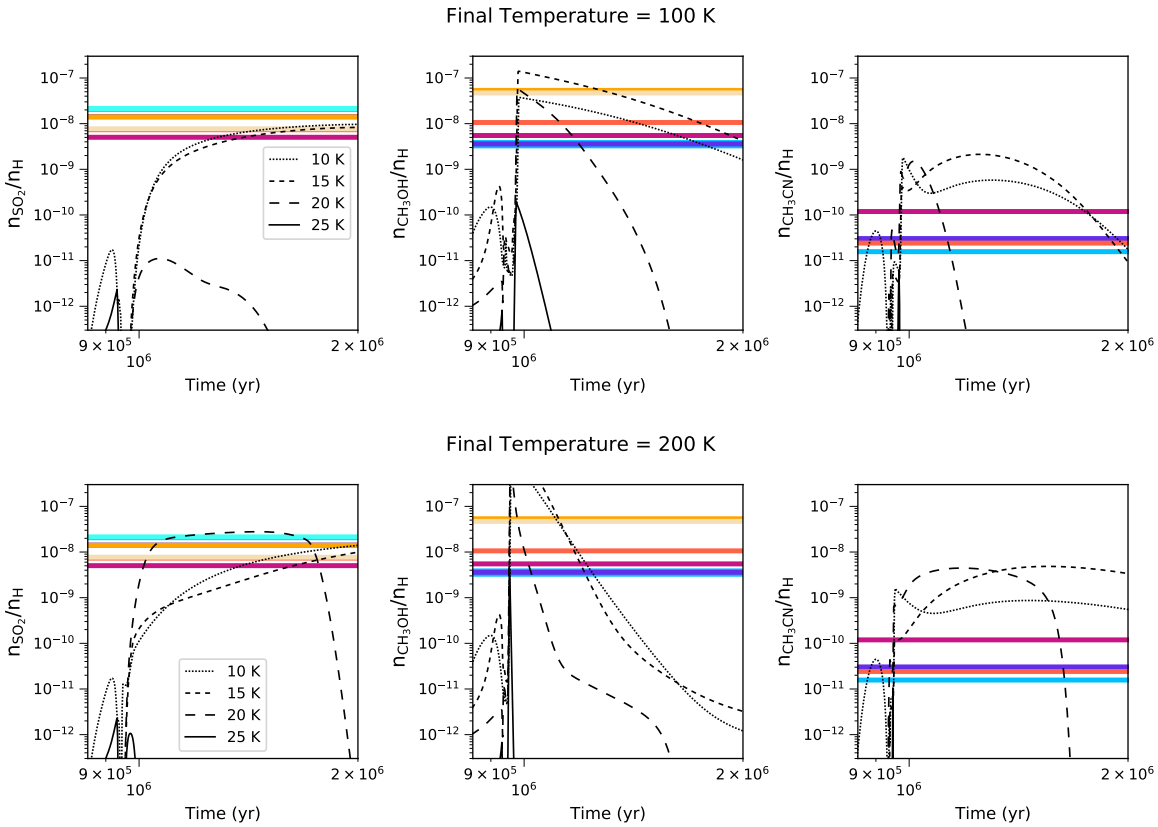


Figure 3.14: Comparisons of abundances for SO_2, CH_3OH, and CH_3CN from observations of the seven hot cores detected in this galaxy and the LMC hot core models for the final hot core temperature of 100 K (*top*) and 200 K (*bottom*). The black curves show abundances over time for an initial dust temperature of 10 (dotted curve), 15 (dashed curve), 20 (larger dashed curve), and 25 K (the solid curve). The horizontal colored line shows the single abundance value for each hot core and follows the same color code as Fig. 3.13 (see the text for more details).

abundances. The chemical model with an initial highest dust temperature of 25 K results in molecular abundances that are much lower than the observed ones. Based on the comparison with the chemical models of Acharyya & Herbst (2018), a high initial dust temperature does not seem to be a reason for a possible lack of COMs in the hot cores of the LMC since chemical models with initial dust temperatures in the range 10 to 20 K (similar to star-forming regions in the MW) can better reproduce the molecular abundances observed in the LMC.

3.4.3 Hot cores in the LMC, SMC, and MW

A logical next step when studying the chemistry in low-metallicity environments is to compare the molecular abundances from the hot cores in the LMC, SMC, and outer Galaxy to those found in star-forming regions in the inner Galaxy. To achieve this goal, we collected a sample of Galactic hot cores studied in the literature and added

them to the seven hot cores found in the LMC (see Section 3.4.2), the two hot cores recently discovered in the SMC (Shimonishi et al., 2023), and the WB 89−789 SMM1 hot core found in the outer regions of the Galaxy (Shimonishi et al., 2021). In the case of WB 89−789 SMM1, we used the abundances calculated for a source with a size of 0.1 pc (from Table 4 of Shimonishi et al. (2021)). In the interest of matching spatial scales, we focused on single-dish observations of Galactic hot cores. In particular, we considered the Orion Hot Core (Sutton et al., 1995), Sgr B2(N) (Nummelin et al., 2000) and W3(H_2O) (Helmich & van Dishoeck, 1997) to represent the standard conditions and properties of hot cores in the MW.

In Fig. 3.15, we present a comparison of the abundances of four molecular species corresponding to the selected list of hot cores. For the LMC hot cores, we first applied a correction factor to account for the different gas-to-dust mass ratio every study assumes (see Section 3.4.1). Then we applied a correction factor of 5, 2.6, and 4 to the abundances of the hot cores in the SMC, LMC, and extreme outer Galaxy[7] to account for differences in metallicity. The original values are shown with single color bars in Fig. 3.15, while the scaled values are depicted as an excess with dotted patterns.

The methanol abundances vary by an order of magnitude among the hot cores in the LMC, except for ST11, for which only an upper limit is estimated. While the methanol abundances show an ascending trend from the low metallicity of the SMC to the LMC and to the inner regions of the MW, the only hot core in the outer region of the Galaxy, with a factor of four lower metallicity, shows the highest methanol abundance. We note that CH_3CN was not detected in all the hot cores, making the comparison less robust. However, one can see that the abundance of CH_3CN in the hot core in the outskirts of the Galaxy is higher than those in the LMC. In contrast to higher abundances of CH_3OH and CH_3CN in the outer Galaxy compared to the LMC and SMC, SO_2 and SiO are less abundant. This raises the question of whether the abundance of different molecular species is only a function of metallicity. We note that the outskirts of the Galaxy are more quiescent due to the low star-formation activity, while the star-forming regions of the LMC and the SMC are more active. While comparisons of the chemistry in different conditions still need better observational statistics, we acknowledge the necessity of chemical modeling to further investigate the effect of metallicity, strength of UV radiation, cosmic ionization rate, and shock chemistry on the observed molecular abundances.

Shimonishi et al. (2020) classified the LMC hot cores as "organic-poor" and "organic-rich" based on the comparison of only four hot cores in the LMC. Sewiło et al. (2022) placed N105-2 A and N105-2 B in the organic-rich class, suggesting a larger sample

[7]We adopted $Z_{Gal}/Z_{SMC} = 5$, $Z_{Gal}/Z_{LMC} = 2.6$, $Z_{Gal}/Z_{ExtOutGal} = 4$. We note that metallicity decreases with the Galactocentric radius in the MW, resulting in varying metallicities across the outer Galaxy (e.g., **?**). The metallicity value we present for the outer Galaxy corresponds to the position of WB 89-789.

to verify this classification. We also acknowledge the necessity of larger samples for a better understanding of hot core chemistry in the LMC. At the same time, we revise the classification of organic-poor and organic-rich based on the findings of this study. Shimonishi et al. (2020) classified ST11 and ST16 as organic-poor and N113 A1 and N113 B3 as organic-rich hot cores to emphasize the detection of more complex compounds with comparable scaled abundances to the Galactic hot cores. Our survey study, however, demonstrates a different picture. All the hot cores in our sample show comparable chemical complexity. A slightly different chemistry may relate to the evolutionary stage of the hot core and surrounding gas. For example, we detected isotopologues of SO_2, $^{33}SO_2$, and $^{34}SO_2$ in the hot core 4A but had no detection of deuterated molecules. In contrast, hot core 14A shows emission lines from HDCO but no emission from SO_2 isotopologues. The common association of deuterated species with early evolutionary stages (e.g. Fontani et al., 2011; Treviño-Morales et al., 2014) and the connection of SO_2 with the presence of shocks and ionized gas (e.g. Minh et al., 2016; Gieser et al., 2021) suggest that different evolutionary stages and physical conditions are likely relevant factors of the chemical content of the hot cores in the LMC. Within this picture from the hot cores in the LMC, the only organic-poor hot core that remains is ST11.

In Fig. 3.16, we present pair-wise comparisons of the abundances of CH_3CN, CH_3OH, SO_2, SO, and SiO. Based on these comparisons, we observed that the hot cores in the LMC appear to show lower abundances of CH_3CN relative to CH_3OH compared to hot cores in the MW but higher abundances of SO_2 relative to SO. Although this study should be extended to a larger sample of targets and evolutionary effects may play a role in the observed abundances, the first results favor the idea that hot cores in the LMC may be brighter in SO_2 lines compared to other molecular species commonly found in hot cores. The comparison and correlation between CH_3OH and SO_2 with SiO suggest that shocks may play an important role in the observed abundances of these species.

3.4.4 Location of hot cores in the LMC

In Fig. 3.17, we show the location of all the detected hot cores in the LMC. So far, all the hot cores associated with COMs are located in the central region of the galaxy, which is known as the LMC bar. This region has a mildly higher ($\sim 2\%$) metallicity compared to the surrounding regions, as suggested by narrow-band near-IR observations (Choudhury et al., 2021). Inspection of the atomic(Kim et al., 1998; Smith et al., 2000), molecular gas (e.g. Fukui et al., 1999), and dust maps (Meixner et al., 2013) of the LMC revealed that the dense cold gas and dust are located within a zigzag shape in the bar region and surrounded by bubbles of dispersed dust and gas (known

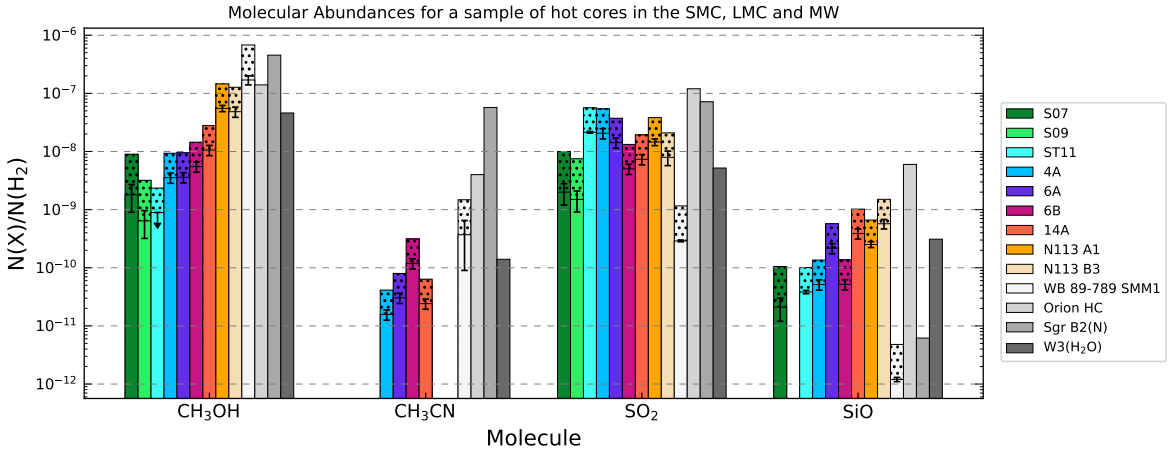


Figure 3.15: Abundances of CH_3OH, CH_3CN, SO_2, and SiO for all known hot cores in the SMC and LMC and for a selection of Galactic hot cores. The SMC hot cores are included, S07 and S09 (Shimonishi et al., 2023). The LMC hot cores are ST11 (Shimonishi et al., 2016a), 4A, 6A, 6B and 14A (this work), and N113 A1 and N113 B (Sewiło et al., 2022). We selected four Galactic hot cores: an outer Galaxy hot core (Shimonishi et al., 2020), Orion Hot Core (HC) (Sutton et al., 1995), Sgr B2(N) (Nummelin et al., 2000), and W3(H_2O) (Helmich & van Dishoeck, 1997). The extent of each bar with a dotted pattern represents the abundances scaled to the Galactic metallicity.

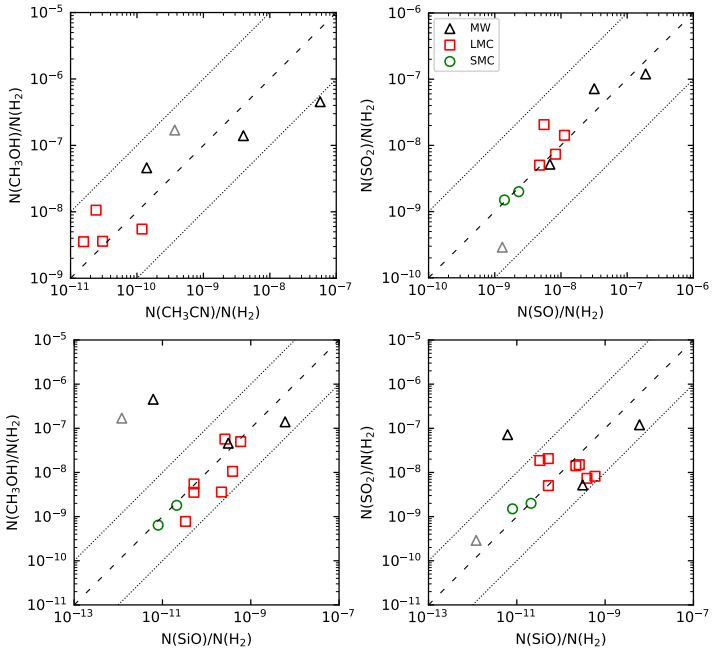


Figure 3.16: Comparisons of the abundances of CH_3OH and CH_3CN and SO_2 and SO for the hot cores in the SMC (open green circles), LMC (red rectangles), and MW (black triangles for inner Galactic hot cores and gray triangle for outer Galactic hot core). Dashed lines show abundance relations of 1:1 for the top-right panel and 1:100 for the other panels. The dotted lines show a variation of a factor of ten above and below the relations described by the dashed lines.

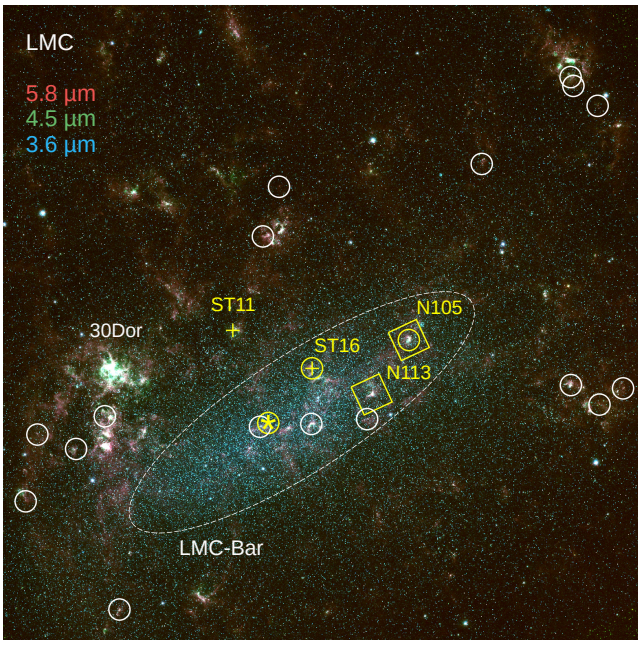


Figure 3.17: Three color composite image of the LMC combining 3.6 μm (blue), 4.5 μm (green), and 5.8 μm (red Meixner et al., 2006) images to highlight the position of the stellar bar. The dashed ellipse marks the bar region. The 20 ALMA fields from the current study are overlaid with white circles 15 times larger than the field of view of our ALMA observations. The fields accommodating hot cores are highlighted in yellow, including the YSO ST16 and N105 star-forming region. The field marked with a star shows the position of the new hot core detected in our survey. The location of the hot cores in N105 (Sewiło et al., 2022) and N113 (Sewiło et al., 2018) are marked with yellow rectangles. The hot cores ST11 (Shimonishi et al., 2016b) and ST16 (Shimonishi et al., 2020) are shown with yellow plus signs. The hot core ST11 with no COMs is the only hot core detected out of the LMC bar.

as HI holes; Staveley-Smith et al., 2003). This implies that expanding material from different sides results in compressed material into this zigzag region. Based on this observational evidence, we speculate that star formation in the bar must have been triggered at some point when the interstellar medium in the bar was enriched and the metallicity was increased relative to other areas of the LMC. This might explain the preferential detection of hot cores with complex chemistry only toward the LMC bar.

For this scenario to be plausible, one needs to consider if the ignition of the new generation of stars that resulted in the currently detected hot cores took place after the chemical enrichment of the interstellar medium of the LMC bar. Different works in the literature explore the origin of the current distribution of gas and dust in the bar region as well as the existence of possible events in the history of the LMC that may have caused an increase of metallicity in the bar and the triggering of a new generation of stars. In the following, we summarize the main findings and connect them to the presence of hot cores in the LMC bar.

Hydrodynamic simulations (Tenorio-Tagle et al., 1986) infer the creation of HI holes and shells as a result of the interaction between high-velocity clouds and the galactic disk. At the same time, the study of the morphology and kinematics of stellar populations and HI gas in the LMC, SMC, Magellanic Bridge (MB), and the Leading Arm (LA) suggests the interaction between the LMC and SMC (e.g. Zivick et al., 2019, and references therein). Furthermore, numerical simulations of the evolution of the Magellanic Clouds favor the sporadic replenishment of low-metallicity gas from the SMC to the LMC's disk over the last 2 Gyr as a result of their tidal interaction (known as Magellanic Squall; Bekki & Chiba, 2007b). This stripped high-velocity gas can be responsible for some of the HI holes observable in the LMC. Bekki & Chiba (2007b) argues that the triggering of the star formation could be a direct impact of clouds of the SMC interacting with those of the LMC. In addition, numerical models of Besla et al. (2012) investigate the history of interaction between the SMC, LMC, and MW. Besla et al. (2012) argue that the off-center warped stellar bar of the LMC and its one-armed spiral can be explained by a recent direct collision with the SMC. Given the uncertainties of the model parameters, the exact time of the collision and its impact on star formation cannot be strictly defined. However, a time range from 100 to 300 Myr seems a reasonable approximation (Besla et al., 2012). Analysis of the proper motions of stars from Gaia data supports the direct collision and suggests that this event was not a grazing interaction but that the SMC went directly through the LMC, allowing the interstellar medium of both galaxies to interact (Zivick et al., 2019). Furthermore, Choudhury et al. (2021) presumed that the mixing of the metallicity of the two galaxies, caused by tidal interaction, could be a reason for the asymmetry metallicity distribution observed in the LMC. With all this, and given the timescale of formation of hot molecular cores ($\sim 1 \times 10^5$ yr, Wilner et al. 2001; Furuya et al. 2005;

Herbst & van Dishoeck 2009), the detected hot cores in the LMC bar region have most likely been formed in the inhomogeneous and slightly metallicity-richer interstellar gas that emerged after the severe interactions of the LMC and the SMC.

3.5 Conclusions

We have observed 20 star-forming sites distributed throughout the LMC with ALMA in four frequency ranges between 241 and 260 GHz and at an angular resolution of $\approx 0.35''$ (corresponding to 0.08 pc). We detected a total of 65 continuum cores whose physical properties (e.g., mass, density, size) are presented in Paper II. In this work, we have studied the chemical content of these compact cores. The main findings are summarized as follows:

1. The extracted spectra at the location of the cores show different levels of chemical complexity in the cores. There are cores with no molecular line emission and cores with single-line detection of dense or warm gas tracers, such as CS, SO, or $H^{13}CO^+$. These include 28% of all the cores. In addition, other cores contain CH_3OH. These cores can be put into two distinct groups: cores with emission lines from simple molecules, such as SO_2,H_2CS, $H^{13}CN$, $HC^{15}N$, and SiO, and sources with detection of simple species and COMs, such as CH_3CN, or tentative detection of NH_2CHO, CH_3OCHO, and CH_3OCH_3.

2. The detection of multiple transitions from a single molecule allowed for the determination of the temperature. The CH_3OH molecule, detected in 72% of the cores, is our main temperature tracer in this study. We estimated the temperature with both LTE and non-LTE assumptions and compared the two temperatures with the SO_2 temperature, where it was reliably detected. Our temperature determination was further confirmed by estimating the CH_3CN temperature where it was detected.

3. Molecular line width is a tracer of the gas kinematics. We investigated the line width of different molecular species (fit with XCLASS), and CH_3OH showed the lowest line width value in 51% of the cores. However, only a small sample of cores showed an average line width above 5 km/s.

4. Comparing the abundance of different molecular species in the 65 cores showed that S-bearing molecules are in general more present and abundant than N- and O-bearing species. Therefore, the detection of N- and O-bearing species, especially the COMs, needs higher sensitivity in future observations.

5. Four hot molecular cores were detected in this study, confirmed by their size ($\sim$ 0.1 pc), chemical richness, temperatures above 100 K, and high abundances of CH_3OH and SO_2.

The four hot cores in our sample reveal the detection of one new hot core, bringing the number of hot cores in the LMC to seven. Shimonishi et al. (2023) suggest SO_2 as a tracer of hot cores in a low-metallicity environment. Our survey study supports this suggestion by detecting strong lines of SO_2 and its isotopologues only in the hot cores. We note that (six out of the seven) hot cores with detections of methanol or other COMs are preferentially located in the LMC bar. The metallicity-scaled abundances of different molecular species in these hot cores are comparable with those in the MW. Shimonishi et al. (2020) have suggested the initial high dust temperature to be responsible for the lower abundances of COMs in the low metallicity of the LMC. However, comparisons of our observed abundances with the LMC hot core chemical models of Acharyya & Herbst (2018) do not support high initial dust temperatures.

Chapter 4

Filaments, outflow and radiative feedback

The content of this chapter may be partially or entirely included in future publications by Hamedani Golshan et al.

Star-forming regions are characterized by dynamic and interconnected processes. These processes, from the collapse of molecular clouds to the formation of dense substructures and prestellar cores, are accompanied by substantial flows of mass and energy. Mass inflows sustain star-forming clumps and cores, initiating bursts of radiation and mass ejection. These radiative and mechanical feedback mechanisms play a crucial role in shaping the surrounding environment and regulating the star formation dynamics.

In this chapter, I investigate the morphology of gas in star-forming regions by utilizing tracers of dense, shocked, and ionized gas to identify filaments, outflows, and HII regions. Section 4.1 focuses on the spatial distribution of molecular gas, using dense and shocked gas tracers derived from ALMA observations. Section 4.2 presents ionized gas maps from ATCA observations and examines the nature of the sources powering the HII regions. Finally, Section 4.3 provides a detailed comparison of the target fields and proposes a possible evolutionary scenario for star-forming regions in the LMC.

4.1 Morphology of the molecular gas

Molecular gas emission is an excellent tracer of highly obscured environments where stars form deep within molecular gas and dust. Investigating these emissions is therefore crucial for understanding the processes that govern star formation. This section focuses on the extended structures of molecular gas beyond the cores discussed in previous chapters. Additionally, I analyze molecular lines with notably broader profiles, which may signify dynamic processes such as outflows.

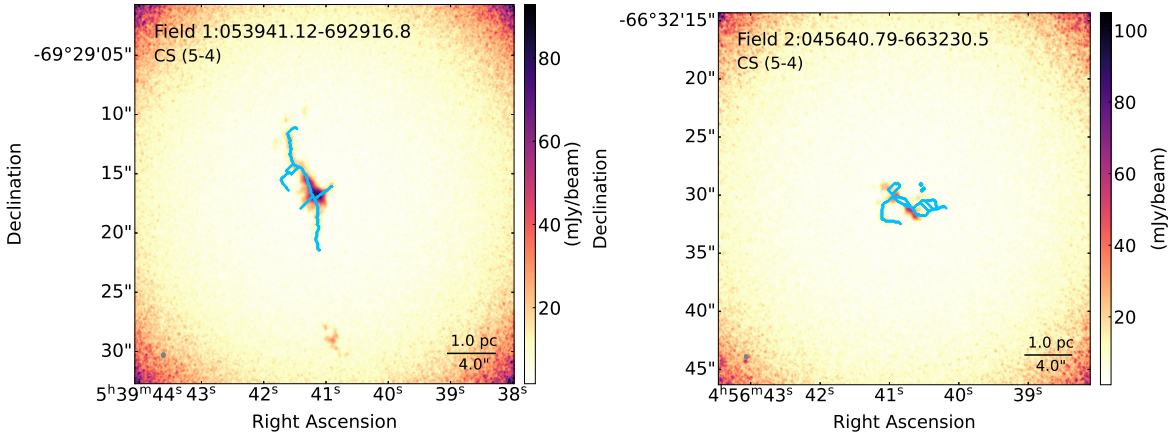


Figure 4.1: Filaments detected in the CS peak-intensity maps for Fields 1 and 2.

4.1.1 Molecular filaments

Filaments are elongated structures within molecular clouds, typically characterized by a width of $\sim$ 0.1 pc (e.g., Arzoumanian et al., 2019; André et al., 2022, and references therein). These structures are ubiquitous and central to the Galactic star formation process (e.g., Hacar et al., 2023, and references therein). Despite their prominence, the mechanisms governing their formation and fragmentation remain poorly understood in Galactic star-forming regions (Hacar et al., 2023). In extragalactic environments, where metallicity, cooling, and heating efficiencies differ, the processes responsible for forming and sustaining molecular clouds and their internal structures may not operate in the same way. In low-metallicity environments, it is unclear whether filamentary molecular clouds, commonly observed in star-forming regions within the solar neighborhood, form and persist under similar conditions (Tokuda et al., 2025).

Extragalactic filaments have been detected primarily in nearby systems such as the LMC and SMC. In the LMC, a systematic survey identified the hub-filament systems (HFS) in approximately 50% of the observed regions (Tokuda et al., 2023). These complexes typically emerge during the later stages of their parent cloud evolution and are closely associated with prominent HII regions and stellar clusters. This finding suggests that the formation of extremely luminous, high-mass stellar clusters -capable of eventually dispersing their natal clouds- relies on a critical intermediate stage characterized by massive filaments and hub-filament systems.

In contrast, a survey of massive YSOs in the SMC revealed that approximately 40% of the star-forming regions lack filamentary structures and appear more evolved than filamentary clouds (Tokuda et al., 2025). This finding suggests that while filaments may initially form during the star formation process, their structures can dissipate over time, transitioning into a lower-temperature state. Observations of such structural and thermal transitions, which have not been reported in metal-rich regions, highlight a

distinctive behavior of the interstellar medium and star formation in low-metallicity environments.

In this section, we conduct a systematic search to identify and characterize filaments. For this purpose, I examined the channel and moment maps of dense gas tracers in our sample, including CS, SO, $H^{13}CN$, $H^{13}CO^+$, and H_2CS. Among these tracers, CS emission is consistently detected across all fields, allowing for a uniform analysis of dense regions within the sample. Notably, CS exhibits significant spatial extension compared to other molecular species and correlates strongly with 1.2 mm continuum emission, which primarily traces dust. This makes CS especially useful for identifying filamentary and clumpy structures that host protostellar cores.

The CS (5-4) transition, with a critical density of approximately 10^6 cm^{-3} for temperatures between 20 and 100 K (Shirley, 2015), serves as a prominent tracer of dense structures. This high critical density ensures that CS emission originates primarily from compact, dense regions within molecular clouds, closely linked to the star formation process. By comparing CS peak intensity maps with 1.2 mm continuum maps, we identify gas structures visible in CS emission that are absent in dust emission, offering deeper insights into the morphology and kinematics of the dense gas.

Characterizing filaments

To identify filaments in the CS peak intensity map, I used the automated algorithm `FilFinder` (Koch & Rosolowsky, 2015), which extracts elongated structures based on intensity thresholds and continuity criteria. The setup included flattening the intensity distribution (`flatten_percent = 95`), applying a noise threshold varying from 3 to $7\sigma_{\rm rms}$ to avoid noise peaks, and selecting regions larger than five times the beam size. The recommended values of `adapt_thresh = 0.1` pc and `smooth_size = 0.05` pc were used to extract filaments with widths near 0.1 pc. Filament spines were identified within the mask, excluding filament branches shorter than one beam size.

Filaments are identified in all but two fields, Field 9 and 20. Figure 4.1 shows CS peak intensity maps for two example fields, with the identified filaments overlaid. The remaining maps are provided in Appendix D. Using the parameters provided by the output table of `FilFinder` analysis, the filaments are further characterized by calculating their masses. To this goal, I use the Equation 82 from (Mangum & Shirley, 2015), which is particularly suited for submillimeter transitions. Incorporating the Einstein A coefficient ($A_{\rm ul}$) and intrinsic intensity transition ($S\mu^2$) relation:

$$A_{\rm ul} = \frac{64\pi\nu_{\rm ul}}{3hc^3}\frac{S\mu^2}{g_{\rm u}} \tag{4.1}$$

into Equation 82 from (Mangum & Shirley, 2015), I write the total CS colomn density

Table 4.1: Properties of the filaments derived from `Filfinder` analysis of the CS peak intensity maps.

Field Number	Number of Branches	$l_{\rm fil}$ (pc)	$\omega_{\rm fil}$ (pc)	$I_{\rm tot}$ (Jy/beam)	$N_{\rm tot}$ (H_2) (cm^{-2})	$M_{\rm line}$ ($M_\odot$/pc)	Fragmentation[a]	Main[b] Filament
1	9	3.60	0.08	24.25	1.13×10^{21}	14.84	–	m
2	20	2.52	0.07	13.03	6.67×10^{21}	132.38	✓	m
3	8	2.22	0.15	36.42	1.18×10^{22}	198.86	✓	m
3	1	0.69	0.08	2.52	8.18×10^{20}	44.35	–	
4	8	1.86	0.11	22.23	5.77×10^{20}	8.98	–	m
5	1	0.79	0.19	6.63	7.11×10^{21}	50.72	✓	m
6	1	0.70	0.06	1.90	1.27×10^{20}	12.54	–	
6	1	2.08	0.20	21.93	1.47×10^{21}	48.53	–	
6	7	3.22	0.16	65.60	4.39×10^{21}	93.72	✓	m
7	1	1.44	0.04	2.57	1.93×10^{21}	53.51	✓	
7	3	1.71	0.07	8.64	6.48×10^{21}	151.25	✓	m
7	1	0.67	0.10	1.09	8.19×10^{20}	48.79	✓	
8	1	0.63	0.04	1.01	2.49×10^{20}	2.39	–	m
10	1	1.78	0.05	5.59	2.42×10^{21}	23.88	–	m
11	3	2.03	0.03	1.24	3.63×10^{20}	4.09	–	m
12	1	0.98	0.05	2.64	1.50×10^{21}	19.57	–	m
12	1	0.45	0.11	1.50	8.49×10^{20}	24.33	–	
13	1	1.23	0.10	6.08	1.54×10^{21}	41.37	–	
13	1	2.31	0.18	38.30	9.67×10^{21}	138.10	✓	m
14	3	2.13	0.02	2.26	1.89×10^{19}	0.22	–	m
15	3	1.70	0.14	11.89	2.45×10^{21}	38.17	–	m
15	3	0.76	0.07	2.44	5.02×10^{20}	17.64	–	
16	1	1.31	0.10	2.27	1.50×10^{21}	14.39	–	m
17	1	1.36	0.09	14.36	2.84×10^{21}	25.72	–	m
18	3	2.88	0.15	28.33	5.29×10^{21}	70.64	✓	m
18	1	0.85	0.11	4.28	7.99×10^{20}	36.23	–	
19	1	1.04	0.08	3.88	6.09×10^{20}	5.51	–	m

Notes.

[a] The thermal Jeans mass per unit length ($M_{\rm line}$) of the filaments is calculated using the median temperature derived from the cores in each field, as presented in Chapter 3. If the $M_{\rm line}$ of the filament exceeds the thermal Jeans $M_{\rm line}$, a ✓ to indicate that the filament may undergo fragmentation in the absence of non-thermal support.

[b] The longest filament associated with the protostellar core(s) in each field, considered for further analysis in Section 4.3, is marked with "m" to denote the main structure.

as:

$$N_{\rm tot}({\rm CS}) = (\frac{8\pi k\nu^2}{hc^3 A_{\rm ul}})(\frac{Q(T_{\rm ext})}{g_{\rm u}^2})\ exp(\frac{E_{\rm u}}{kT_{\rm ext}}) \int T_{\rm R} d\nu \tag{4.2}$$

Constants were sourced from the CDMS database (Müller et al., 2005). The following values were used; $\nu = 244935.5565 MHz$, $A_{ul} = 0.000298064 s^{-1}$, $g_u = 2J + 1 = 11$, $E_u = 35.3K$, and $T_{ext} = T_{kin}$ derived from the median core temperature in each fields. The partition function $Q(T_{\rm ext})$ interpolated from CDMS data, and $\int T_{\rm R} d\nu$ is the total observed intensity. Using CS abundances ($N({\rm CS})/N({\rm H_2}) \sim 10^{-11} - 10^{-10}$) derived from the cores (see Table B.2), the total molecular hydrogen column density along the filaments ($N_{\rm tot}({\rm H_2})$) was calculated. From $N_{\rm tot}({\rm H_2})$ and area of filament, the filament mass and mass per unit length ($M_{\rm line}$) are derived.

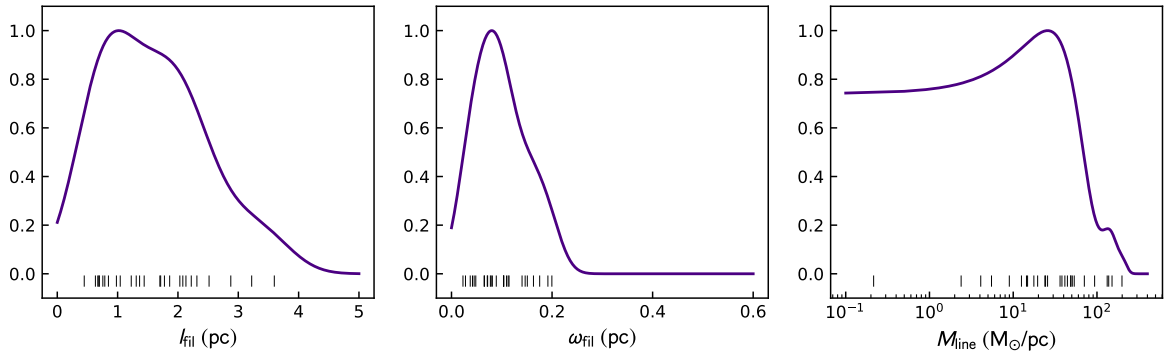


Figure 4.2: KDE of filaments properties.

The thermal Jeans $M_{\rm line}$ was estimated following Equation 4 from Treviño-Morales et al. (2019), varying between 30 to 200 $M_\odot$/pc across the filaments. The ratio of observed to Jeans $M_{\rm line}$ indicates whether filaments may undergo fragmentation in the absence of non-thermal support. Using Equation 5 from Treviño-Morales et al. (2019) a non-thermal line width of 0.65 km/s was calculated to sustain the filaments. Given the median linewidth at cores positions ($\sim$ 3 km/s), non-thermal motions likely contribute significantly to filament stability, though further analysis of velocity structures is needed.

Table 4.1 summarizes the derived filament parameters. Figure 4.2 represents a KDE distribution of filament properties, including length, width, and mass per unit length. Filament lengths range from 0.5 to 4 pc, widths from 0.02 to 0.2 pc (peaking at 0.1 pc), and $M_{\rm line}$ values from 0.2 to 110 $M_\odot$/pc. Comparing filament lengths and widths with Tokuda et al. (2023), we observe similar length distributions but narrower structures in our study, which likely accounts for the smaller $M_{\rm line}$ values we derived.

4.1.2 Molecular outflows

Protostellar cores accrete mass from their surrounding molecular envelope, while the outflow of material plays a crucial role in stabilizing the system by conserving angular momentum. This outflow occurs in two opposing directions, forming bipolar outflows. The energetic nature of this process generates shocks[1] that can erode or destroy dust particles, releasing silicon (Si) that was previously trapped in the dust grains into the gas phase. As Si interacts with oxygen, SiO is formed—a well-known tracer of shocks in star-forming regions (e.g., Schilke et al., 1997). Therefore, the outflow from protostellar objects can be traced through SiO emission.

The SiO emission maps show a high signal-to-noise ratio in three fields (see Fig. 4.3), which also coincide with the locations of the hot cores detected in Chapter3. The SiO

[1]Shocks are a characteristic feature of fluids, occurring when material flows at speeds exceeding the sound speed in a medium.

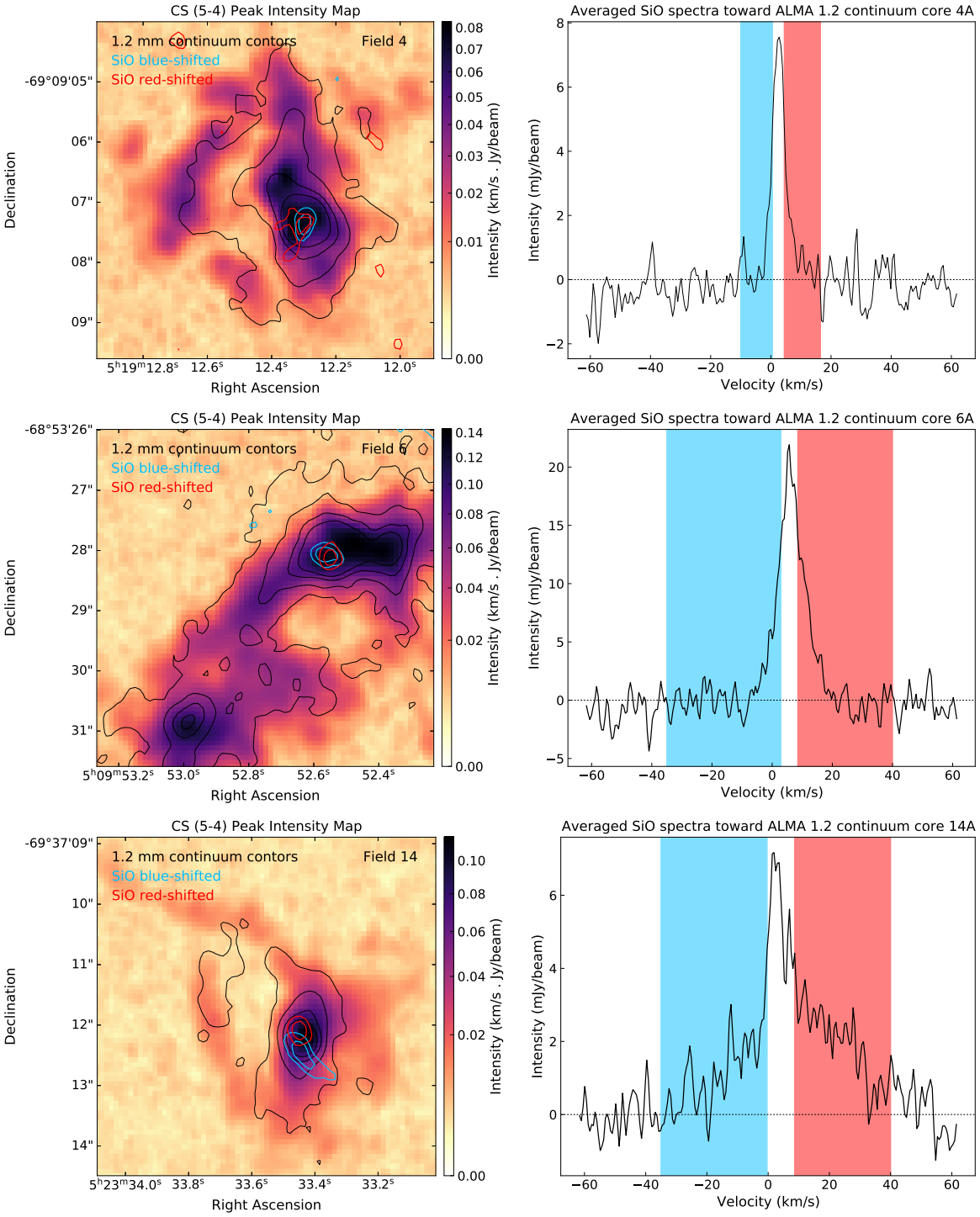


Figure 4.3: Outflows detected toward continuum cores 4A (top panel), 6A (middle panel), and 14A (bottom panel). The left panel in each row shows the CS peak intensity map overlaid with continuum contours at 5, 15, 30, and 45 $\sigma_{\rm rms}$, as well as red- and blue-shifted outflow lobes at 0.6 and 0.75 of the maximum value from the integrated intensity maps over the velocity range highlighted in the right panel. The right panel displays the SiO spectra averaged over the source polygon, with red- and blue-shifted lobes marked using the corresponding color spans.

emission is concentrated at the positions of the continuum cores, providing strong evidence for their association with these star-forming cores. Outflows are identified by broad SiO line emission (approximately 10 km/s and more), originating from regions about 0.1 pc in size. The average SiO spectra are decomposed into red- and blue-shifted lobes, as shown in the right panels of Fig. 4.3. These lobes are defined from the 60% peak emission to the noise level. Contours of the integrated flux density for the two lobes are also shown in the right panels of Fig. 4.3.

The outflows exhibit varying inclination angles and line profiles, with differences in width. The outflow associated with core 4A appears to be slightly inclined in the plane of the sky, with a possible component along the line of sight. The SiO line width is slightly less than 10km/s. Core 6A is associated with an outflow that seems to be aligned along the line of sight, suggesting that we are observing through the outflow cone. The SiO emission line at this core is wider (approximately 12km/s) and very strong. For core 14A, the red- and blue-shifted lobes are slightly overlapping compared to the other cores, with an exceptionally broad line width exceeding 20 km/s.

Rotation associated with outflow-cores

The detection of outflows may also indicate accretion of material into the star-forming core. To explore this possibility, I constructed position-velocity (PV) diagrams for a slice centered on the core, 0.5 pc wide and 2 pc long. The PV diagram, taken at an inclination angle nearly perpendicular to the defined outflow direction, shows velocity gradients of up to 8 km/s for core 4A and 10 km/s for core 14A. The diagram exhibits an almost butterfly-shaped pattern, with enhanced gradients at the center that decrease toward the edges, suggesting a rotating structure. This hints at the presence of rotation in these two hot cores. However, the resolution of our ALMA observations is insufficient to determine whether the rotation is due to an accreting disk, as seen in a massive YSO in the LMC (McLeod et al., 2024). Nevertheless, our survey provides a promising foundation for identifying candidate sources for accreting disks in the LMC. While I have focused on detecting rotation and accretion signatures in outflow sources, it would be valuable to examine other fields, as accretion may begin before the outflow stage and cease earlier. This scenario, however, could be influenced by radiation pressure in the low-metallicity environment of the LMC, warranting further investigation.

4.2 Ionized gas: Radiative feedback

When a stellar embryo forms and begins to grow, it emits UV radiation. In the case of massive stars, this radiation is present during the accretion phase. As mass continues to accrete onto the central source, the intensity of the radiation increases. This UV

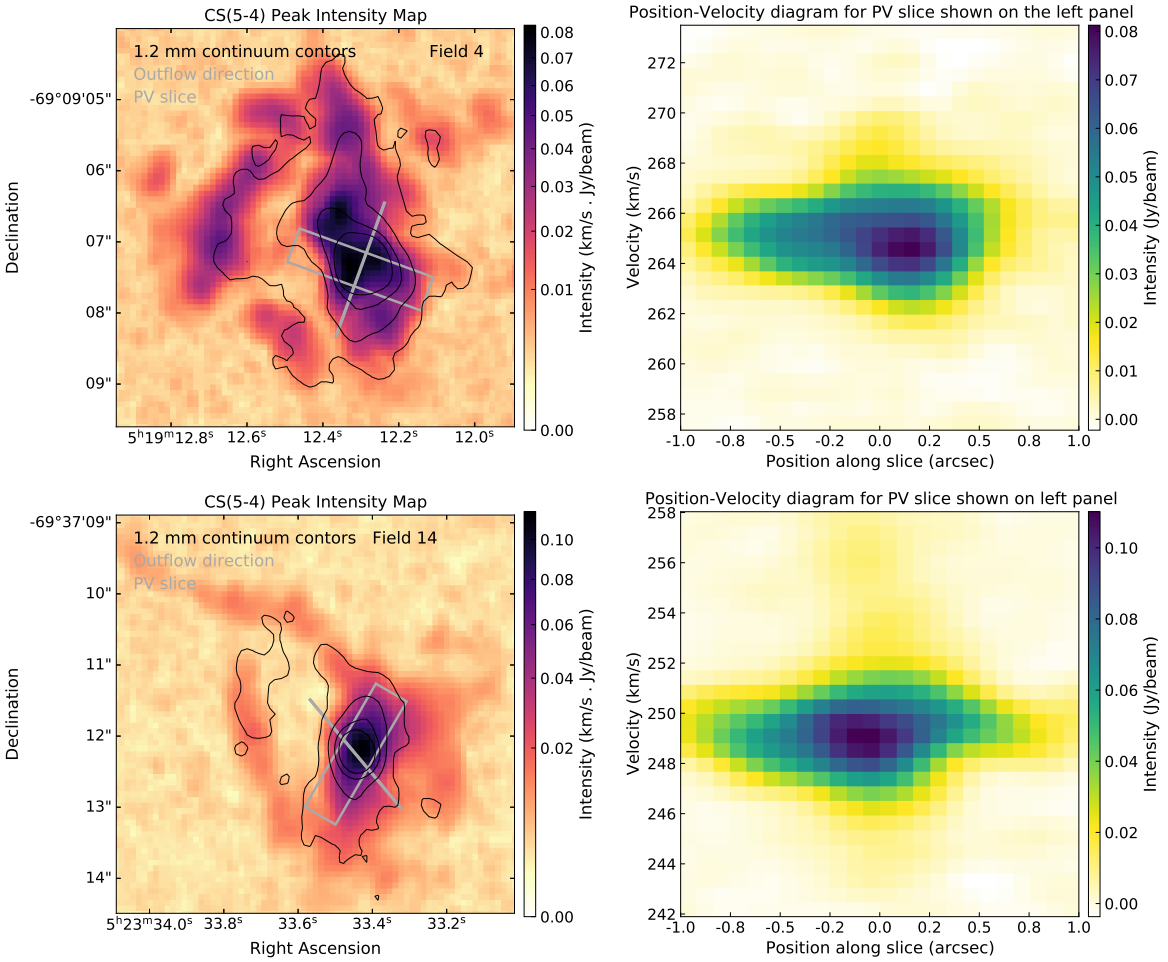


Figure 4.4: Rotation detected toward continuum cores 4A (top panel) and 14A (bottom panel) in a direction approximately perpendicular to the outflow direction. The left panel in each row shows the CS peak intensity map overlaid with continuum contours at 5, 15, 30, and 45 $\sigma_{\rm rms}$, along with the outflow direction and a position-velocity (PV) slice. The right panel displays the PV diagram along the PV slice depicted in the left panel.

radiation ionizes the surrounding material and exerts radiation pressure on the ambient dust and gas, leading to the formation and expansion of an HII region.

HII regions evolve through different stages, starting as hyper-compact (radii of 0.01-0.05 pc) transitioning to ultra-compact (radii of $\sim$ 0.1 pc) and eventually becoming compact HII regions (radii of $\sim$ 0.5 parsecs). These regions are characterized by a high density of free electrons, whose thermal interactions generate continuum emission at radio wavelengths. This free-free emission, detectable at centimeter wavelengths, serves as a prominent tracer of evolved young stars and provides valuable insights into the properties of HII regions and the effects of radiative feedback on the surrounding gas.

To identify HII regions in our sample, we complemented our ALMA data with an ATCA observation conducted on April 10th and 19th 2022. These observations

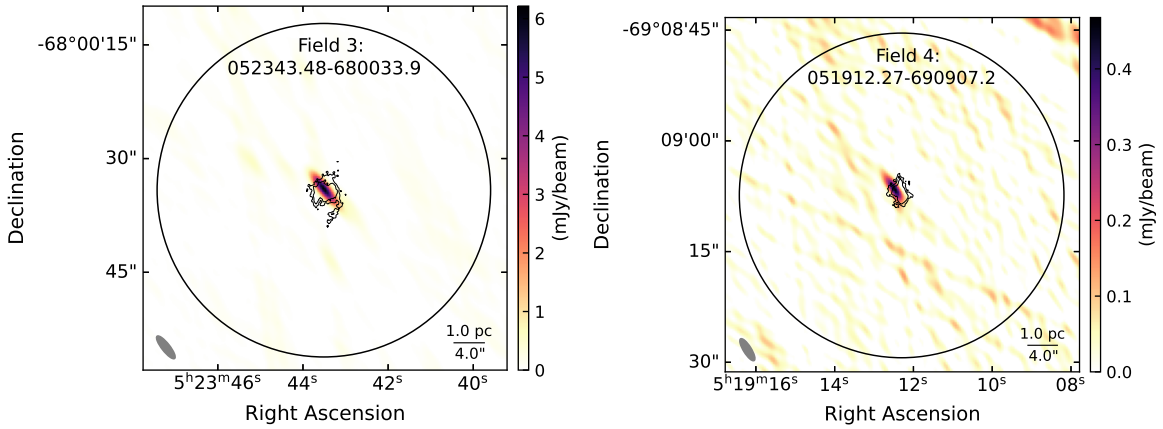


Figure 4.5: ATCA 4 cm maps, tracing the free-free continuum emission for Fields 3 and 4. ALMA 1.2 mm continuum contours are overlaid at 4, 8, 12 times the $\sigma_{\rm rms}$.

used the Compact Array Broadband Backend (CABB; Wilson et al. 2011) correlators, covering two bands centered at 6.5 and 22GHz with a total bandwidth of 2 GHz per band. The 6km and 1.5km array configurations were used for the 6.5 GHz and 22 GHz bands, respectively, to achieve comparable spatial resolutions. The resulting synthesized beams were $3.6'' \times 1.0''$ at 6.5 GHz and $0.9'' \times 0.8''$ at 22 GHz. Each field was observed for 9 minutes in the 6.5 GHz band and 18 minutes in the 22 GHz band. Data reduction, including the calibration and imaging the visibility files were performed using the MIRIAD software package (Sault et al., 1995).

In this section, we focus on the radio continuum sources detected in the 6.5GHz band. Imaging of the 22GHz band requires further refinement. Figures 4.5 and E.1 to E.1 show ATCA 4cm continuum emission overlaid with ALMA 1.2mm continuum contours. We report the detection of HII regions in 13 out of 20 fields. A catalog of these HII regions, including their physical properties, is provided in Table 4.2.

Following Sánchez-Monge et al. (2013a), we calculate the physical parameters of the radio continuum sources, assuming they trace optically thin HII regions. Table 4.2 provides a detailed summary of these parameters, including the name of the LMC field, the integrated flux density of the sources, and the effective radius ($R_{\rm eff}$), which is determined by approximating the area of each source as a circle with an area of $\pi R_{\rm eff}^2$. The number of ionizing photons ($N_{\rm i}$) emitted per second is derived for each region, along with the spectral type of a zero-age main sequence (ZAMS) star that would produce the measured $N_{\rm i}$, based on the calibration by Panagia (1973). Additional parameters include the emission measure (EM), representing the column density of ionized gas, the average electron density ($n_{\rm e}$) within the HII region, and the mass of the ionized gas ($M_{\rm i}$).

This analysis offers crucial insights into the physical characteristics of HII regions and highlights the role of radiative feedback in shaping the surrounding interstellar

Table 4.2: Physical properties of the HII regions derived from ATCA 4 cm maps.

Field Number	Flux density Jy	$R_{\rm eff}$ ($''$)	$N_{\rm i}$ (1/s)	Spectral type	EM ($\rm cm^{-6}$ pc)	$n_{\rm e}$ ($\rm cm^{-3}$)	$M_{\rm i}$ ($\rm M_\odot$)
3	7.60×10^{-3}	3.32	1.34×10^{48}	O8.5 – O9	4.47×10^{5}	7.46×10^{2}	5.02
4	4.17×10^{-4}	1.92	7.36×10^{46}	B0 – B0.5	7.34×10^{4}	3.97×10^{2}	0.52
5	1.56×10^{-3}	2.05	2.76×10^{47}	O9.5 – B0	2.41×10^{5}	6.96×10^{2}	1.10
7	9.30×10^{-4}	2.59	1.64×10^{47}	B0 – B0.5	8.99×10^{4}	3.78×10^{2}	1.21
8	3.18×10^{-4}	2.41	5.61×10^{46}	B0 – B0.5	3.55×10^{4}	2.47×10^{2}	0.63
12	6.06×10^{-4}	3.10	1.07×10^{47}	B0 – B0.5	4.09×10^{4}	2.33×10^{2}	1.28
13	1.57×10^{-3}	3.14	2.76×10^{47}	O9.5 – B0	1.03×10^{5}	3.68×10^{2}	2.10
15	3.72×10^{-4}	2.89	6.57×10^{46}	B0 – B0.5	2.89×10^{4}	2.03×10^{2}	0.90
15-SE	4.35×10^{-4}	2.81	7.68×10^{46}	B0 – B0.5	3.58×10^{4}	2.29×10^{2}	0.94
16	7.14×10^{-4}	2.69	1.26×10^{47}	B0 – B0.5	6.40×10^{4}	3.13×10^{2}	1.12
17	1.59×10^{-4}	1.50	2.80×10^{46}	B0.5 – B1	4.58×10^{4}	3.55×10^{2}	0.22
19	1.52×10^{-4}	1.69	2.68×10^{46}	B0.5 – B1	3.45×10^{4}	2.90×10^{2}	0.26
20	3.00×10^{-4}	2.51	5.29×10^{46}	B0 – B0.5	3.09×10^{4}	2.25×10^{2}	0.66

Notes. See Section 4.2 for detailed description of each parameter.

medium. An additional step involves estimating the spectral index of the free-free emission in these HII regions, which would enable us to quantify the contribution of free-free emission at 1.2 mm through extrapolation. Such an estimate would refine the mass calculations for the ALMA continuum cores by accounting for and excluding free-free emission contamination. However, due to the resolution mismatch between the ALMA and ATCA observations, this task remains an objective for future work.

4.3 Morphology and feedback deriving the star formation evolution

In this section, I provide an overview of the findings presented in this chapter. Filaments have been identified in 18 ALMA fields, outflows in three fields, and HII regions in 13 fields. I also explore the qualitative correlations among these detections. To present a clearer picture, the results are summarized in Table 4.3. Beyond the detection of filaments, outflows, and HII regions, I have assigned descriptive tags to each filamentary structure to characterize the morphology of dense gas structures. For this purpose, I classified the filaments into four distinct categories: "spaghetti", representing highly complex and intertwined filamentary network; "HFS" (hub-filament systems), where filaments converge at a central hub; "elongated" filaments, referring to long, nearly linear structures; and "tiny-single" filaments, denoting fields with a single, very small filamentary structure.

As discussed earlier, infall and accretion, outflows, and HII regions characterize star-forming regions and can be arranged into an evolutionary sequence. From Table 4.3,

Table 4.3: Summary of internal gas morphology and feedback in the 20 star-forming regions.

Field Number	Filaments Detection	Filaments Structure	Outflow Detection	HII region Detection
1	✓	HFS		
2	✓	spaghetti-structure		
3	✓	HFS		✓
4	✓	HFS	✓	✓
5	✓	tiny-single		✓
6	✓	HFS	✓	
7	✓	elongated		✓
8	✓	tiny-single		✓
9				
10	✓	HFS		
11	✓	HFS		
12	✓	elongated		✓
13	✓	elongated		✓
14	✓	HFS	✓	
15	✓	elongated		✓
16	✓	elongated		✓
17	✓	elongated		✓
18	✓	HFS		
19	✓	elongated		✓
20				✓

Notes. See Section 4.2 for details description of each parameter.

it is evident that the only spaghetti dense gas structure appears in a field without any detection of outflows or HII regions, suggesting that this field represents an earlier stage of evolution. Among the 20 fields analyzed, eight exhibit HFS. Of these, two are associated with outflows but lack HII regions, one is associated with both outflows and HII regions, and six are associated only with HII regions. Seven fields contain elongated filaments, all of which are associated with HII regions. Additionally, two fields contain tiny-single filaments, both of which are located in regions where HII regions are detected. Notably, two fields lack filamentary structures entirely; one of these fields shows no detection of outflows or HII regions, while the other is associated with an HII region.

Based on the observations from the 20 target fields explored in this study, I propose an evolutionary scenario for star formation in the LMC. Star formation appears to be closely correlated with the emergence and evolution of filaments. Initially, filamentary structures emerge as a highly complex network of mass transfer channels. As star formation progresses, these structures simplify in morphology, transitioning from intricate networks to more linear, elongated, and eventually single filaments. As outflows

and HII regions develop, the filamentary structures gradually disperse, positioning the star-forming regions in increasingly simplified gas morphology. Figure 4.6 visualizes the proposed evolutionary sequence of star formation, indicating the number of fields associated with each stage.

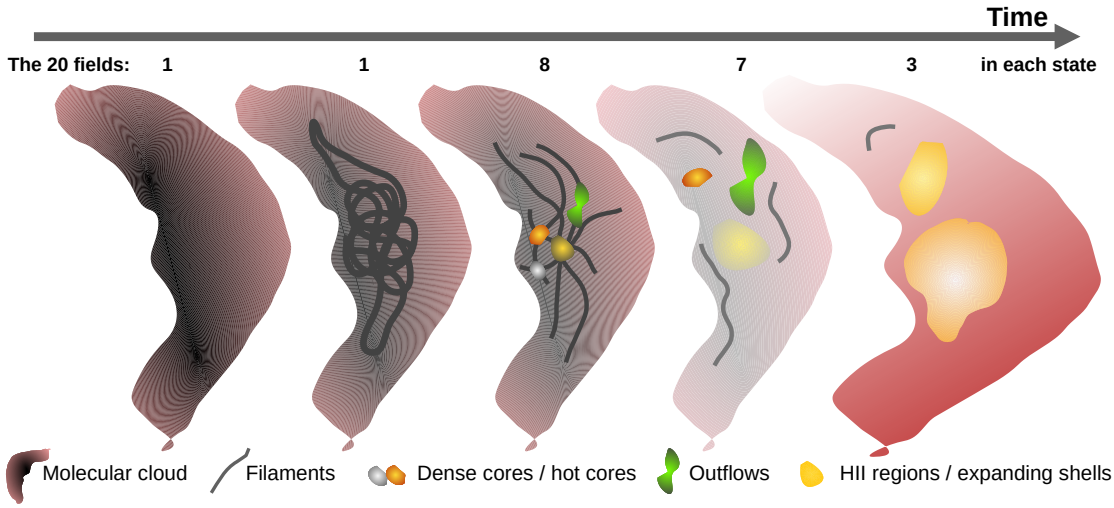


Figure 4.6: Proposed evolutionary sequence of star formation in the LMC. Based on the study of gas morphology and the detection of filaments, outflows, and HII regions in the 20 target fields, I propose an evolutionary sequence for star-forming regions in the LMC. Arrow indicates the direction of evolution. The number of fields at each stage is shown, and a legend explains the symbols used for different object types. For a detailed explanation, see Section 4.3.

Chapter 5

A multi-wavelength view

The dynamics of interstellar gas and dust are not confined only to the densest regions of molecular clouds where stars form. Rather, global dynamics play a crucial role in shaping the star formation process. This chapter presents a multi-wavelength perspective on the environments of the 20 target fields. To provide a comprehensive understanding, five figures are presented for each field (see Fig. 5.1 for Field 1, and Appendix F for other fields), each illustrating different aspects of the star formation. Section 5.1 outlines the spatial extent and physical processes traced by each figure. In Section 5.2, I describe the local conditions of our target fields, addressing each one individually. The chapter concludes in Section 5.3 with an effort to classify the fields based on the morphology of ionized, atomic, and molecular gas, along with the dust emission, to gain insights into the different phases of star formation and their interrelationships.

5.1 Multi-wavelength tracers of star formation

This section provides a detailed perspective on the multi-wavelength tracers of star formation in the target fields, spanning spatial scales from giant molecular clouds (GMCs), typically $\sim$ 100 pc in size, to smaller molecular clouds and clumps around $\sim$ 10 pc. In the following we take Fig. 5.1 as an example to describe the content shown in each of the five panels. The same description of the panels applies to the Figures shown in Appendix F for the other LMC fields. The top-most panel of the figure illustrates the larger-scale structure of the clouds hosting our target fields (denoted by small white circle), encompassing regions of $\sim$ 150 pc, approximately 15 times the size of our ALMA field of view (indicated by the larger white circle). These figures are color composites combining Herschel 350 μm (red, Meixner et al., 2013), Spitzer 8 μm (green, Meixner et al., 2006) and Hα (blue, Smith et al., 2000) emission maps.

The Herschel 350 μm primarily traces thermal emission from cold dust grains in the ISM, with temperatures typically ranging from 10 to 40 K. It is particularly effective in identifying dense regions of gas and dust that are potential sites for star formation.

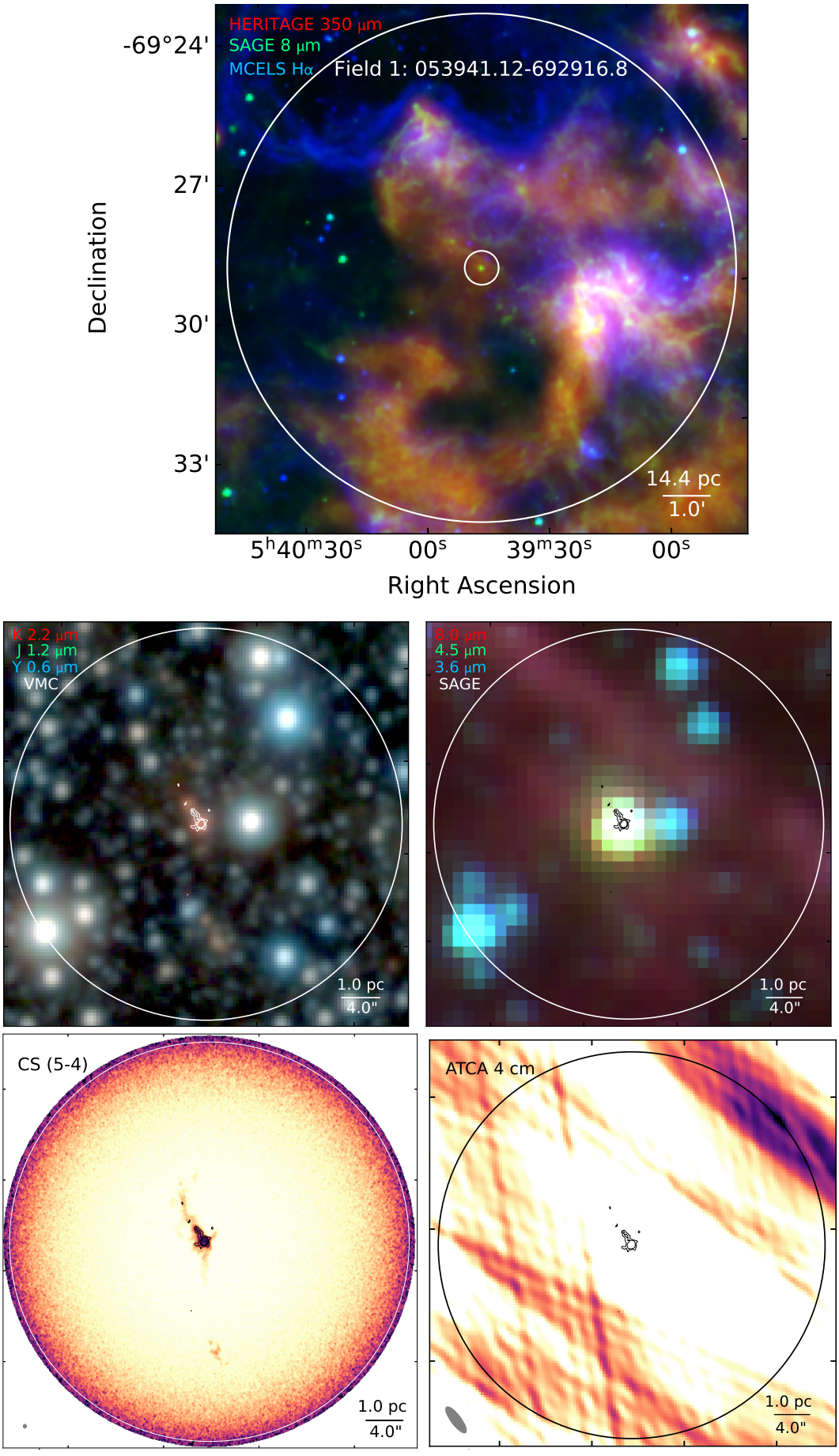


Figure 5.1: Multi-wavelength view of Field 1. For caption details see Appendix F.

The Spitzer 8 μm band captures the emission from PAHs, which are excited by UV radiation from young, massive stars. This emission highlights photodissociation regions (PDRs) at the edges of molecular clouds, where UV radiation interacts with gas and dust. It also traces warm dust and outlines the morphology of HII regions and PDRs. Hα refers to light emitted at 656.3 nm when electrons in hydrogen atoms transition from the n=3 to n=2 energy level. It is a signature of ionized gas in star-forming regions, where young stars actively ionize their surroundings, creating HII regions. Hα emission also provides insights into feedback processes, as stellar radiation heats and ionizes the surrounding medium.

The second image (left panel in the middle row) presents color composites of near-infrared Y (0.6 μm), J (1.2 μm) and K (2.2 μm) bands, provided by the PI (Maria-Rosa, Cioni) of the VISTA for Magellanic Clouds (VMC) survey[1]. The Y and J bands trace the stellar objects and ISM structure that is lightly obscured by dust. The K-band images can penetrate deeper into dusty regions, making them particularly effective for detecting sites of embedded active star formation. Additionally, the frequency coverage of the K-band filter includes emission lines from H_2 and Brγ[2]. H_2 emission at 2.2 μm is excited in highly shocked regions, while Brγ traces ionized gas. Together, these bands are instrumental in studying stellar populations, extinction, and star formation activity (Cioni et al., 2011). The extent of these images are 10 pc with a resolution of 0.12 pc ($\sim$ 0.5").

The third image (right panel in the middle row) combines Spitzer bands at 3.6, 4.5 and 8.0 μm. The 3.6 and 4.5 μm emission trace protostars, YSOs and evolved dusty stars, as these wavelengths are less affected by dust extinction. In these composite images, the extended green objects (EGOs) are often visible, characterized by excess emission at 4.5 μm. EGOs trace shocked regions, where H_2 and CO emission lines are excited by the interaction of outflows with the surrounding ISM. These images span the size of the ALMA field of view, with a resolution of $\sim$ 0.3 pc (1.2"). The massive YSOs selected for this study are bright in all composite wavelengths, and the ALMA field of view is predominantly occupied by these point sources.

The final two panels (bottom row) in the multi-wavelength view are single-wavelength images from CS emission and ATCA 4 cm band emission (see Chapter 4). We have seen in the previous chapter that CS traces the densest regions within star-forming clumps, highlighting the gas reservoirs feeding star formation. ATCA 4 cm emission reveals HII regions associated with protostellar cores, capturing the radiative feedback from young stars on their immediate surroundings. In all but the first panel, ALMA 1.2 mm continuum contours are overlaid to highlight the compact structures detected in the

[1]https://star.herts.ac.uk/ mcioni/vmc/

[2]A spectral emission line at 2.166 μm, produced when electrons in hydrogen atoms transition from the n=7 to n=4 energy level. It is a tracer of ionized gas, often associated with regions of active star formation and the presence of young, massive stars.

observations. These overlays are present in Figures 5.1 and F.1 to F.19, providing a detailed view of the physical conditions and processes in the target fields.

5.2 Morphology of the gas and dust in each field across scales

In this section, I briefly describe the main aspects of star formation in each of the 20 fields of the LMC studied in this thesis. I use the multi-wavelength figures of each field (see Fig. 5.1 and Appendix F) to describe the ambient gas and dust morphology of the different star-forming regions.

Field 1 053941.12-692916.8: This region is located in the central eastern part of the LMC, just south of the highly active star-forming region 30 Doradus (30-Dor). Our target field lies within an extended molecular cloud, approximately 50 pc in size, curved like a snake around the target object. The cold and warm dust, traced by red and green colors in the large-scale composite image, predominately occupies the ALMA field of view, while the ionized gas, depicted in blue, is mostly confined to the west and west-north. Notably, there are few point sources, suggesting that the cloud is in early stages of star formation.

The position of ALMA 1.2 continuum contours, tracing colder dust coincides with bright K-band emission in the VMC image. The 1.2 mm continuum emission is also well-correlated with dense CS gas. No ionized emission is detected at the location of the ALMA protostellar cores, further supporting the idea that this region may be in the early stages of star formation. Spitzer spectra from this source reveal the presence of CO_2 ices, indicating the presence of cold, iced dust. Our James Web Space Telescope (JWST) observations (PI: Sewi'lo; private communication) of this source have identified more complex molecular ices, enabling direct comparisons with the ALMA observations, as the resolution is comparable.

Field 2 045640.79-663230.5: Field 2 is located in the north-western part of the LMC, within an extended cloud of $\sim$ 40 pc in size, containing filamentary warm dust and prominent ionized gas. The target field is primarily positioned at the peak of the cold and warm dust emission, although no clear emission from ionized gas is present. Multiple point sources, particularly in the Hα emission, are visible. The inner part of the field, where the Spitzer composite image is brightest, is traced by an EGO extended to the western part of the region, extended K-band emission, ALMA 1.2 mm, and CS emission, but not ionized gas. This suggests that while there is external feedback in the immediate surroundings of the field, star formation within the field itself is still in its early stages.

Field 3 052343.48-680033.9: Located in the northern part of the LMC, Field 3 is characterized by cold and warm dust that shapes the hosting cloud, with emission elongated from the center to the west and continuing in two directions: north and

southwest. At least three active star-forming regions are located within 30 to 60 pc of our target field. However, our target field appears to be situated in a more quiescent region of the cloud. Despite this, there are strong indications of active star formation and internal feedback, as seen in the Hα emission in the large-scale map at the position of the target field. Additionally, the combined extended K- and J-band emission, and ionized gas detected in the ATCA 4 cm emission map further support the presence of ongoing star formation processes.

Field 4 051912.27-690907.3: Field 4 is situated at the intersection of ionized gas and a cloud containing both cold and warm dust, with the warm dust exhibiting a more extended distribution. Overall, the morphology looks like a broken shell. The ALMA continuum cores are notably bright in the near-IR VMC image, suggesting the presence of evolved stellar objects. This is further confirmed by the presence of EGOs in the Spitzer image and the detection of an HII region in the ATCA map.

Field 5 045358.57-691106.7: This field, located in the south-western part of the LMC, is situated at the center of an active star-forming cloud. The cloud is characterized by regions of dust and ionized gas, indicative of the formation of massive stars emitting UV radiation and illuminating the surrounding material. Spanning approximately 50 pc, the cloud is nearly centered on the target field, which lies in close proximity (within $\sim$ 5 pc) to bright cold dust, warm dust and Hα clumps indicating active star formation.

The northern protostellar core within the ALMA field of view aligns with a bright 2.2 μm peak and an HII region, suggesting the presence of internal feedback processes at smaller scales within the star-forming cores. The spitzer spectra of the central YSO in this field reveal bright PHA emission along with a subtle CO_2 ice absorption feature (see Chapter 1). Recent JWST observations of this region, resolve the source into two cores at different evolutionary stages; one containing significant ice deposit and the other dominated by warmer dust (Nayak et al., 2024).

Field 6 050953.89-685336.7: Situated at the heart of the active star-forming region N105, this field lies within the central Bar of the LMC. The large-scale ISM is predominantly characterized by warm dust and ionized gas, both exhibiting extended emission with prominent filamentary structures. The filament spine detected within the ALMA field of view appears to be a continuation of large-scale filaments, channeling material toward the hub of star formation. This filament, or lane of star-forming material, is visible only in the K-band of the near-IR regime. It is surrounded by active star formation to the northwest, while the southern region is highly extincted, obscuring it in near-infrared images.

Field 7 052423.39-693904.7: Located in the central regions of the LMC-Bar, this field is part of an extended cloud of warm dust, with multiple point source objects suggesting a relatively evolved parent cloud. The cold dust and ionized gas appear to

be clumpy and patchy, with the peak cold dust emission centered on the ALMA field and extending $\sim$ 10 pc to the west. An elongated line of emission is in 2.2 μm, warm dust emission and dense gas traced by CS from the southeastern side of the ALMA field to the northwest, with an HII region detected approximately 2 pc away from the 1.2 mm continuum emission.

Field 8 044854.41-690948.3: Field 8 is located in the southwestern region of the LMC. The parent cloud is characterized by extended warm dust, associated with cold, clumpy emission at its center. Two nearby point sources exhibit bright dust emission, with a prominent bright region to the southeast displaying Hα emission and a bubble-shaped structure. However, these features are approximately 40 pc away, leaving the target cloud largely unaffected by large-scale radiative feedback. Despite this, ALMA observations resolve a compact core at the position of a YSO, which is bright in the K-band and associated with a compact HII region.

Field 9 054248.90-694446.3: The molecular cloud exhibits a complex morphology centered around a spherical Hα emission region, which appears to fill the interior of a bubble-like structure. This bubble is surrounded by both warm and cold dust emission. Notably, the bubble is open on one side, and on the other side there are elongated protrusions extending outward. The target region of interest is located at the base of one of these extensions, marking the transition between the bubble-like structure and the protruding features.

Field 10 051916.87-693757.5: In the central region of the LMC-Bar, Field 10 is located at the intersection of ionized and molecular gas, a common configuration that facilitates star formation through the compression of material at the edge of an expanding ionized gas bubble. The parent cloud, traced by cold dust, forms an elongated arc-shaped structure approximately $\sim$ 10 pc wide and $\sim$ 70 pc long. In the large-scale image, the ALMA field consists of cold and warm dust to the north and a mixture of dust and ionized gas to the south. At smaller scales, an ATCA-identified HII region is located to the northeast of the central dense gas and dust structure.

Field 11 045100.16-691934.4: Located in the southwestern region of the LMC, Field 11 features a dispersed cloud with two main filaments, illuminated by 8μm emission, one of which also exhibits elongated cold dust emission. No significant Hα emission is detected in this cloud. The elongation of the ALMA 1.2 mm emission and the VMC image, extending from the west to the center and further branching toward the east-northeast and east-southeast of the ALMA field, traces filaments that connect large to small scales. No bright emission is observed in the ATCA 4 cm map.

Field 12 050355.87-672045.1: Field 12 situated in the northwestern part of the LMC, appears to be part of a cluster within a parent cloud approximately $\sim$ 30 pc in size. The parent cloud is relatively isolated, with no significant neighboring structures within a radius of at least $\sim$ 30 pc. The target ALMA field also shows evidence of

clustering, indicated by the detection of multiple compact cores and bright ATCA 4 cm emission.

Field 13 053952.11-710930.7: Located in the southern part of the LMC Molecular Ridge, which extends from the 30-Dor region to the south, this field lies within an extended cloud approximately 50pc in size. The cloud is predominantly composed of cold dust, with Hα emission detected toward its southeastern region. Warm dust filaments connect to cold dust clumps, and several compact 8μm-bright sources are embedded within the main cloud, indicating a clustered environment. The parent cloud hosts a cluster, but also the YSO observed with ALMA is fragmented into multiple cores, forming a cluster on scales of 0.5pc. Southeast of the ALMA cluster, located at the center of the field, a bright HII region is visible. This HII region is prominent in VMC and Spitzer images and is accompanied by a one-sided extended EGO.

Field 14 052333.40-693712.2: Located in the center of the LMC Bar, this field features a clump of material that may be connected to an extended region in the southeast. The main clump lies near an Hα emission region approximately 10 pc in size and contains a single compact source visible in 8 μm emission. Similarly, CS observations reveal a single core in ALMA fields. A bright EGO is also present, while the region exhibits minimal brightness at 2.2 μm.

Field 15 051344.99-693510.6: Field 15, located in the LMC Bar region, lies within a cold, clumpy dust structure approximately 15 pc in size. This structure hosts three 8 μm point sources, with the target source positioned at its center. Beyond this cold dust clump, extended 8 μm emission illuminates a triangular-shaped cloud in the southern and southwestern regions. The warm dust displays filamentary structures, which are more prominently accompanied by cold, embedded dust filaments.

Two of the three 8 μm point sources are within the ALMA field of view and are associated with 1.2 mm continuum peaks. Both sources are bright at 2.2μm. The source to the east exhibits clear EGO feature, while the central source is fragmented into two cores: one core, bright in Spitzer images and ATCA 4 cm maps, and another core to the northeast, which is associated with a faint EGO. The third 8 μm point source, located at the edge and outside the ALMA field of view, is notably bright in the VMC K-band and Spitzer images. This source also harbors an HII region.

Field 16 054629.32-693514.2: This region, located east of the 30-Dor region, lies within a cloud predominantly covered by cold dust in the southwest. The cold dust converges through filaments toward the center, where a bright filament of warm dust becomes visible. To the north of the ALMA field, near the 8 μm filament, faint Hα emission is observed in a bubble-shaped structure. The ALMA continuum emission appears resolved out at scales of 0.1 pc, indicating the presence of extended emission. In the Spitzer image, a bright, extended EGO (Extended Green Object) spanning 3 pc is visible. This EGO extends in the same direction as a detected HII region.

Field 17 054826.21-700850.2: Located southeast of the 30-Dor region, Field 17 lies within a cloud composed of cold and warm dust, illuminated from the north by strong Hα emission. However, the Hα emission is approximately 30 pc away, likely having minimal impact on the target field. Within the ALMA field, an arc-shaped extension of warm dust embedded within the cold dust is evident. On one side of this arc, a bright YSO is detected, showing a slight EGO (Extended Green Object) feature to the north. This YSO is associated with ALMA continuum emission, CS dense gas, and an HII region located near the EGO.

Field 18 045622.61-663656.9: Located in the northwestern region of the LMC, Field 18 resides in a cloud of cold dust with a single prominent warm dust point source. The immediate vicinity of this field is relatively sparse, with multiple dispersed clumpy clouds of cold dust visible to the south. Filaments of warm dust extend from the northern regions toward the center, where the field is situated. The ALMA continuum emission is associated with the central YSO and slight to the north. Additionally, an extension of warm dust, is evident in the Spitzer RGB composite image. This feature can also be traced in the 2.2 μm band, extending from the southwest to the center of the field.

Field 19 045406.43-664601.4: Located in the proximity of Field 18 in the northwestern part of the LMC, Field 19 exhibits a large-scale image with no significant emission in any of the tracers, except for four bright warm dust point sources and multiple faint Hα point sources. The only cold dust emission is observed within the ALMA field. The ALMA continuum emission reveals fragmentation along the extension of the dust emission from southeast to northwest, with an HII region visible at the center.

Field 20 052210.08-673459.6: This region, located in the northern part of the LMC, is even more sparsely populated than Field 19. The only faint cold dust emission, along with point-like 8μm emission, is observed within the ALMA field. The Spitzer YSO is located at the end of a spiral feature that extends from the north to the center, visible in both the 2.2 and 8.0 μm bands. A compact core is visible in the ALMA image, which coincides with an ATCA detection.

5.3 Classifying the target fields

Spitzer bands. To classify these fields based on feedback mechanisms, we use large-scale Hα emission as a tracer of external feedback and the presence of extended green objects (EGOs), outflows, and HII regions as indicators of internal feedback. Based on the strength and nature of both large- and small-scale feedback exerted on them, the fields are categorized as follows (see Table 5.1):

External feedback only: Fields 1, 2, 9, 10

Internal feedback only: Fields 3, 7, 8, 12, 13, 15, 16, 17, 19, 20

Both external and internal feedback: Fields 4, 5, 6, 14, 16
No feedback detected: Fields 11, 18
This classification highlights the diversity of feedback mechanisms influencing our survey fields. While all fields are relatively evolved and actively forming stars, they represent a broad spectrum of environments—from isolated regions and quiescent clouds to highly active, star-forming parent clouds. This range provides a unique opportunity to investigate how feedback processes shape star formation under different environmental conditions.

5.4 Are we witnessing an evolutionary sequence?

In this section, I integrate the multi-wavelength results presented in this chapter with the findings from earlier chapters to construct a cohesive view of star formation across the target fields. This analysis spans scales from 100 pc to 1 pc, combining insights into the physical and chemical properties of protostellar cores, the morphology of dense gas structures, feedback processes, and the larger surrounding environment. By correlating these multi-scale observations, I aim to present a comprehensive picture of star formation and its evolutionary stages in these regions. A detailed summary of key characteristics and evolutionary indicators for the observed star-forming environments is provided in (see Table 5.1).

Table 5.1: Summary of internal and external gas and dust morphology and feedback in the 20 star-forming regions.

Field Number	Number of Fragments	Hot core Detection	Filaments Detection	Filaments Structure	Outflow Detection	HII region Detection	Internal Classification	EGO Detection	External Feedback	Evolutionary Stage
1	1		✓	HFS			I		✓	Out-In star forming
2	4		✓	spaghetti-structure			I	✓?	✓	Out-In star forming
3	4	✓?	✓	HFS		✓	II		✓?	Out-In star forming
4	1	✓	✓	HFS	✓	✓	II	✓	✓	Out-In star forming
5	2		✓	tiny-single		✓	IV		✓	Active Cluster
6	6	✓	✓	HFS	✓		II		✓	Out-In star forming
7	2		✓	elongated		✓	III			In-Out star forming
8	3		✓	tiny-single		✓	IV			In-Out star forming
9	1						Pre-I		✓	Out-In star forming
10	4		✓	HFS			I		✓	Out-In star forming
11	4		✓	HFS			I			Out-In star forming
12	4		✓	elongated		✓	III			In-Out star forming
13	9		✓	elongated		✓	III			In-Out star forming
14	1	✓	✓	HFS	✓		II	✓	✓	Out-In star forming
15	3		✓	elongated		✓	III	✓		In-Out star forming
16	2		✓	elongated		✓	III			In-Out star forming
17	2		✓	elongated		✓	III			In-Out star forming
18	4		✓	HFS			I			Out-In star forming
19	4		✓	elongated		✓	III			In-Out star forming
20	1					✓	Post-IV			In-Out star forming

Notes. See Section 5.4 for details description of each parameter.

Building on the star formation scenario proposed in Section 4.3, I categorize the fields into four evolutionary stages:
Stage I: Presence of complex filamentary structures without internal feedback.
Stage II: Complex filamentary structures with internal feedback.
Stage III: Simpler, elongated filaments with internal feedback.
Stage IV: Single, compact dense gas structures with internal feedback.
Additionally, I classify the only field without detected filaments and no internal feedback as pre-I and the one with no filaments but exhibiting internal feedback as post-IV. Based on this classification, 10 fields are in earlier stages, pre-I, I, or II, while the remaining 10 are in later stages, III, IV, or post-IV.

In this section, I revise the classification from the previous chapter by incorporating the impact of the ambient ISM on the target clouds. A striking finding is that 80% of the fields in the early stages (8 out of 10) are subject to strong external radiative feedback, whereas 90% of the fields in later stages (9 out of 10) lack external feedback. The two early-stage fields not exposed to external feedback show strong evidence of mass transfer from large-scale filaments to smaller scales. I classify these fields in earlier stages as "Out-In star-forming", emphasizing that star formation in these regions may have been externally induced.

The only later-stage field exhibiting both internal and external feedback resides in an active star-forming cluster, which I designate as "Active Cluster". In contrast, the remaining early-stage fields are classified as "In-Out star-forming" to highlight their role in dispersing their parent clouds. This process likely facilitates the next generation of star formation by compressing surrounding material. Figure 5.2 illustrates the proposed evolutionary sequence of star formation in relation to the surrounding gas and dust morphology.

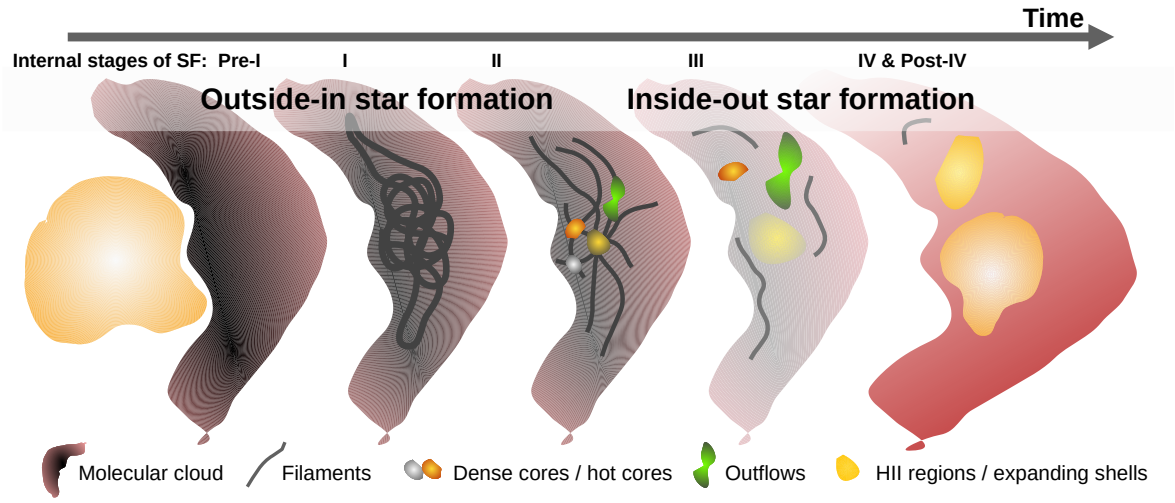


Figure 5.2: Proposed evolutionary sequence of star formation in the LMC. Based on the study of gas morphology and the detection of filaments, outflows, and HII regions within the 20 target fields, as well as the morphology of gas and dust on larger scales surrounding these regions, I expand the evolutionary sequence presented in Figure 4.6 for star-forming regions in the LMC. Arrow indicates the direction of evolution. Internal stages of star formation (as defined in the text and Table 5.1) are shown. Two categories of star formation, based on the nature of the large-scale ambient gas and dust, are shown to highlight a correlation between early-stage star formation and externally active environments, and later stages with more quiescent surroundings. A legend explains the symbols used for different object types. For a detailed explanation, see Section 5.4.

Chapter 6

Conclusion and outlook

Star formation, particularly high-mass star formation ($M > 8M_{\odot}$), is a cornerstone of galactic evolution, driving energy input, chemical enrichment, and the lifecycle of galaxies. This thesis represents the first systematic survey of 20 massive star-forming regions in the Large Magellanic Cloud (LMC), a galaxy with unique environmental conditions. The LMC's lower metallicity, enhanced UV radiation, reduced cosmic ionization, and large-scale dynamical interactions provide an excellent laboratory for studying the interplay of fragmentation, chemistry, and feedback mechanisms in star formation. Combining high-resolution ALMA observations (~ 0.1 pc) with data from ATCA, Herschel, Spitzer, and VMC, this work provides new insights into the processes that govern star formation in extreme environments.

- **Compact continuum cores and fragmentation** ALMA 1.2mm continuum observations revealed 65 compact continuum cores, with an average separation of ~ 0.5 pc. Fragmentation was observed in 80% of the 20 fields, and the data support non-thermal Jeans fragmentation as the dominant mechanism across scales from 10 pc to 0.1 pc. Despite the LMC's lower metallicity, the core formation efficiency (CFE, $\sim 5\%$) and the core mass function (CMF) are remarkably similar to those in Milky Way regions. However, LMC cores exhibit a tendency toward higher masses, that could be driven by environmental factors such as metallicity and feedback, although further observations reaching higher mass sensitivities are necessary to confirm this.

- **Chemical richness and hot Cores** Spectral analysis of the cores revealed multiple molecular line transitions, including CH_3OH, SO_2, CS, and $H^{13}CN$. Four hot cores and one candidate were identified, marking an addition to the known hot cores in the LMC. This new detection brings the total number of identified hot cores in the LMC to seven. Notably, there is a strong correlation between chemical richness and location within the LMC. Six of the seven hot cores are

concentrated in the stellar Bar region, where metallicity is higher, while the lone hot core outside the Bar lacks complex organic molecules (COMs). This pattern suggests that metallicity gradients within the LMC play a crucial role in driving chemical complexity and hot core formation.

- **Filamentary structures and star formation evolution** Molecular line emissions revealed complex filamentary networks in all but two regions, accompanied by evidence of outflows in three fields. Additionally, HII regions were detected in 13 regions using ATCA centimeter-wavelength emission maps. Combining ALMA data with ATCA observations, I propose an evolutionary sequence for star formation: it begins within complex filamentary structures that channel mass into star-forming cores. Over time, these structures simplify, evolving from intricate networks to single, elongated filaments. As star formation progresses, outflows and HII regions disperse the surrounding gas, leaving behind isolated star-forming regions with simplified morphologies.

- **Multi-wavelength and multi-scale perspective** The integration of multi-wavelength data across parsec to sub-parsec scales strongly supports the proposed evolutionary sequence. A clear trend emerges, with star formation in the earlier stages likely induced by external feedback, while in the later stages, the dispersal of parent clouds dominates. Based on this classification, the fields are evenly divided: half exhibit In-Out star formation, where star-forming regions disperse their surrounding material, potentially triggering new generations of stars, while the other half display Out-In star formation, where external feedback channels material inward to drive star formation.

This thesis provides a robust foundation for future studies of star formation in low-metallicity environments, yet many questions remain unanswered. Key directions for future research include:

- **Large-scale to small-scale dynamics** Understanding the transition from large-scale molecular clouds to small-scale star-forming cores is crucial for unraveling the mechanisms driving star formation. The LMC offers an exceptional testbed for this investigation, with single-dish surveys, such as APEX ($\sim$ 5 pc resolution), providing insights into large-scale structures, and interferometric ALMA archival CO data enabling the study of small-scale dynamics. Future research should focus on the mass transfer processes across these scales, shedding light on how environmental factors influence star formation from the cloud to core scale.

- **Exploration of other low metallicity regions** Expanding this research to other low-metallicity environments, such as the SMC ($\sim$ 0.2 Z$\odot$) and the outer Galaxy, will provide valuable comparisons. Additionally, the low-metallicity regions of the Magellanic Bridge and Leading Arm ($\sim$ 0.1 Z$\odot$) present an opportunity to study star formation in even harsher conditions.

- **Advancing chemical studies with JWST** The advent of the JWST opened new frontiers for studying ice chemistry in star-forming regions. Its near- and mid-IR Integral Field Unit (IFU) spectroscopy, with unprecedented spectral and spatial resolution, complements ALMA observations. Future work should integrate gas and solid-phase molecular abundances with advanced chemical models, while accounting for local ISM conditions to minimize biases.

- **Star Formation at Disk Scales** The findings of this thesis provide a strong basis for extending the study of star formation in the LMC to disk scales. Contradictory results regarding the impact of metallicity on accretion timescales from infrared observations of stellar clusters confirms the need for further investigation at these scales.

In summary, this thesis advances our understanding of high-mass star formation in the LMC, highlighting the complex interplay of environmental conditions and star formation processes. The LMC's unique conditions provide invaluable insights into the role of metallicity and UV radiation in shaping star formation, offering a framework for exploring other low-metallicity systems. With the continued evolution of observational capabilities, particularly ALMA and JWST, the future of star formation research promises to unravel the complexities of stellar birth across diverse galactic environments.

Appendix A

Continuum images and their analysis

A.1 Continuum Maps

Figures A.1 to A.18 present the ALMA Band 6 continuum maps observed across the LMC. Each figure shows both the full field of view and a zoomed-in view of the regions with bright emission. In the zoomed-in images, continuum contours are overlaid, with additional contours indicating the positions of the detected cores.

A.2 Physical parameters of 1.2 mm cores

In this appendix, two tables present the estimated parameters for the 65 ALMA 1.2 mm continuum cores.

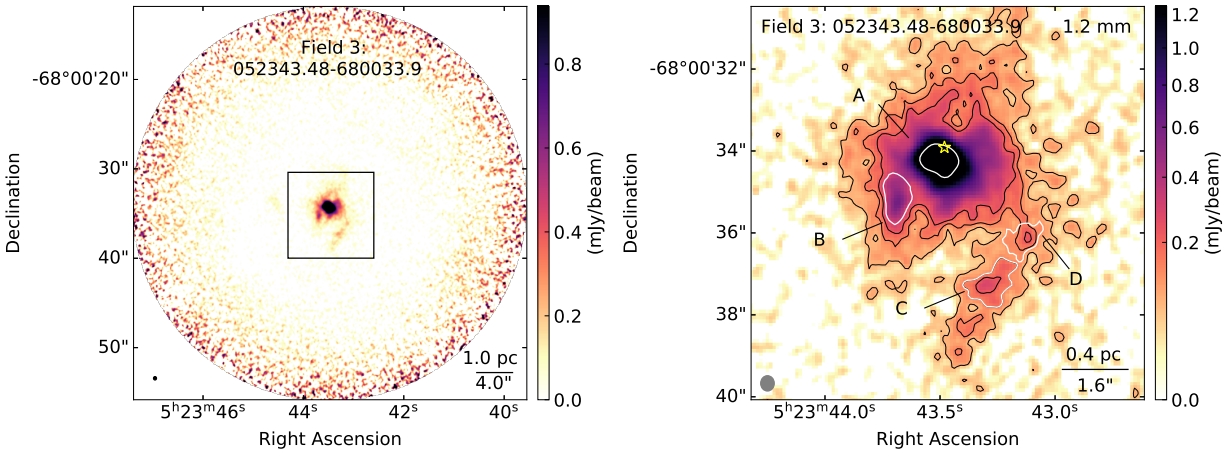


Figure A.1: The 1.2 mm pb-corrected continuum maps for Field 3: *left* an overview to the field, *right* a detailed view to the region inside the black rectangle(s) on the left side panel. The contours show the 3, 6, and 9 times the $\sigma_{\rm rms}$. The identified cores are highlighted with white contours at 50% of the peak emission. The position of the YSOs is marked with a yellow star. The position of H_2O, and OH and H_2O masers are also marked with a pentagon and triangle, respectively, where there is a detection (only in Fields 6 and 17). The synthesized beam of the images and a scale bar are shown in the bottom-left and -right corners of each panel.

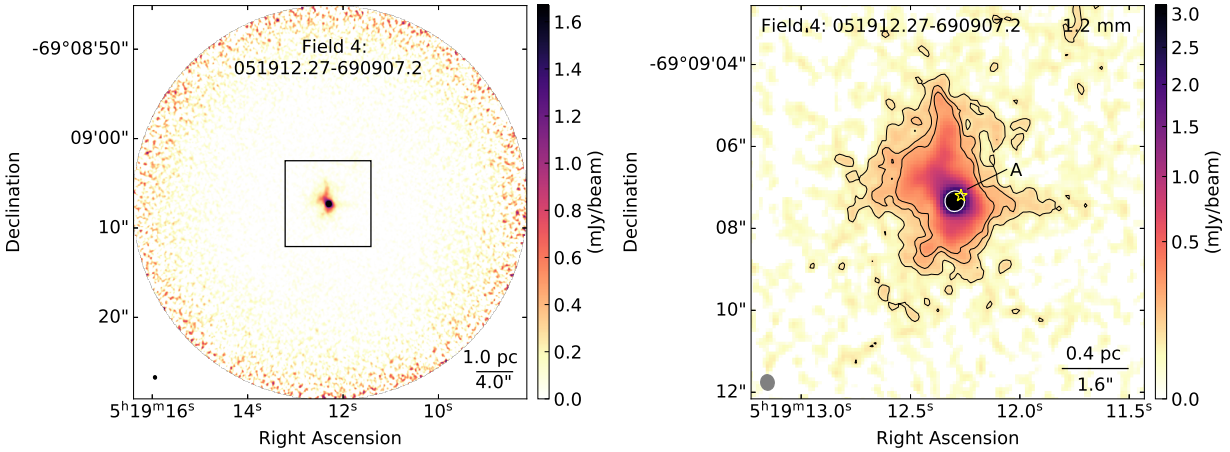


Figure A.2: Same as Fig. A.1 for Field 4.

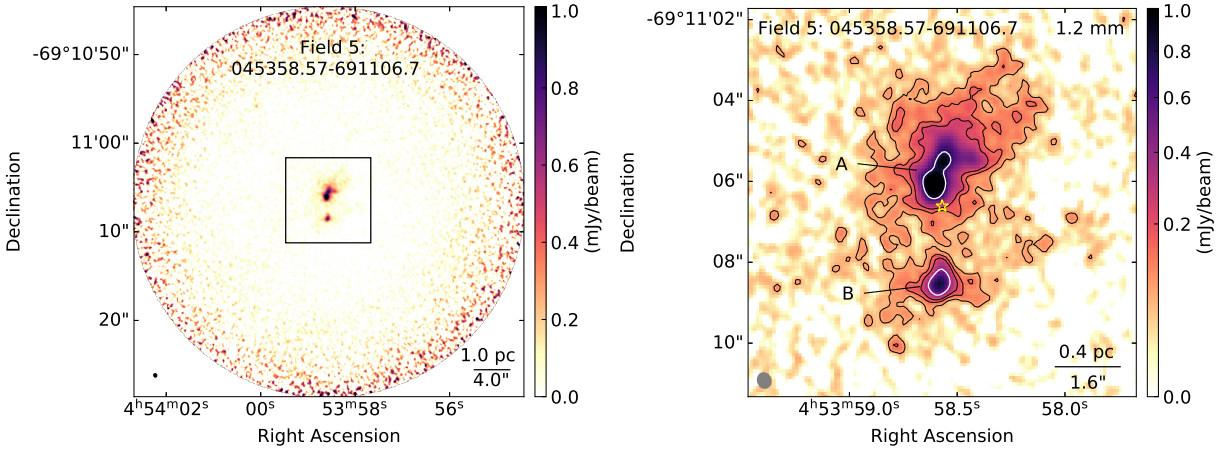


Figure A.3: Continued.

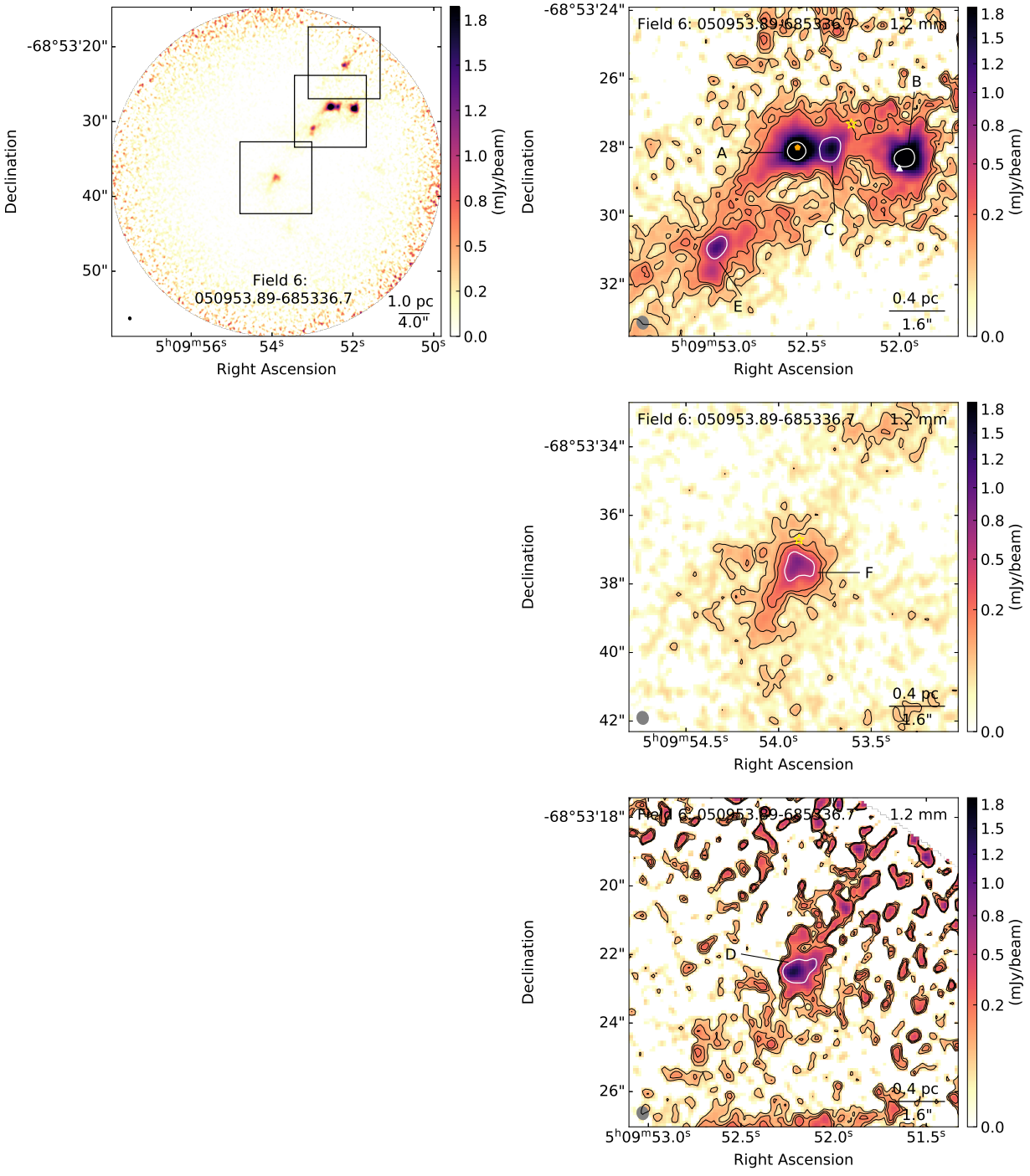


Figure A.4: Continued.

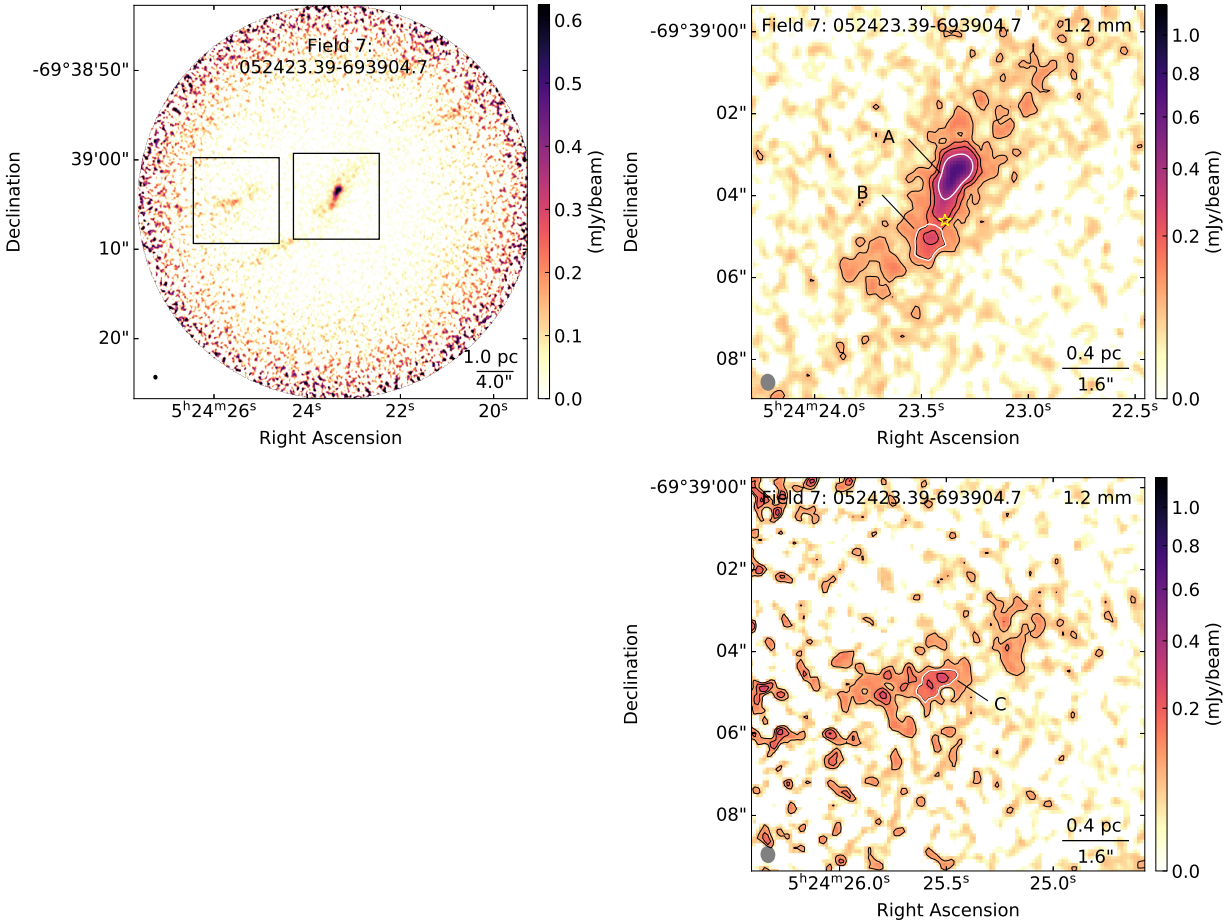


Figure A.5: Continued.

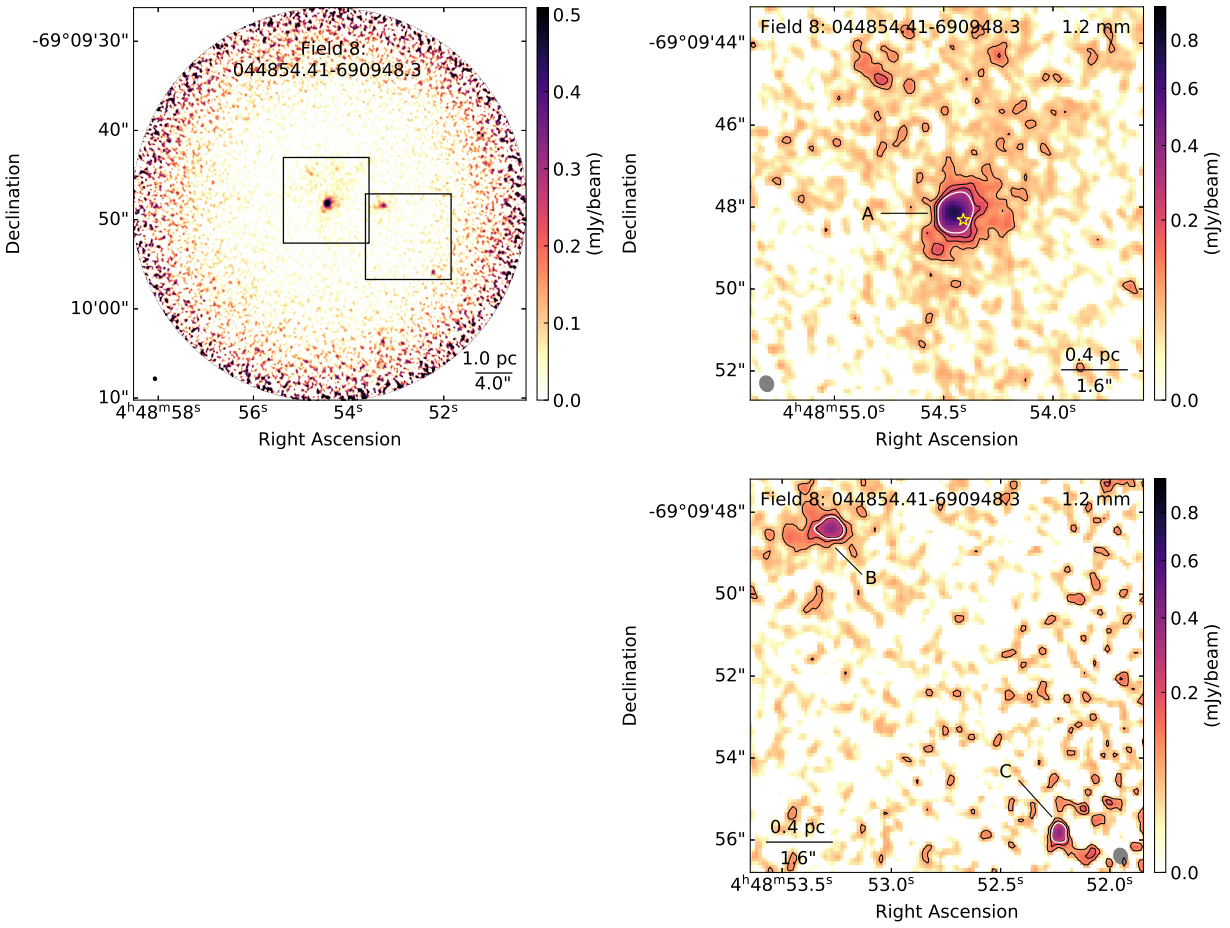


Figure A.6: Continued.

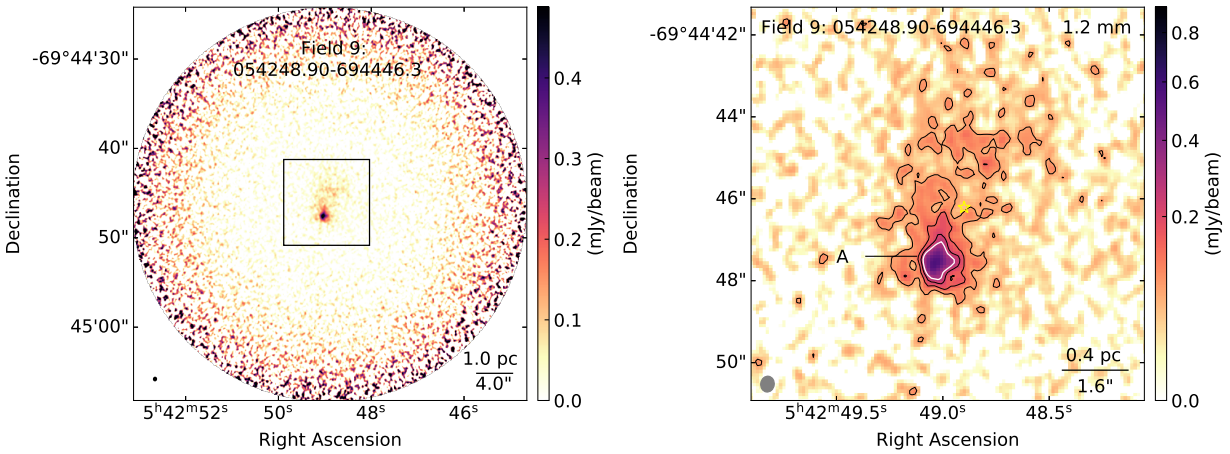


Figure A.7: Continued.

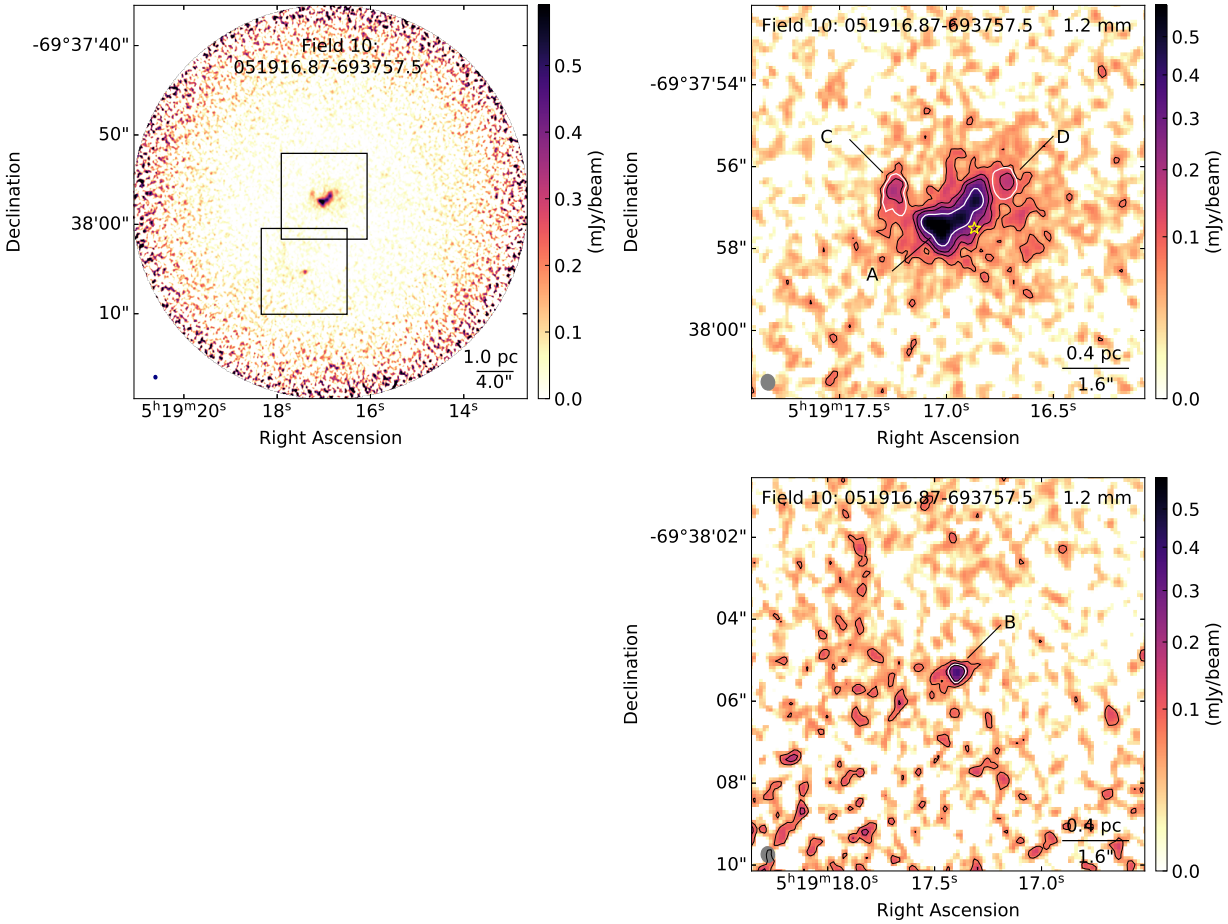


Figure A.8: Continued.

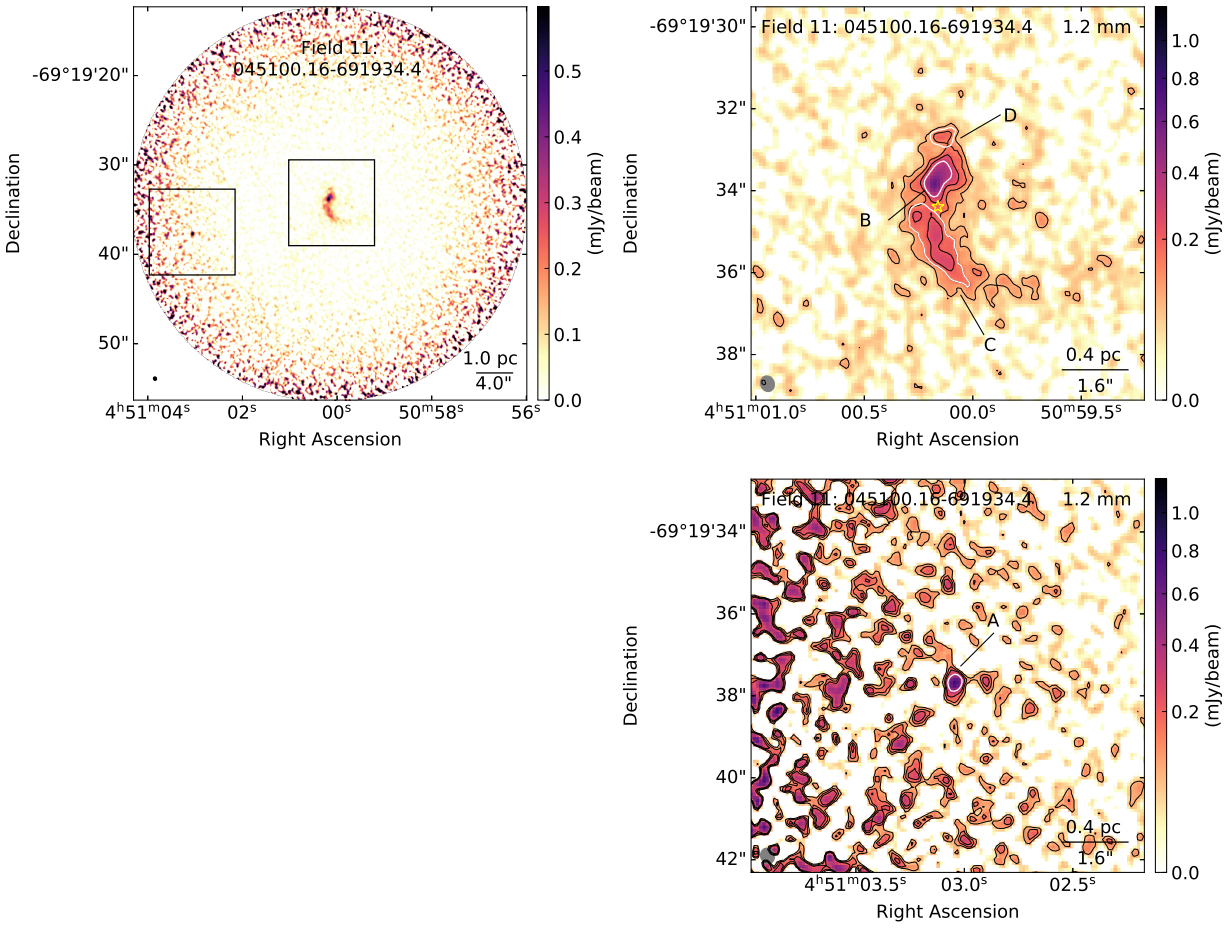


Figure A.9: Continued.

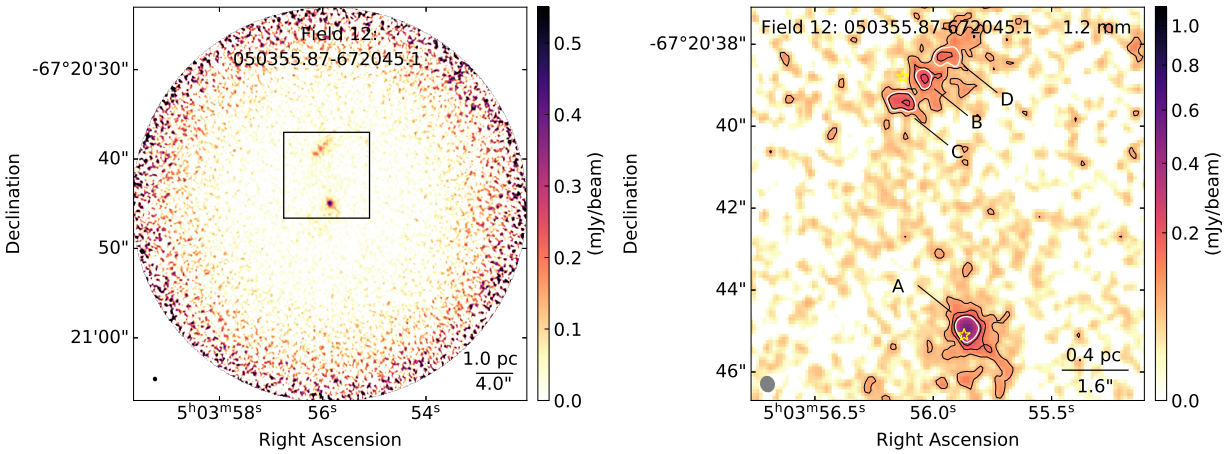


Figure A.10: Continued.

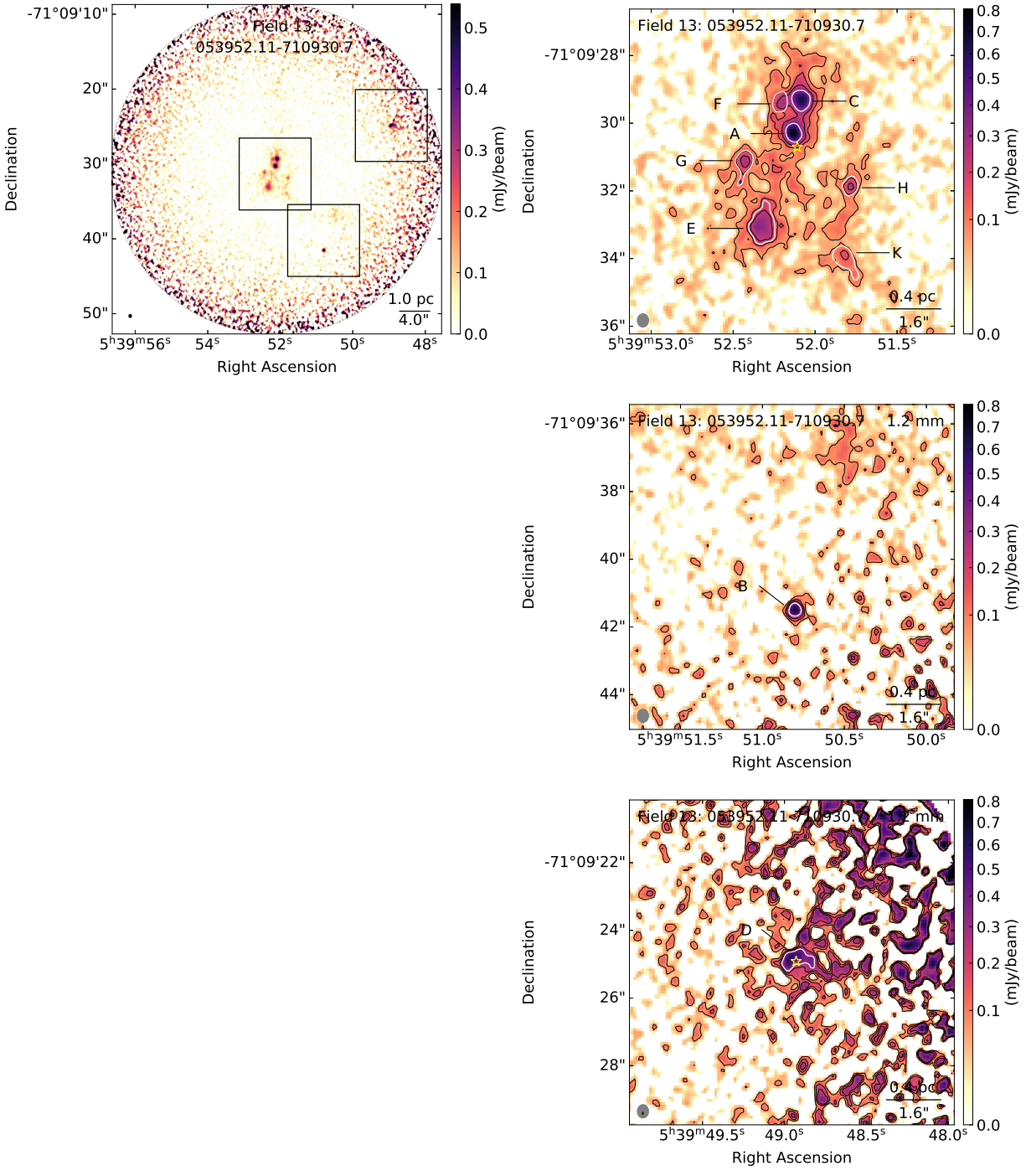


Figure A.11: Continued.

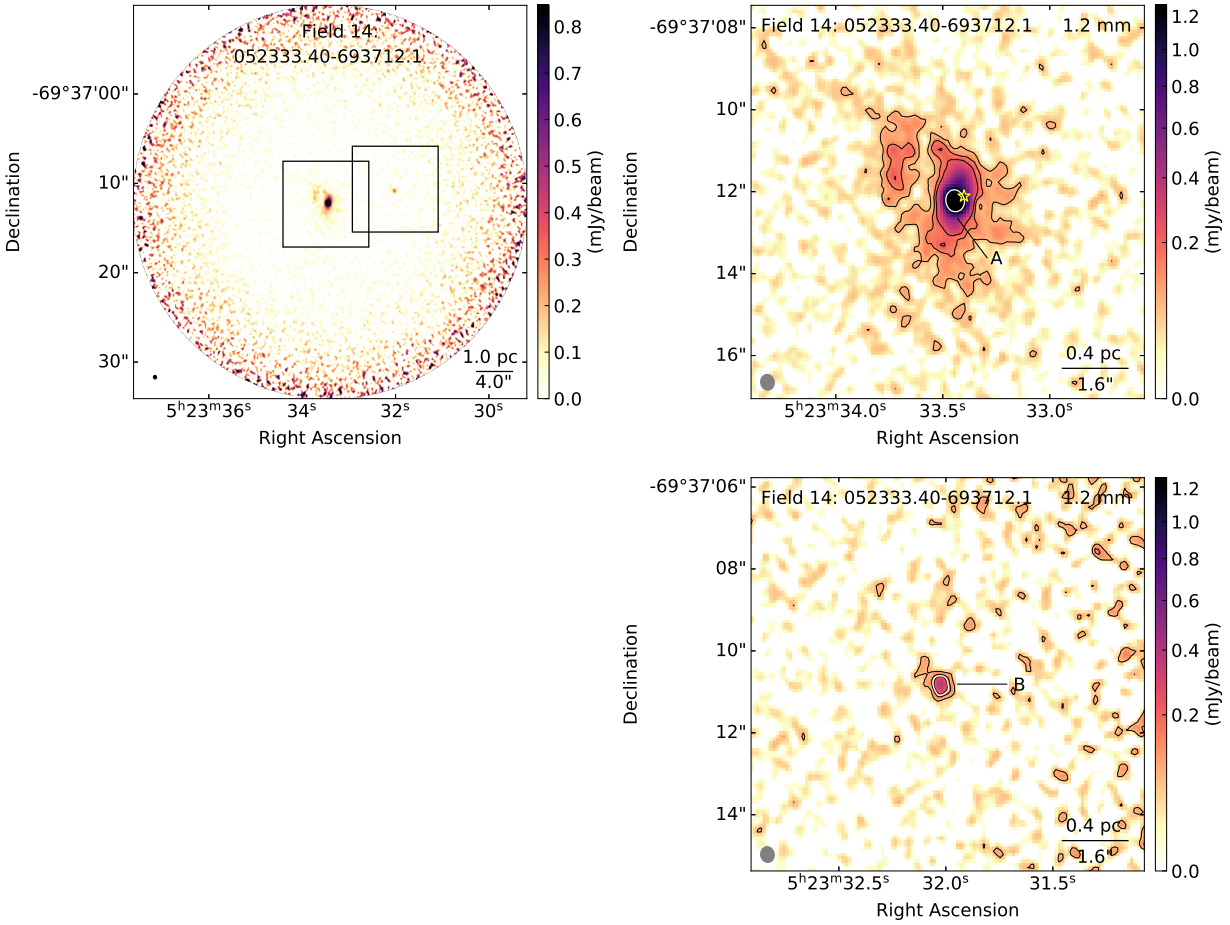


Figure A.12: Continued.

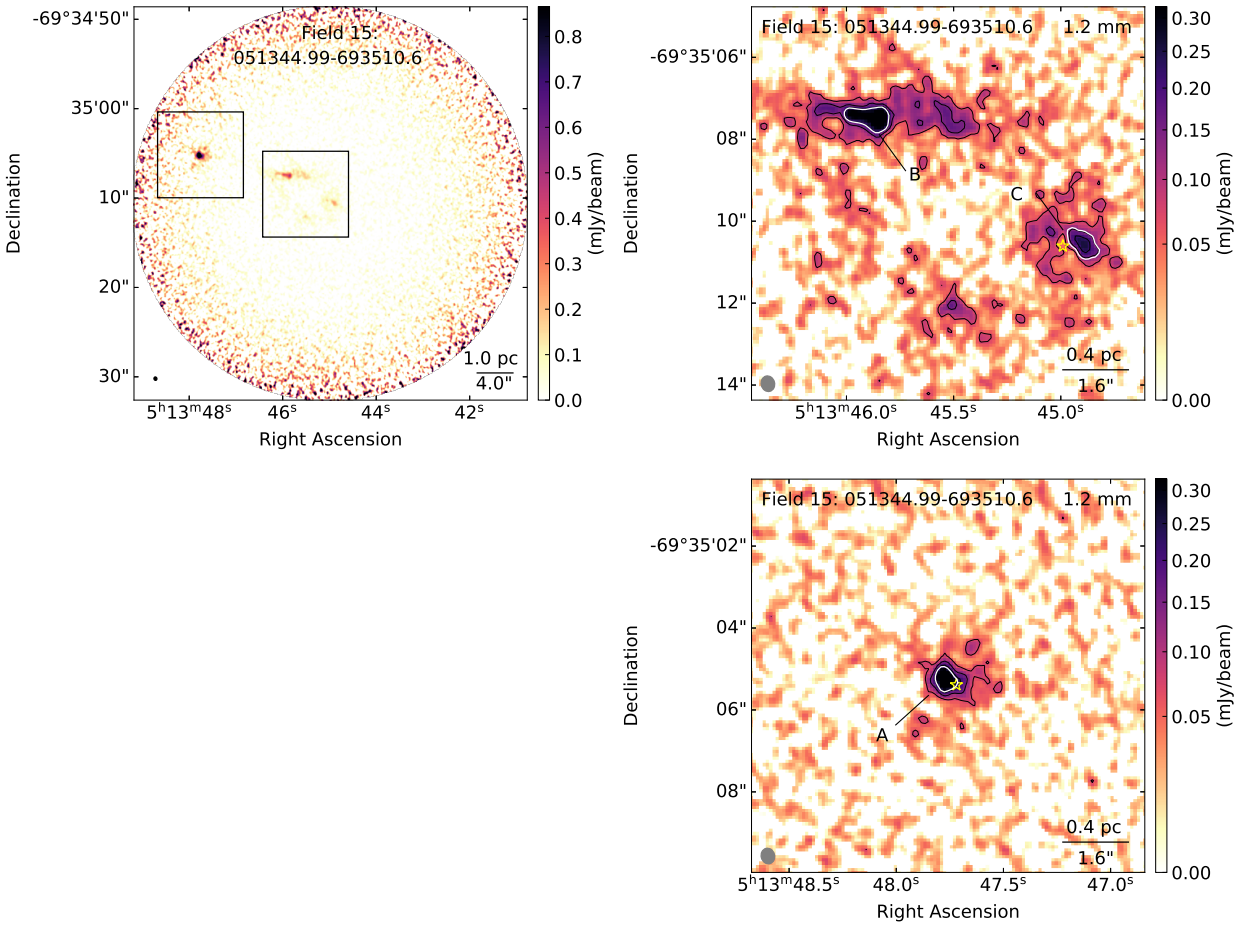


Figure A.13: Continued.

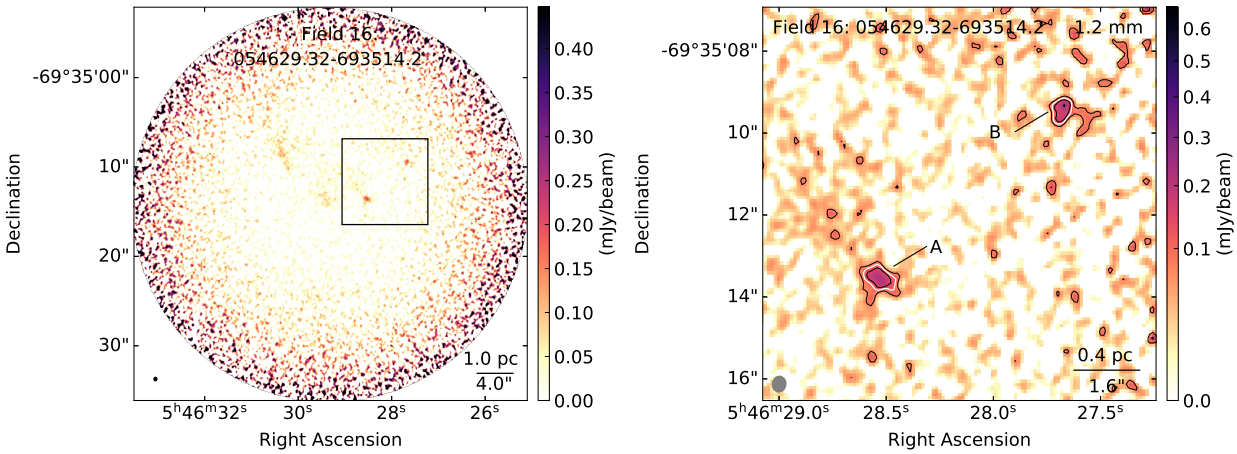


Figure A.14: Continued.

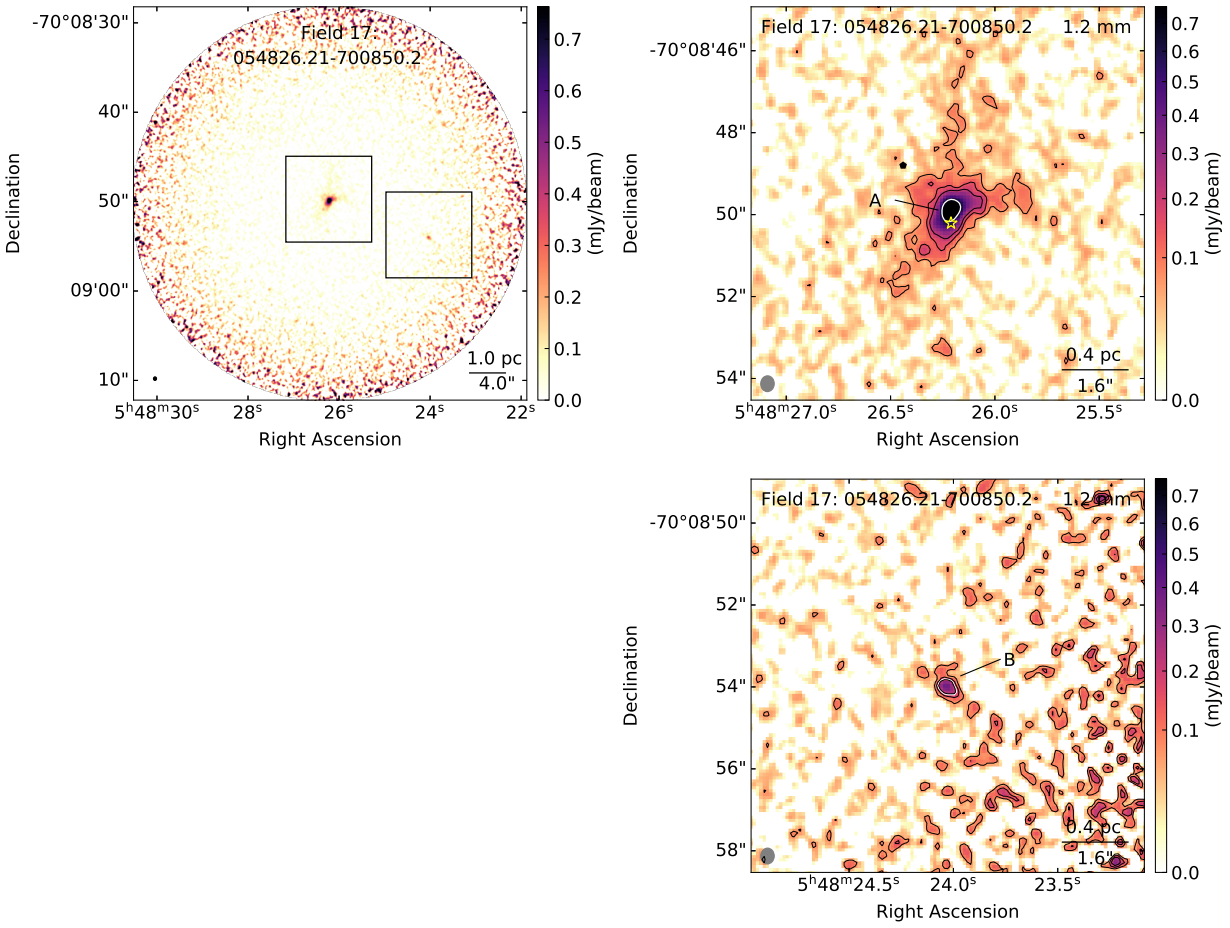


Figure A.15: Continued.

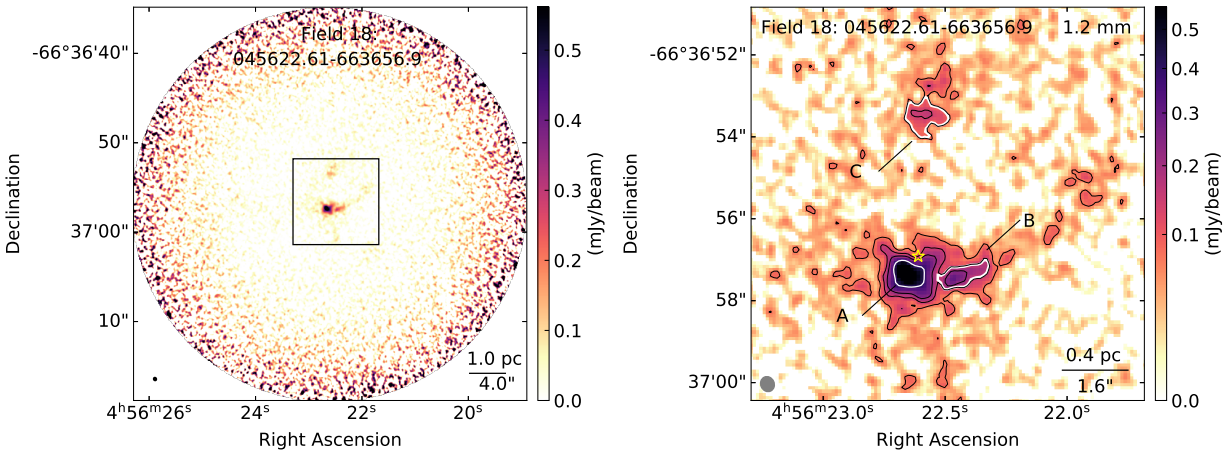


Figure A.16: Continued.

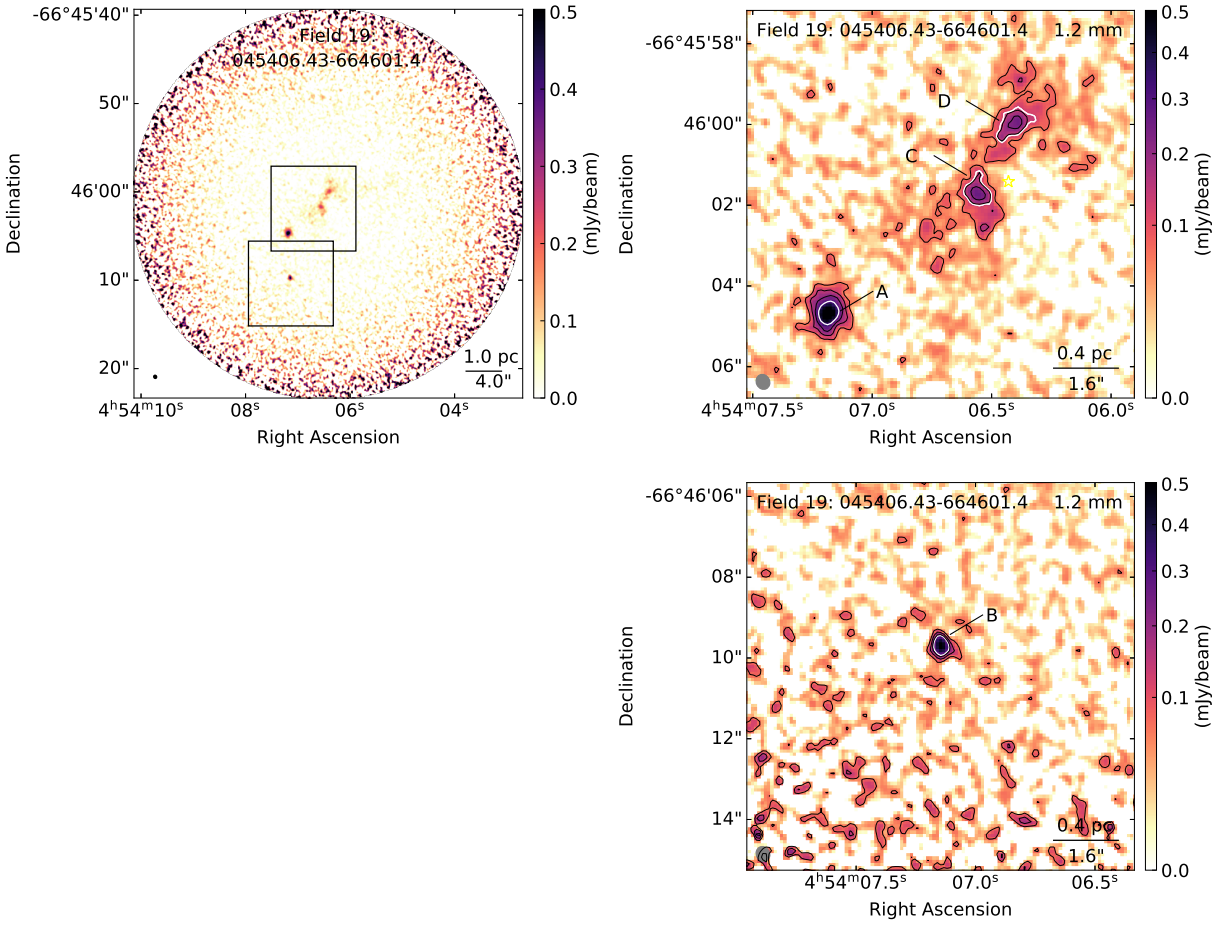


Figure A.17: Continued.

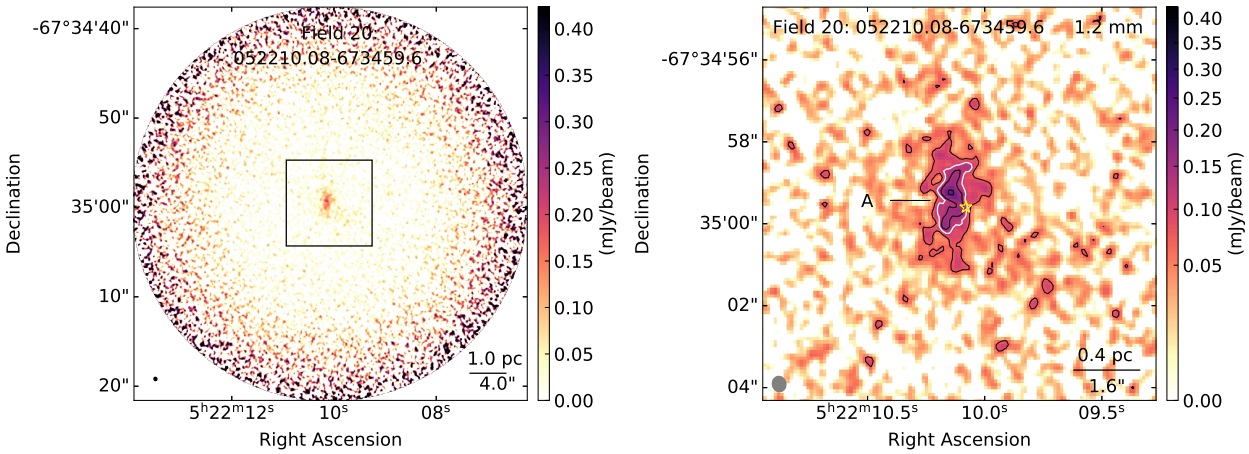


Figure A.18: Continued.

Table A.1: Physical properties of 1.2 mm continuum cores.

Source	RA (h:m:s)	Dec (d:m:s)	$\theta_{\rm obs/decov}$ ($''$)	$I_{\rm peak}$ (mJy/beam)	F_{50} (mJy)	$T_{\rm core}$ (K)	$M_{\rm core}$ ($M_\odot$)	$n_{\rm core}$ (H_2) (10^6 cm^{-3})	$N_{\rm core}$ (H_2) (10^{23} cm^{-2})	$L_{\rm core}$ (10^3 $L_\odot$)
1A	5:39:41.13	-69:29:16.72	0.56 / 0.14	0.93±0.003	1.65±0.16	58±12	59.87±14.51	0.65±0.16	1.82±0.44	93.62±74.89
2A	4:56:40.77	-66:32:30.40	0.45 / 0.11	1.10±0.003	1.31±0.11	23±5	141.34±38.16	2.98±0.80	6.70±1.81	1.48±1.19
2B	4:56:40.72	-66:32:31.04	0.79 / 0.19	0.59±0.003	2.19±0.33	22±4	250.39±75.19	1.00±0.30	3.91±1.17	3.78±3.02
2C	4:56:40.88	-66:32:30.00	0.64 / 0.16	0.47±0.003	1.10±0.22	67±13	33.91±10.00	0.25±0.07	0.80±0.24	213.72±170.97
2D	4:56:40.63	-66:32:31.92	0.64 / 0.16	0.30±0.003	0.74±0.22	55±11	28.49±10.48	0.21±0.08	0.68±0.25	97.05±77.64
2E	4:56:40.55	-66:32:30.80	0.84 / 0.20	0.21±0.003	0.87±0.37	11±2	272.79±147.12	0.90±0.49	3.76±2.03	0.27±0.21
2F	4:56:41.64	-66:32:28.64	0.59 / 0.14	0.15±0.003	0.30±0.18	27±5	26.18±17.35	0.25±0.17	0.74±0.49	4.73±3.79
3A	5:23:43.51	-68:0:34.07	0.85 / 0.21	3.75±0.003	15.39±0.41	35±7	991.33±235.77	3.16±0.75	13.36±3.18	28.01±22.41
3B	5:23:43.67	-68:0:35.19	0.89 / 0.22	0.61±0.003	2.74±0.45	13±3	656.04±227.80	1.81±0.63	8.02±2.78	0.59±0.47
3C	5:23:43.30	-68:0:37.19	1.02 / 0.25	0.29±0.003	1.62±0.59	51±10	67.75±28.93	0.12±0.05	0.63±0.27	183.68±146.94
3D	5:23:43.10	-68:0:36.07	0.83 / 0.20	0.24±0.003	0.86±0.39	37±7	51.67±26.52	0.17±0.09	0.72±0.37	33.79±27.03
4A	5:19:12.29	-69:9:7.28	0.49 / 0.12	5.01±0.003	6.78±0.12	26±5	626.10±156.87	10.56±2.65	25.60±6.41	2.81±2.25
5A	4:53:58.59	-69:11:5.96	0.75 / 0.18	1.50±0.003	4.48±0.29	15±3	865.76±257.97	3.98±1.19	14.88±4.43	0.74±0.59
5B	4:53:58.57	-69:11:8.44	0.57 / 0.14	0.85±0.003	1.54±0.17	19±4	214.16±62.33	2.23±0.65	6.35±1.85	1.11±0.88
6A	5:9:52.54	-68:53:28.07	0.53 / 0.13	5.46±0.003	8.68±0.15	36±7	540.75±127.58	7.19±1.70	18.86±4.45	12.11±9.69
6B	5:9:51.96	-68:53:28.23	0.58 / 0.14	4.91±0.003	9.29±0.18	50±10	396.84±89.64	3.98±0.90	11.48±2.59	54.35±43.48
6C	5:9:52.35	-68:53:27.99	0.68 / 0.17	1.69±0.003	4.54±0.25	30±6	351.83±87.58	2.15±0.54	7.32±1.82	9.79±7.83
6D	5:9:52.20	-68:53:22.47	0.79 / 0.19	1.46±0.003	4.54±0.34	46±9	213.24±50.98	0.83±0.20	3.28±0.78	73.13±58.50
6E	5:9:52.97	-68:53:30.87	0.58 / 0.14	1.20±0.003	2.39±0.18	38±8	139.60±34.22	1.40±0.34	4.04±0.99	18.13±14.51
6F	5:9:53.89	-68:53:37.27	0.81 / 0.20	0.86±0.003	3.38±0.35	27±5	297.78±80.13	1.08±0.29	4.36±1.17	9.13±7.30
7A	5:24:23.33	-69:39:3.36	0.87 / 0.21	0.71±0.003	3.11±0.39	29±6	251.07±68.82	0.75±0.21	3.24±0.89	13.80±11.04
7B	5:24:25.51	-69:39:4.56	0.77 / 0.19	0.27±0.003	0.85±0.30	27±5	74.47±32.41	0.32±0.14	1.23±0.53	8.12±6.49
7C	5:24:23.44	-69:39:4.96	0.79 / 0.19	0.27±0.003	0.91±0.32	27±5	80.44±34.47	0.32±0.14	1.25±0.54	8.57±6.85
8A	4:48:54.44	-69:9:48.07	0.93 / 0.23	0.76±0.003	3.12±0.43	25±5	302.28±86.70	0.73±0.21	3.38±0.97	8.78±7.03

Continued ...

Table A.1: Inferred properties of the cores.

Source	RA (h:m:s)	Dec (d:m:s)	$\theta_{\rm obs/decov}$ ($''$)	$I_{\rm peak}$ (mJy/beam)	F_{50} (mJy)	$T_{\rm core}$ (K)	$M_{\rm core}$ ($M_\odot$)	$n_{\rm core}$ (H_2) (10^6 cm^{-3})	$N_{\rm core}$ (H_2) (10^{23} cm^{-2})	$L_{\rm core}$ (10^3 $L_\odot$)
8B	4:48:52.22	-69:9:55.75	0.41 / 0.10	0.41±0.003	0.40±0.08	27±5	35.11±11.46	0.96±0.31	1.98±0.65	2.37±1.89
8C	4:48:53.26	-69:9:48.31	0.61 / 0.15	0.39±0.003	0.80±0.19	27±5	70.91±23.99	0.60±0.20	1.83±0.62	5.19±4.15
9A	5:42:49.02	-69:44:47.48	0.73 / 0.18	0.56±0.003	1.69±0.27	50±10	72.04±19.84	0.36±0.10	1.31±0.36	86.17±68.94
10A	5:19:17.01	-69:37:57.42	1.03 / 0.25	0.72±0.003	4.10±0.55	26±5	378.55±107.47	0.67±0.19	3.43±0.97	12.70±10.16
10B	5:19:17.38	-69:38:5.18	0.42 / 0.10	0.37±0.003	0.38±0.09	27±5	33.62±11.67	0.86±0.30	1.81±0.63	2.48±1.98
10C	5:19:17.24	-69:37:56.54	0.76 / 0.18	0.20±0.003	0.63±0.30	39±8	35.97±18.92	0.16±0.08	0.60±0.32	34.84±27.87
10D	5:19:16.69	-69:37:56.30	0.69 / 0.17	0.18±0.003	0.49±0.24	22±4	56.00±31.50	0.33±0.19	1.14±0.64	2.88±2.31
11A	4:51:3.03	-69:19:37.59	0.37 / 0.09	0.78±0.003	0.62±0.07	27±5	54.66±14.91	2.05±0.56	3.81±1.04	1.92±1.53
11B	4:51:0.16	-69:19:33.75	0.67 / 0.16	0.64±0.003	1.52±0.23	24±5	154.95±45.78	1.00±0.30	3.34±0.99	3.87±3.10
11C	4:51:0.16	-69:19:35.03	1.25 / 0.30	0.29±0.003	2.55±0.80	10±2	933.37±434.57	0.92±0.43	5.73±2.67	0.41±0.33
11D	4:51:0.13	-69:19:32.63	0.53 / 0.13	0.20±0.003	0.31±0.14	22±4	35.98±18.62	0.48±0.25	1.25±0.65	1.69±1.35
12A	5:3:55.84	-67:20:44.86	0.59 / 0.14	0.53±0.003	1.05±0.18	19±4	145.34±46.39	1.41±0.45	4.10±1.31	1.16±0.93
12B	5:3:56.02	-67:20:38.78	0.41 / 0.10	0.25±0.003	0.27±0.09	27±5	24.10±9.87	0.66±0.27	1.36±0.56	2.37±1.89
12C	5:3:56.09	-67:20:39.34	0.61 / 0.15	0.23±0.003	0.50±0.19	27±5	44.14±20.08	0.39±0.18	1.16±0.53	5.07±4.06
12D	5:3:55.95	-67:20:38.22	0.53 / 0.13	0.19±0.003	0.30±0.15	38±8	17.73±9.62	0.23±0.12	0.60±0.33	15.48±12.38
13A	5:39:52.11	-71:9:30.23	0.50 / 0.12	0.76±0.003	1.06±0.13	49±10	46.12±11.76	0.70±0.18	1.76±0.45	37.91±30.33
13B	5:39:50.79	-71:9:41.43	0.38 / 0.09	0.69±0.003	0.55±0.07	27±5	48.83±13.70	1.68±0.47	3.22±0.90	2.03±1.62
13C	5:39:52.06	-71:9:29.27	0.57 / 0.14	0.65±0.003	1.19±0.16	27±5	104.54±29.58	1.09±0.31	3.10±0.88	4.51±3.61
13D	5:39:48.94	-71:9:24.71	0.70 / 0.17	0.60±0.003	1.62±0.24	27±5	142.65±41.32	0.81±0.23	2.82±0.82	6.76±5.41
13E	5:39:52.32	-71:9:32.95	0.91 / 0.22	0.35±0.003	1.55±0.41	19±4	215.30±81.17	0.56±0.21	2.53±0.95	2.79±2.23
13F	5:39:52.18	-71:9:29.35	0.50 / 0.12	0.28±0.003	0.42±0.13	42±8	21.67±8.21	0.33±0.13	0.83±0.31	20.46±16.37
13G	5:39:52.41	-71:9:31.03	0.61 / 0.15	0.27±0.003	0.53±0.19	19±4	73.89±32.61	0.62±0.28	1.90±0.84	1.27±1.02
13H	5:39:51.76	-71:9:31.83	0.49 / 0.12	0.24±0.003	0.33±0.12	40±8	18.06±7.88	0.29±0.13	0.71±0.31	16.29±13.03
13K	5:39:51.80	-71:9:33.83	0.70 / 0.17	0.17±0.003	0.43±0.24	27±5	38.06±23.37	0.22±0.13	0.75±0.46	6.76±5.41

Continued ...

Table A.1: Inferred properties of the cores.

Source	RA (h:m:s)	Dec (d:m:s)	$\theta_{\rm obs/decov}$ ($''$)	$I_{\rm peak}$ (mJy/beam)	F_{50} (mJy)	$T_{\rm core}$ (K)	$M_{\rm core}$ ($M_\odot$)	$n_{\rm core}$ (H_2) (10^6 cm^{-3})	$N_{\rm core}$ (H_2) (10^{23} cm^{-2})	$L_{\rm core}$ (10^3 $L_\odot$)
14A	5:23:33.43	-69:37:12.17	0.49 / 0.12	2.54±0.003	3.42±0.12	50±10	146.20±33.30	2.47±0.56	5.98±1.36	38.45±30.76
14B	5:23:32.01	-69:37:10.73	0.43 / 0.11	0.37±0.003	0.40±0.10	27±5	35.44±12.16	0.85±0.29	1.83±0.63	2.59±2.07
15A	5:13:47.76	-69:35:5.17	0.53 / 0.13	1.64±0.004	2.66±0.19	38±8	155.61±37.90	1.98±0.48	5.27±1.28	15.48±12.38
15B	5:13:45.83	-69:35:7.41	0.76 / 0.18	0.50±0.004	1.61±0.37	33±7	111.51±36.94	0.50±0.17	1.89±0.63	17.61±14.09
15C	5:13:44.87	-69:35:10.53	0.71 / 0.17	0.26±0.004	0.73±0.32	27±5	64.51±32.66	0.36±0.18	1.25±0.63	6.88±5.50
16A	5:46:27.65	-69:35:9.25	0.55 / 0.13	0.22±0.003	0.37±0.15	27±5	32.91±15.34	0.39±0.18	1.05±0.49	4.17±3.34
16B	5:46:28.51	-69:35:13.49	0.65 / 0.16	0.21±0.003	0.52±0.21	19±4	71.68±34.65	0.50±0.24	1.63±0.79	1.44±1.15
17A	5:48:26.20	-70:8:49.81	0.49 / 0.12	1.37±0.003	1.83±0.12	31±6	136.31±34.03	2.30±0.57	5.57±1.39	5.68±4.54
17B	5:48:24.03	-70:8:53.89	0.40 / 0.10	0.38±0.003	0.36±0.08	27±5	31.79±10.62	0.94±0.31	1.88±0.63	2.25±1.80
18A	4:56:22.65	-66:36:57.24	0.71 / 0.17	0.79±0.003	2.20±0.26	26±5	203.37±56.08	1.12±0.31	3.95±1.09	5.91±4.73
18B	4:56:22.45	-66:36:57.40	0.79 / 0.19	0.30±0.003	1.01±0.32	33±7	69.89±27.68	0.28±0.11	1.09±0.43	19.12±15.29
18C	4:56:22.56	-66:36:53.32	0.86 / 0.21	0.16±0.003	0.68±0.38	23±5	73.23±45.39	0.22±0.14	0.95±0.59	5.40±4.32
19A	4:54:7.17	-66:46:4.62	0.52 / 0.13	0.66±0.003	1.01±0.14	25±5	98.45±28.26	1.37±0.39	3.54±1.02	2.73±2.19
19B	4:54:7.13	-66:46:9.58	0.42 / 0.10	0.50±0.003	0.53±0.09	27±5	46.48±14.14	1.19±0.36	2.50±0.76	2.48±1.98
19C	4:54:6.54	-66:46:1.66	0.66 / 0.16	0.26±0.003	0.66±0.23	27±5	58.07±24.74	0.39±0.16	1.27±0.54	6.09±4.87
19D	4:54:6.38	-66:45:59.82	0.74 / 0.18	0.25±0.003	0.79±0.29	42±8	41.03±17.69	0.19±0.08	0.72±0.31	44.88±35.91
20A	5:22:10.12	-67:34:59.19	1.09 / 0.26	0.22±0.003	1.37±0.61	27±5	120.84±61.39	0.18±0.09	0.99±0.50	16.35±13.08

Note. The first three columns indicate the source's name and position. The following three columns are the observed and deconvolved source size ($\Omega_{\rm deconv} = \sqrt{\Omega^2_{\rm obs} - \Omega^2_{\rm beam}}$), peak intensity, and the flux density of the source inside the 50% contour from the 1.2-mm continuum images. $T_{\rm core}$ is the adapted temperature for each source, taken from the best-fit parameter for CH_3OH. The last five columns are the core total mass, molecular hydrogen density, column density, surface density and luminosity, respectively.

Table A.2: Inferred properties of the cores.

Source	Δv_{obs} (km/s)	Δv_{th} (km/s)	Δv_{nonth} (km/s)	$M_{vir,\ core}$ ($M_\odot$)	α_{vir}	$M_{J-th,\ core}$ ($M_\odot$)	$M_{J-th+nonth,\ core}$ ($M_\odot$)	$l_{J-th,\ core}$ (pc)	$l_{J-th+nonth,\ core}$ (pc)
1A	2.60±0.50	0.97±0.10	2.40±0.60	$(1.0\pm0.4)\times10^2$	1.7	3.50±1.10	$(6\pm4)\times10^1$	0.053±0.008	0.138±0.034
2A	1.28±0.26	0.61±0.06	0.90±0.40	19.00±7.00	0.13	0.40±0.13	2.10±1.90	0.016±0.003	0.027±0.009
2B	1.80±0.40	0.60±0.06	1.60±0.40	67.00±27.00	0.27	0.65±0.22	15.00±10.00	0.026±0.005	0.074±0.021
2C	2.00±0.40	1.05±0.10	1.60±0.50	68.00±27.00	2	6.90±2.30	43.00±30.00	0.091±0.016	0.170±0.050
2D	1.43±0.29	0.95±0.09	0.80±0.50	33.00±13.00	1.2	5.60±2.00	13.00±10.00	0.090±0.019	0.120±0.040
2E	1.80±0.40	0.42±0.04	1.60±0.40	72.00±29.00	0.26	0.24±0.10	16.00±12.00	0.019±0.006	0.078±0.028
2F	2.80±0.60	0.66±0.07	2.60±0.60	$(1.2\pm0.5)\times10^2$	4.4	1.80±0.80	$(1.2\pm0.8)\times10^2$	0.058±0.020	0.230±0.090
3A	3.90±0.80	0.76±0.08	3.80±0.80	$(3.3\pm1.3)\times10^2$	0.33	0.73±0.24	$(1.0\pm0.6)\times10^2$	0.019±0.003	0.094±0.022
3B	1.73±0.35	0.46±0.05	1.50±0.40	67.00±27.00	0.1	0.22±0.08	9.00±7.00	0.015±0.003	0.051±0.015
3C	1.77±0.35	0.91±0.09	1.30±0.50	81.00±33.00	1.2	6.50±2.40	37.00±27.00	0.113±0.027	0.200±0.060
3D	1.47±0.29	0.78±0.08	1.00±0.40	46.00±18.00	0.9	3.40±1.30	15.00±13.00	0.081±0.022	0.130±0.050
4A	4.50±0.90	0.65±0.07	4.40±0.90	$(2.5\pm1.0)\times10^2$	0.41	0.26±0.08	$(8\pm5)\times10^1$	0.009±0.001	0.060±0.014
5A	2.70±0.50	0.50±0.05	2.50±0.60	$(1.4\pm0.5)\times10^2$	0.16	0.18±0.06	26.00±17.00	0.011±0.002	0.056±0.015
5B	2.10±0.40	0.56±0.06	1.90±0.50	65.00±26.00	0.3	0.35±0.12	16.00±11.00	0.016±0.003	0.058±0.016
6A	3.70±0.70	0.77±0.08	3.50±0.80	$(1.8\pm0.7)\times10^2$	0.33	0.51±0.16	52.00±33.00	0.013±0.002	0.058±0.014
6B	4.30±0.90	0.90±0.09	4.20±0.90	$(2.8\pm1.1)\times10^2$	0.7	1.10±0.40	$(1.2\pm0.7)\times10^2$	0.020±0.003	0.094±0.022
6C	3.60±0.70	0.70±0.07	3.40±0.70	$(2.2\pm0.9)\times10^2$	0.63	0.71±0.23	$(9\pm6)\times10^1$	0.021±0.003	0.104±0.025
6D	3.40±0.70	0.87±0.09	3.20±0.70	$(2.3\pm0.9)\times10^2$	1.1	2.20±0.70	$(1.2\pm0.8)\times10^2$	0.041±0.006	0.160±0.040
6E	2.60±0.50	0.79±0.08	2.40±0.60	$(1.0\pm0.4)\times10^2$	0.73	1.20±0.40	41.00±27.00	0.029±0.005	0.093±0.023
6F	1.90±0.40	0.66±0.07	1.70±0.40	76.00±30.00	0.26	0.85±0.28	16.00±12.00	0.028±0.005	0.075±0.020
7A	1.77±0.35	0.69±0.07	1.50±0.40	69.00±28.00	0.27	1.10±0.40	15.00±11.00	0.035±0.006	0.082±0.022

Continued ...

Table A.2: Inferred properties of the cores.

Source	Δv_{obs} (km/s)	Δv_{th} (km/s)	Δv_{nonth} (km/s)	$M_{vir,\ core}$ ($M_\odot$)	α_{vir}	$M_{J-th,\ core}$ ($M_\odot$)	$M_{J-th+nonth,\ core}$ ($M_\odot$)	$l_{J-th,\ core}$ (pc)	$l_{J-th+nonth,\ core}$ (pc)
7B	2.80±0.60	0.66±0.07	2.60±0.60	$(1.5\pm0.6)\times10^2$	2.1	1.60±0.60	$(1.1\pm0.7)\times10^2$	0.051±0.012	0.210±0.060
7C	2.90±0.60	0.66±0.07	2.80±0.60	$(1.7\pm0.7)\times10^2$	2.1	1.60±0.60	$(1.2\pm0.8)\times10^2$	0.051±0.012	0.220±0.070
8A	2.00±0.40	0.64±0.06	1.70±0.50	$(9\pm4)\times10^1$	0.31	0.92±0.31	23.00±16.00	0.033±0.006	0.095±0.026
8B	0.00±0.00	0.66±0.07	···	0.00±0.00	0	0.90±0.31	···	0.030±0.006	···
8C	2.80±0.60	0.66±0.07	2.60±0.60	$(1.2\pm0.5)\times10^2$	1.7	1.10±0.40	$(8\pm5)\times10^1$	0.037±0.007	0.150±0.040
9A	1.80±0.40	0.90±0.09	1.40±0.50	60.00±24.00	0.8	3.70±1.20	23.00±16.00	0.066±0.011	0.120±0.033
10A	2.90±0.60	0.65±0.07	2.70±0.60	$(2.2\pm0.9)\times10^2$	0.58	1.03±0.34	$(8\pm5)\times10^1$	0.035±0.006	0.150±0.040
10B	3.60±0.70	0.66±0.07	3.40±0.70	$(1.4\pm0.6)\times10^2$	4.1	0.95±0.33	$(1.4\pm0.9)\times10^2$	0.031±0.006	0.160±0.040
10C	1.45±0.29	0.80±0.08	1.00±0.40	41.00±16.00	1.1	3.90±1.50	15.00±13.00	0.087±0.025	0.140±0.050
10D	5.90±1.20	0.60±0.06	5.80±1.20	$(6.1\pm2.4)\times10^2$	11	1.10±0.50	$(1.0\pm0.7)\times10^3$	0.045±0.014	0.440±0.150
11A	0.00±0.00	0.66±0.07	···	0.00±0.00	0	0.62±0.20	···	0.020±0.003	···
11B	2.00±0.40	0.63±0.06	1.70±0.40	66.00±26.00	0.43	0.74±0.25	19.00±13.00	0.027±0.005	0.080±0.022
11C	1.54±0.31	0.40±0.04	1.30±0.40	76.00±30.00	0.08	0.21±0.08	8.00±6.00	0.018±0.005	0.062±0.021
11D	2.20±0.40	0.60±0.06	2.00±0.50	64.00±26.00	1.8	0.90±0.40	38.00±27.00	0.038±0.010	0.130±0.040
12A	1.60±0.32	0.56±0.06	1.30±0.40	38.00±15.00	0.26	0.44±0.15	8.00±6.00	0.020±0.004	0.053±0.016
12B	2.40±0.50	0.66±0.07	2.20±0.50	62.00±25.00	2.6	1.10±0.40	47.00±32.00	0.036±0.008	0.120±0.040
12C	2.80±0.60	0.66±0.07	2.60±0.60	$(1.2\pm0.5)\times10^2$	2.7	1.40±0.50	$(1.0\pm0.6)\times10^2$	0.047±0.012	0.190±0.060
12D	1.29±0.26	0.79±0.08	0.70±0.50	22.00±9.00	1.3	3.10±1.30	8.00±7.00	0.072±0.021	0.100±0.040
13A	1.80±0.40	0.89±0.09	1.40±0.50	43.00±17.00	0.9	2.60±0.80	18.00±13.00	0.047±0.008	0.088±0.024
13B	0.00±0.00	0.66±0.07	···	0.00±0.00	0	0.68±0.23	···	0.022±0.004	···
13C	3.00±0.60	0.66±0.07	2.80±0.60	$(1.3\pm0.5)\times10^2$	1.2	0.85±0.28	$(7\pm5)\times10^1$	0.028±0.005	0.122±0.031

Continued ...

Table A.2: Inferred properties of the cores.

Source	Δv_{obs} (km/s)	Δv_{th} (km/s)	Δv_{nonth} (km/s)	$M_{vir,\ core}$ ($M_\odot$)	α_{vir}	$M_{J-th,\ core}$ ($M_\odot$)	$M_{J-th+nonth,\ core}$ ($M_\odot$)	$l_{J-th,\ core}$ (pc)	$l_{J-th+nonth,\ core}$ (pc)
13D	4.30±0.90	0.66±0.07	4.20±0.90	$(3.3\pm1.3)\times10^2$	2.3	0.98±0.33	$(2.5\pm1.6)\times10^2$	0.032±0.006	0.210±0.050
13E	1.59±0.32	0.56±0.06	1.30±0.40	58.00±23.00	0.27	0.70±0.25	12.00±9.00	0.033±0.007	0.083±0.026
13F	2.00±0.40	0.83±0.08	1.70±0.50	54.00±21.00	2.5	3.00±1.10	37.00±26.00	0.063±0.013	0.150±0.040
13G	1.71±0.34	0.56±0.06	1.50±0.40	45.00±18.00	0.6	0.66±0.25	14.00±11.00	0.031±0.007	0.086±0.028
13H	1.52±0.30	0.81±0.08	1.10±0.40	29.00±12.00	1.6	3.00±1.10	14.00±11.00	0.066±0.016	0.110±0.040
13K	3.20±0.70	0.66±0.07	3.10±0.70	$(1.9\pm0.7)\times10^2$	5	1.90±0.80	$(2.1\pm1.4)\times10^2$	0.062±0.020	0.300±0.110
14A	3.10±0.60	0.90±0.09	2.90±0.70	$(1.2\pm0.5)\times10^2$	0.8	1.40±0.50	53.00±34.00	0.025±0.004	0.084±0.020
14B	0.00±0.00	0.66±0.07	···	0.00±0.00	0	0.96±0.33	···	0.031±0.006	···
15A	6.00±1.20	0.79±0.08	5.90±1.20	$(4.9\pm1.9)\times10^2$	3.1	1.05±0.34	$(4.5\pm2.8)\times10^2$	0.024±0.004	0.180±0.040
15B	2.20±0.40	0.73±0.07	1.90±0.50	$(9\pm4)\times10^1$	0.8	1.70±0.60	37.00±25.00	0.045±0.009	0.126±0.035
15C	3.10±0.60	0.66±0.07	3.00±0.70	$(1.8\pm0.7)\times10^2$	2.7	1.50±0.60	$(1.4\pm1.0)\times10^2$	0.049±0.013	0.220±0.070
16A	0.00±0.00	0.66±0.07	···	0.00±0.00	0	1.40±0.50	···	0.047±0.012	···
16B	2.10±0.40	0.56±0.06	1.90±0.50	75.00±30.00	1	0.74±0.28	34.00±25.00	0.034±0.009	0.120±0.040
17A	2.80±0.60	0.71±0.07	2.60±0.60	$(1.0\pm0.4)\times10^2$	0.71	0.72±0.23	39.00±26.00	0.021±0.003	0.078±0.019
17B	0.00±0.00	0.66±0.07	···	0.00±0.00	0	0.91±0.31	···	0.030±0.006	···
18A	2.00±0.40	0.65±0.07	1.70±0.50	70.00±28.00	0.34	0.79±0.26	18.00±12.00	0.027±0.005	0.076±0.020
18B	2.30±0.50	0.73±0.07	2.10±0.50	$(1.1\pm0.4)\times10^2$	1.5	2.30±0.80	$(6\pm4)\times10^1$	0.061±0.013	0.180±0.050
18C	1.56±0.31	0.61±0.06	1.20±0.40	53.00±21.00	0.7	1.50±0.60	17.00±14.00	0.057±0.018	0.130±0.050
19A	2.70±0.50	0.64±0.06	2.50±0.60	$(9\pm4)\times10^1$	1	0.67±0.22	44.00±29.00	0.024±0.004	0.096±0.025
19B	0.00±0.00	0.66±0.07	···	0.00±0.00	0	0.81±0.27	···	0.027±0.005	···
19C	4.30±0.90	0.66±0.07	4.20±0.90	$(3.2\pm1.3)\times10^2$	5.5	1.40±0.50	$(3.8\pm2.5)\times10^2$	0.047±0.011	0.300±0.090

Continued ...

Table A.2: Inferred properties of the cores.

Source	Δv_{obs} (km/s)	Δv_{th} (km/s)	Δv_{nonth} (km/s)	$M_{vir,\ core}$ ($M_\odot$)	α_{vir}	$M_{J-th,\ core}$ ($M_\odot$)	$M_{J-th+nonth,\ core}$ ($M_\odot$)	$l_{J-th,\ core}$ (pc)	$l_{J-th+nonth,\ core}$ (pc)
19D	1.43±0.29	0.83±0.08	0.90±0.40	39.00±15.00	0.9	3.90±1.40	13.00±11.00	0.082±0.020	0.120±0.040
20A	3.00±0.60	0.66±0.07	2.90±0.60	$(2.5\pm1.0)\times10^2$	2.1	2.10±0.80	$(1.8\pm1.2)\times10^2$	0.068±0.019	0.300±0.100

A.3 Minimum Spanning Trees

In Section 2.3.3, we applied a MST algorithm using the Python pack- age `Networkx` to the 12 fields in our sample that each contain at least three cores. The MST connects core positions without creating loops, thereby minimizing the total path length between them. Fig. 2.5 illustrates the MST for the most densely populated fields, with additional plots for other fields presented in the appendix. In these figures, circles represent the positions of the cores, scaled according to their masses, and lines denote the connections between them.

A.4 Physical properties in each field

In this section, the physical properties of the cores within each field are illustrated through various figures, with the cores separated according to their corresponding field.

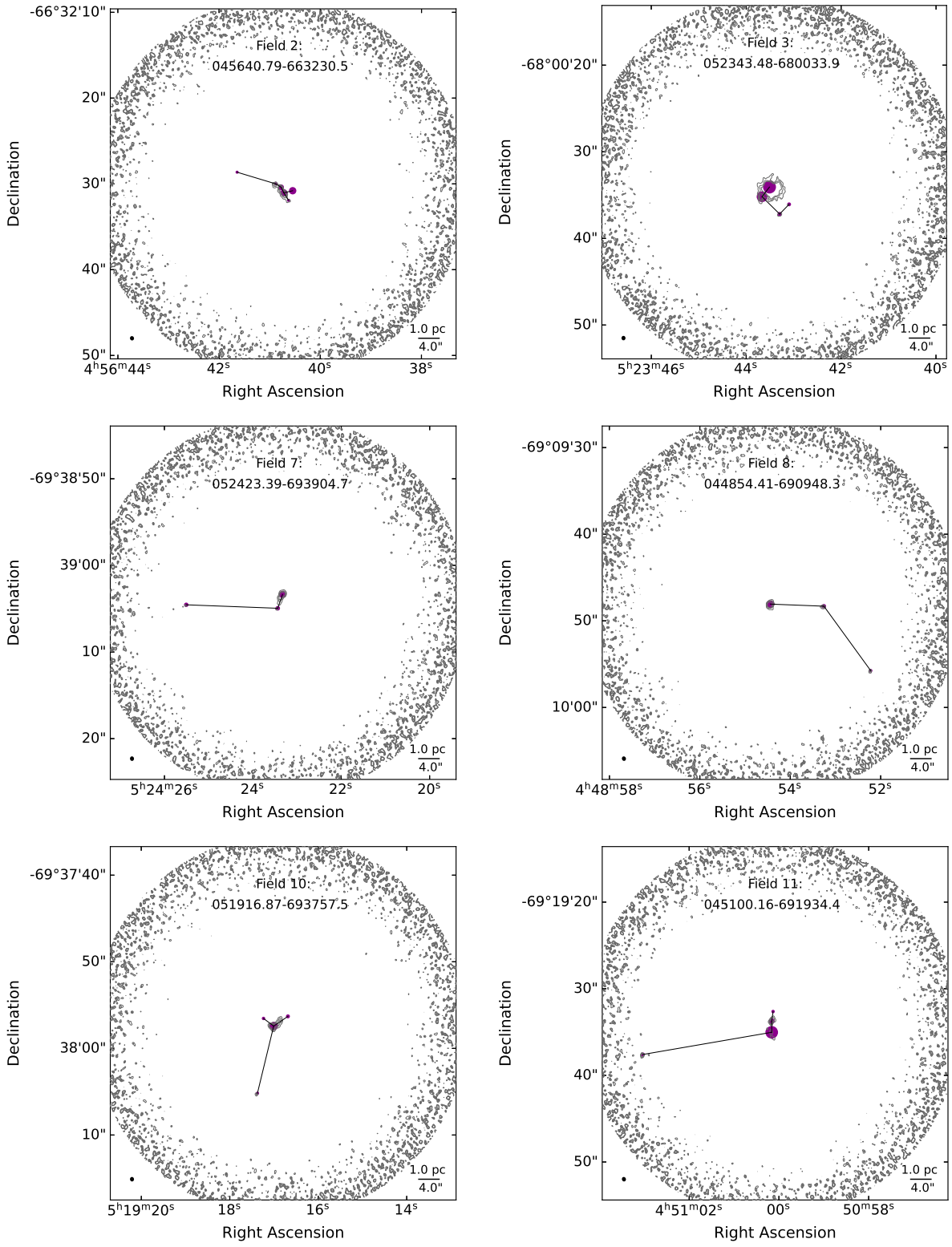


Figure A.19: Minimum spanning tree (MST) for the ALMA continuum cores in Fields 2, 3, 7, 8, 10, 11. The positions of the dense cores are indicated with circles, scaled with the mass of the cores, while the lines mark the tree.

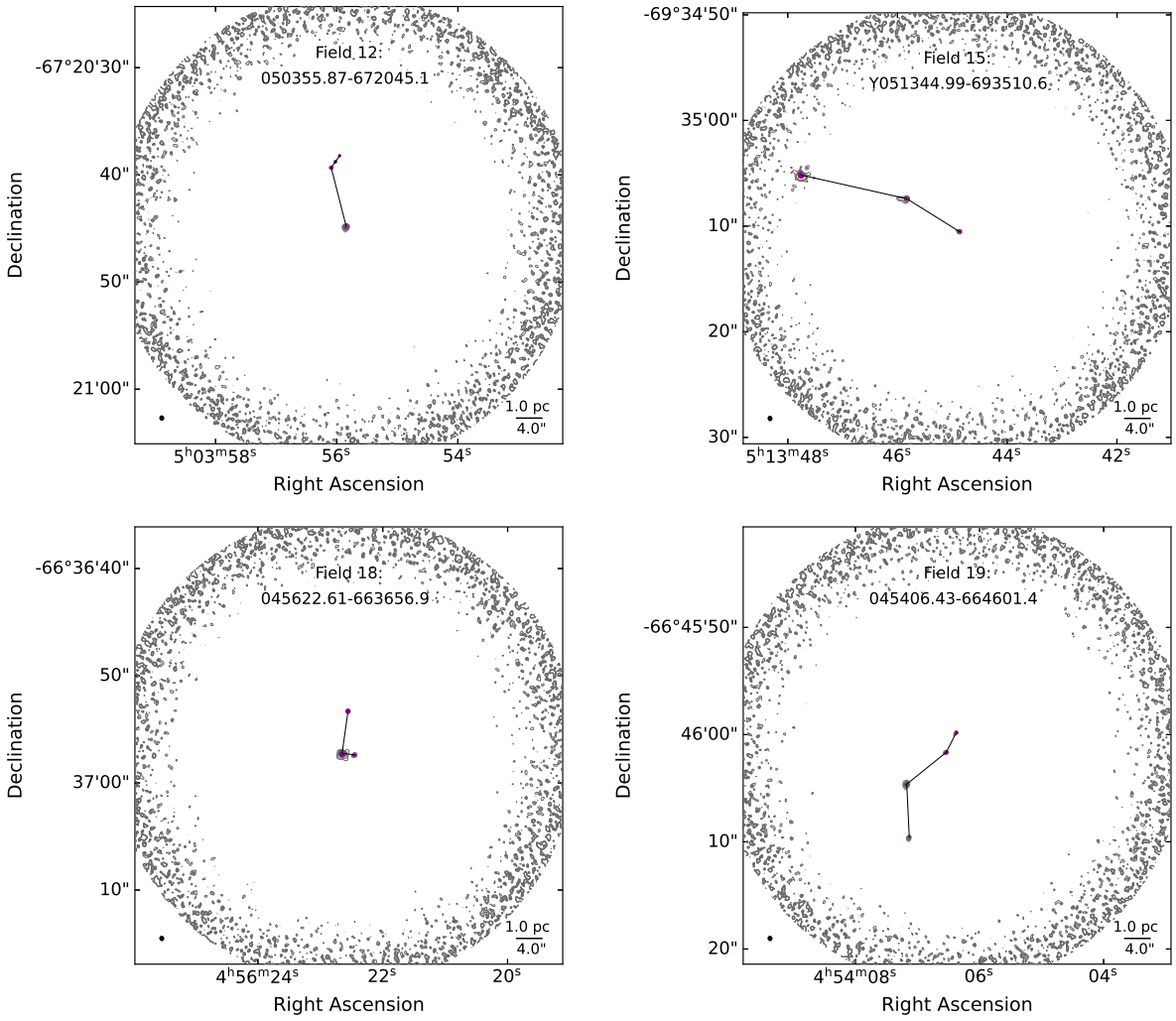


Figure A.20: Same as Fig. A.19 but for Fields 12, 15, 18 and 19.

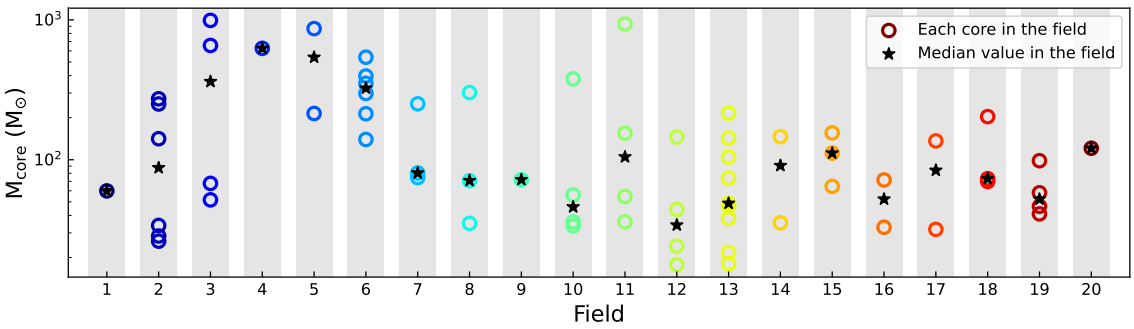


Figure A.21: $M_{\rm core}$ from all the cores in each field. The median core mass in each field is shown with a star mark.

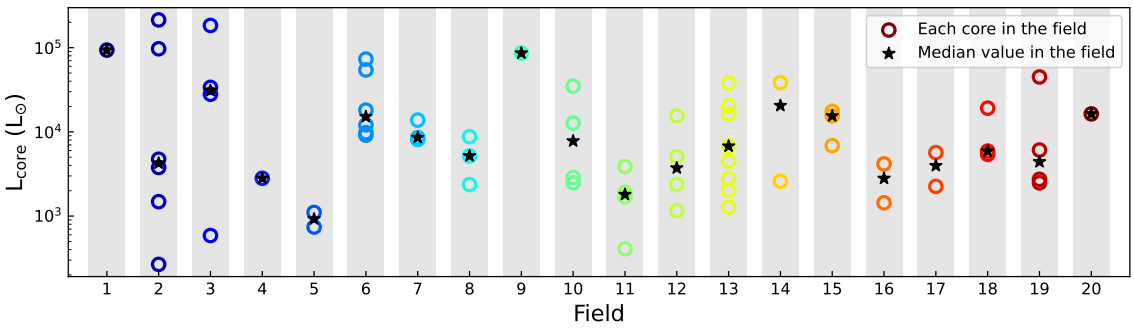


Figure A.22: Like Fig. A.21 for $L_{\rm core}$

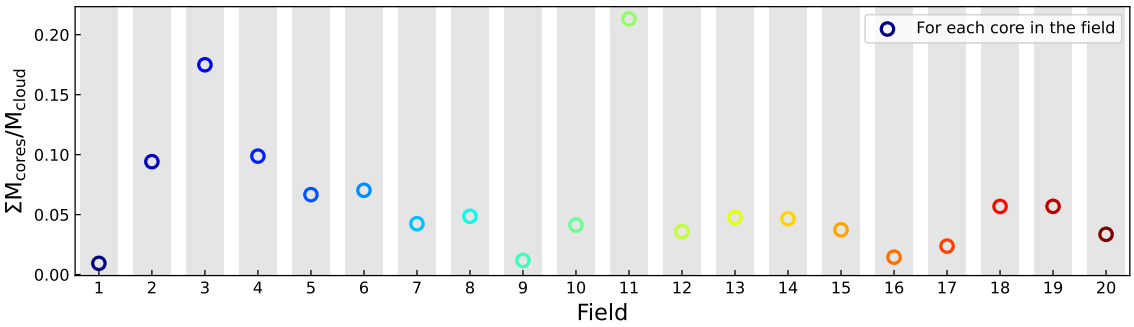


Figure A.23: Core formation efficiency in each field

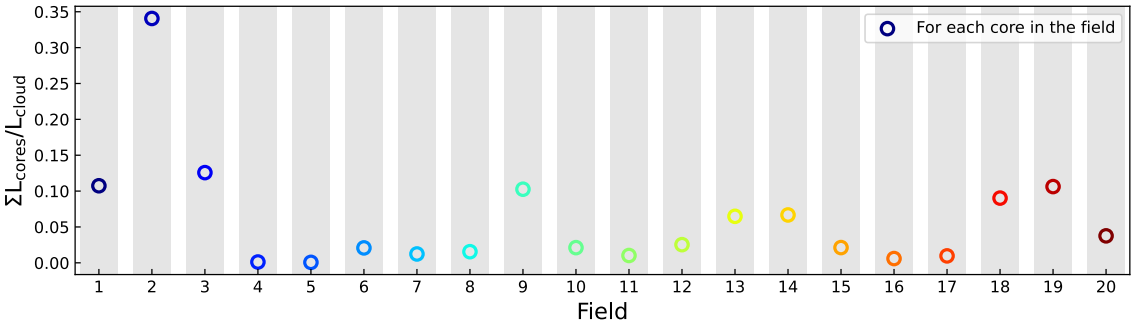


Figure A.24: Luminosity ratio in each field

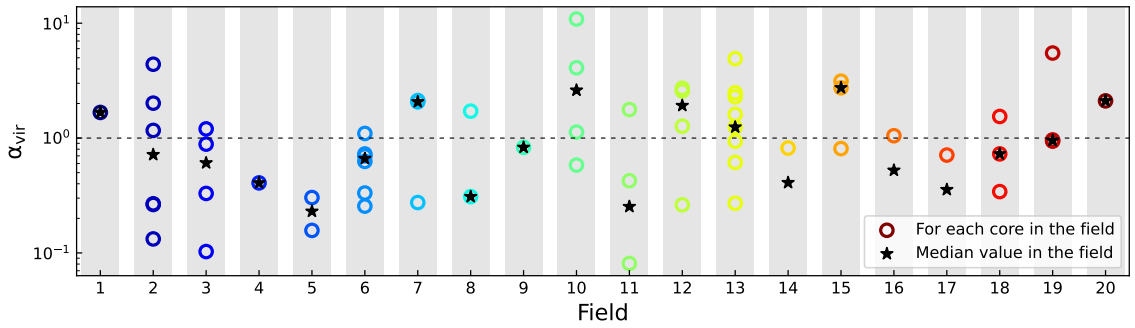


Figure A.25: Estimated Virial parameter ($\alpha_{\rm vir}$)

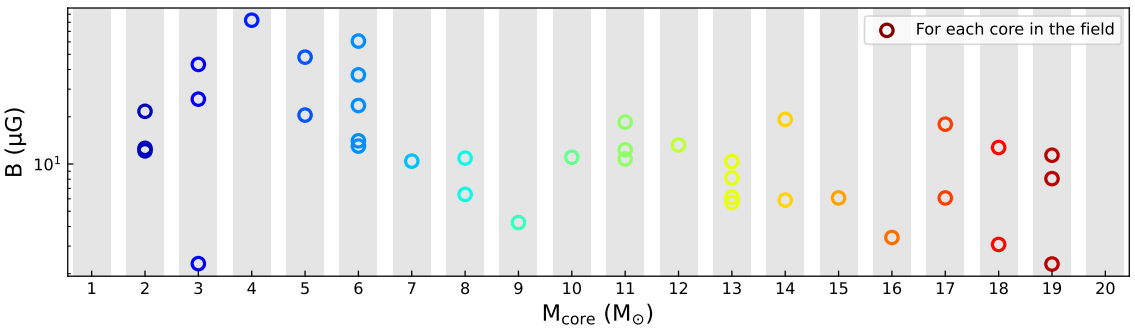


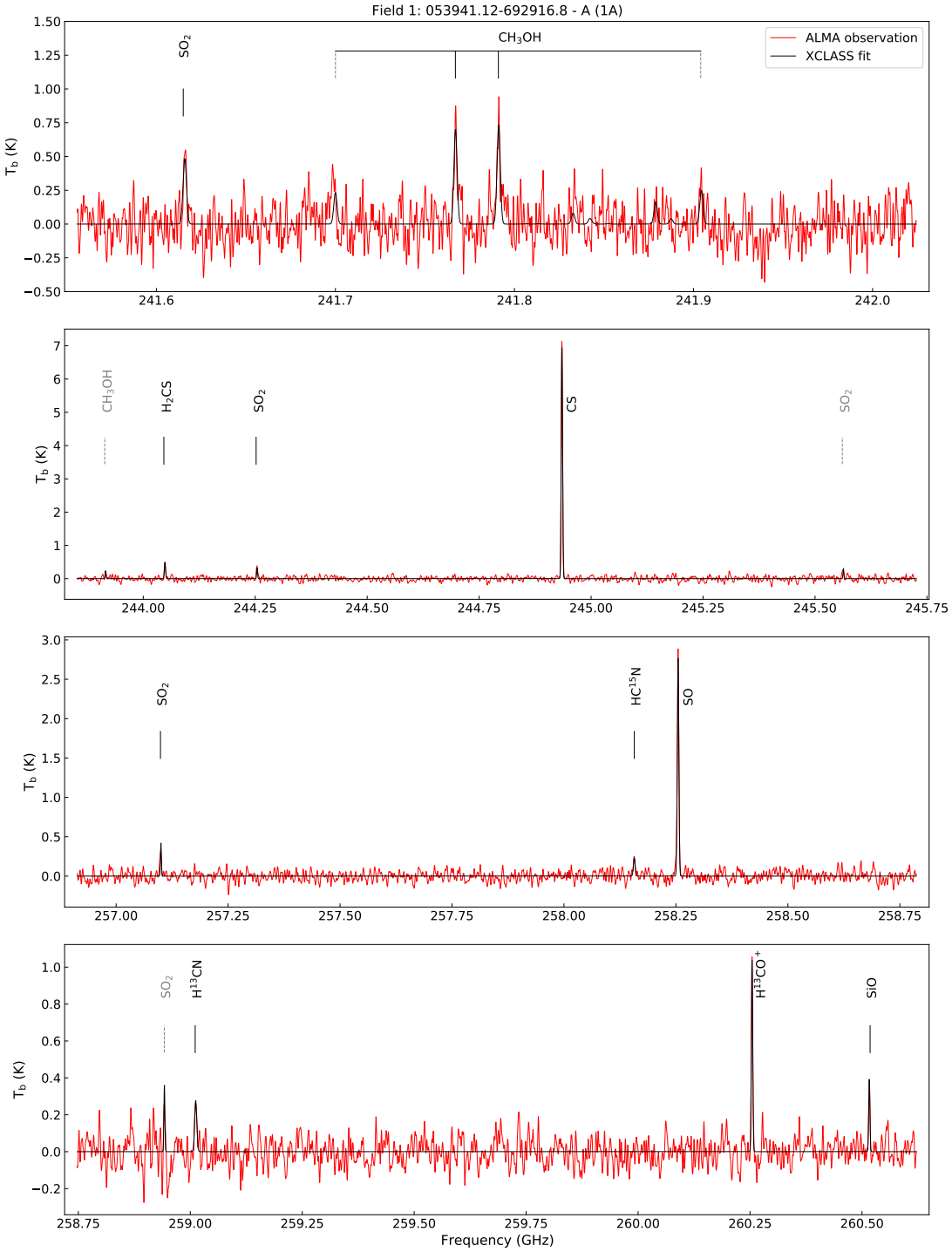
Figure A.26: Estimated magnetic field strength to support the cores from collapse

Appendix B

Observed spectra and XCLASS spectral analysis result

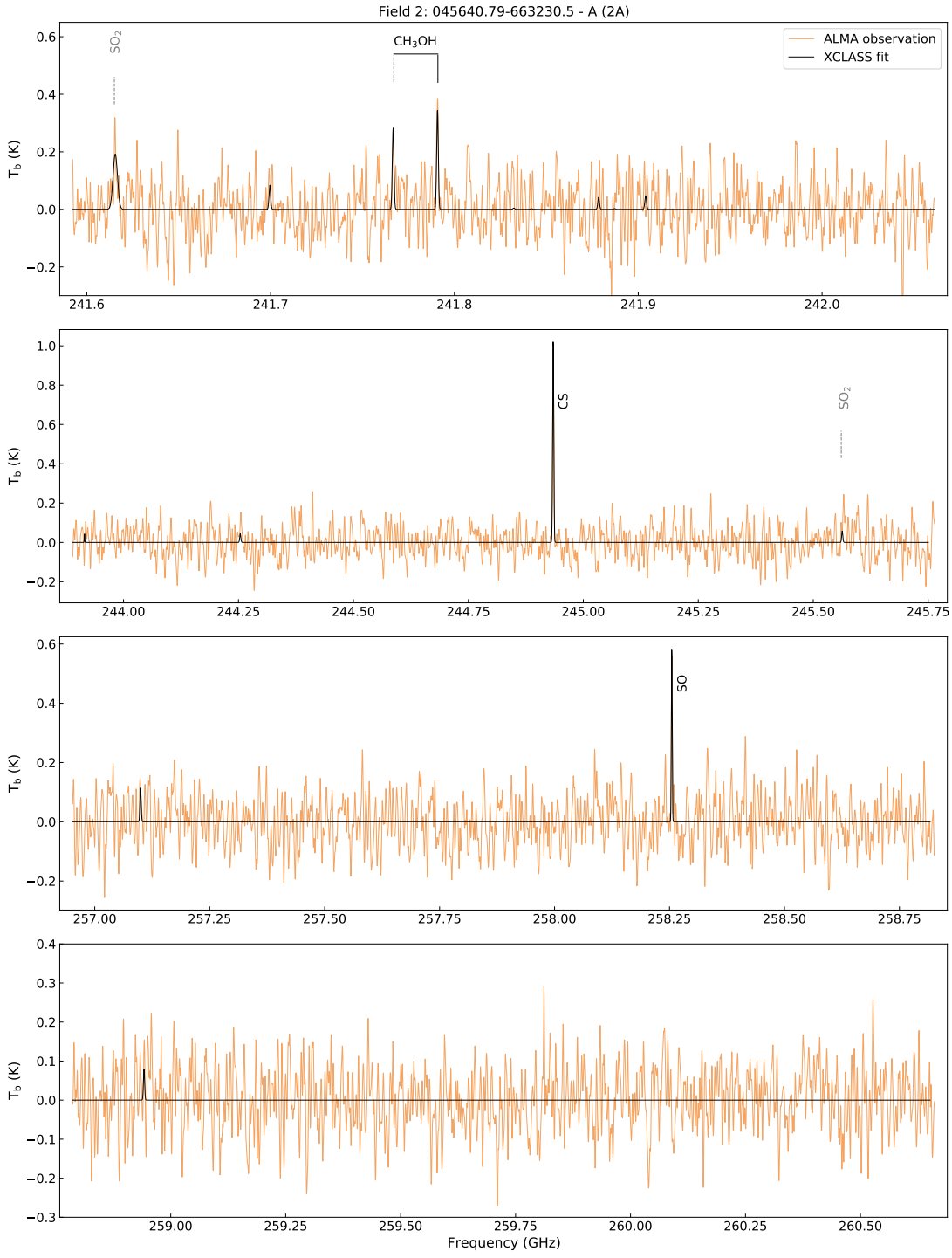
B.1 Spectra and XCLASS fits for 1.2 mm continuum cores

Figures B.1 to B.20 show the ALMA Band 6 spectra observed toward the all cores with identified molecular lines (except the core 14B) in the 20 fields observed throughout the LMC. The observed spectra with line detections were fit using the XCLASS software (see Section 3.3.1), and the results are shown as a black solid line on top of the observed spectra. The molecular species detected in the spectra are marked in black, while the tentative detections are marked in gray.



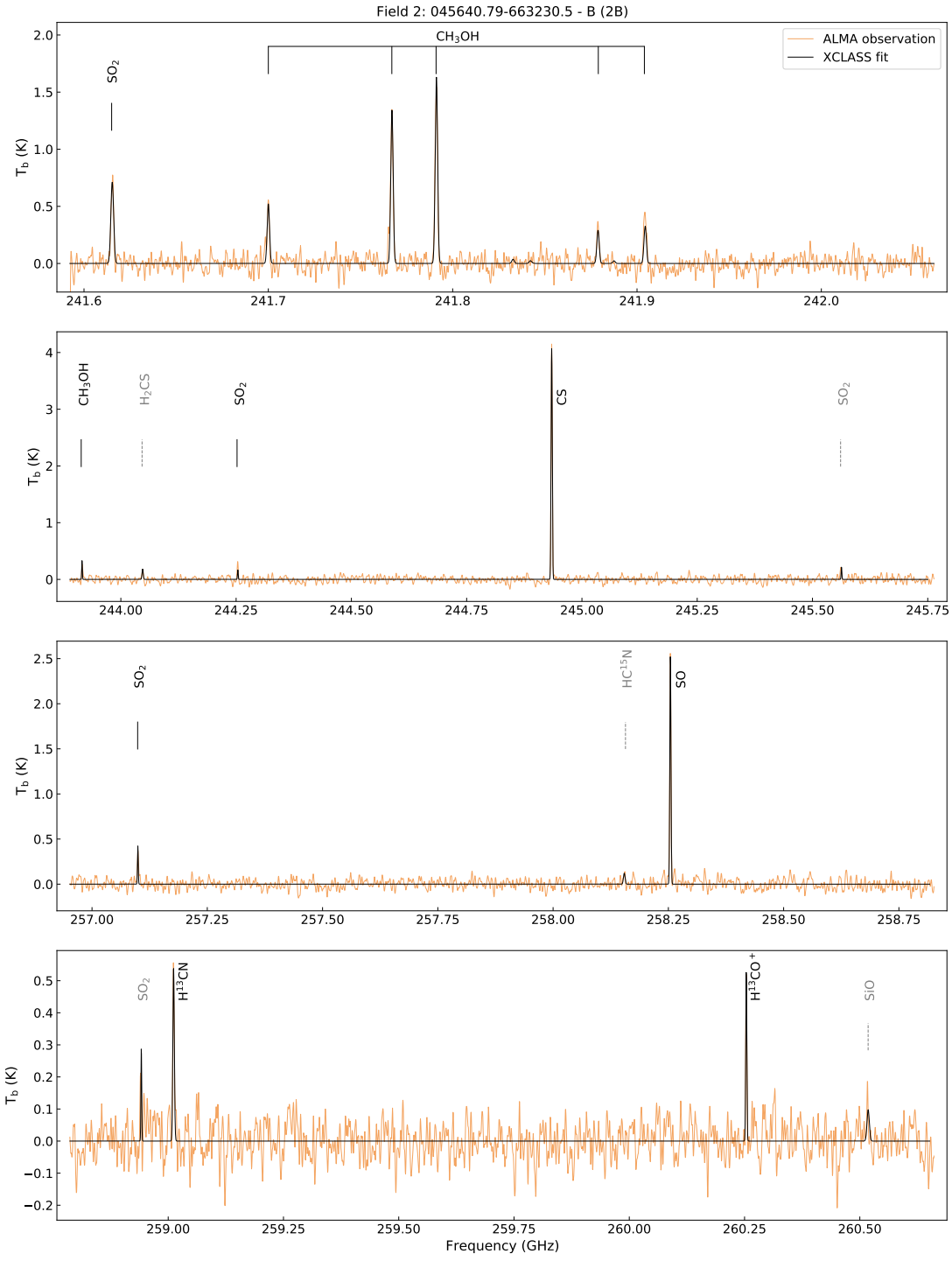
(a)

Figure B.1: ALMA Band 6 observed spectra toward source 1A overlaid with the best-fit XCLASS model. Molecular transitions with definite detections (S/N $>$ 5) are represented by solid black lines, while those with tentative detections (3 $<$ S/N $<$ 5) are denoted by dotted gray lines. Dotted red lines indicate transitions of molecules for which abundance upper limits are provided. (See Section 3.3.1 for more details.)



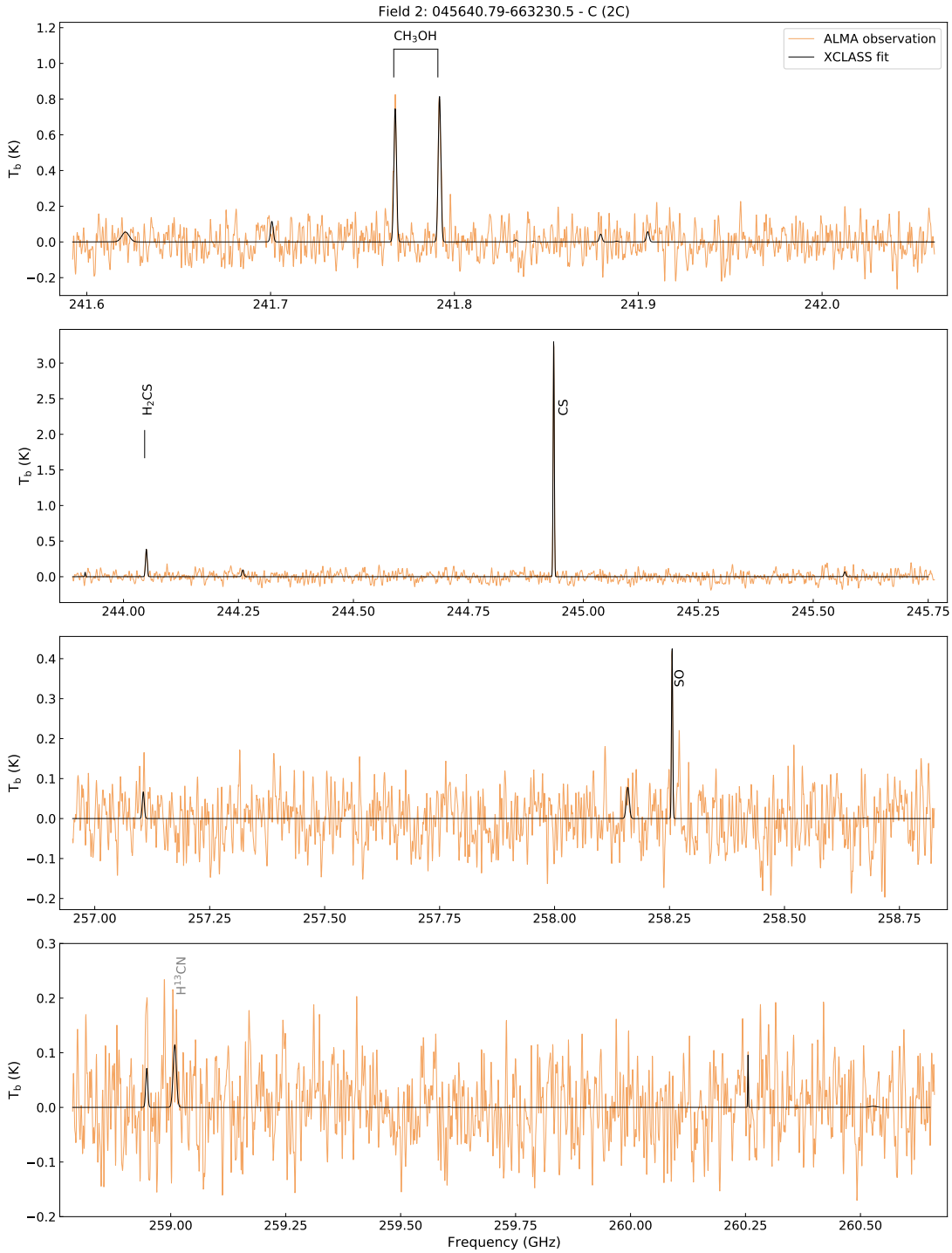
(a)

Figure B.2: Same as Fig. B.1 but for source 2A.



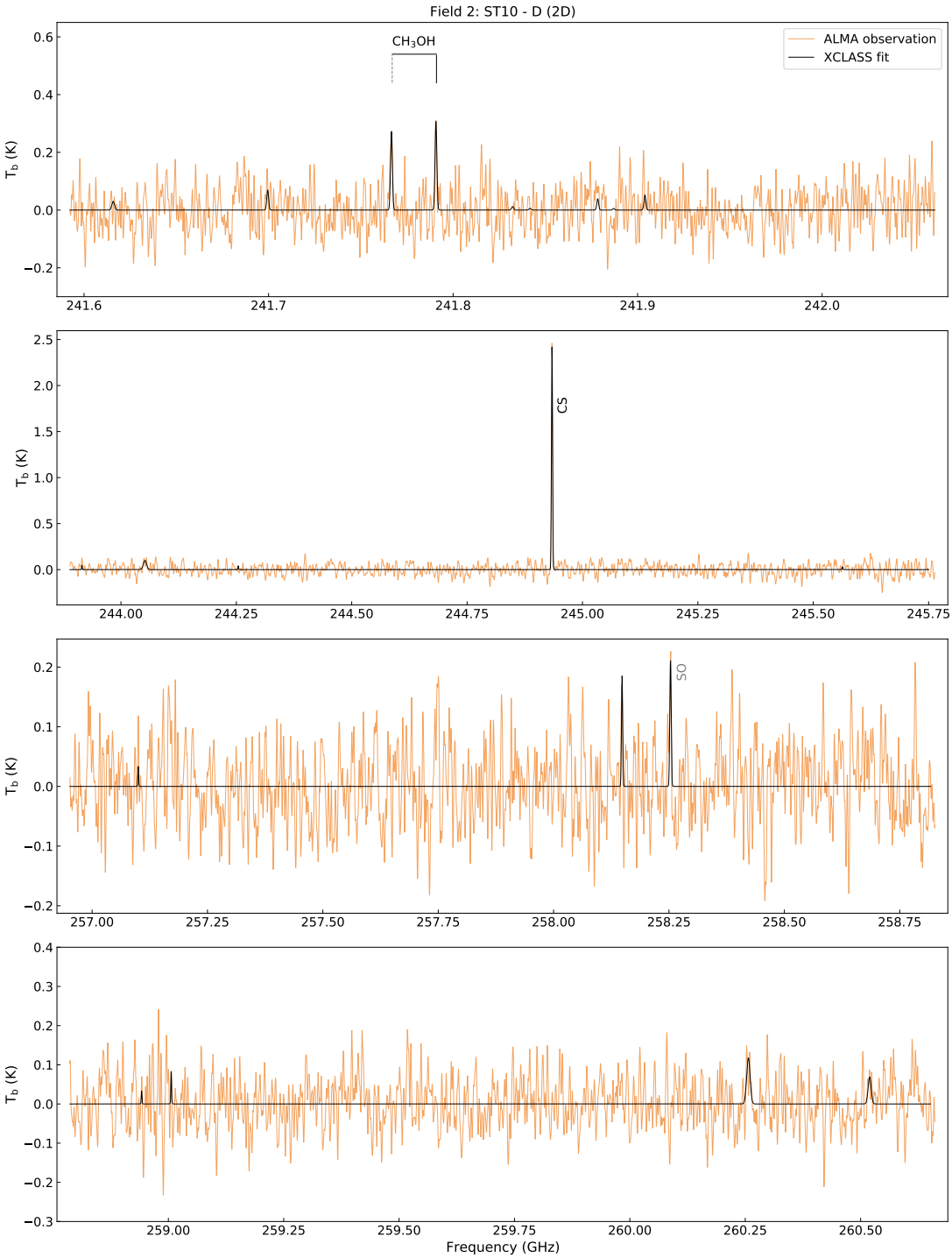
(b)

Figure B.2: Same as Fig. B.1 but for source 2B.



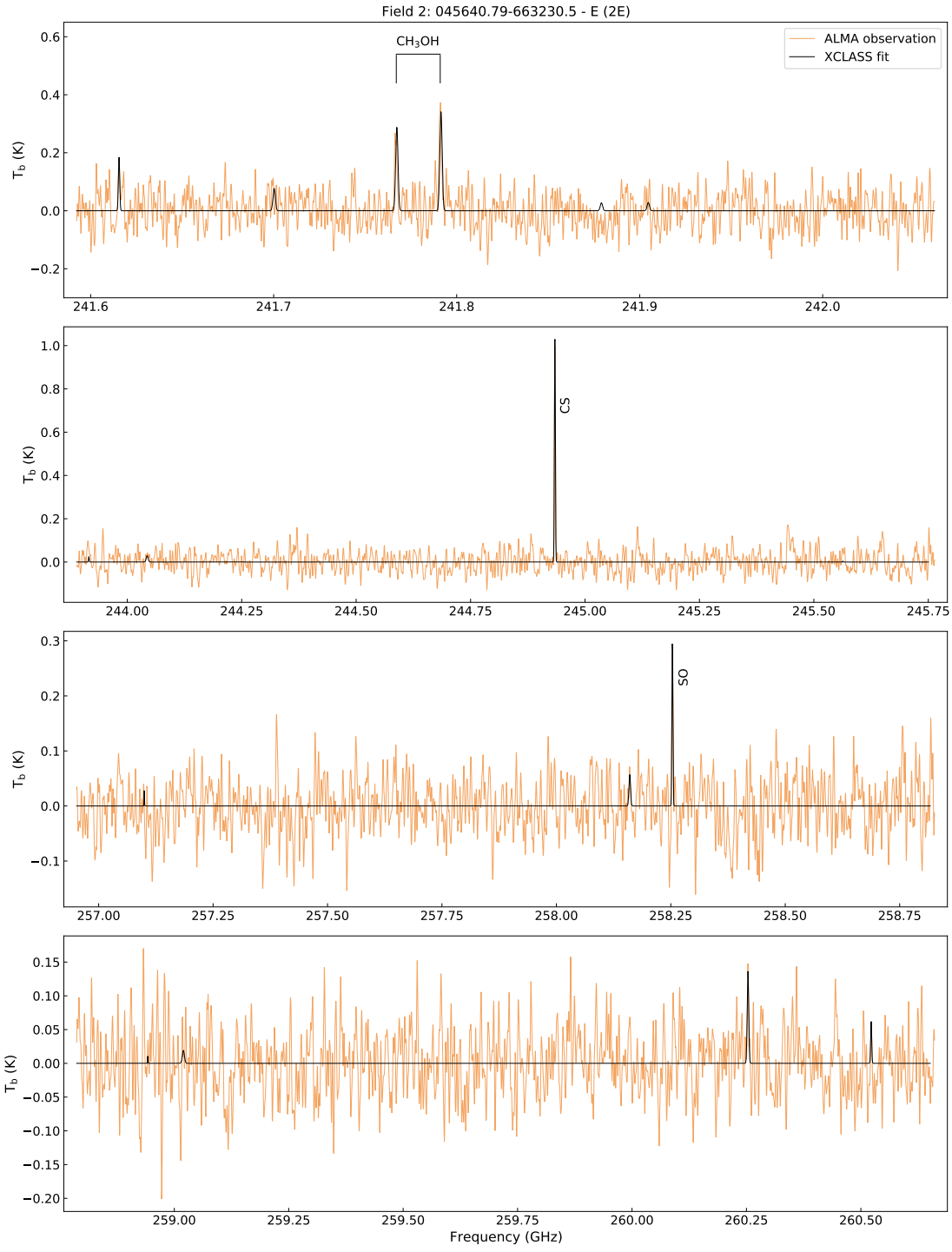
(c)

Figure B.2: Same as Fig. B.1 but for source 2C.



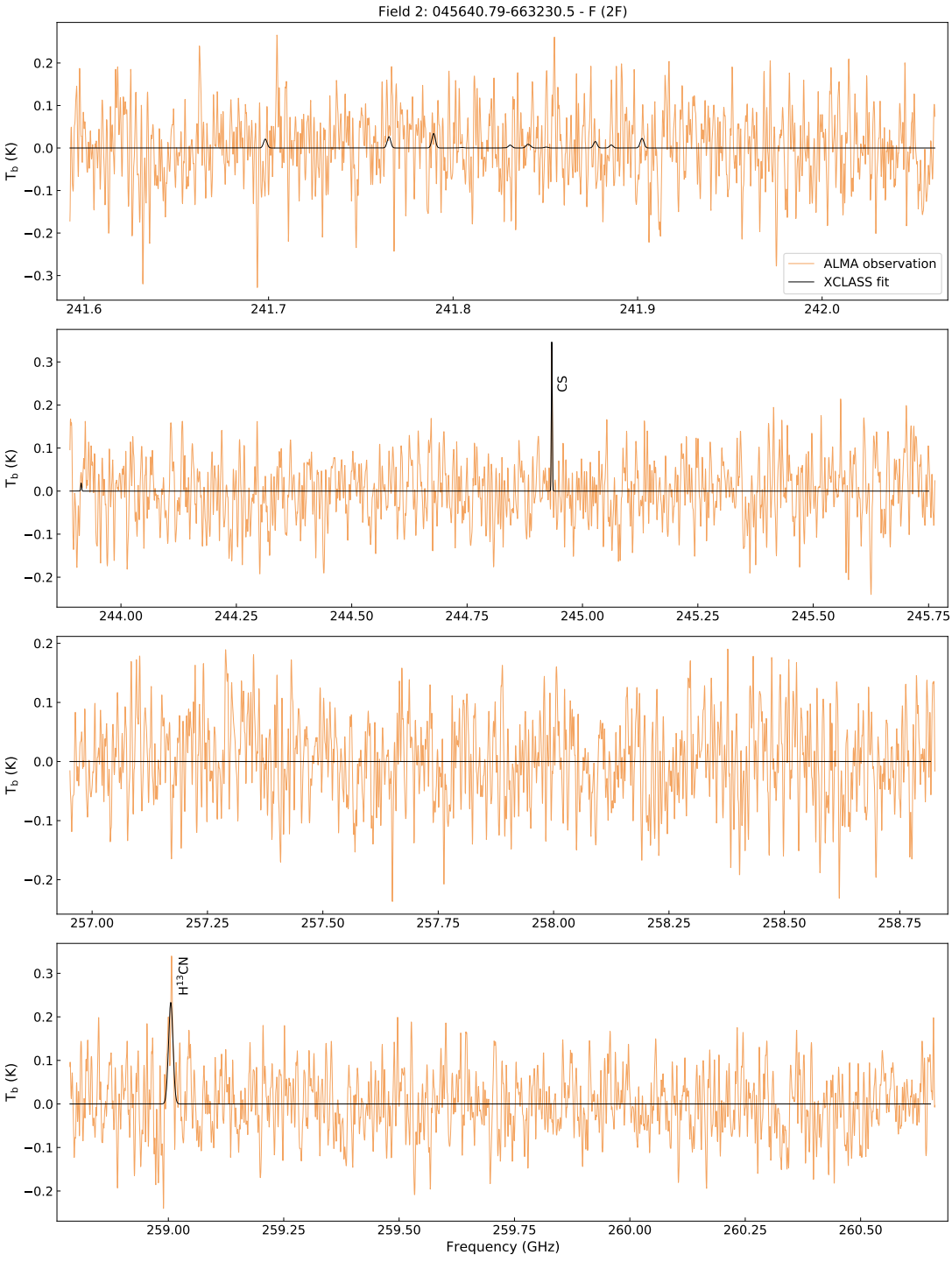
(d)

Figure B.2: Same as Fig. B.1 but for source 2D.



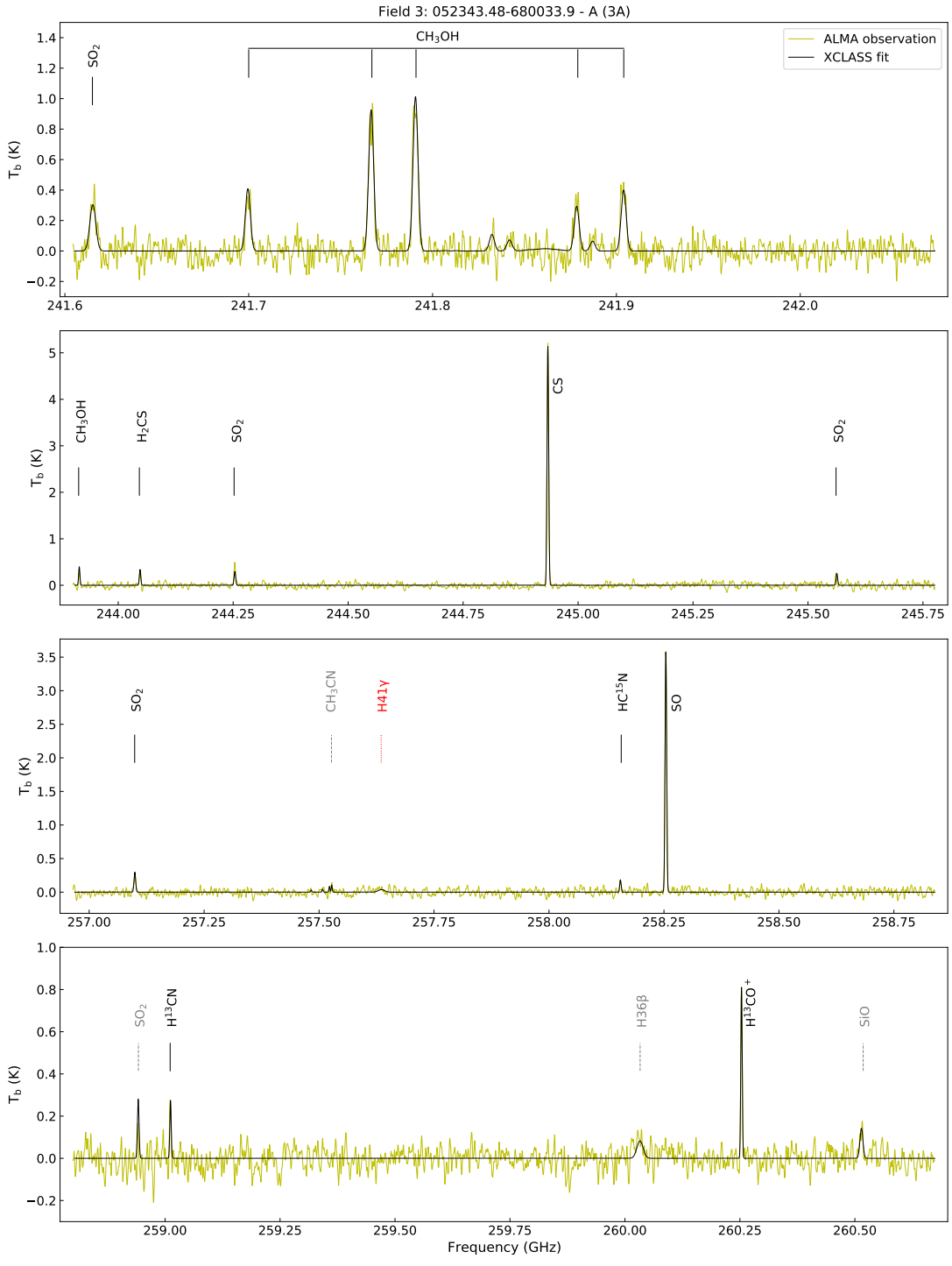
(e)

Figure B.2: Same as Fig. B.1 but for source 2E.



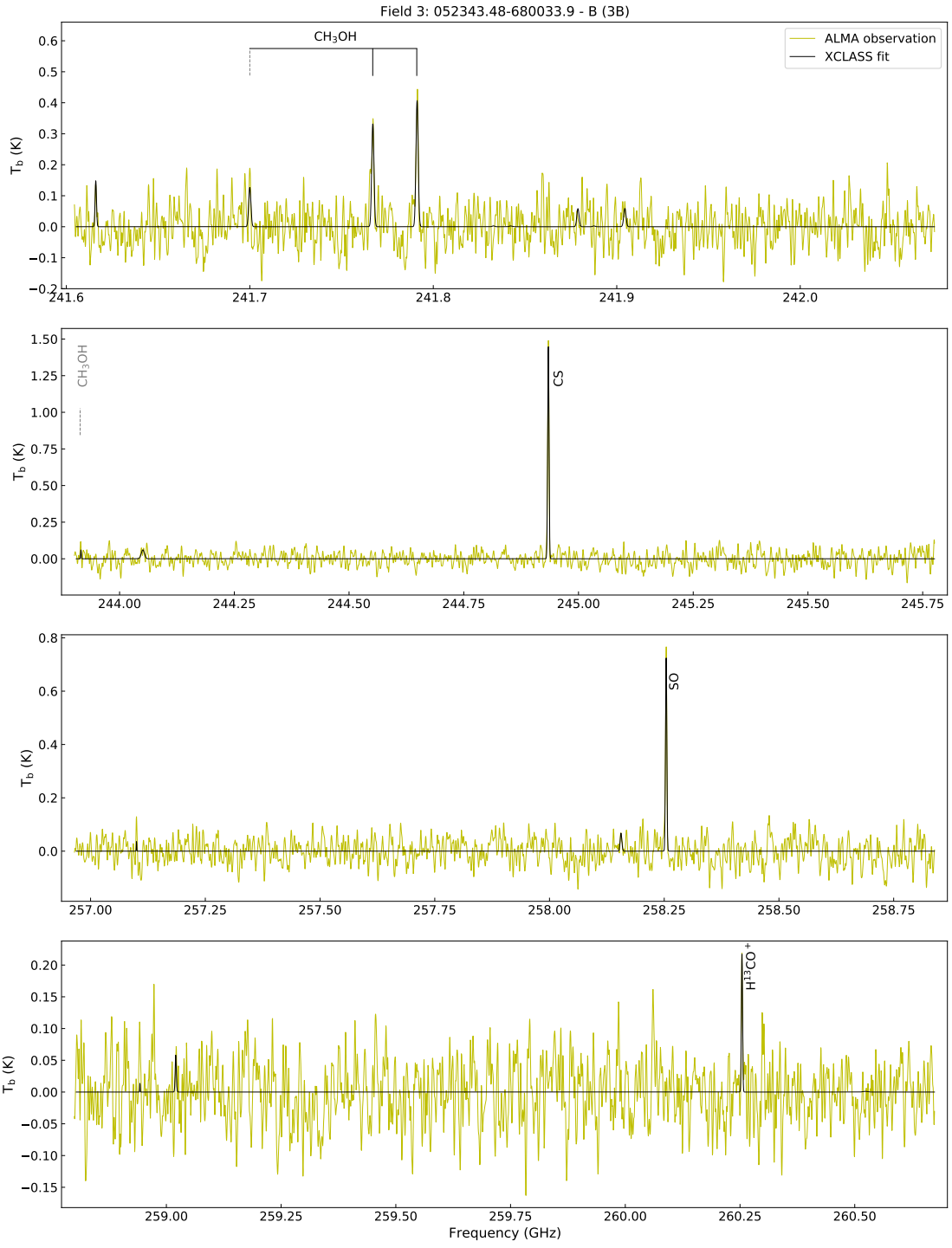
(f)

Figure B.2: Same as Fig. B.1 but for source 2F.



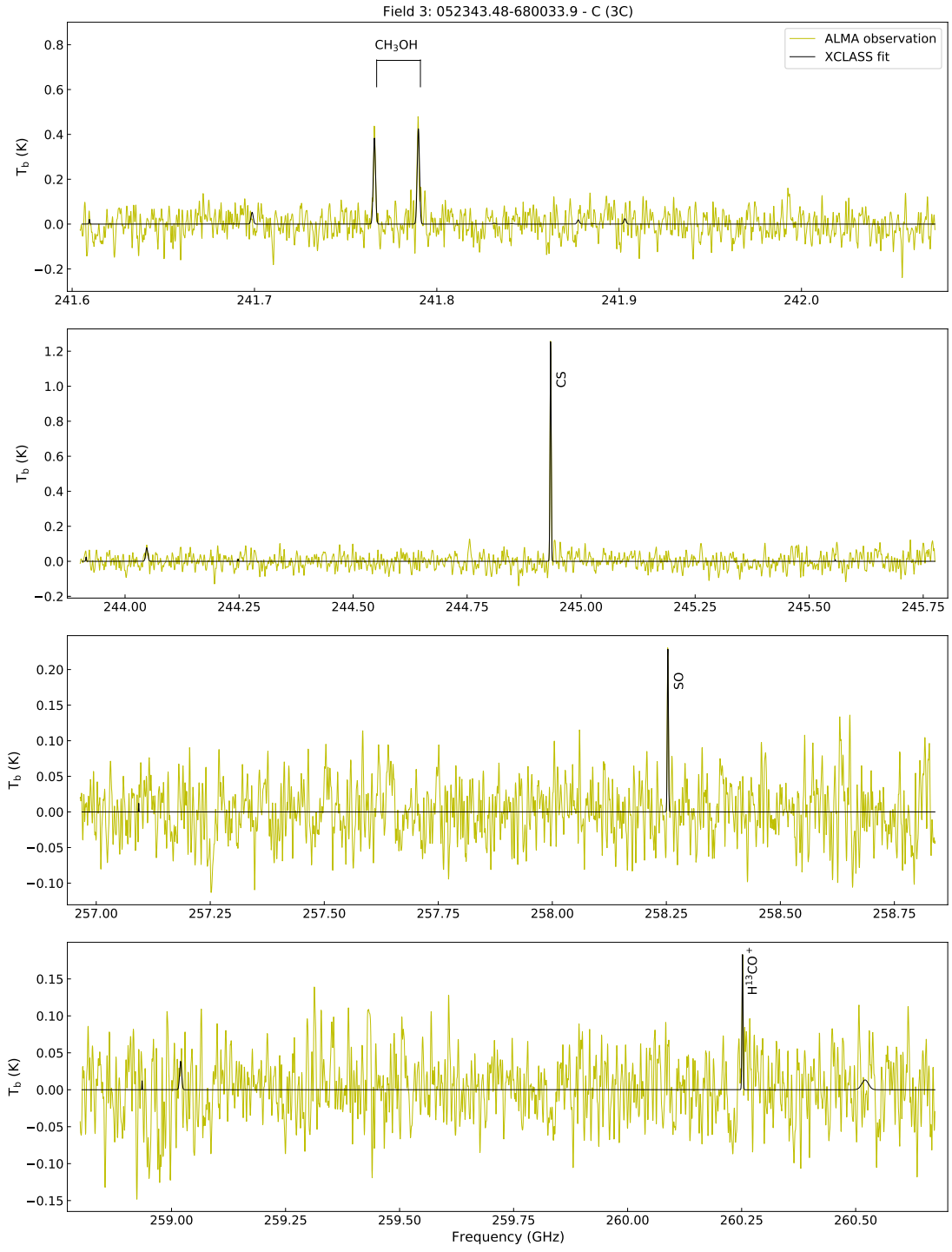
(a)

Figure B.3: Same as Fig. B.1 but for source 3A.



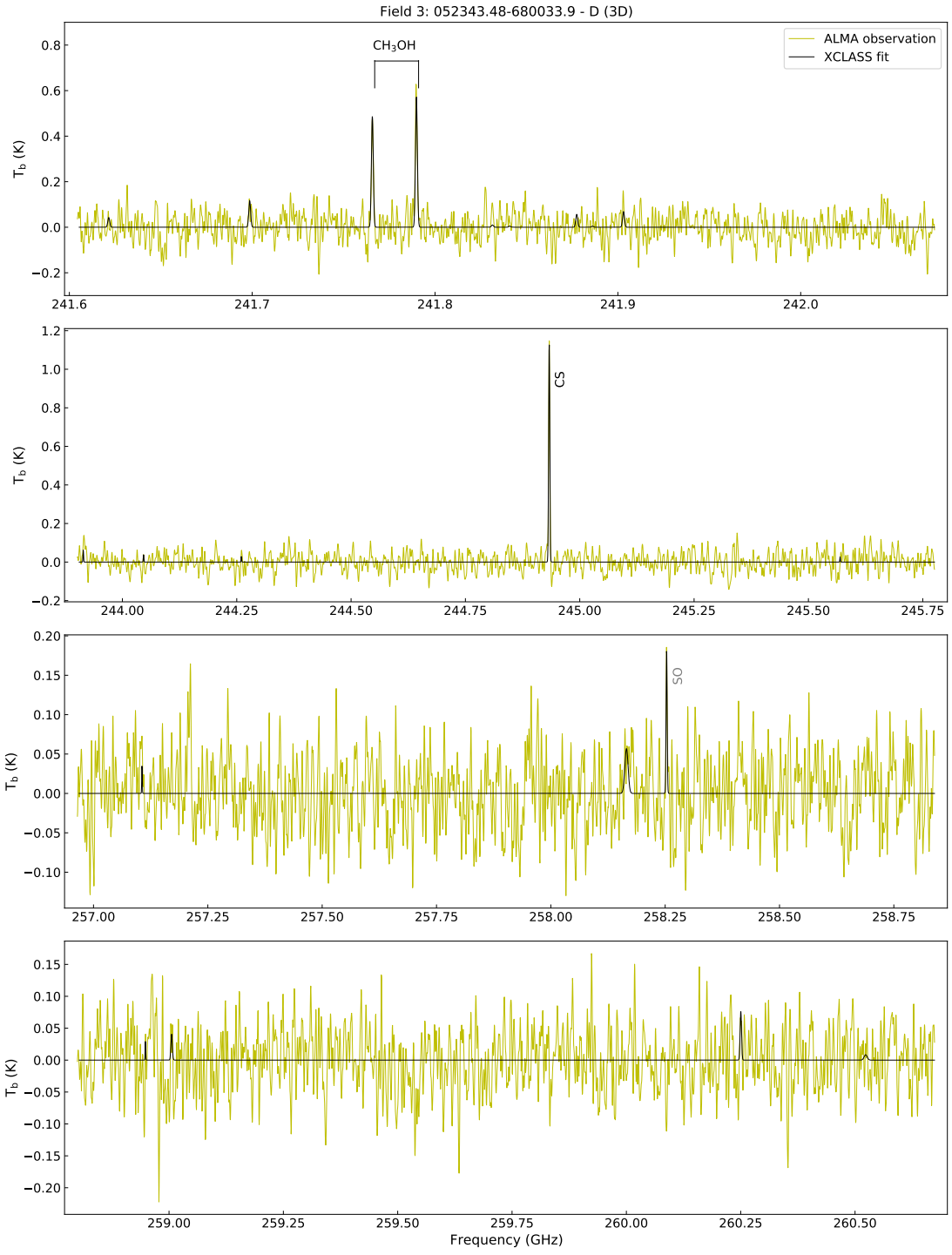
(b)

Figure B.3: Same as Fig. B.1 but for source 3B.



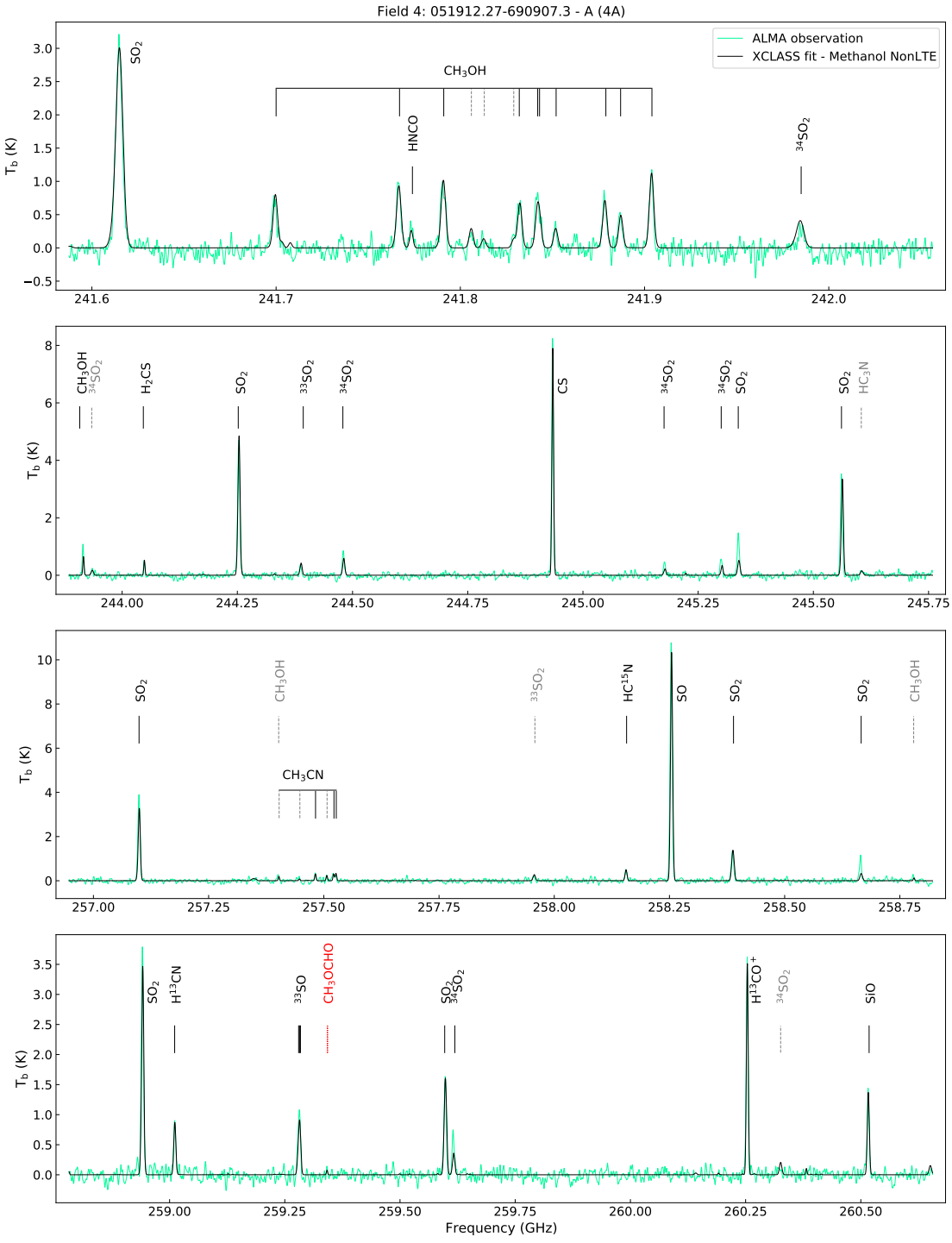
(c)

Figure B.3: Same as Fig. B.1 but for source 3C.



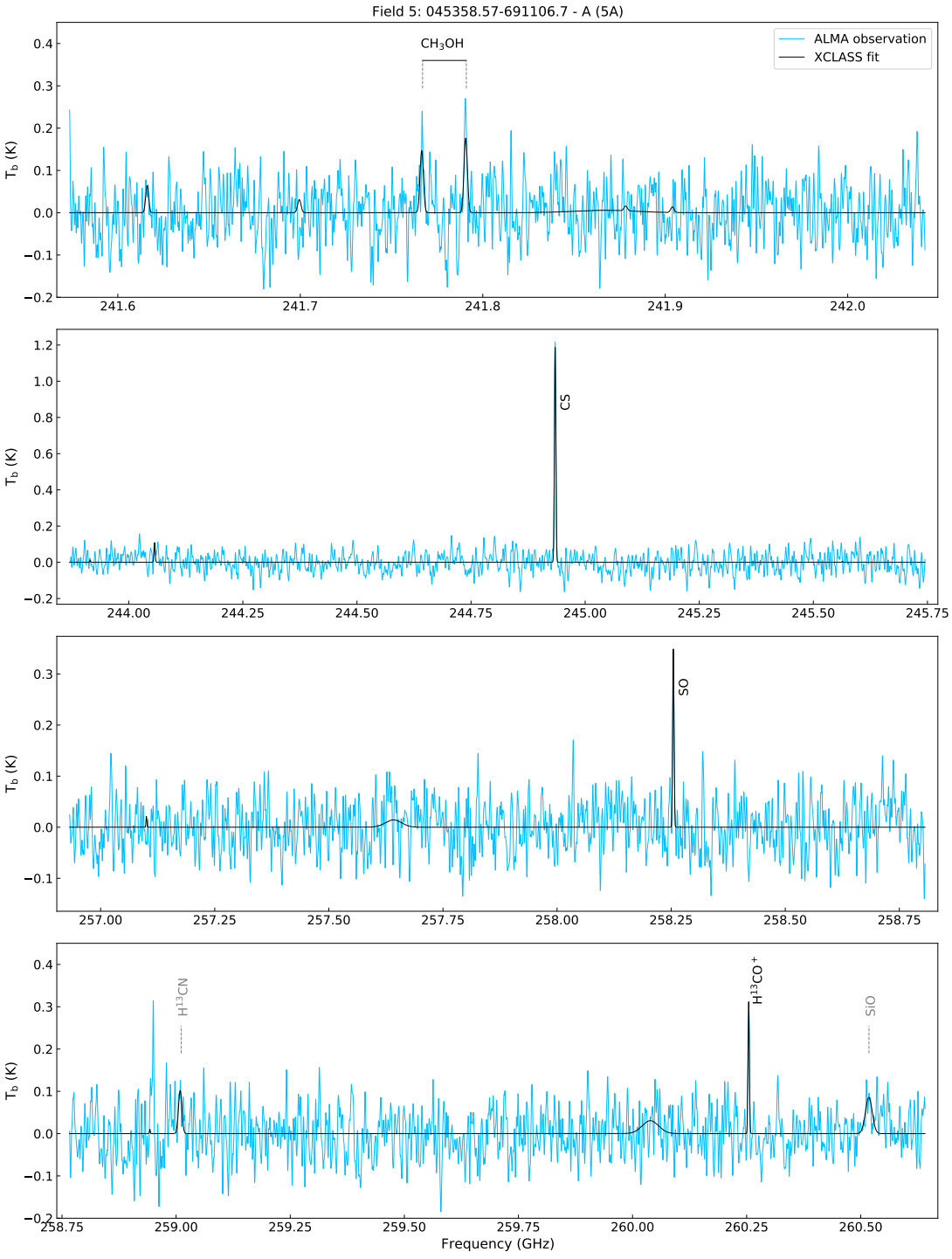
(d)

Figure B.3: Same as Fig. B.1 but for source 3D.



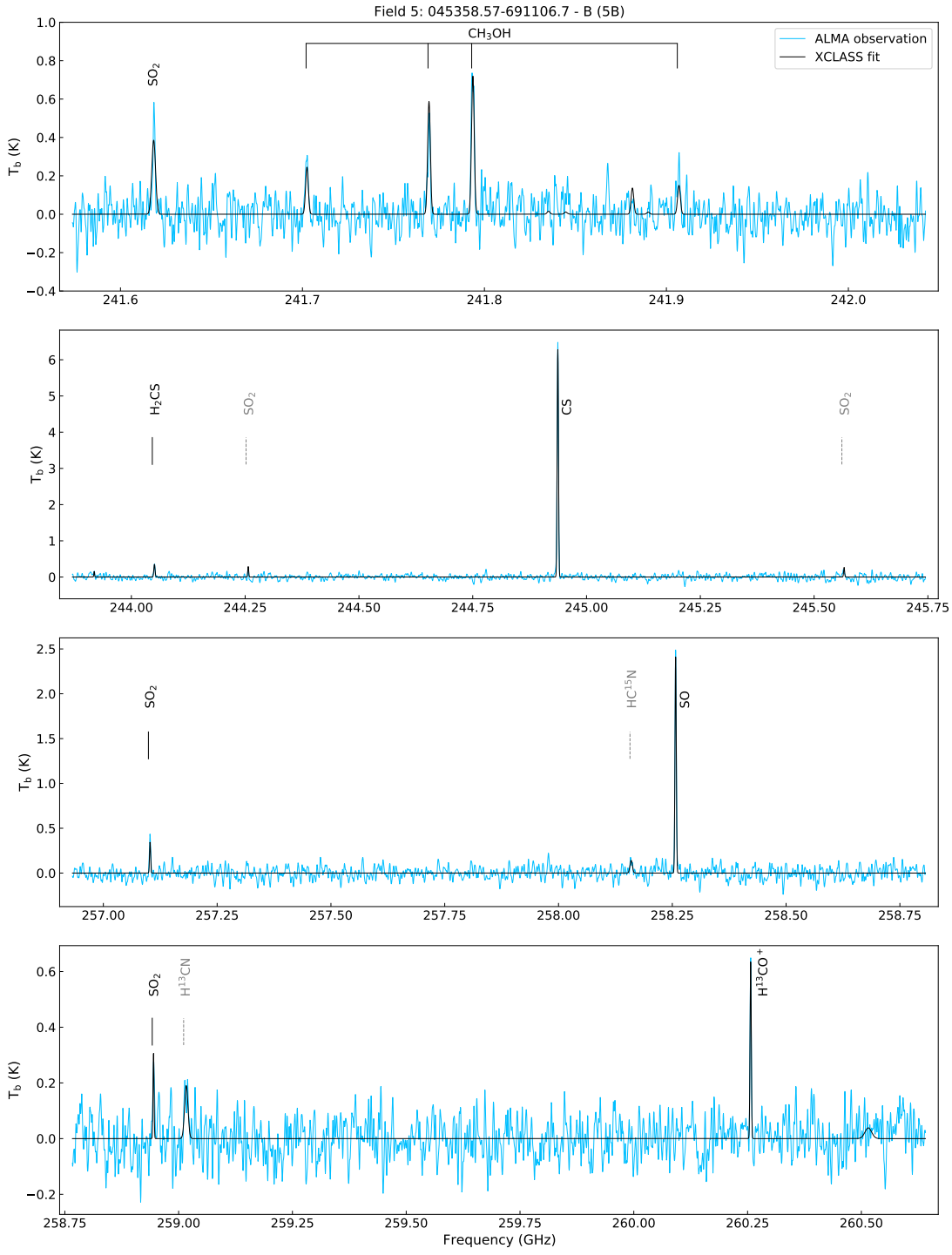
(a)

Figure B.4: Same as Fig. B.1 but for source 4A.



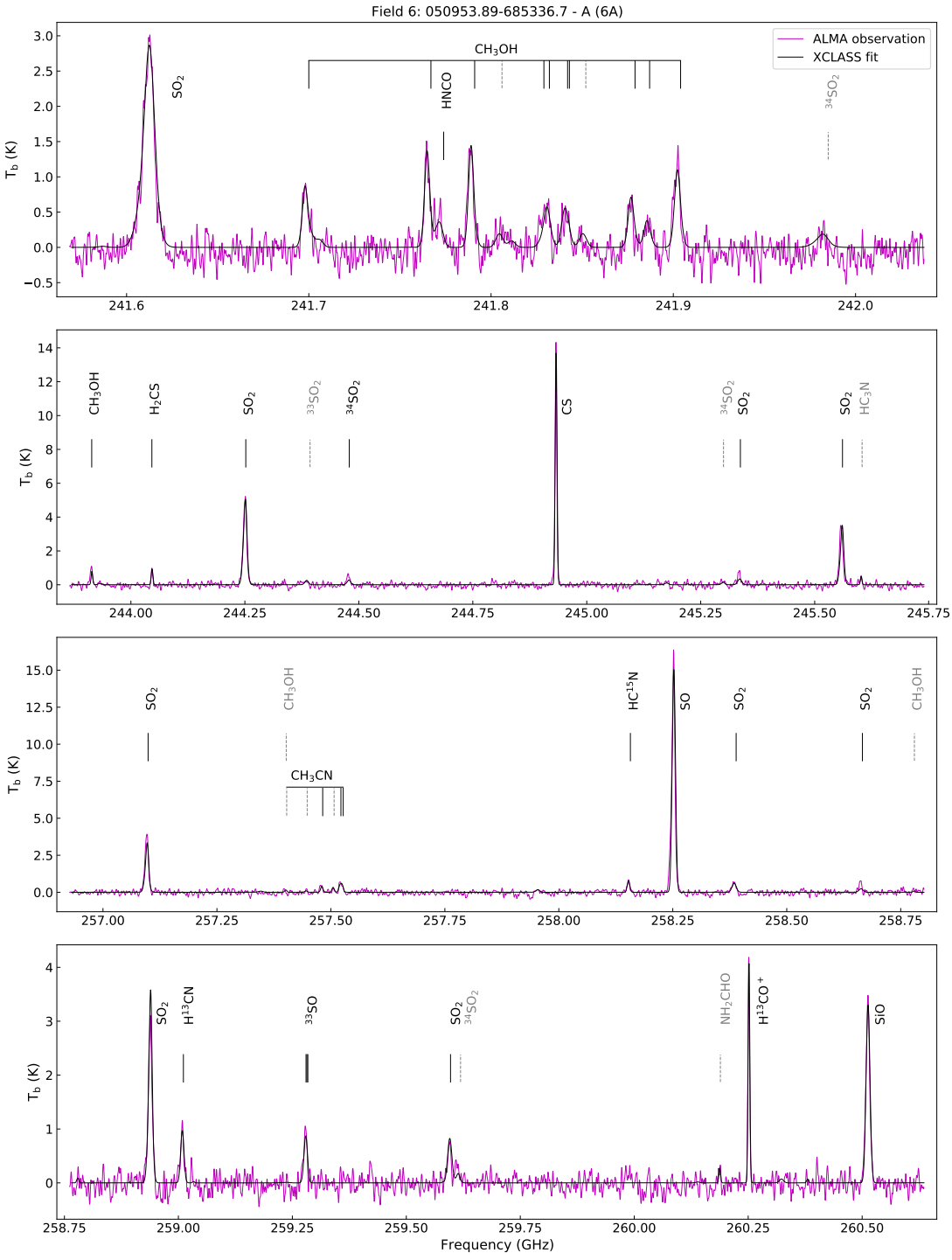
(a)

Figure B.5: Same as Fig. B.1 but for source 5A.



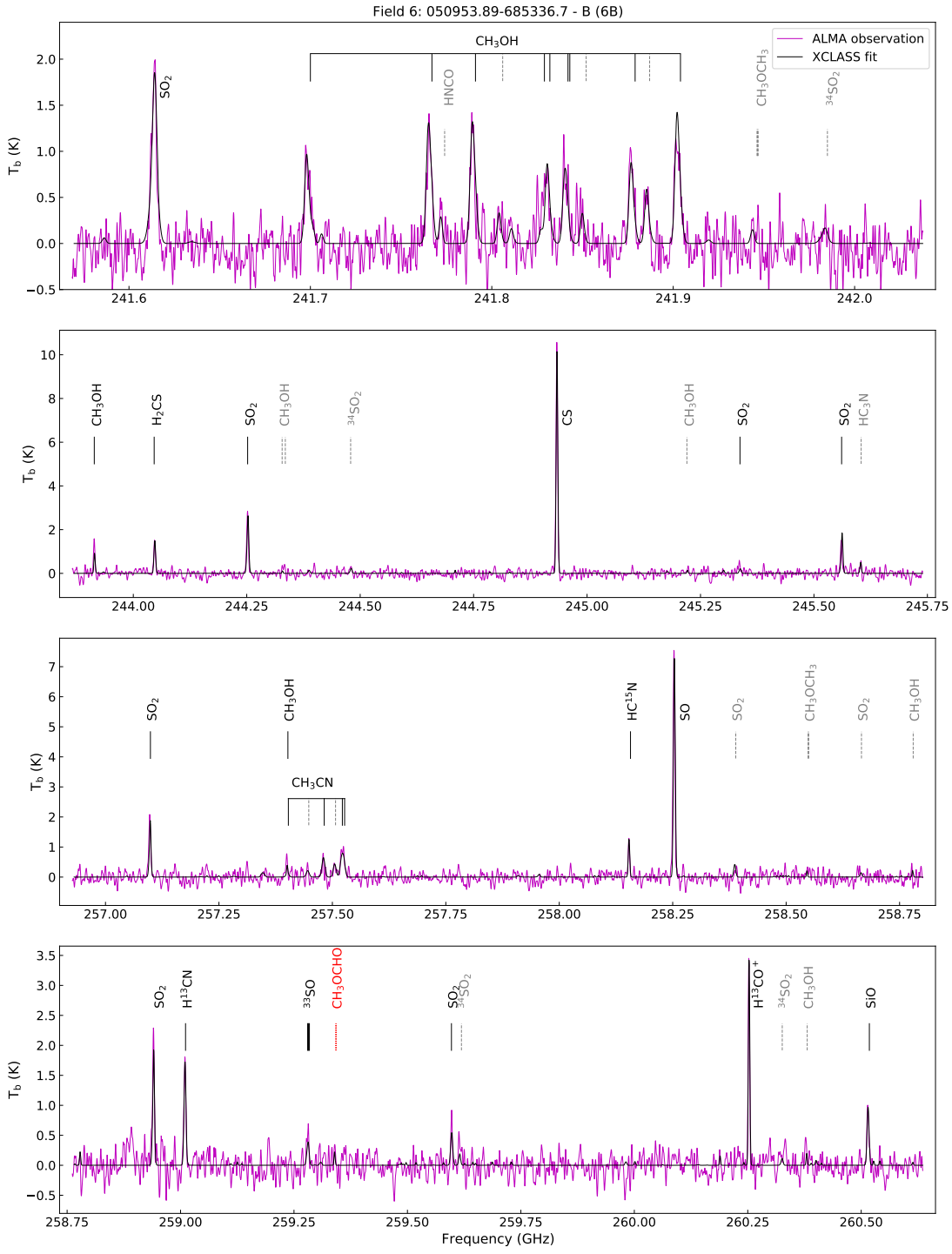
(b)

Figure B.5: Same as Fig. B.1 but for source 5B.



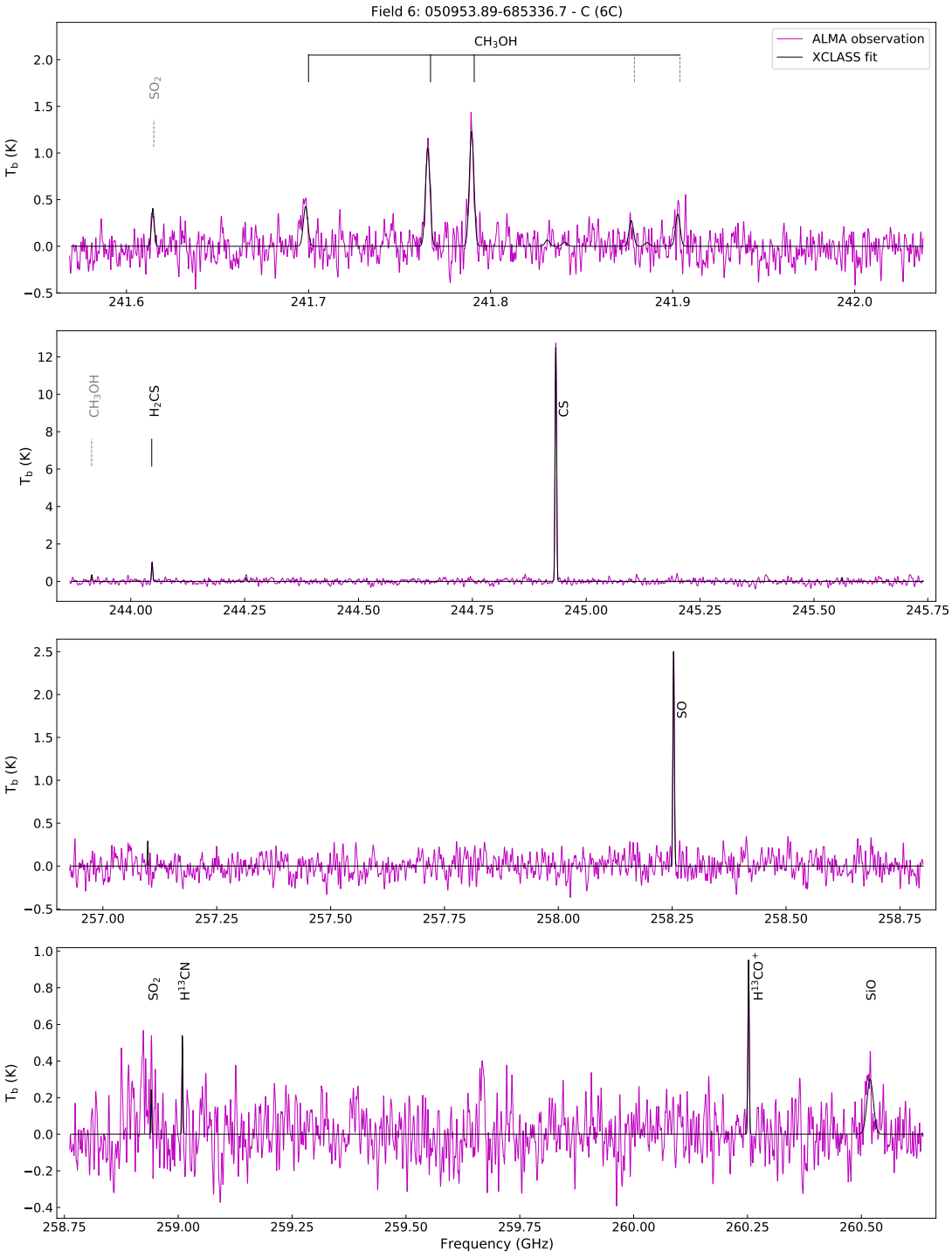
(a)

Figure B.6: Same as Fig. B.1 but for source 6A.



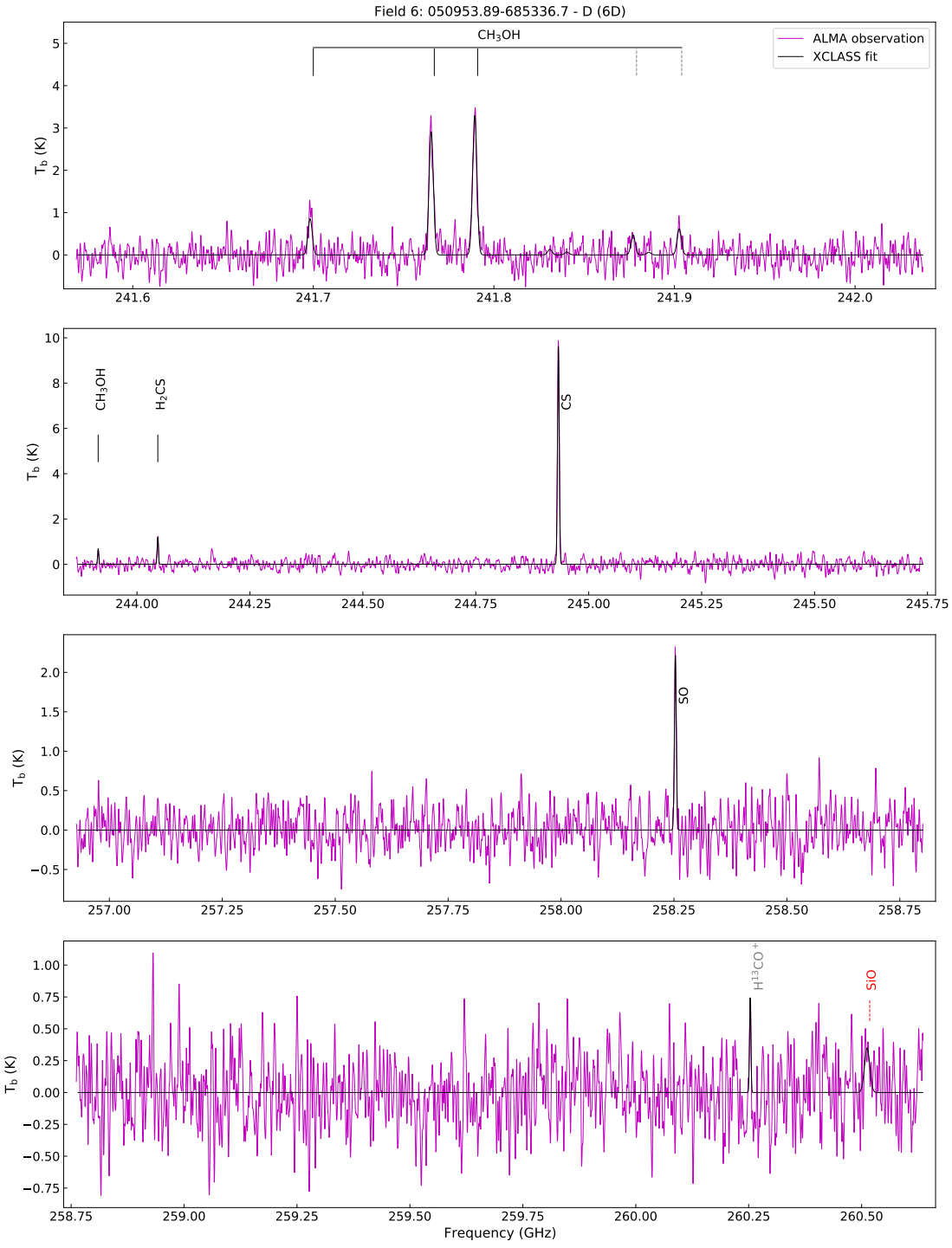
(b)

Figure B.6: Same as Fig. B.1 but for source 6B.



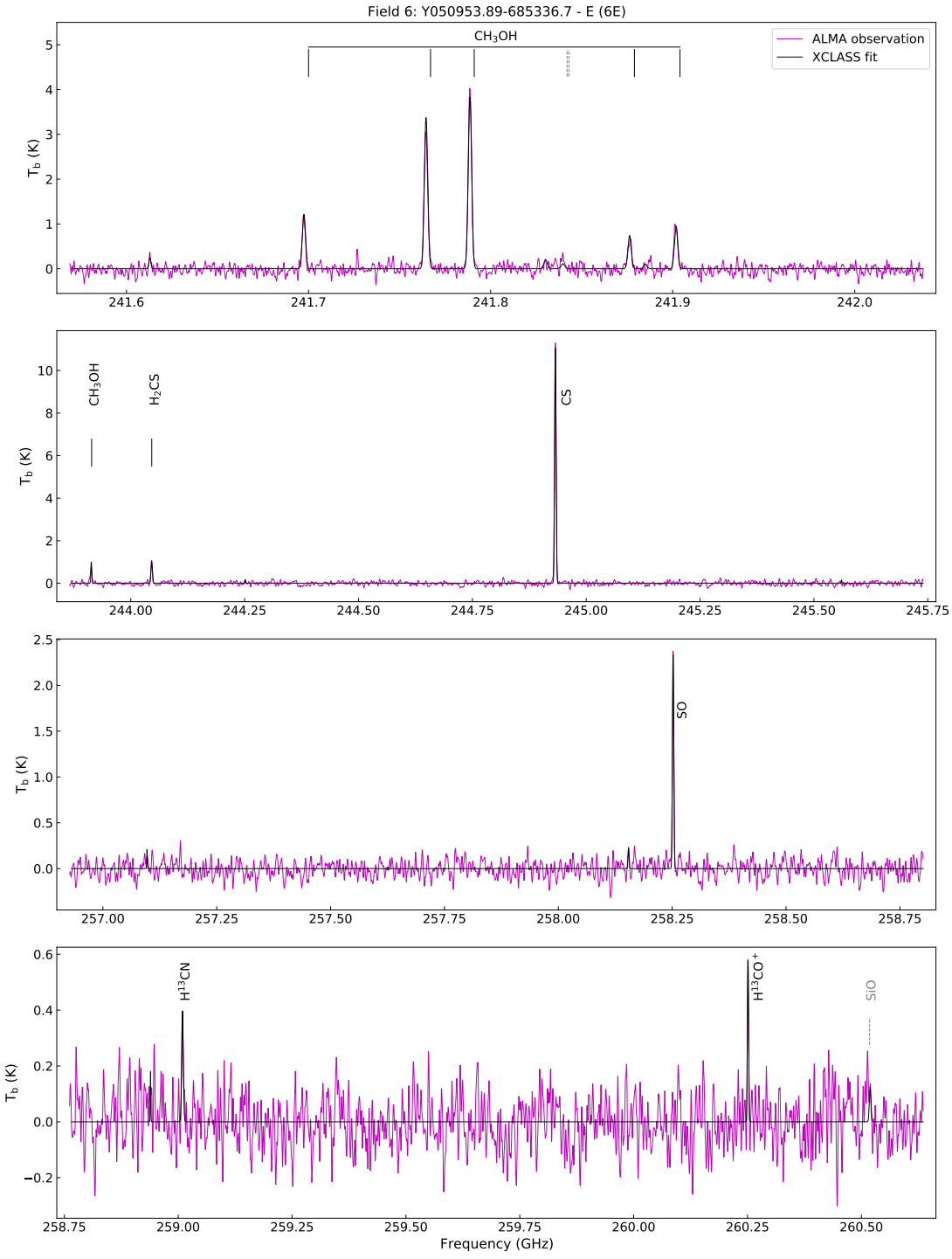
(c)

Figure B.6: Same as Fig. B.1 but for source 6C.



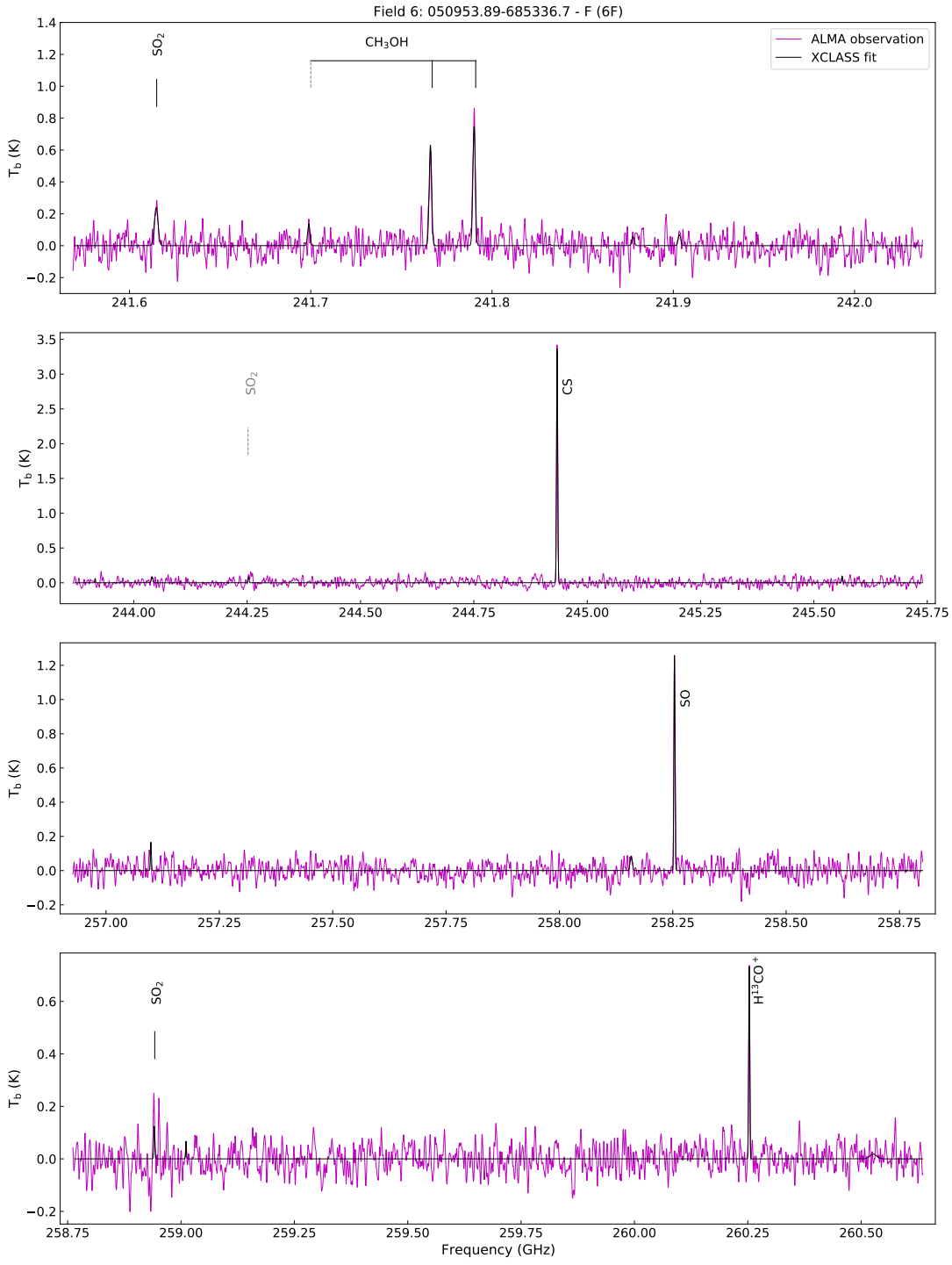
(d)

Figure B.6: Same as Fig. B.1 but for source 6D.



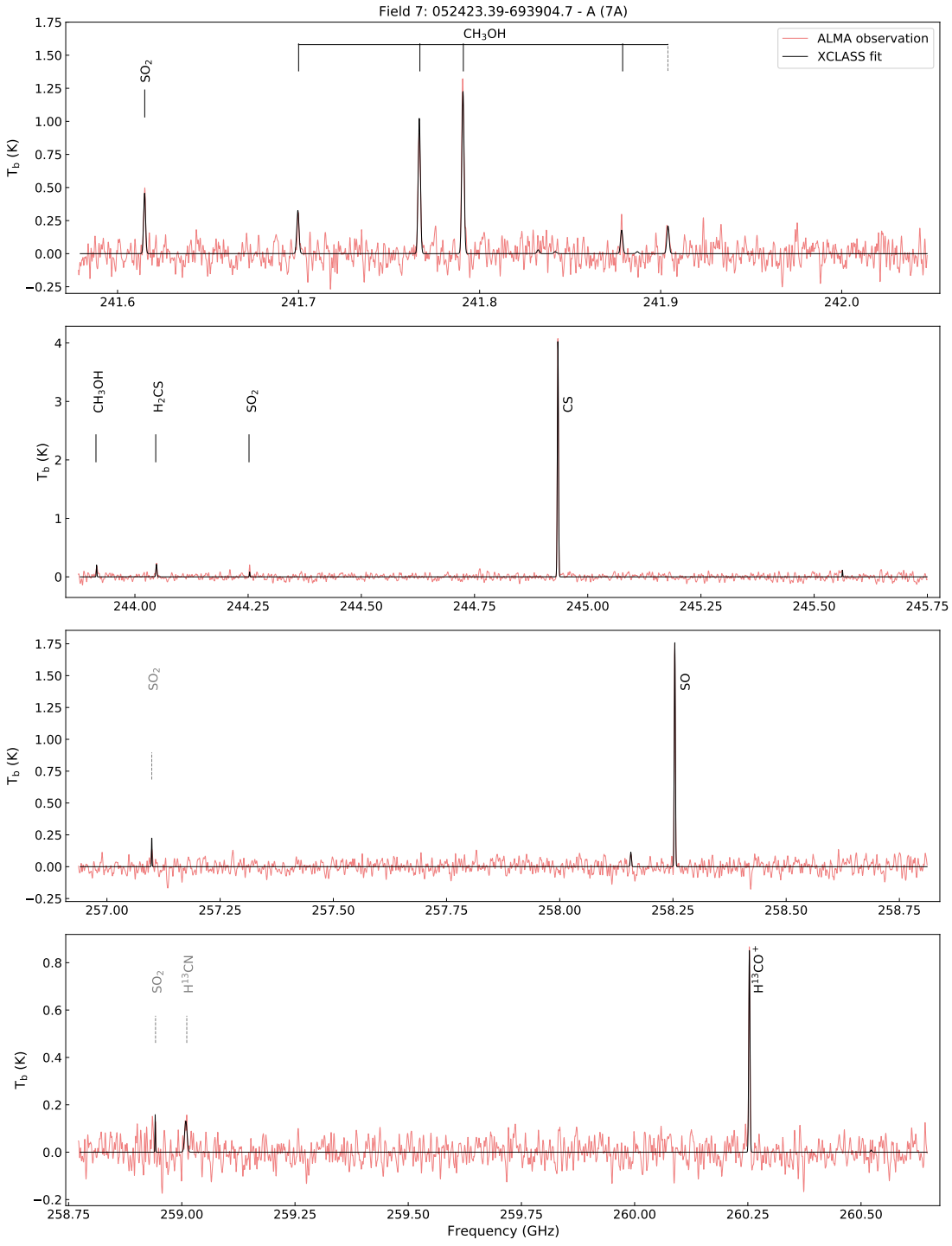
(e)

Figure B.6: Same as Fig. B.1 but for source 6E.



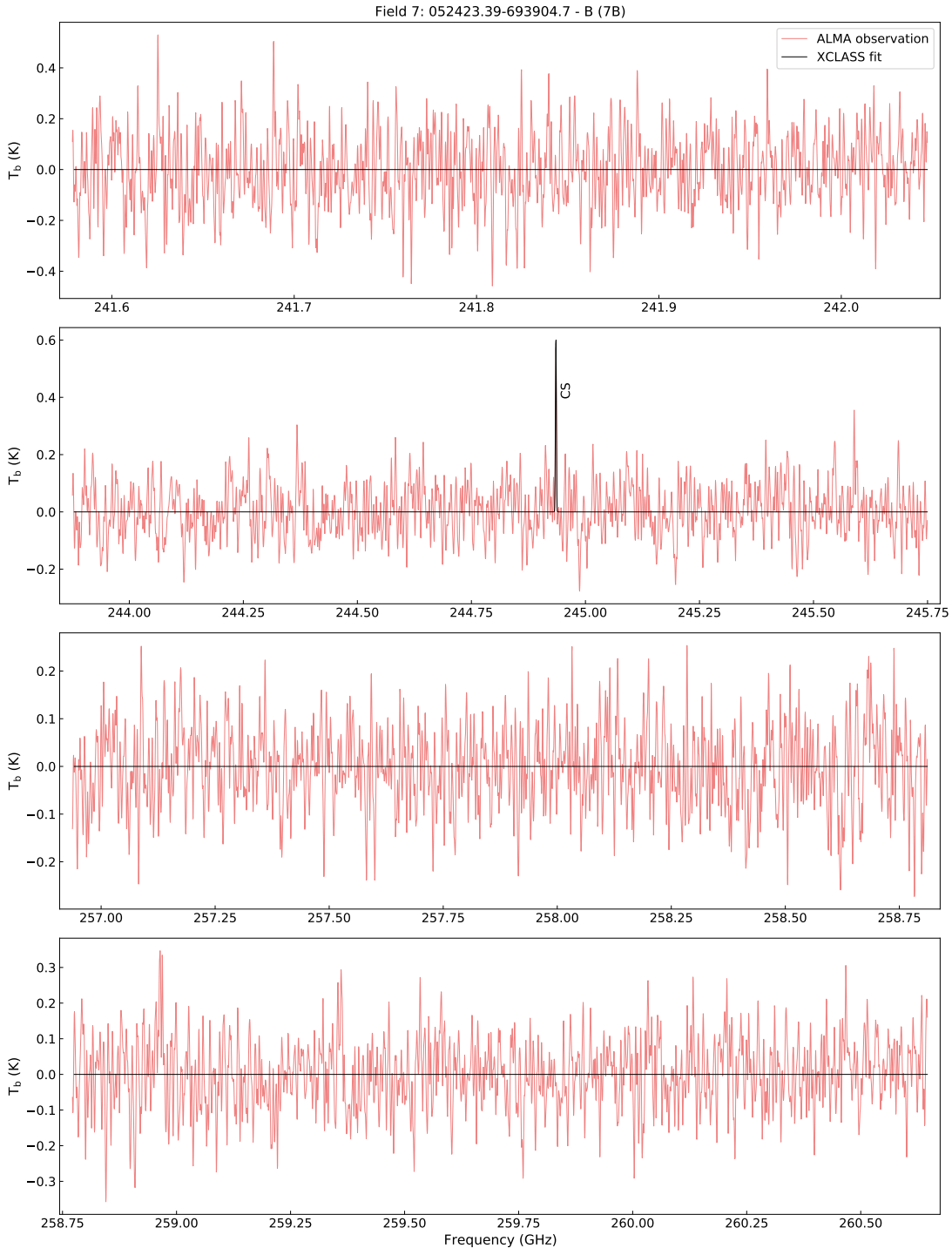
(f)

Figure B.6: Same as Fig. B.1 but for source 6F.



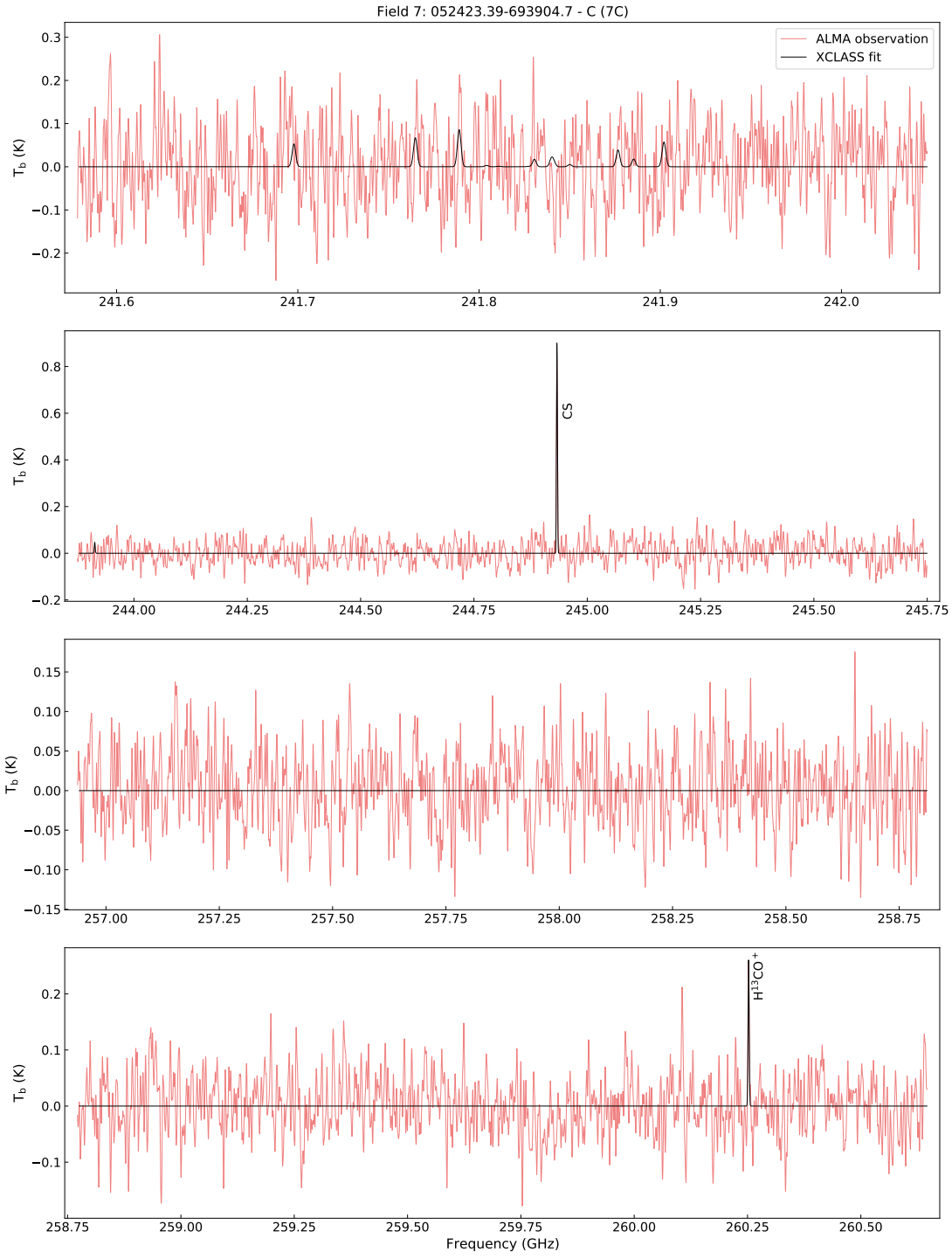
(a)

Figure B.7: Same as Fig. B.1 but for source 7A.



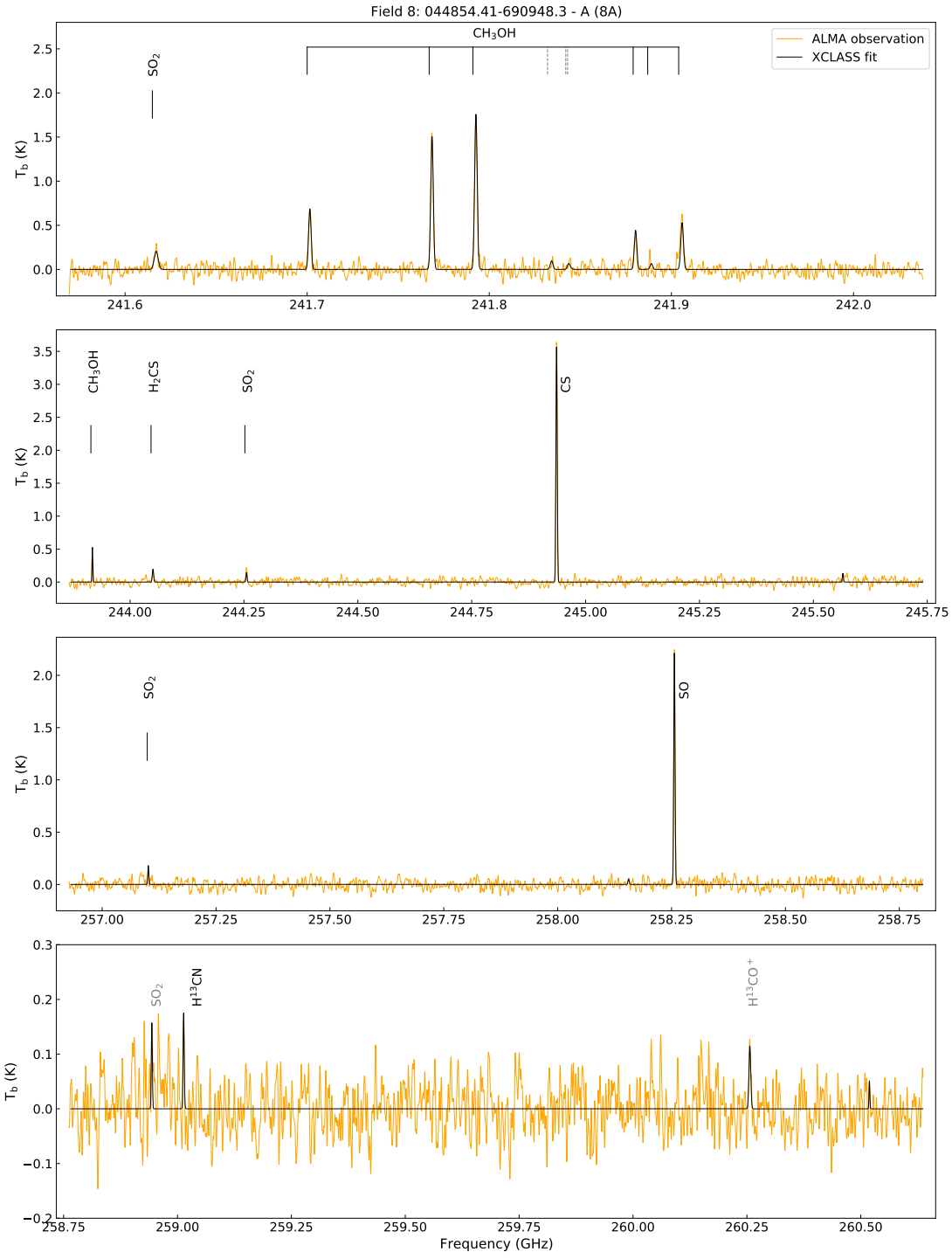
(b)

Figure B.7: Same as Fig. B.1 but for source 7B.



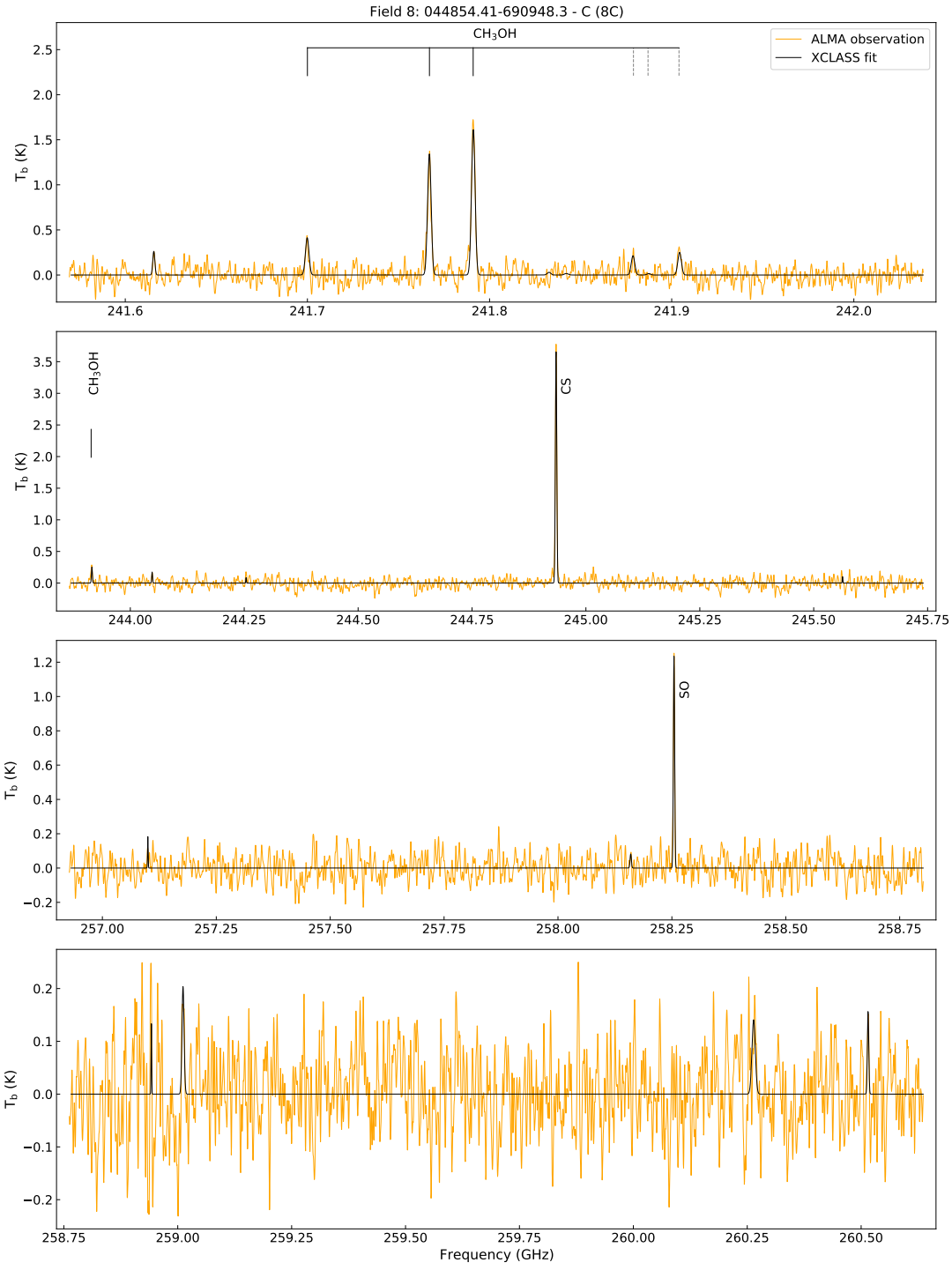
(c)

Figure B.7: Same as Fig. B.1 but for source 7C.



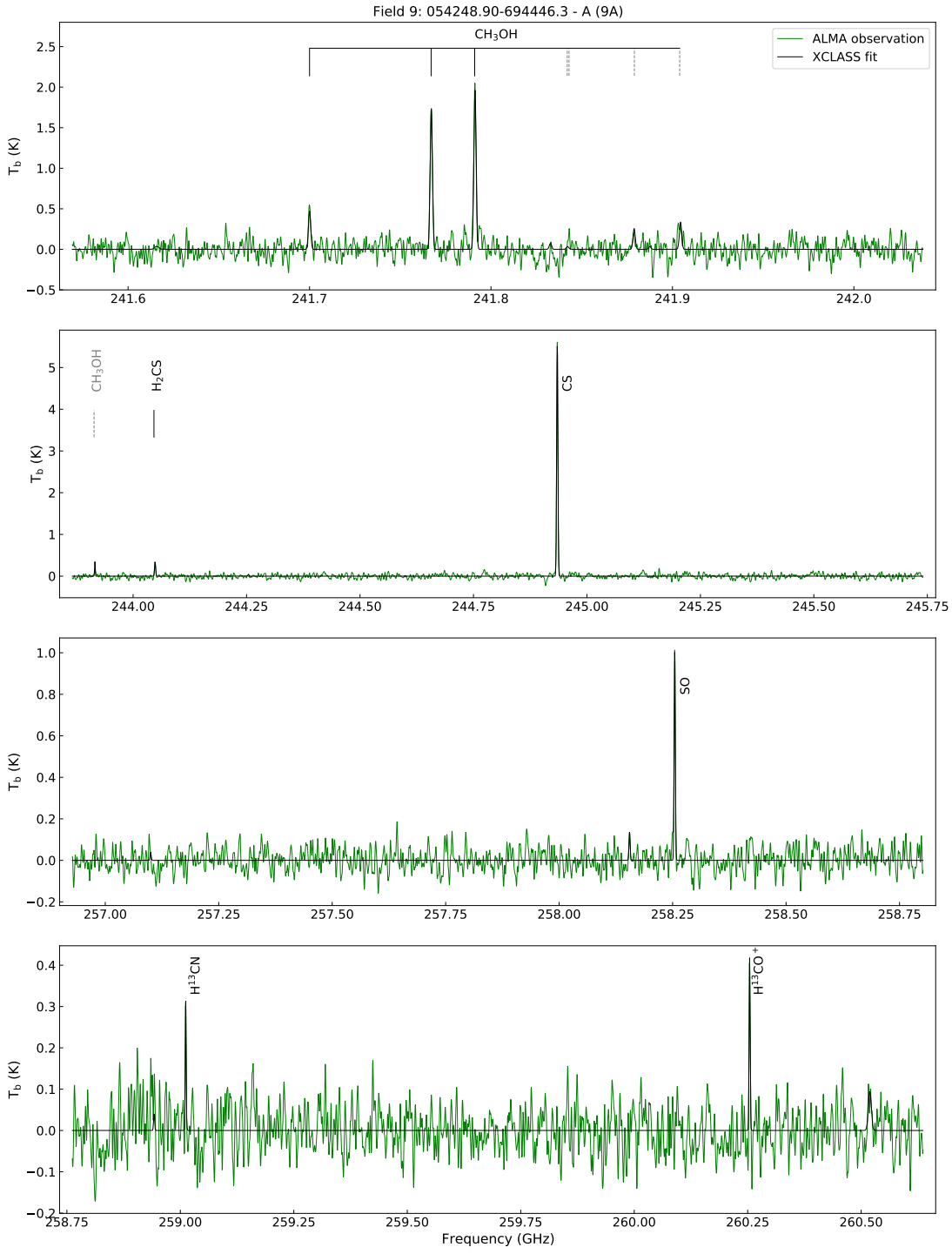
(a)

Figure B.8: Same as Fig. B.1 but for source 8A.



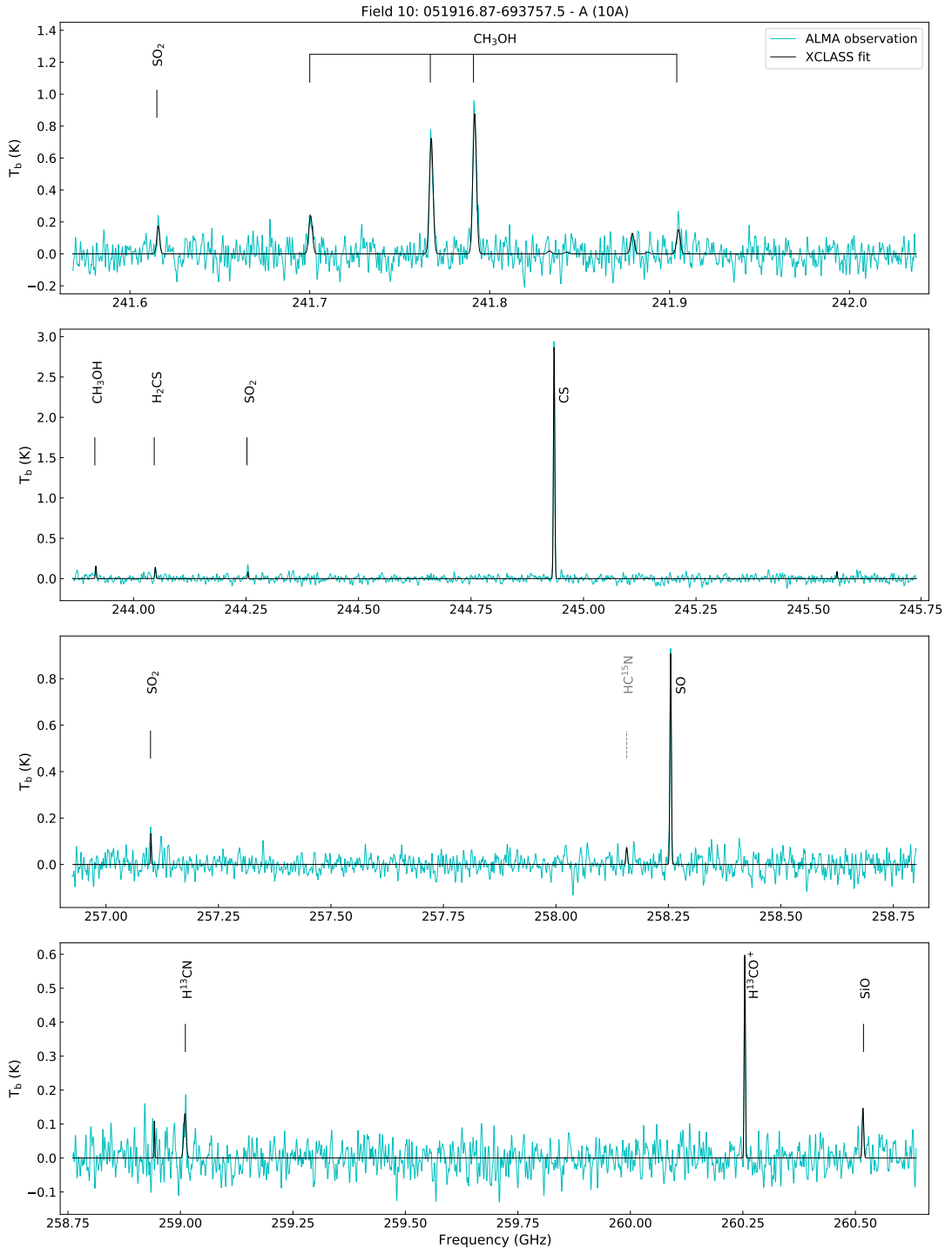
(b)

Figure B.8: Same as Fig. B.1 but for source 8C.



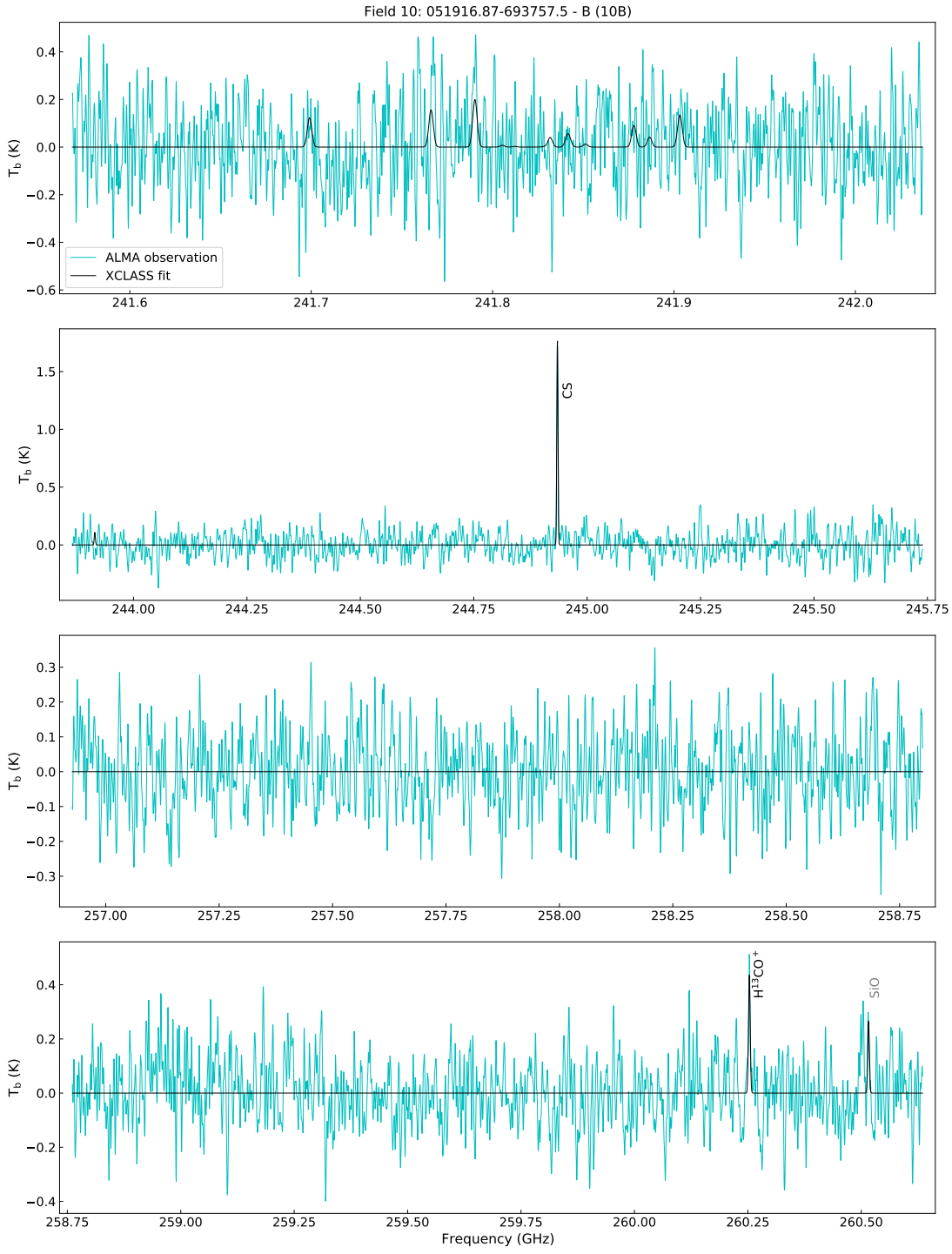
(a)

Figure B.9: Same as Fig. B.1 but for source 9A.



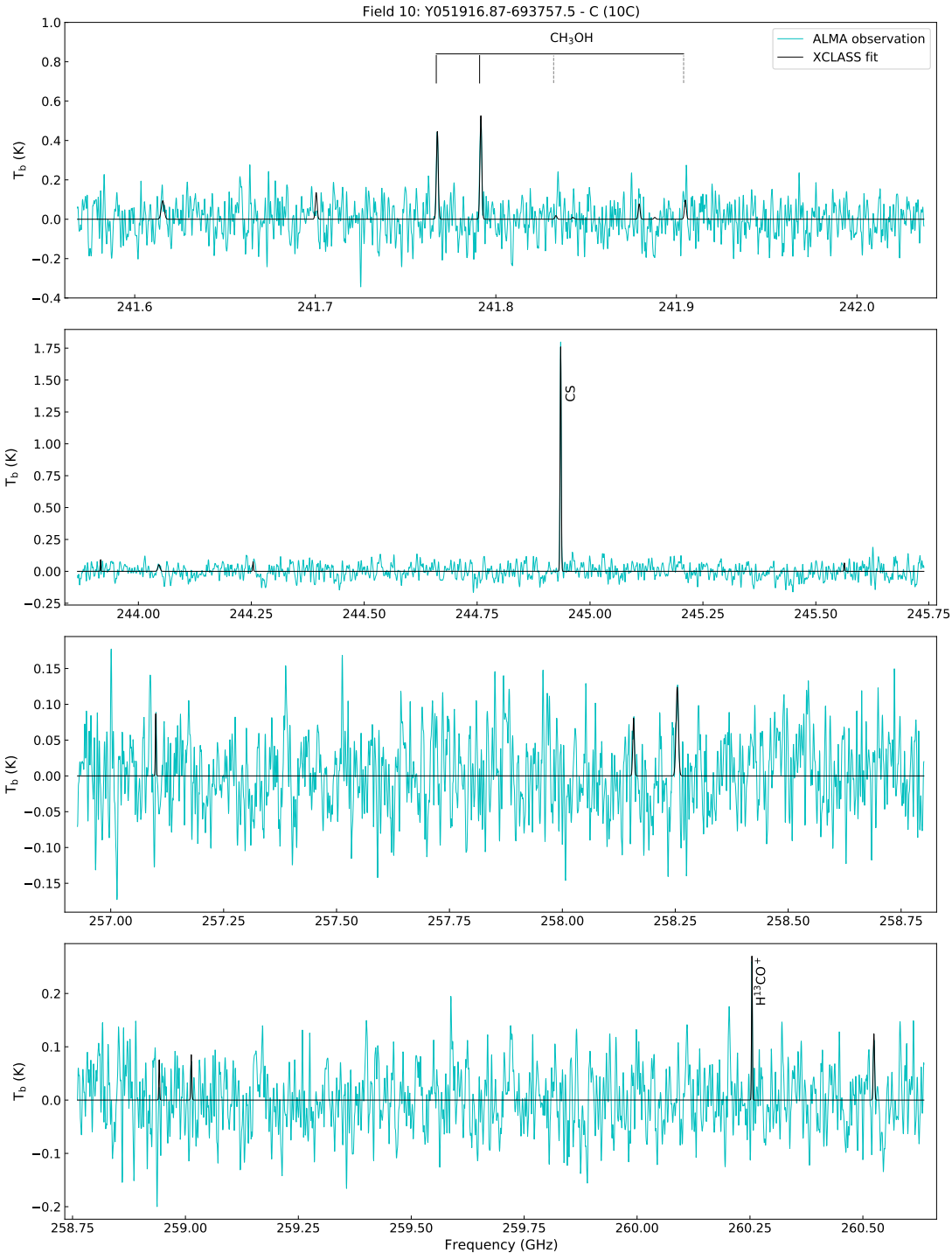
(a)

Figure B.10: Same as Fig. B.1 but for source 10A.



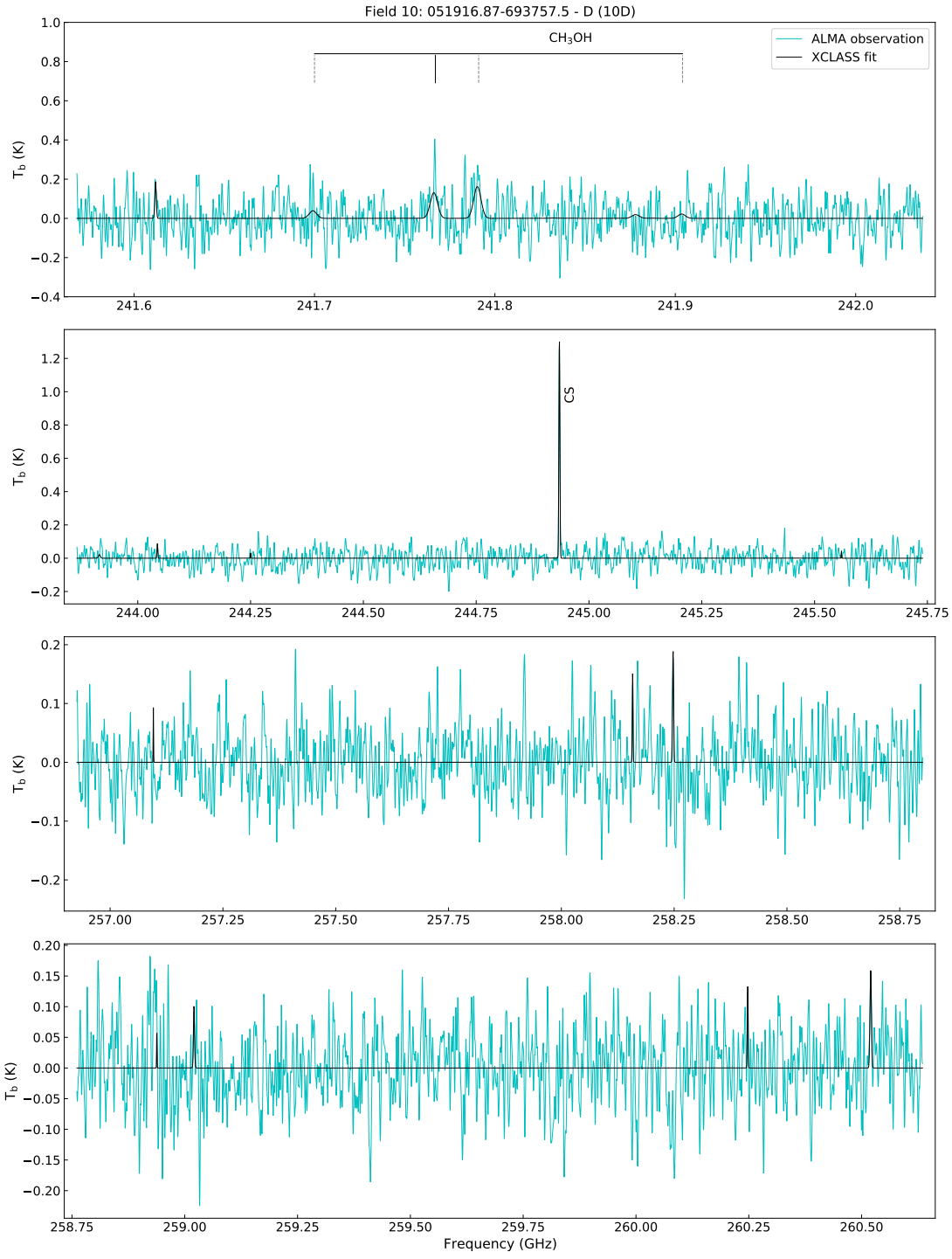
(b)

Figure B.10: Same as Fig. B.1 but for source 10B.



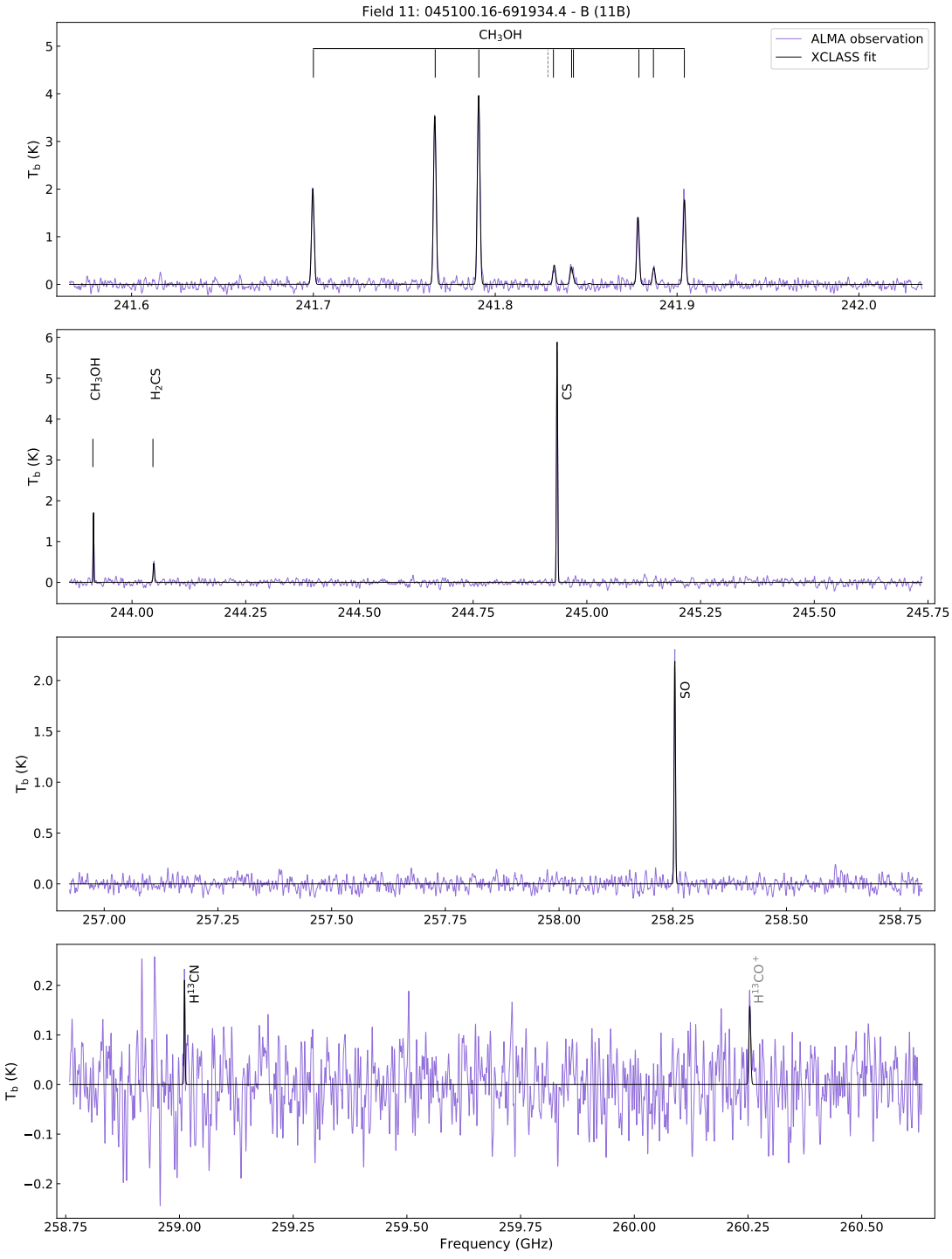
(c)

Figure B.10: Same as Fig. B.1 but for source 10C.



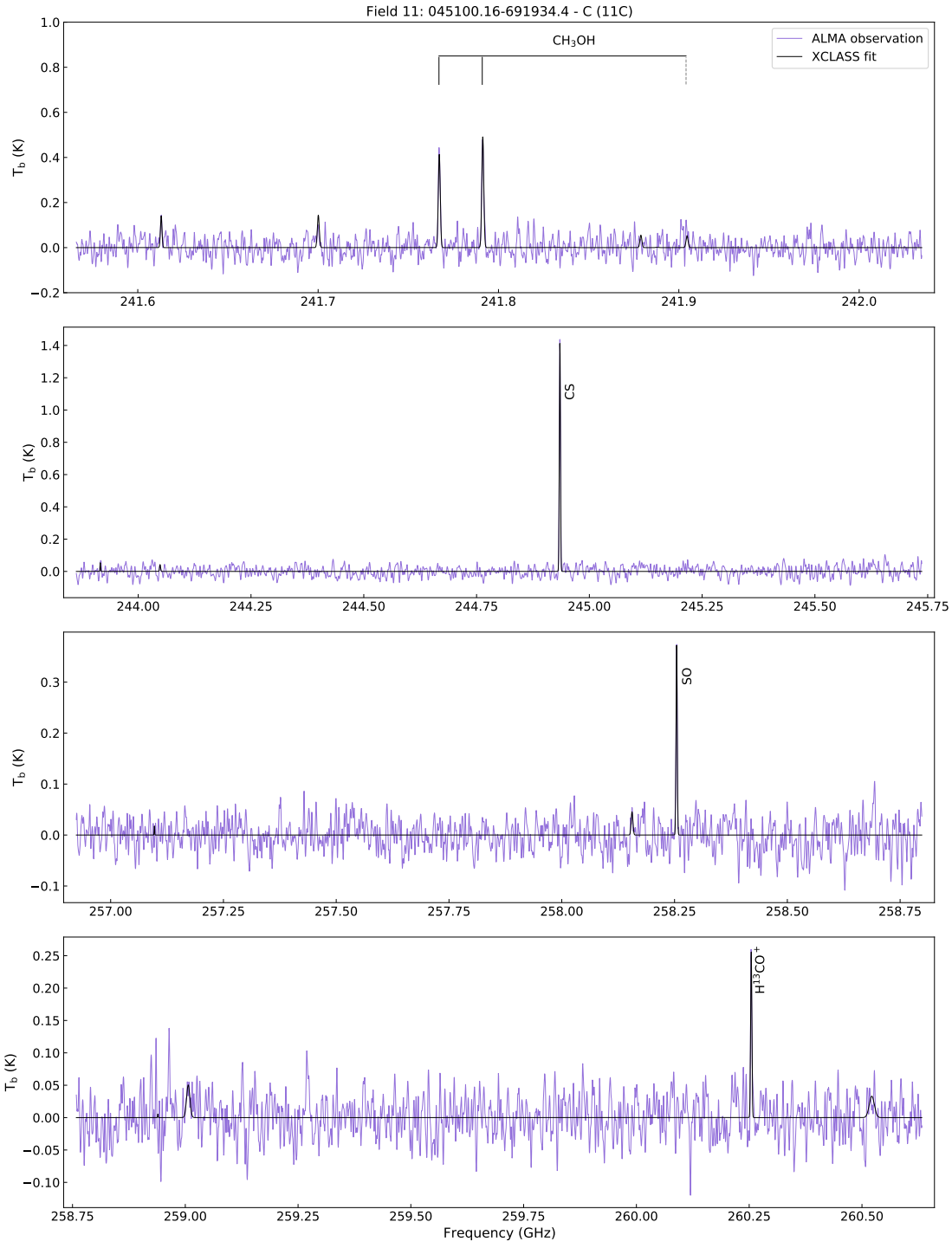
(d)

Figure B.10: Same as Fig. B.1 but for source 10D.



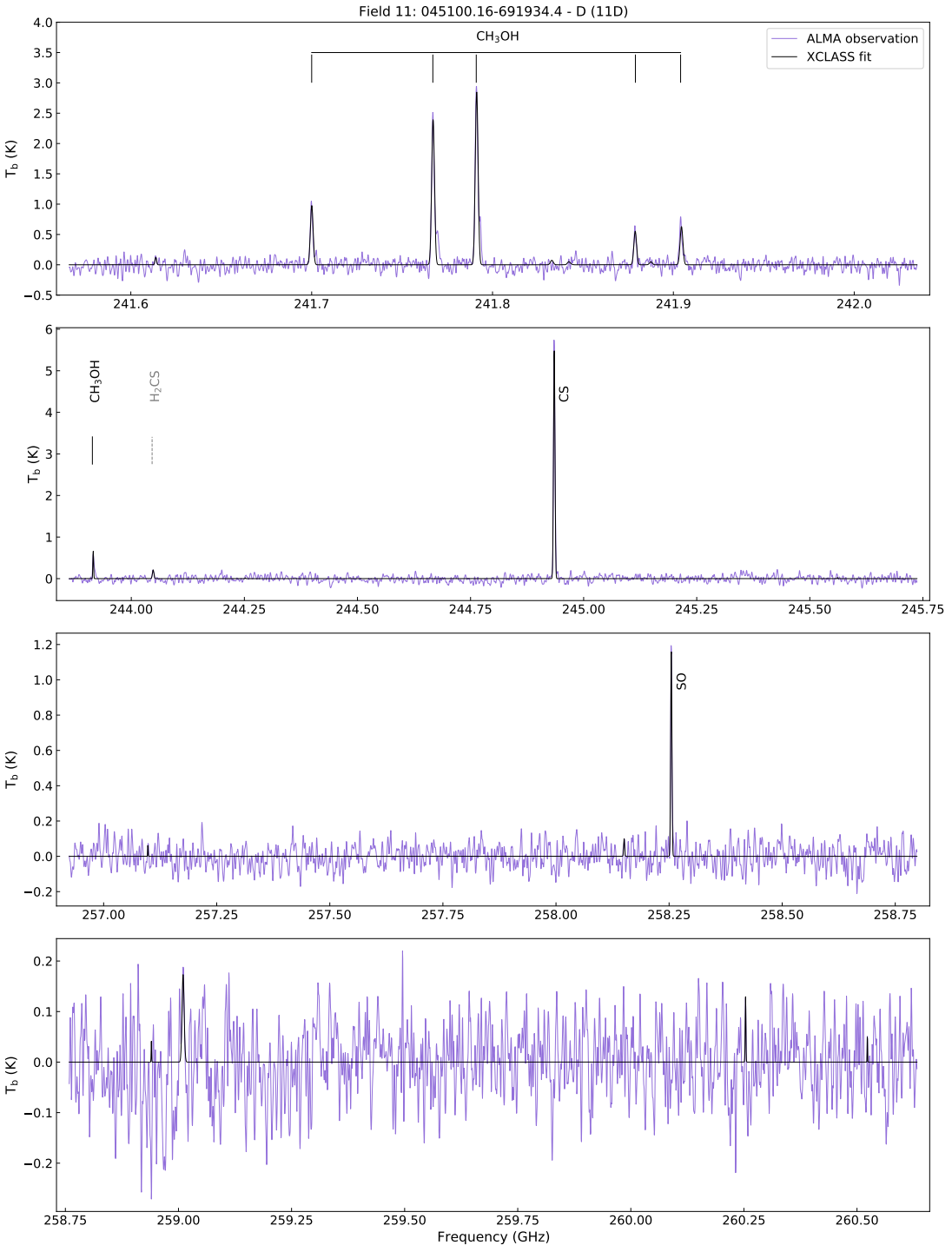
(a)

Figure B.11: Same as Fig. B.1 but for source 11B.



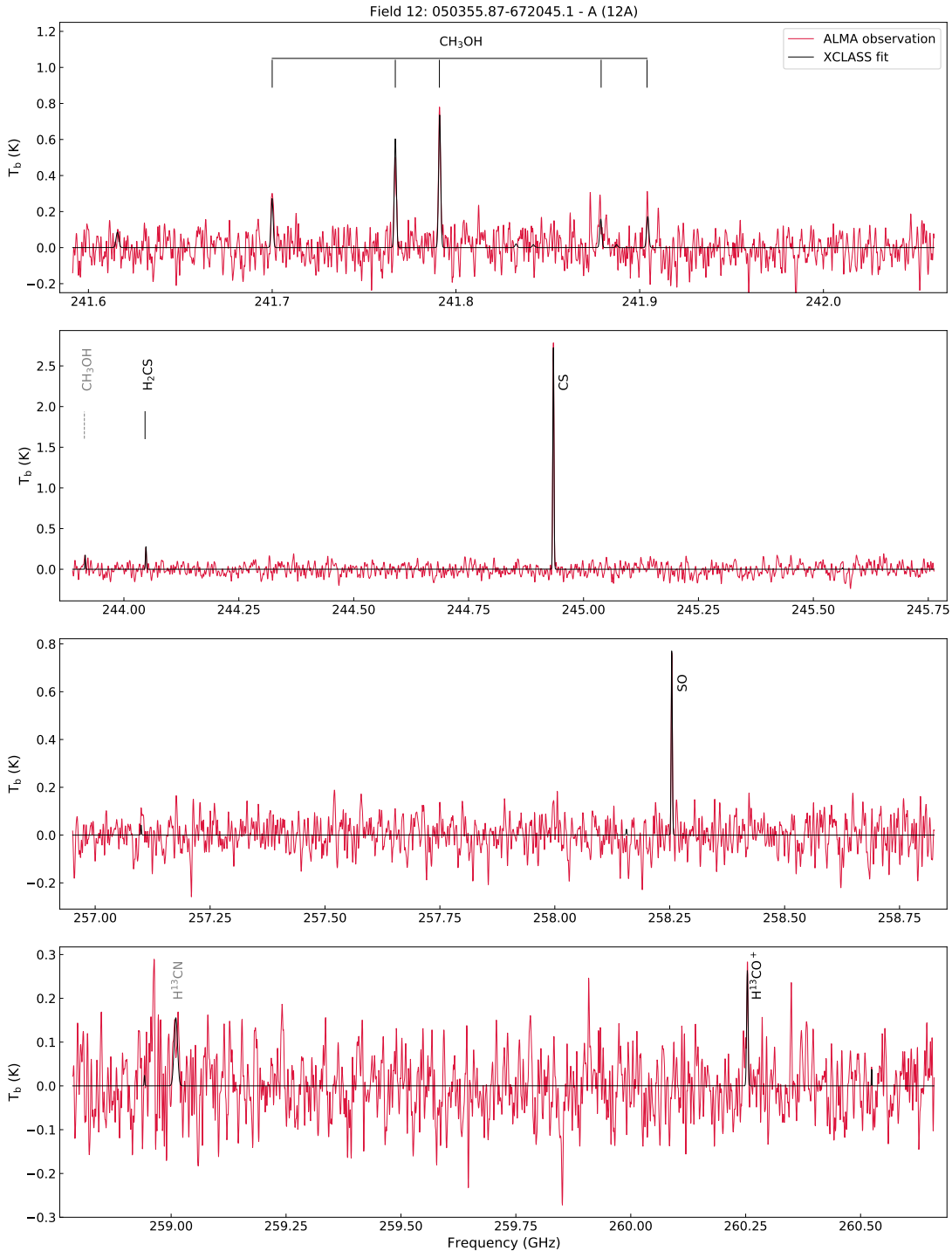
(b)

Figure B.11: Same as Fig. B.1 but for source 11C.



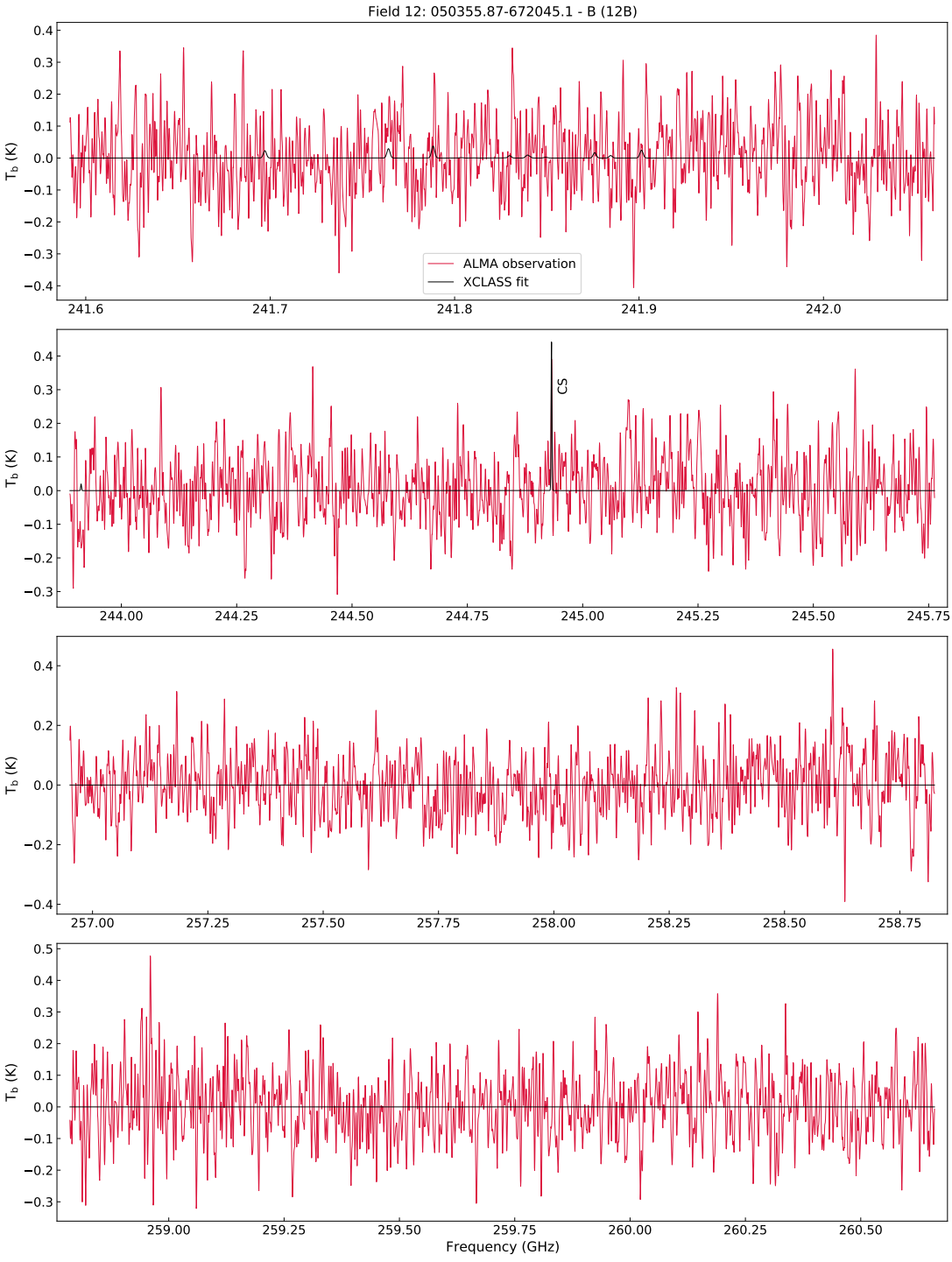
(c)

Figure B.11: Same as Fig. B.1 but for source 11D.



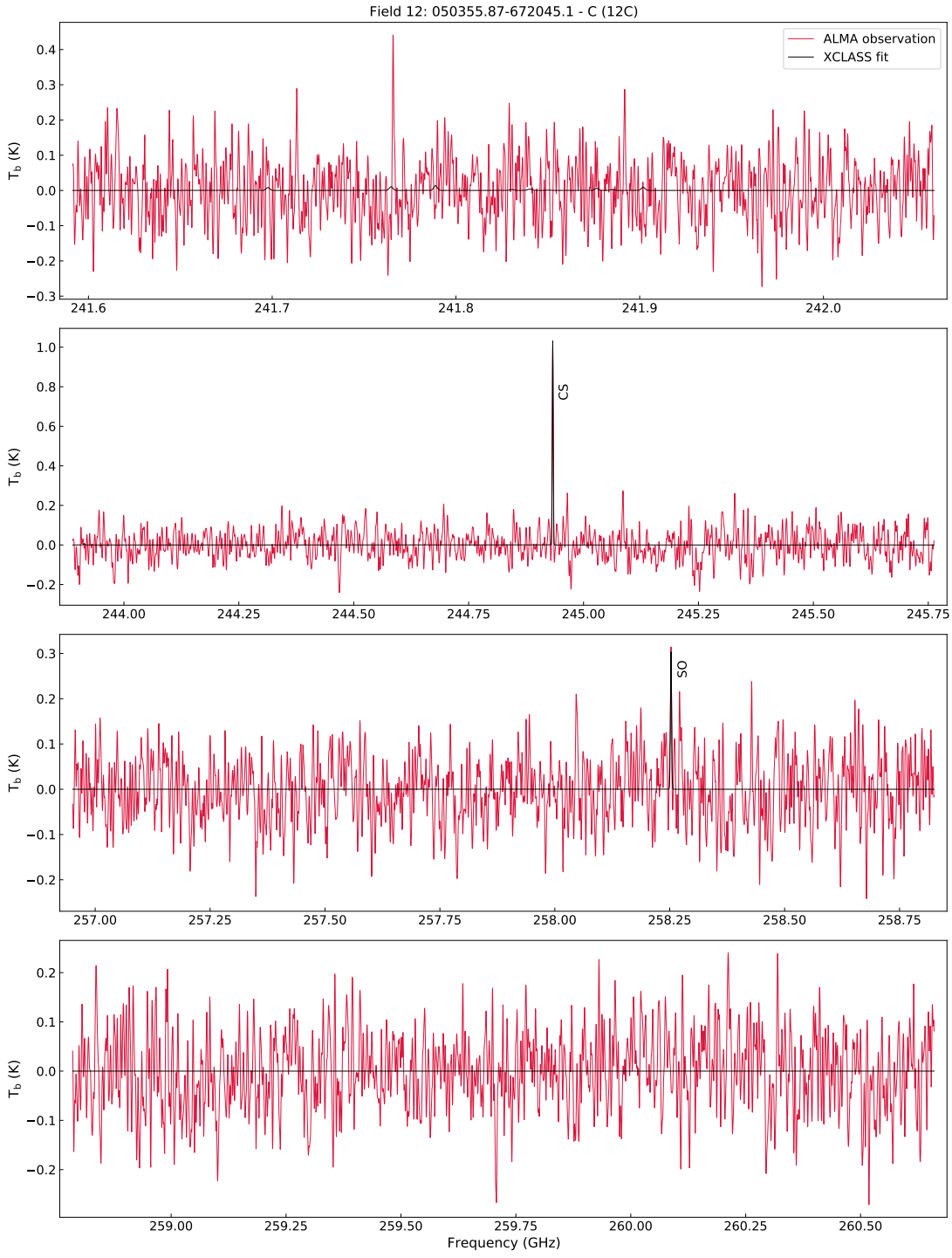
(a)

Figure B.12: Same as Fig. B.1 but for source 12A.



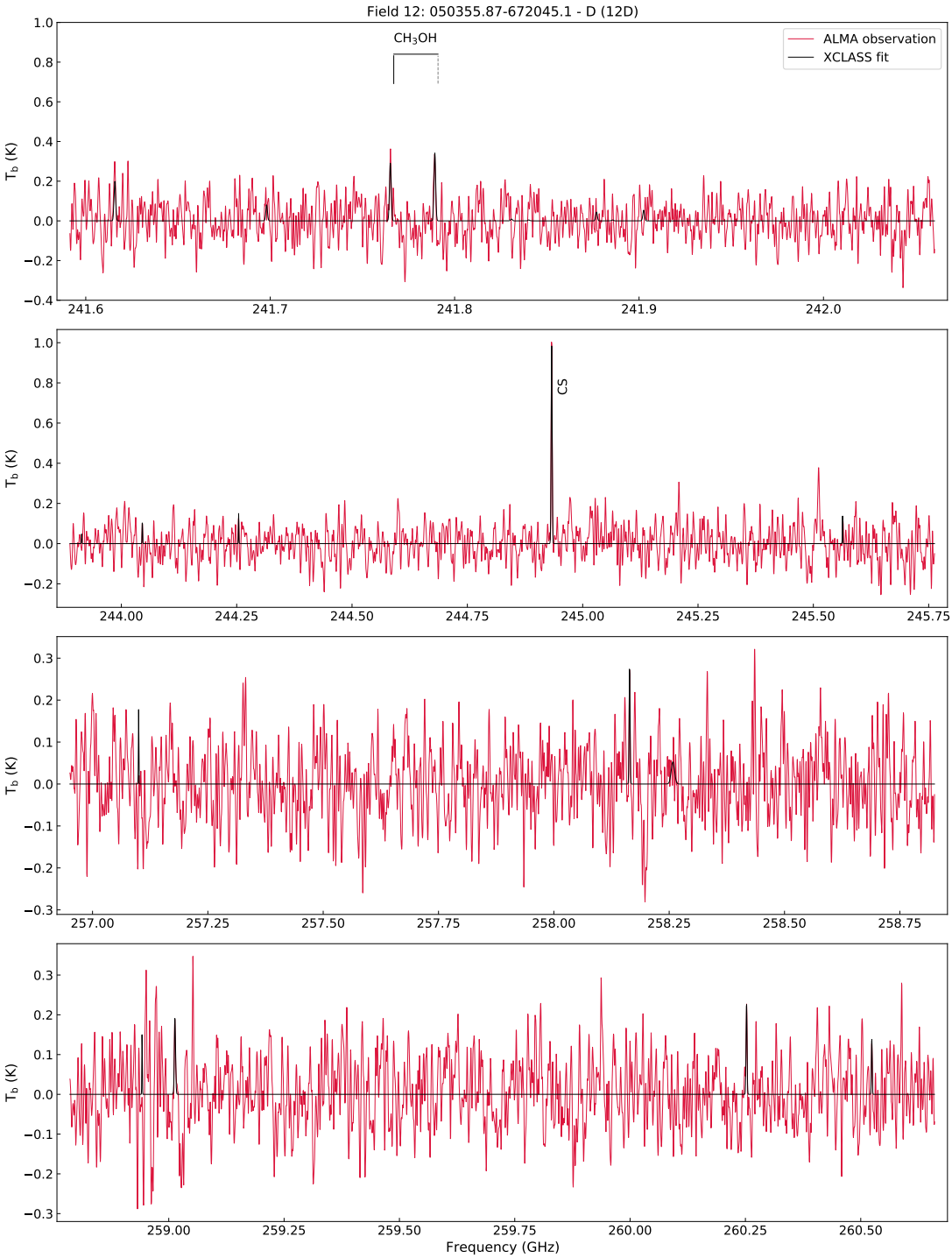
(b)

Figure B.12: Same as Fig. B.1 but for source 12B.



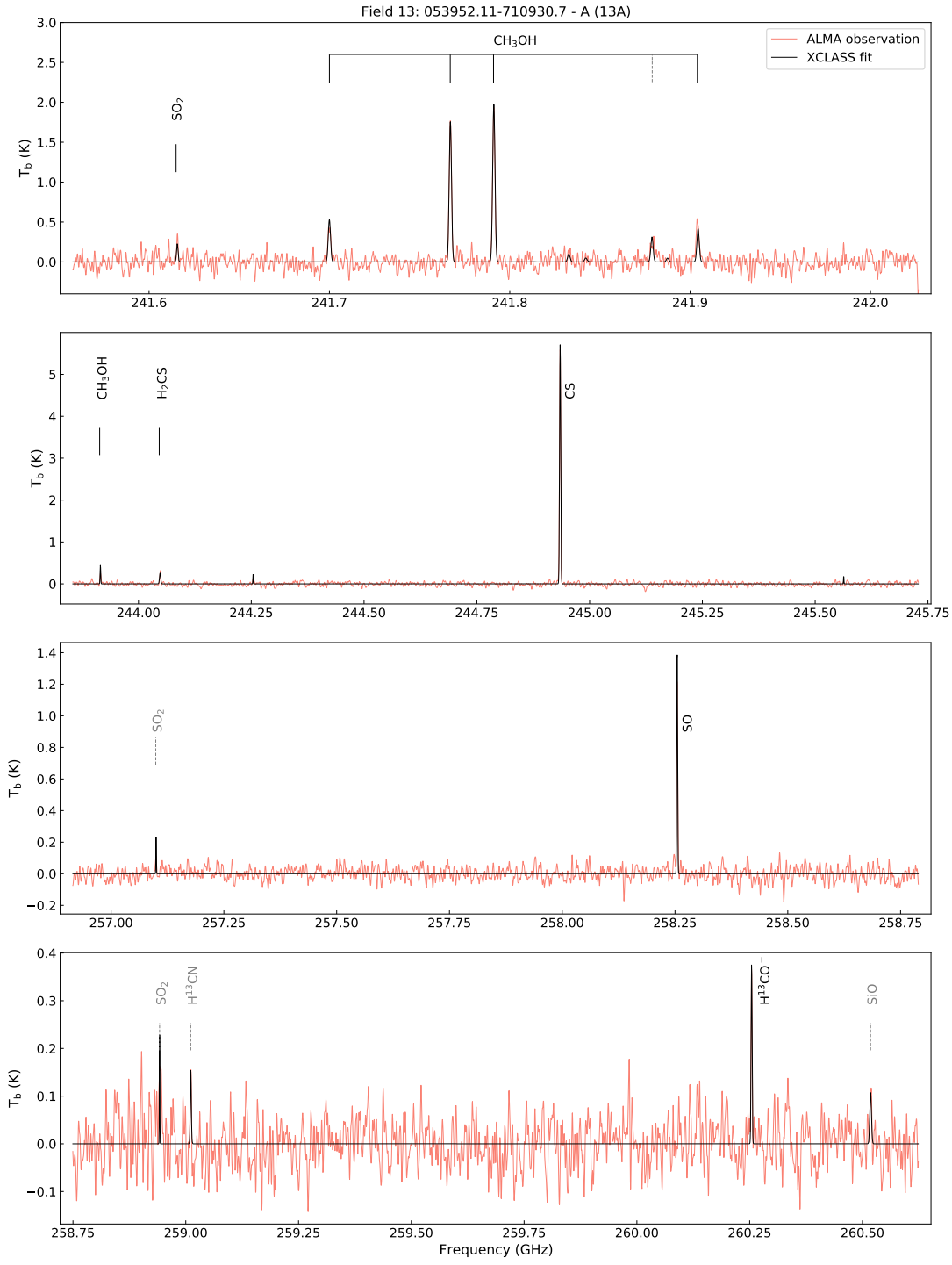
(c)

Figure B.12: Same as Fig. B.1 but for source 12C.



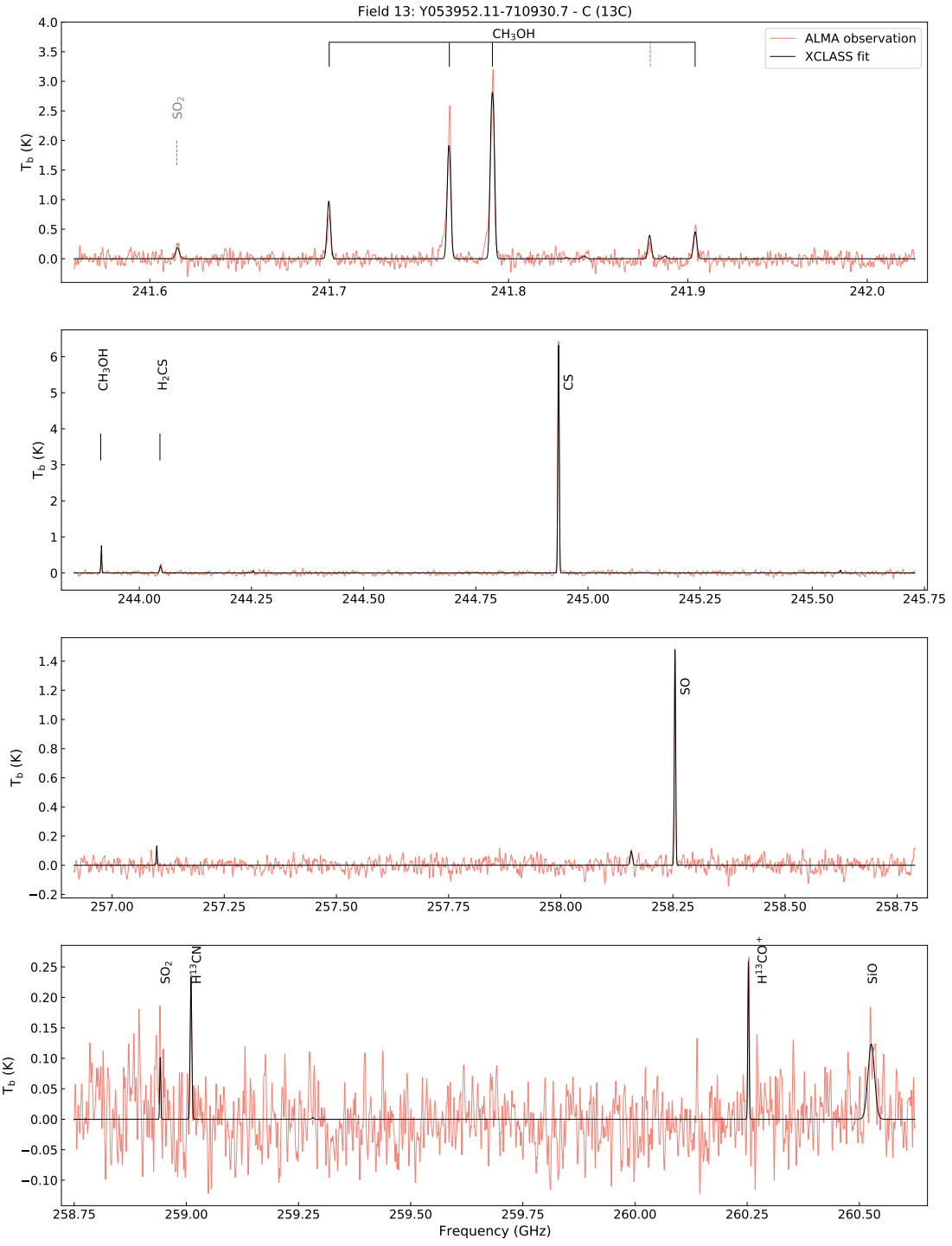
(d)

Figure B.12: Same as Fig. B.1 but for source 12D.



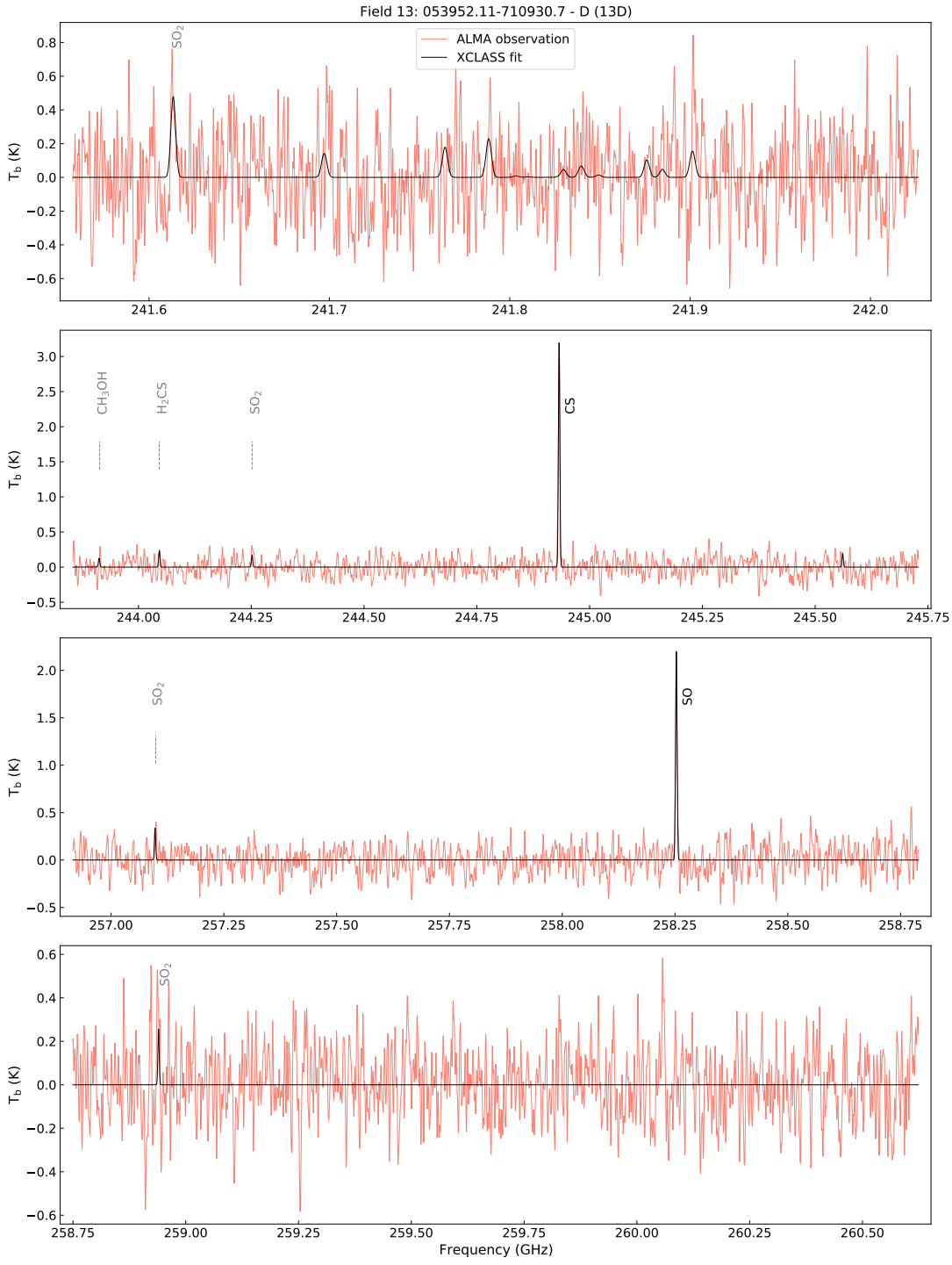
(a)

Figure B.13: Same as Fig. B.1 but for source 13A.



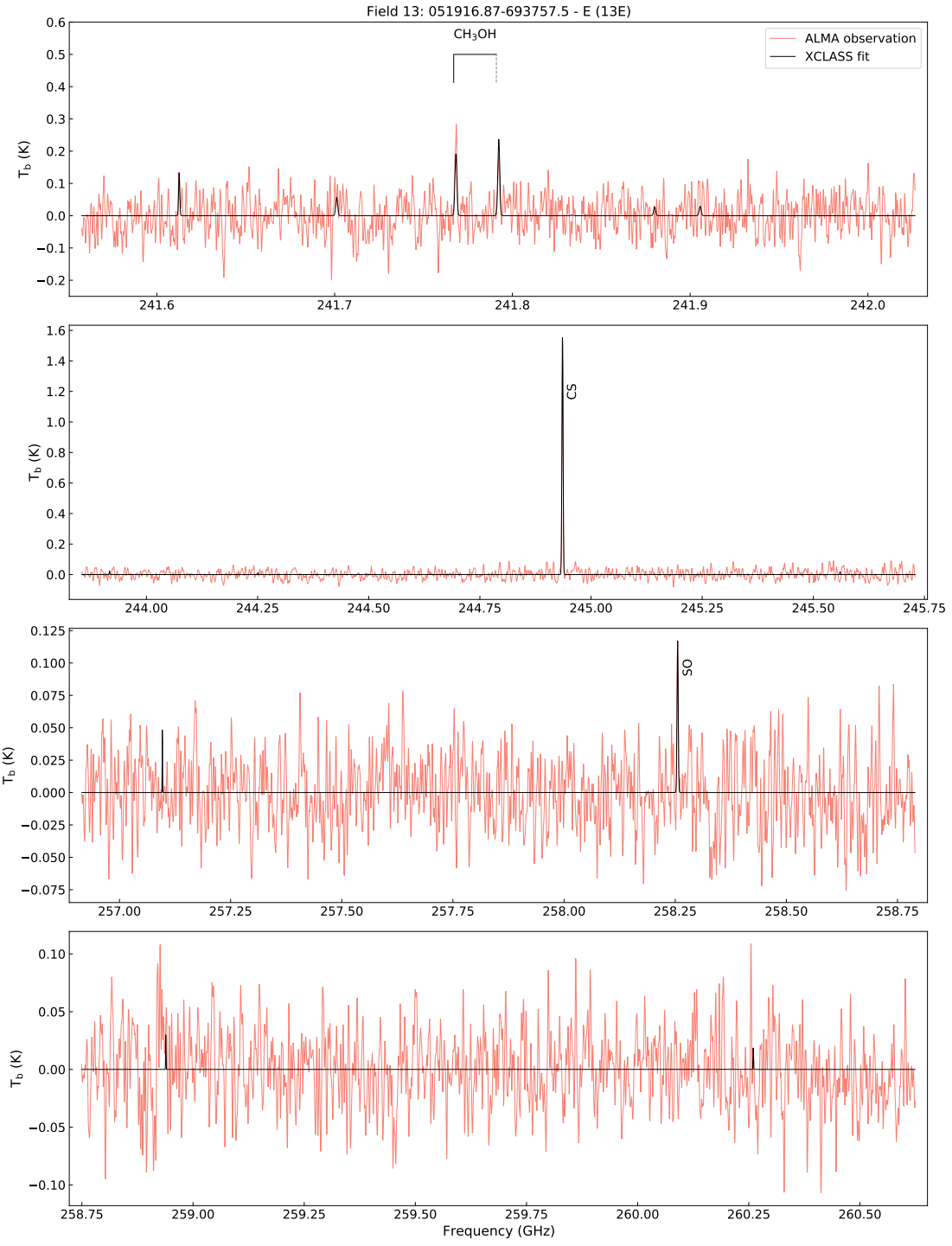
(b)

Figure B.13: Same as Fig. B.1 but for source 13C.



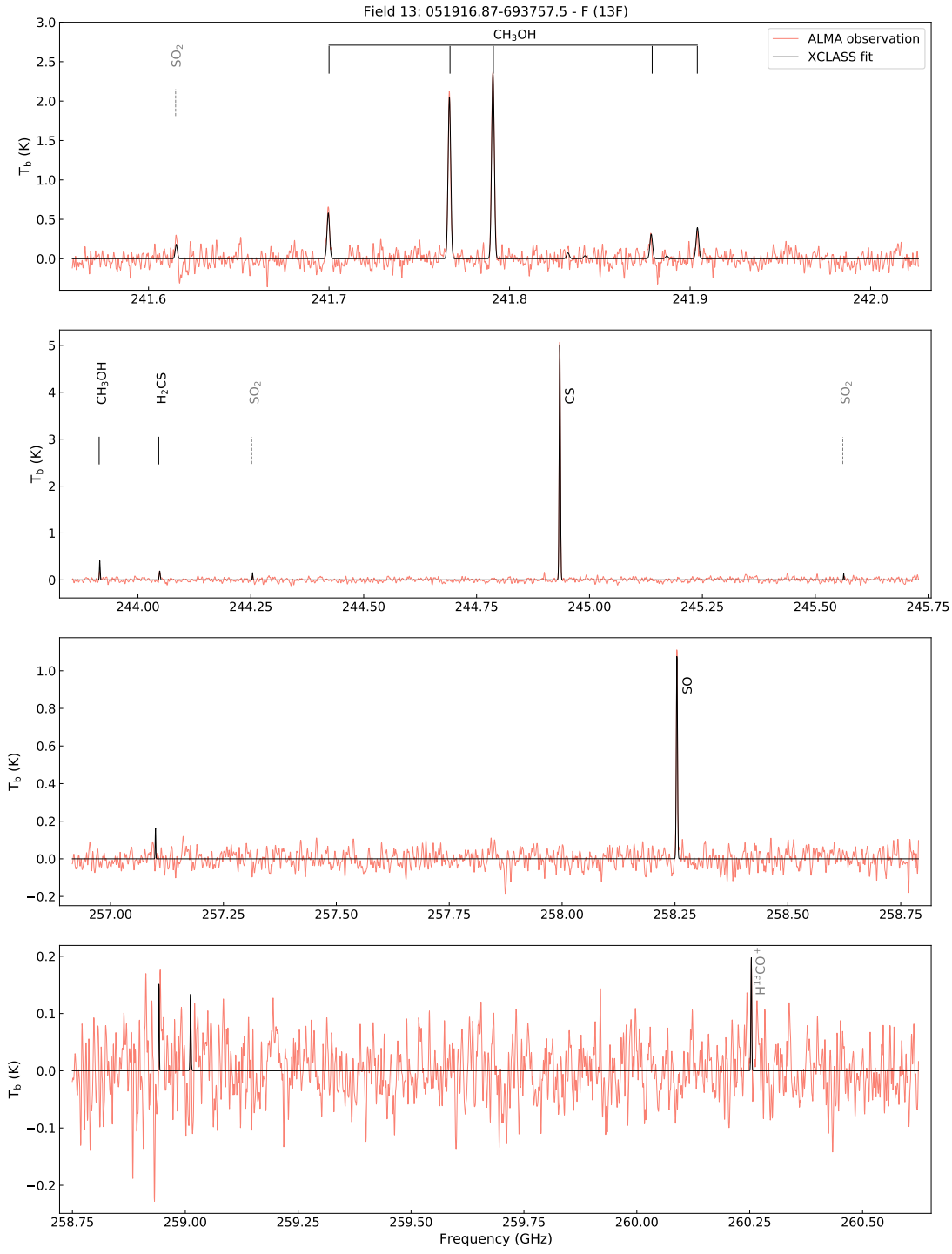
(c)

Figure B.13: Same as Fig. B.1 but for source 13D.



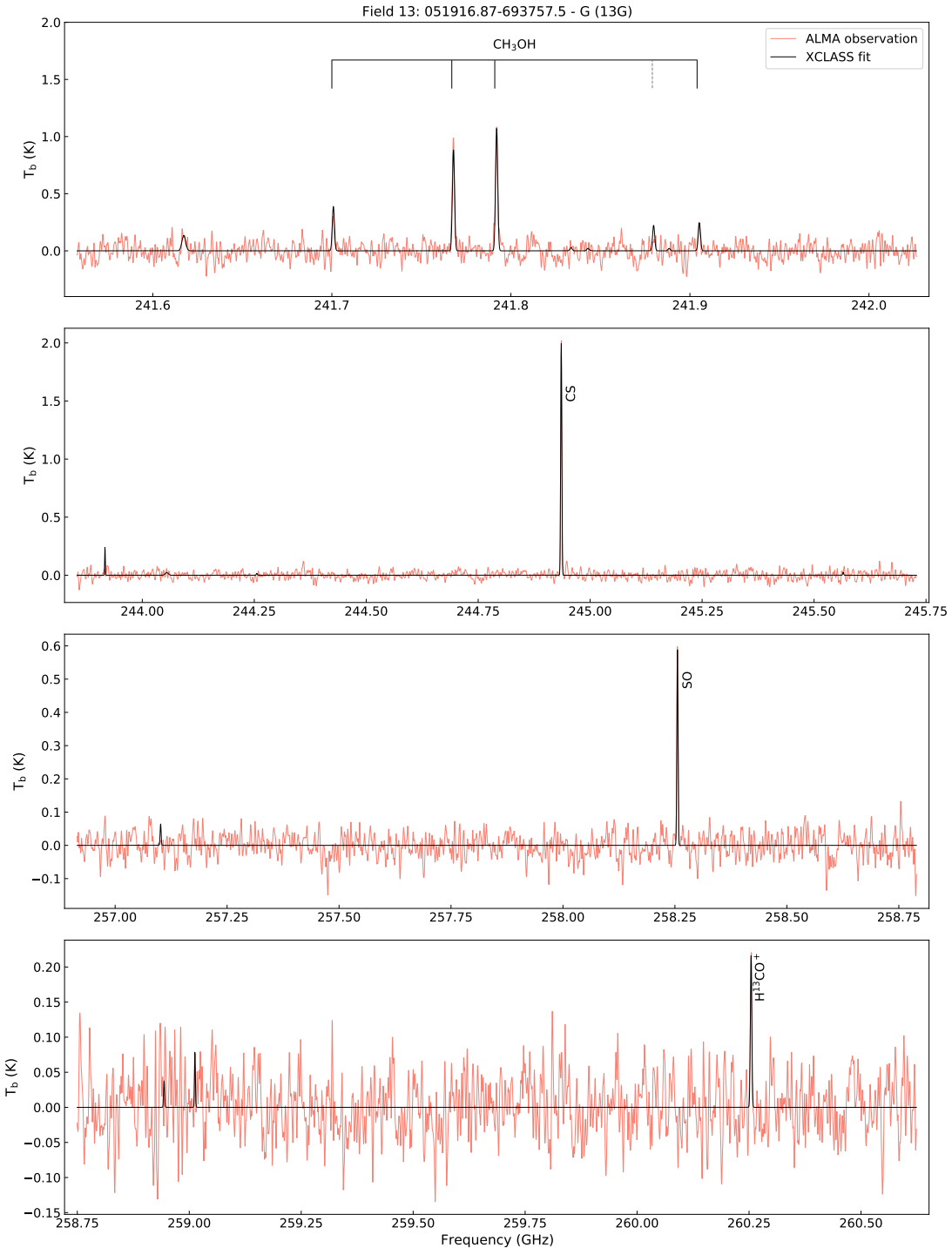
(d)

Figure B.13: Same as Fig. B.1 but for source 13E.



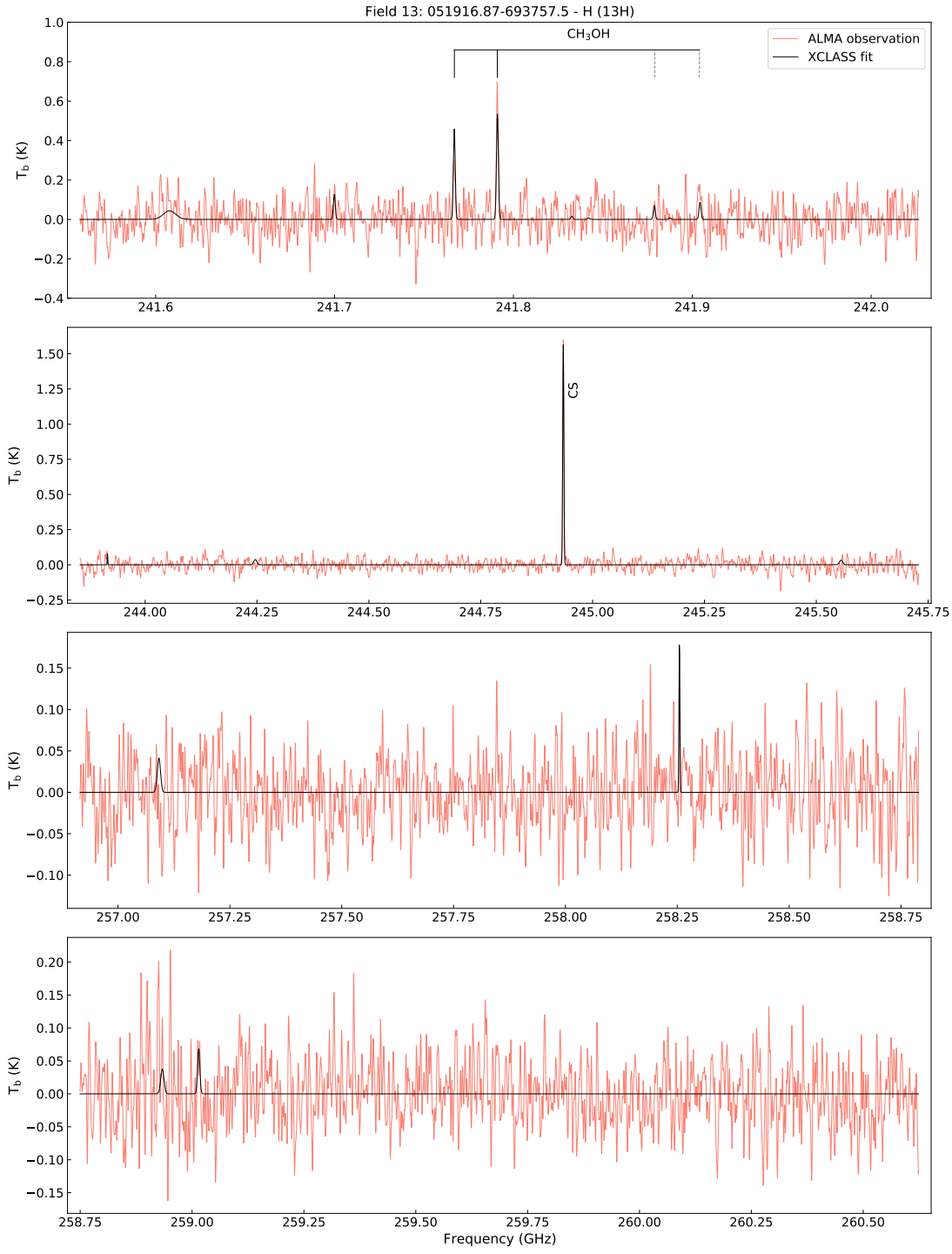
(e)

Figure B.13: Same as Fig. B.1 but for source 13F.



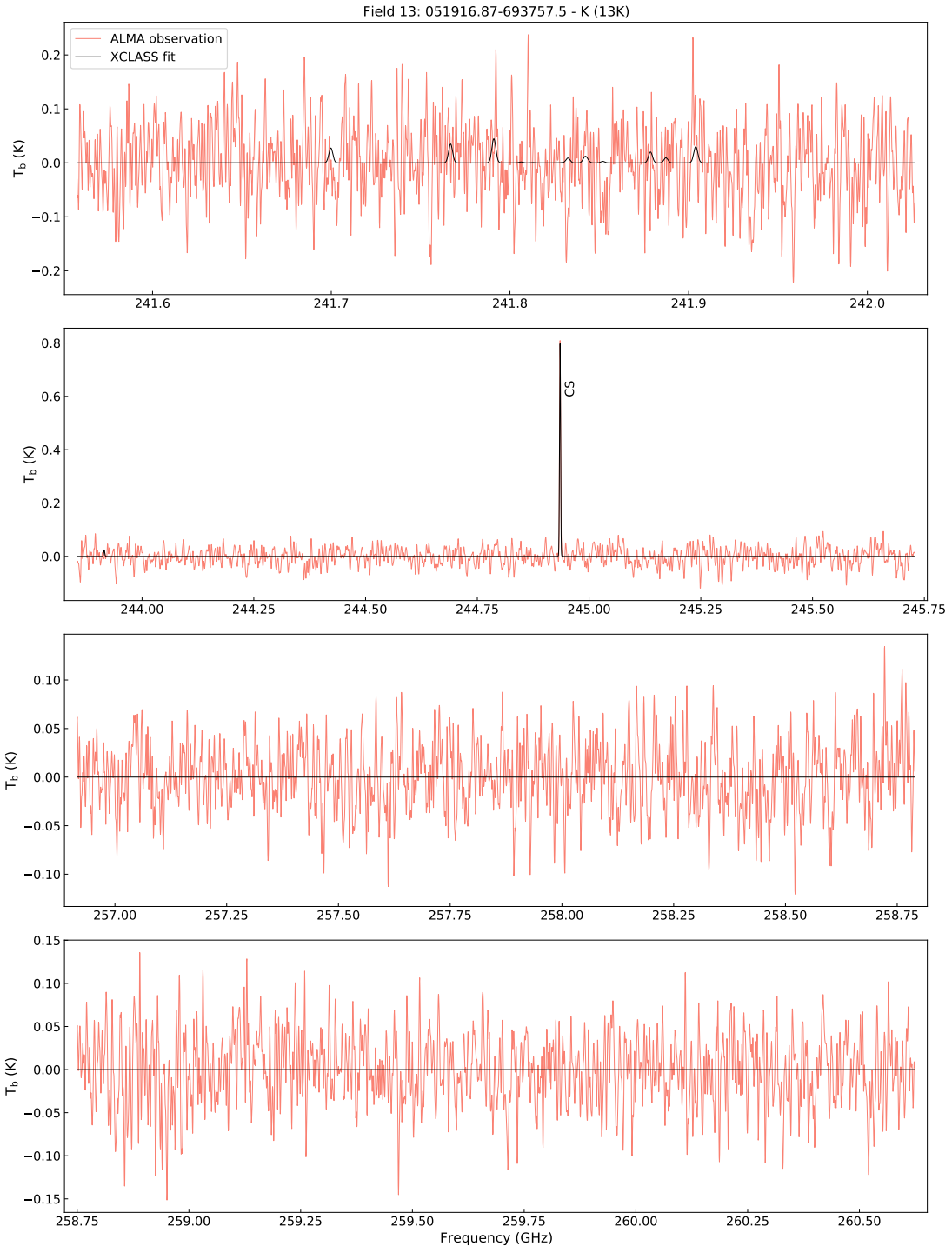
(f)

Figure B.13: Same as Fig. B.1 but for source 13G.



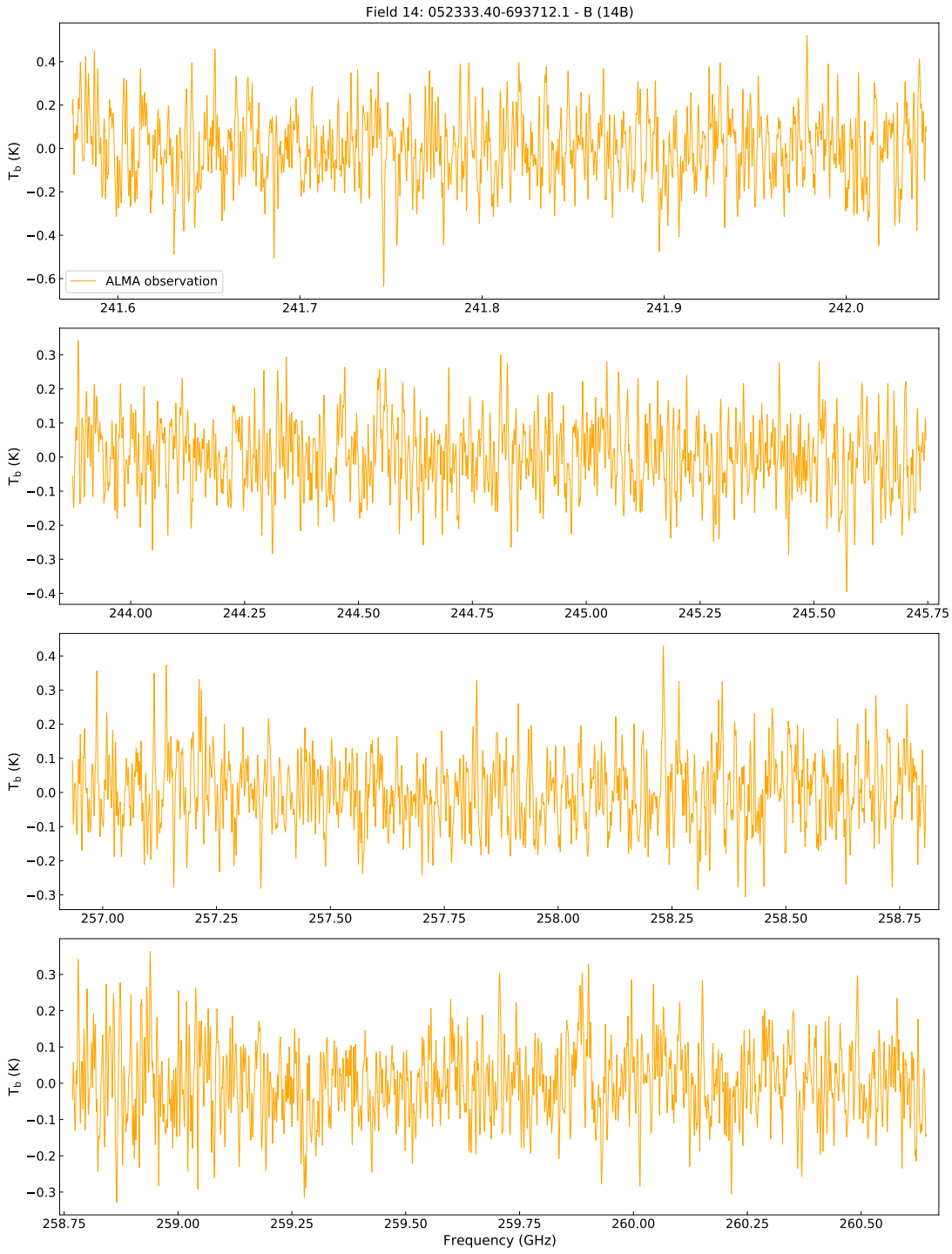
(g)

Figure B.13: Same as Fig. B.1 but for source 13H.



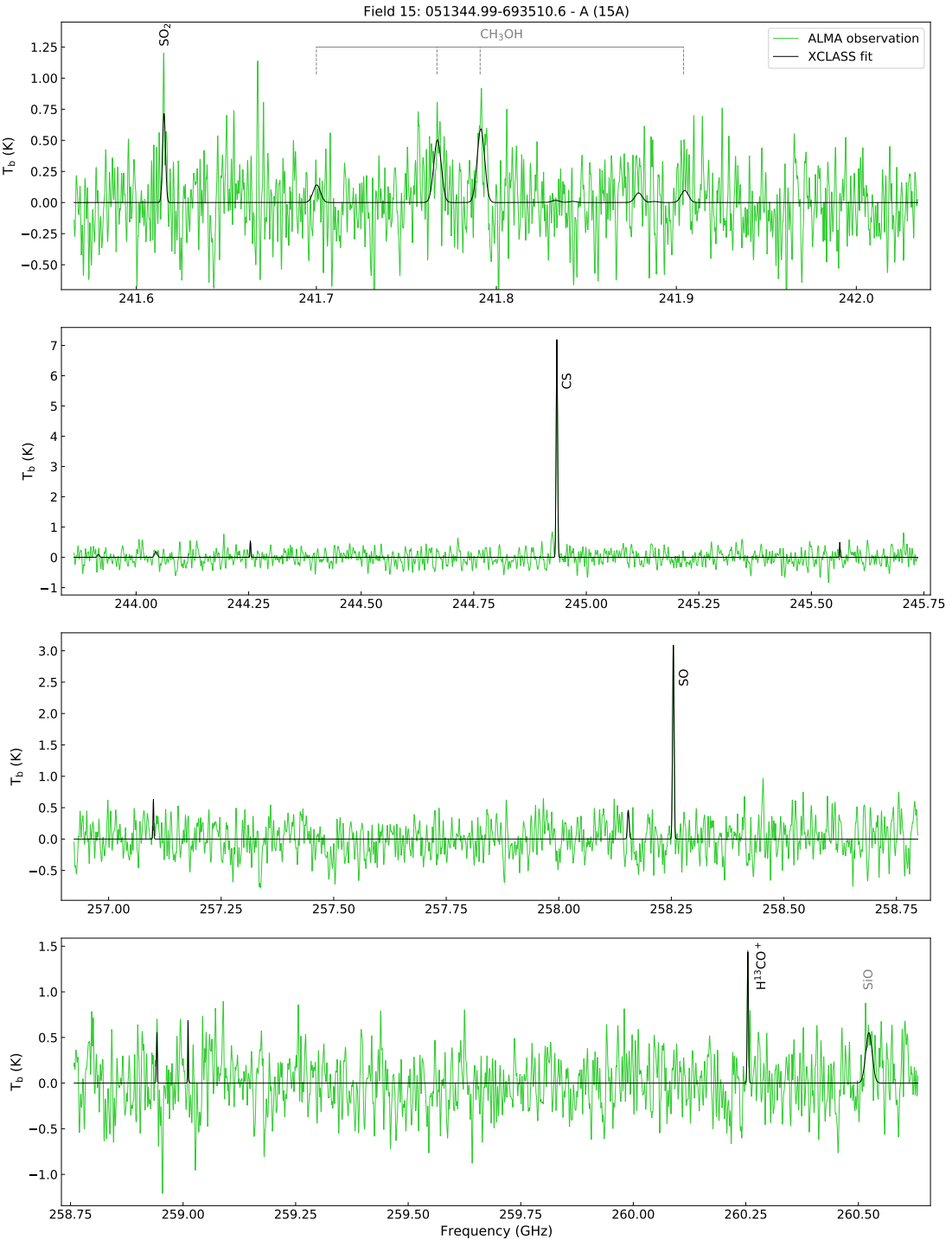
(h)

Figure B.13: Same as Fig. B.1 but for source 13K.



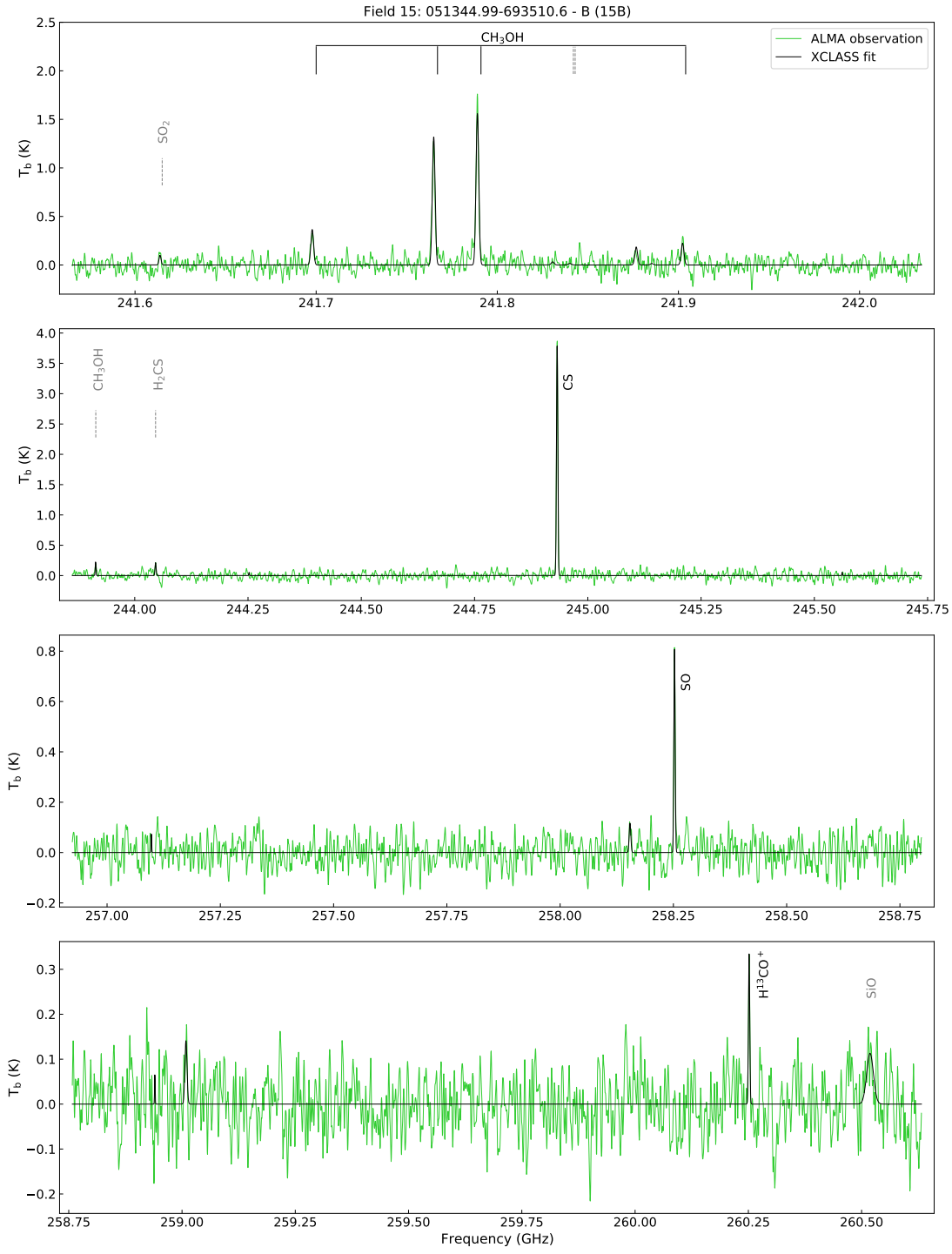
(a)

Figure B.14: ALMA Band 6 observed spectra toward source 14B with no emission line detections. (See Section 3.3.1 for more details.)



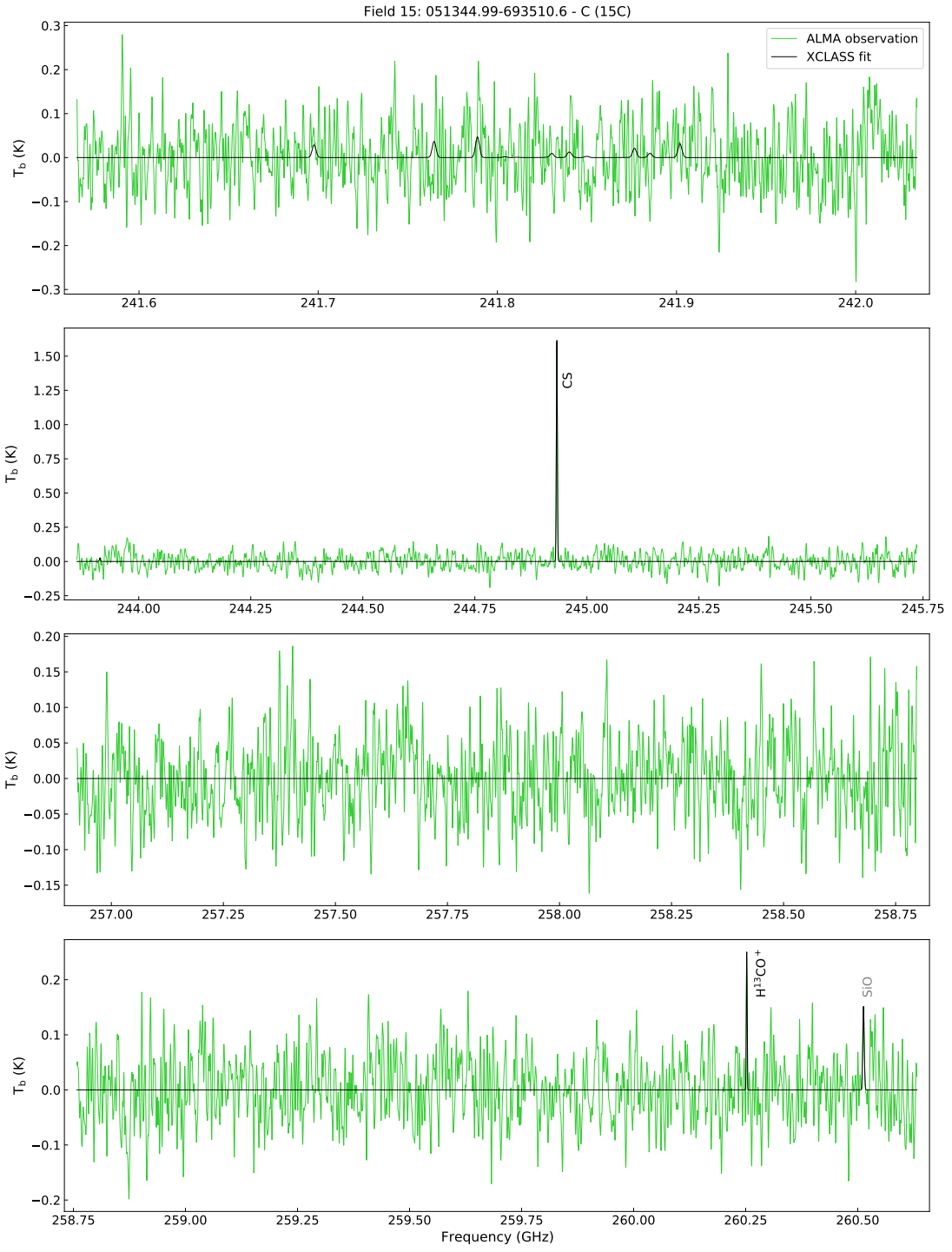
(a)

Figure B.15: Same as Fig. B.1 but for source 15A.



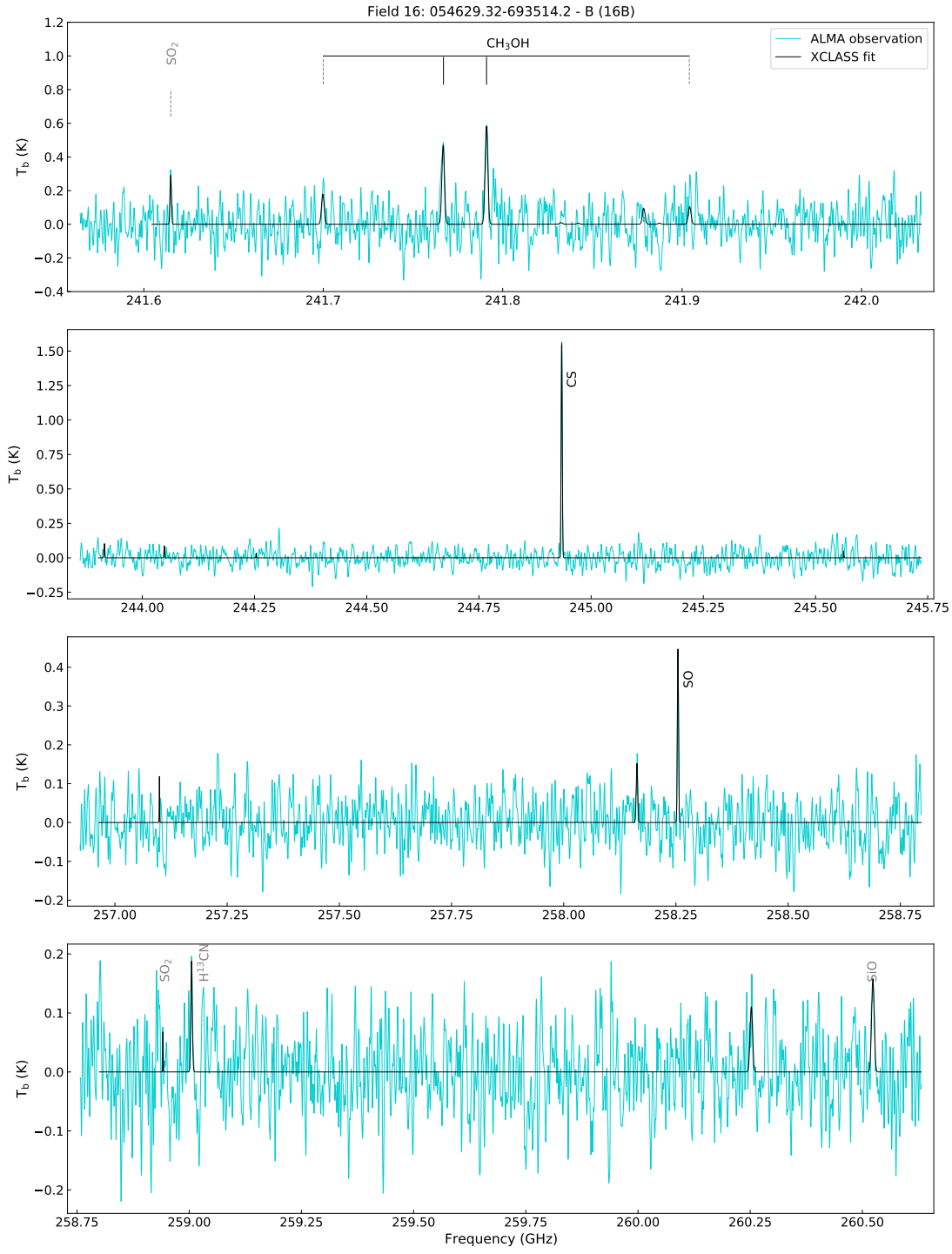
(b)

Figure B.15: Same as Fig. B.1 but for source 15B.



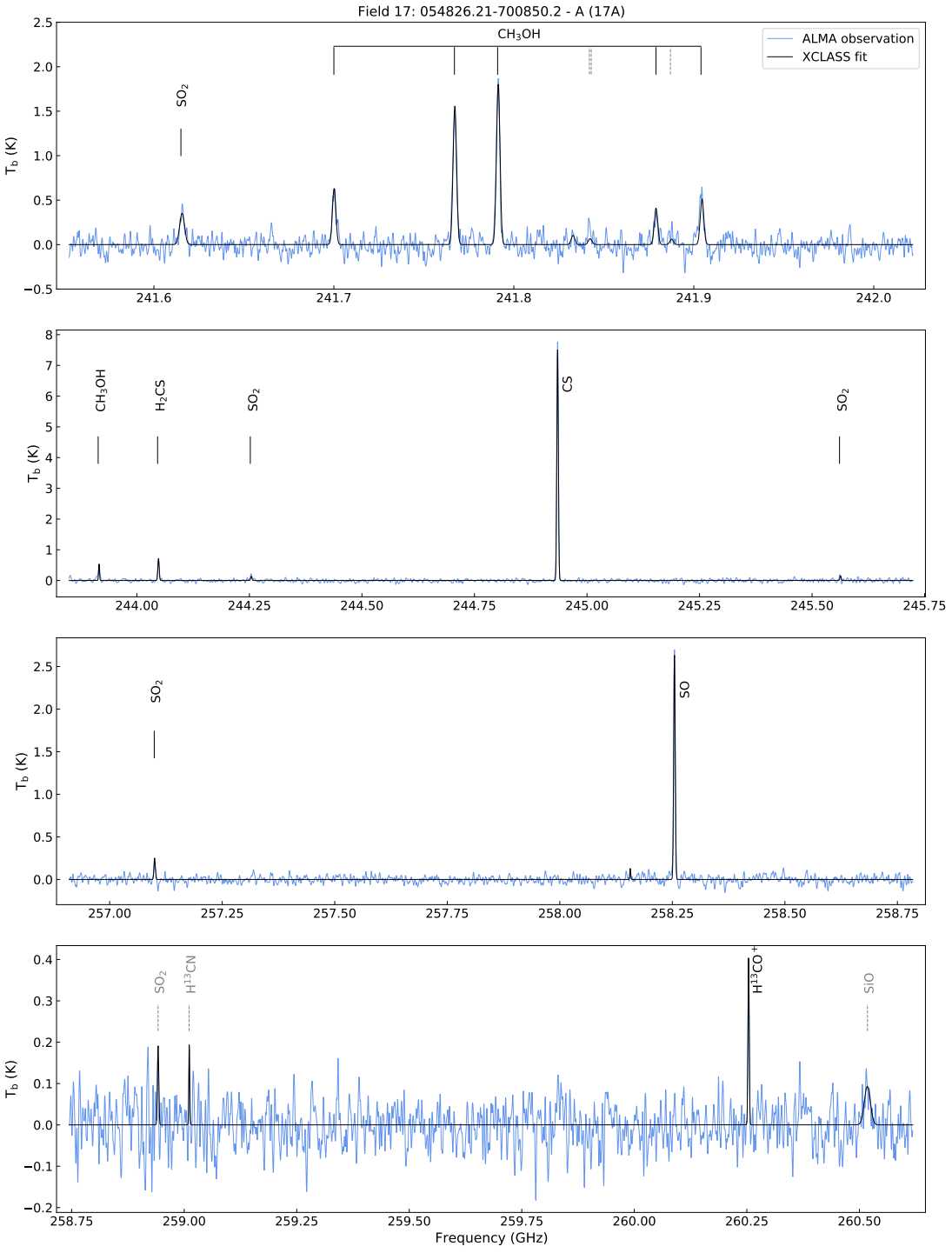
(c)

Figure B.15: Same as Fig. B.1 but for source 15C.



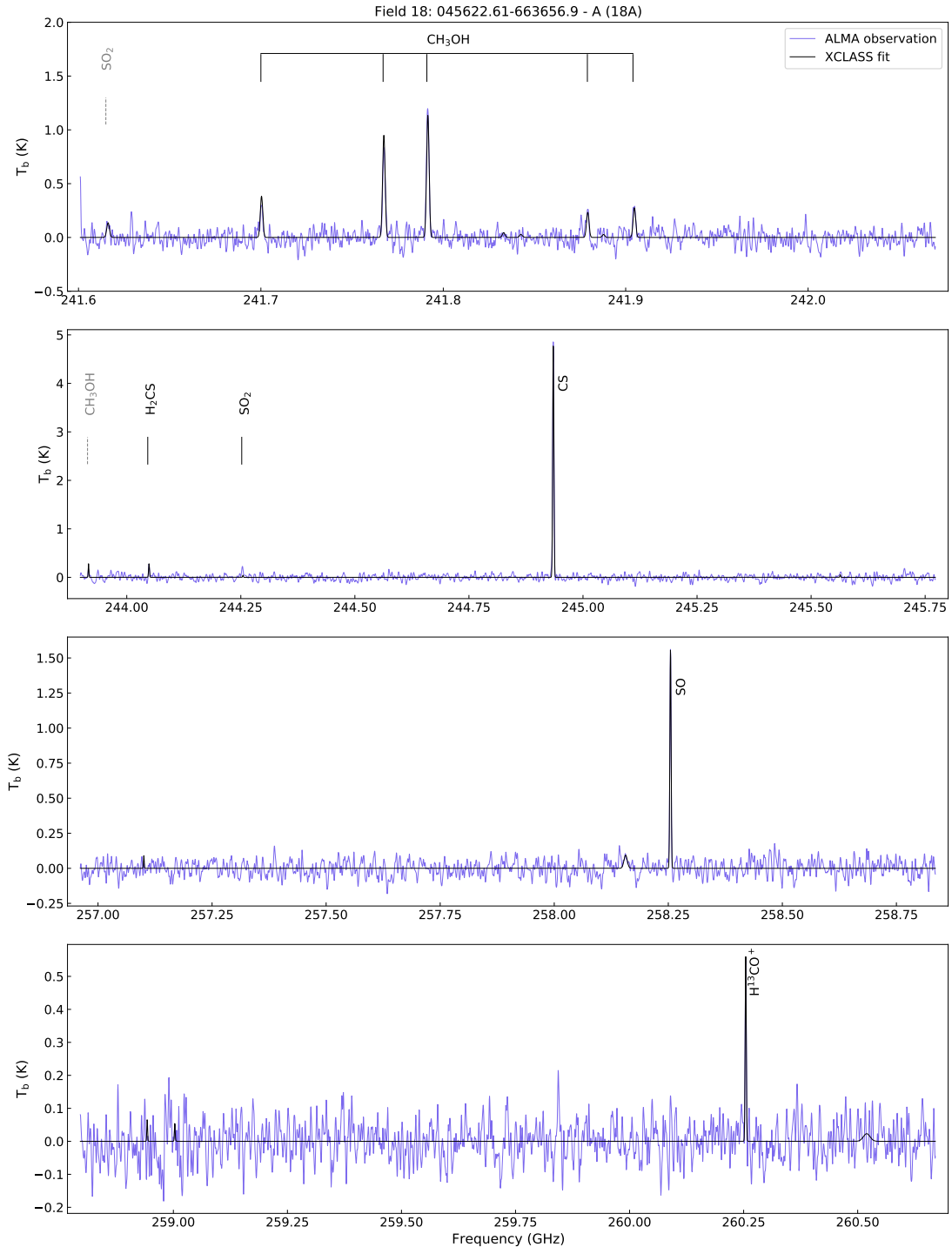
(a)

Figure B.16: Same as Fig. B.1 but for source 16B.



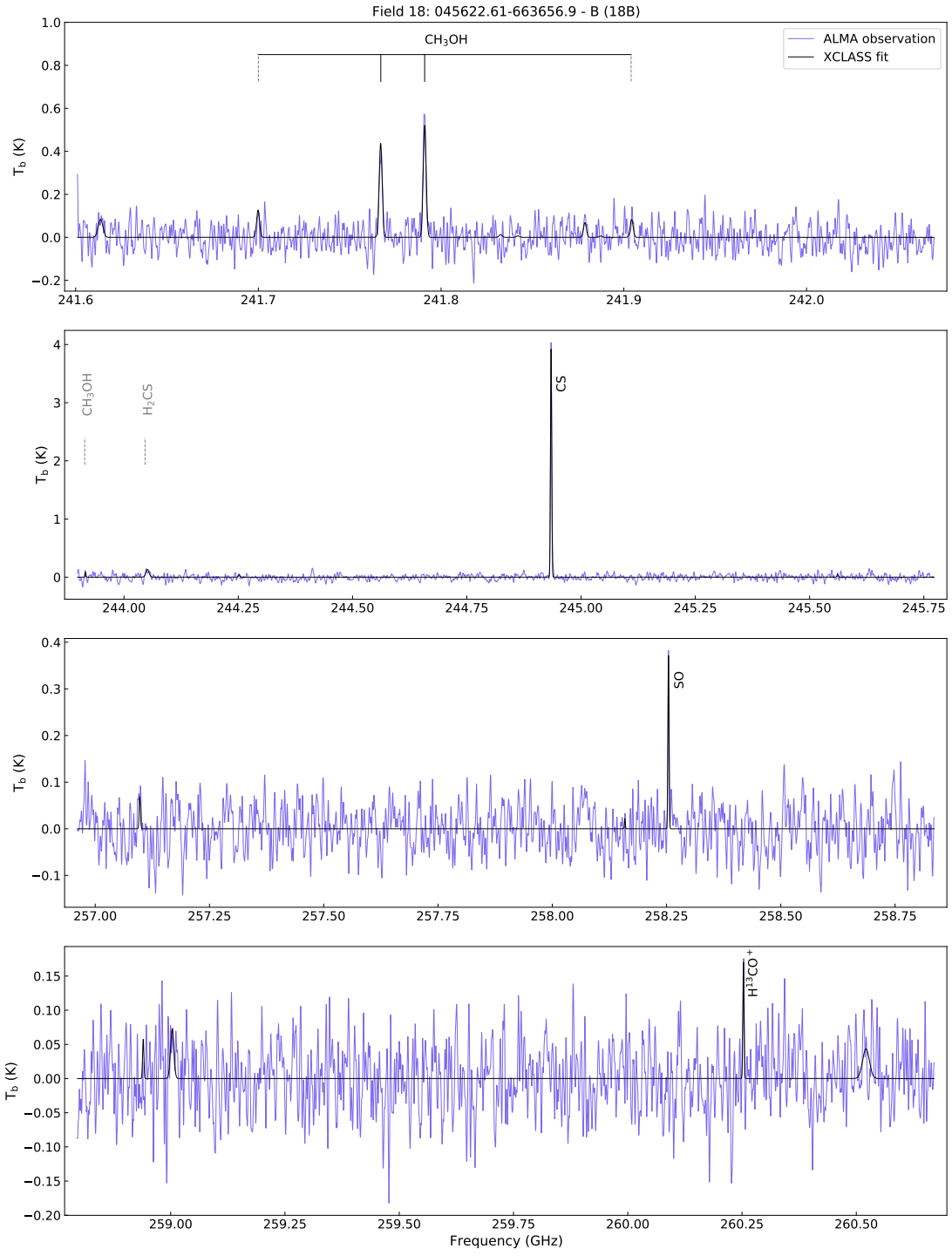
(a)

Figure B.17: Same as Fig. B.1 but for source 17A.



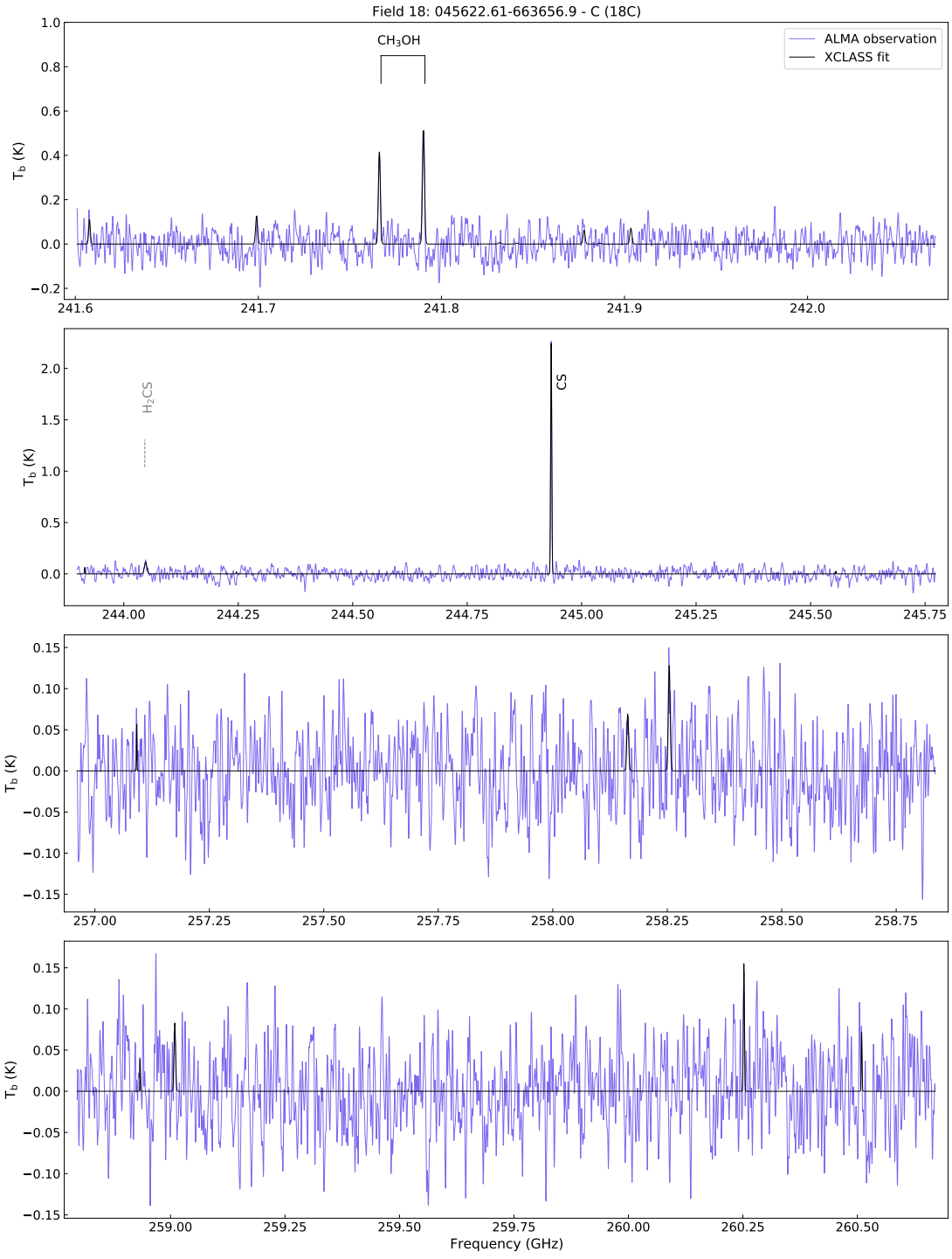
(a)

Figure B.18: Same as Fig. B.1 but for source 18A.



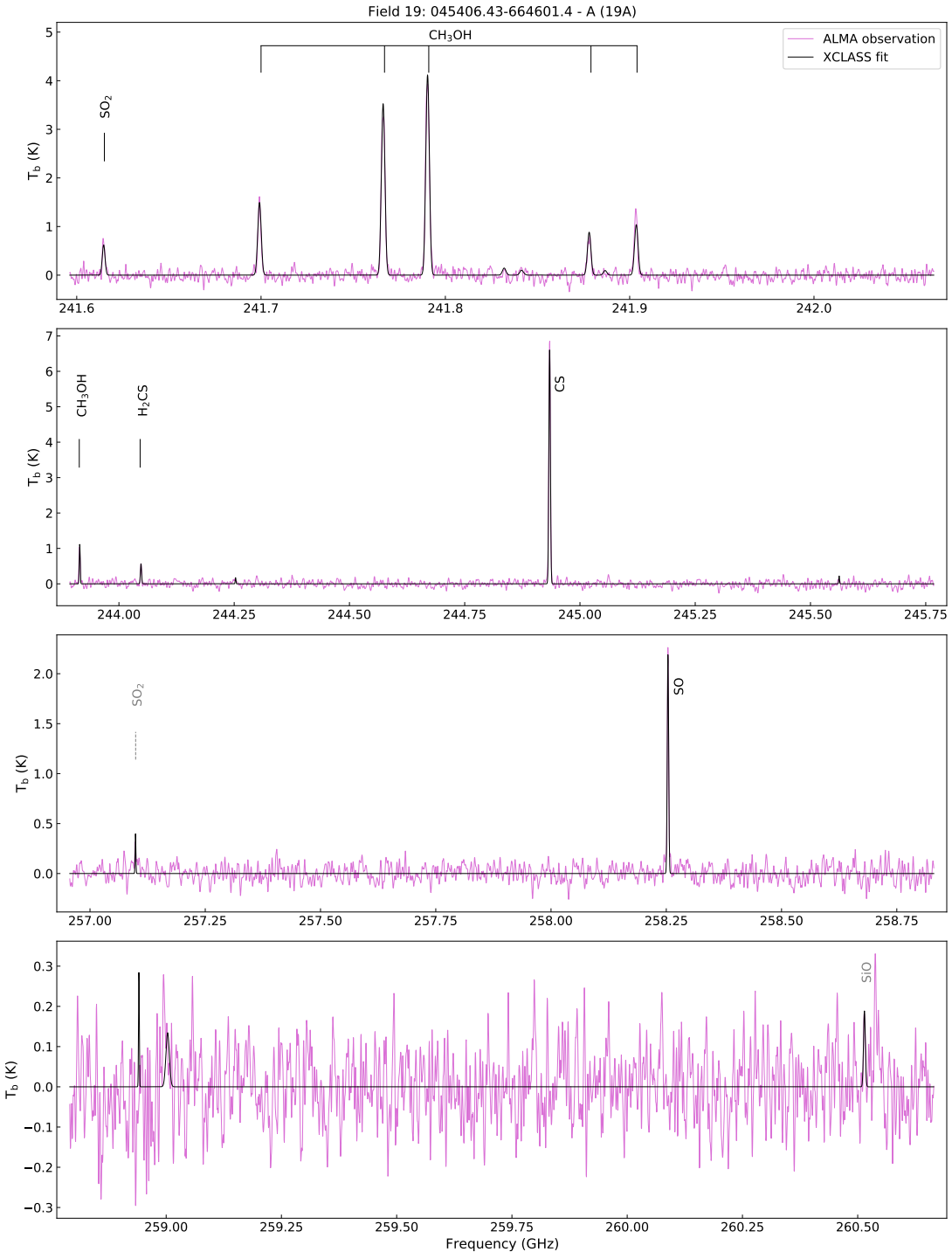
(b)

Figure B.18: Same as Fig. B.1 but for source 18B.



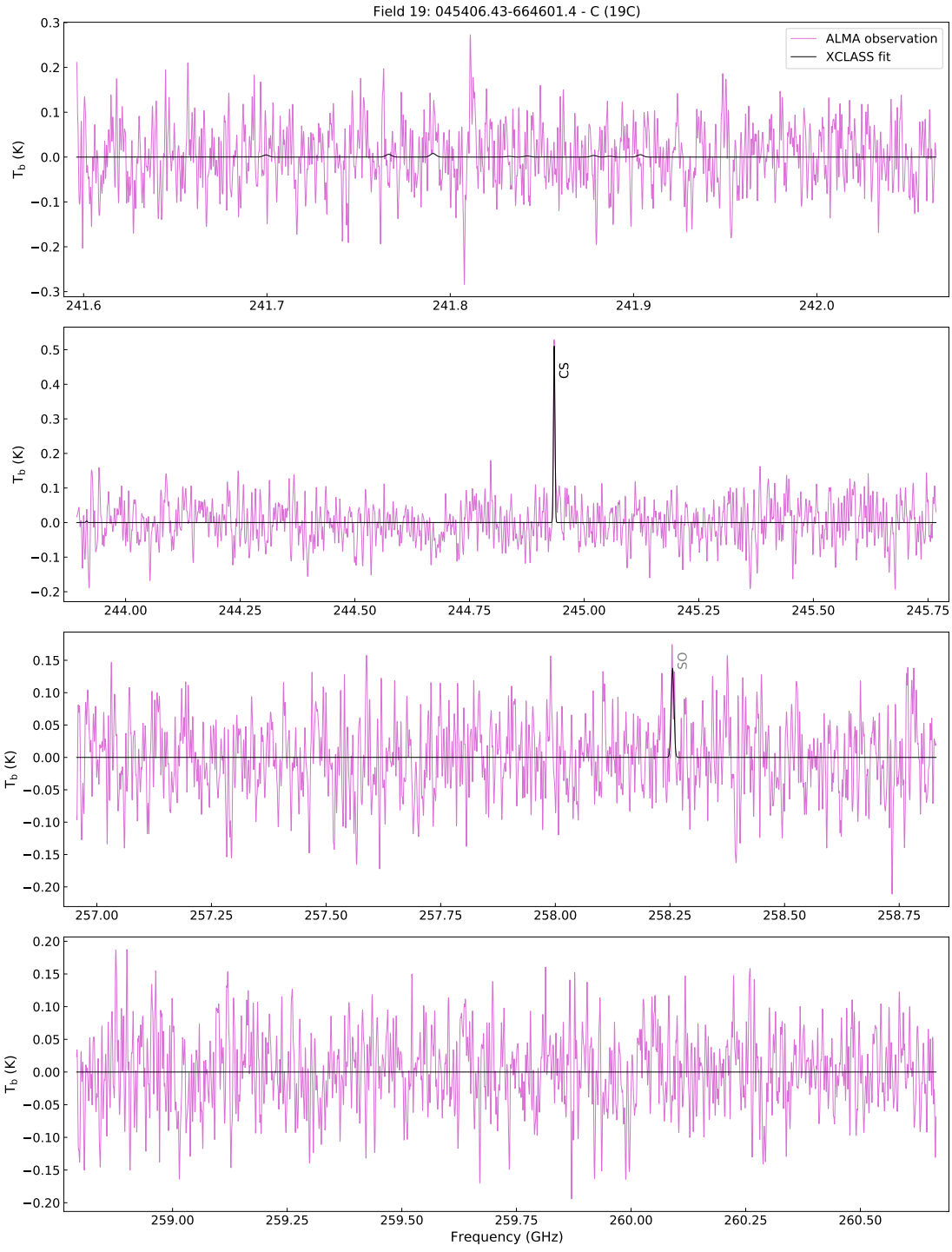
(c)

Figure B.18: Same as Fig. B.1 but for source 18C.



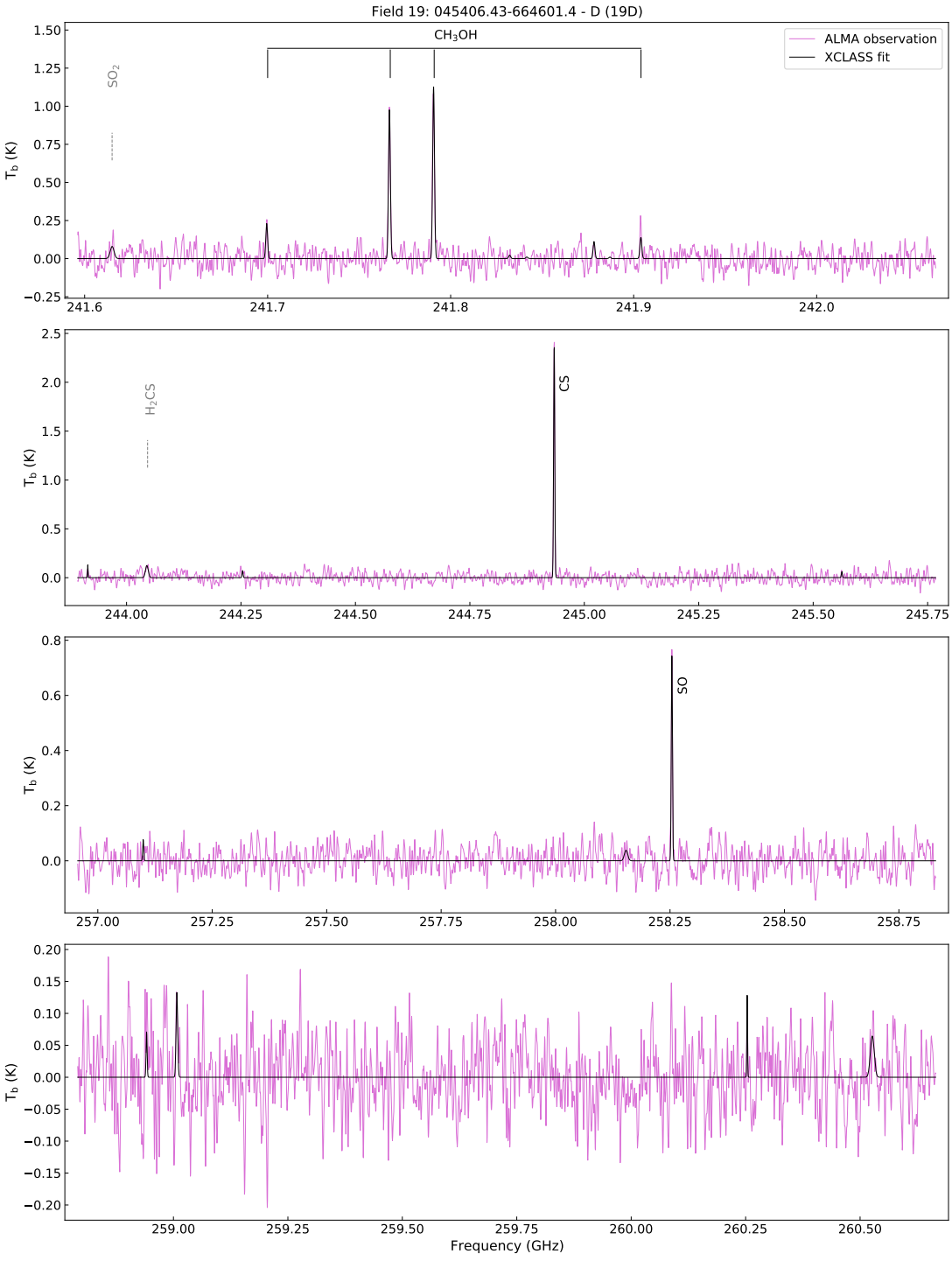
(a)

Figure B.19: Same as Fig. B.1 but for source 19A.



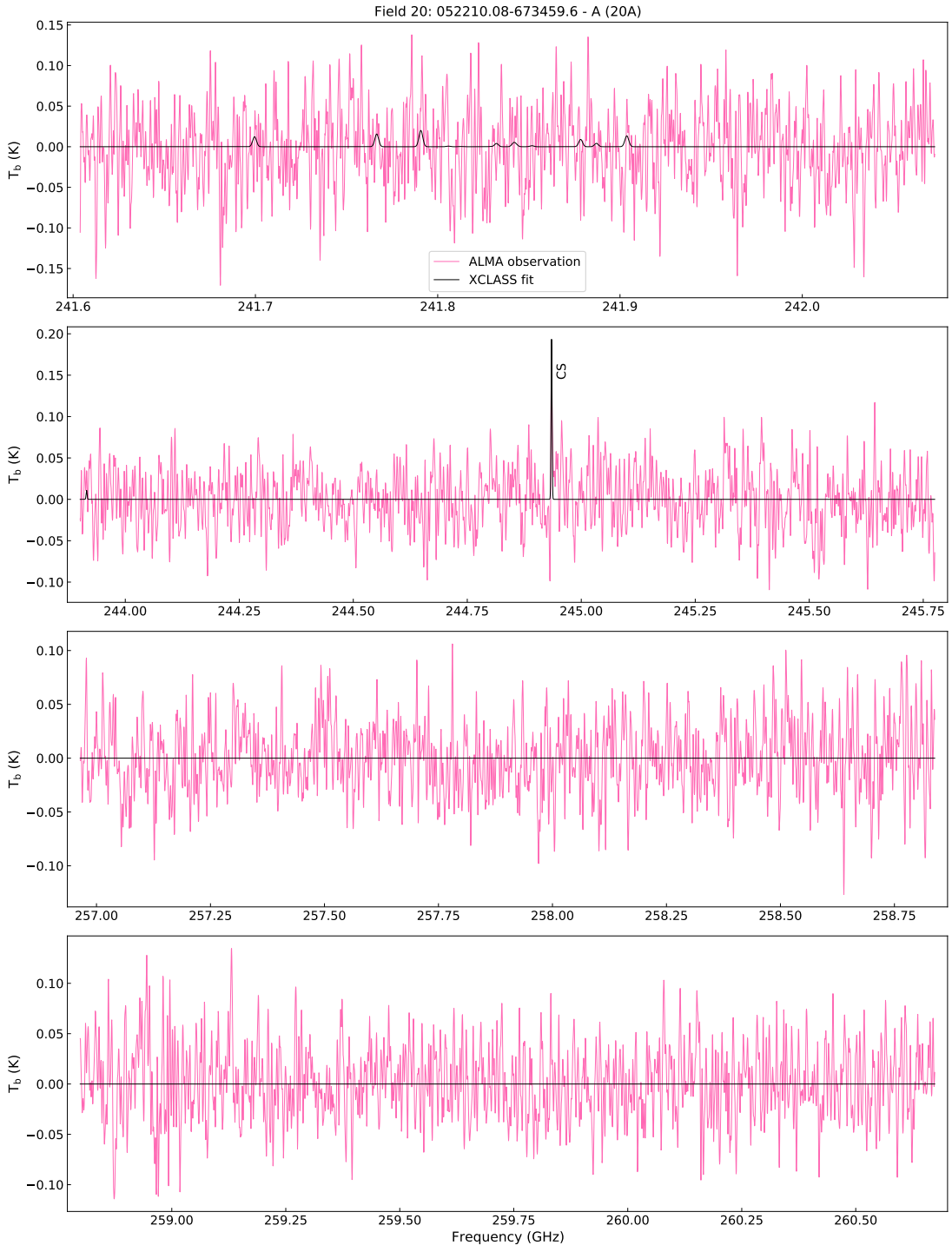
(b)

Figure B.19: Same as Fig. B.1 but for source 19C.



(c)

Figure B.19: Same as Fig. B.1 but for source 19D.



(a)

Figure B.20: Same as Fig. B.1 but for source 20A.

B.2 XCLASS fits parameters

In Table B.1, we list the parameters assuming LTE conditions for the CH_3OH, and Table B.2 collects the fit parameters for CH_3OH in non-LTE. We used the non-LTE temperature for methanol to fit other molecules. Therefore, the fit parameters for other molecules are only presented in Table B.2. (For more details, see Section 3.3.1.) Figure B.21 compares the LTE and non-LTE fit for two methanol lines at 241.767 and 241.792 for two sources, 2C and 14A. While methanol is fit with one component in 2C, 14A gets the best-fitting results with two components for methanol, where the cold foreground component (the envelope) is assumed to be in non-LTE.

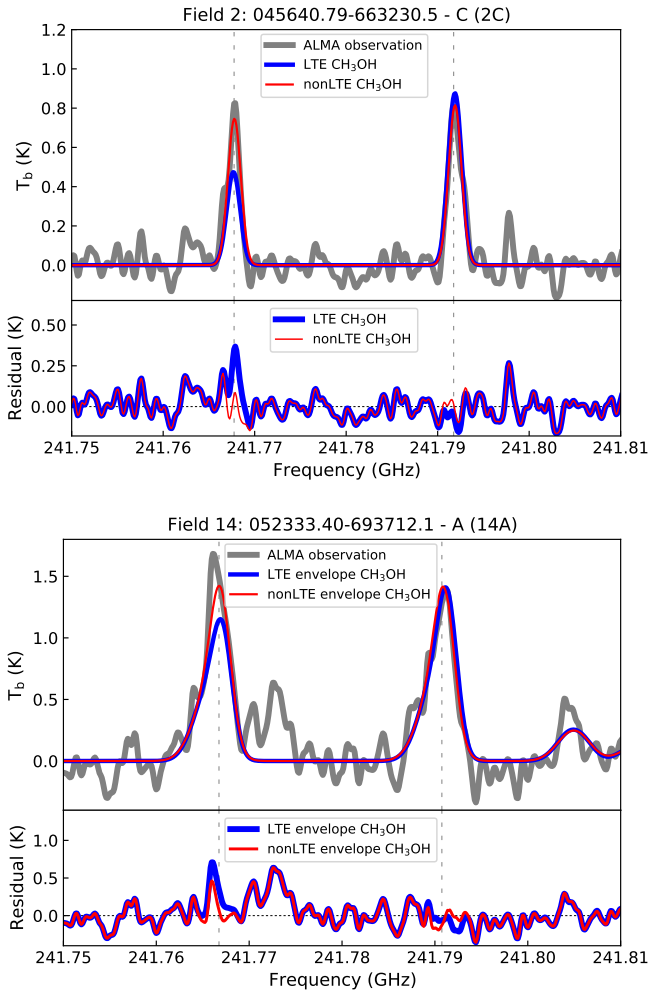


Figure B.21: Comparisons of the LTE and non-LTE fit for two CH_3OH lines at 241.767 and 241.791 GHz.

Table B.1: Parameters of the LTE fits for CH_3OH.

Source	T (K)	N(X) (cm^{-2})	Δv_{FWHM} (km s^{-1})	v_{LSR} (km s^{-1})
1A	16	2.09×10^{14}	4.3	224.8
2A	12	5.29×10^{13}	1.3	269.2
2B	12	3.48×10^{14}	1.8	268.7
2C	9	3.50×10^{14}	2.1	267.8
2D	16	4.51×10^{13}	3.5	268.4
2E	10	1.09×10^{14}	2.0	269.0
3A	16	3.72×10^{14}	3.9	285.2
3B	11	9.17×10^{13}	1.8	284.7
3C	10	1.15×10^{14}	2.1	286.3
3D	10	1.39×10^{14}	1.6	286.3
4A	144	4.88×10^{15}	3.17	264.3
	20	1.35×10^{14}	4.49	264.2
5A	5	1.11×10^{15}	2.0	246.1
5B	15	1.41×10^{14}	2.3	242.3
6A	170	6.56×10^{15}	5.74	242.3
	19	4.17×10^{14}	3.80	242.9
6B	228	9.15×10^{15}	3.21	243.3
	33	3.27×10^{14}	3.47	241.2
6C	12	5.35×10^{14}	3.7	242.0
6D	8	5.36×10^{15}	2.7	242.1
6E	12	1.54×10^{15}	2.5	243.0
6F	9	2.39×10^{14}	1.8	241.3
7A	10	3.84×10^{14}	1.7	252.8
8A	15	4.04×10^{14}	1.9	238.0
8C	10	7.57×10^{14}	2.6	239.9
9A	11	5.31×10^{14}	1.8	241.6
10A	10	3.77×10^{14}	2.9	239.3
10C	11	1.08×10^{14}	1.6	239.3
10D	10	8.89×10^{13}	2.8	239.3
11B	17	8.15×10^{14}	1.9	236.0
11C	10	1.15×10^{14}	1.6	235.5
11D	11	9.39×10^{14}	2.0	235.7
12A	14	1.17×10^{14}	1.6	267.9

Continued ...

Table B.1: Parameters of the LTE fits for CH_3OH.

Source	T (K)	N(X) (cm^{-2})	Δv_{FWHM} (km s^{-1})	v_{LSR} (km s^{-1})
12D	12	5.28×10^{13}	1.6	270.3
13A	12	4.64×10^{14}	1.8	227.1
13C	8	3.19×10^{15}	2.6	227.3
13E	14	3.25×10^{13}	1.5	225.7
13F	10	8.35×10^{14}	2.5	227.0
13G	10	3.03×10^{14}	3.0	226.8
13H	10	1.27×10^{14}	1.6	226.8
14A	160	6.48×10^{15}	4.70	250.0
	26	2.96×10^{14}	3.03	248.0
15A	16	2.70×10^{14}	5.5	235.4
15B	10	5.80×10^{14}	2.2	238.5
16B	12	1.48×10^{14}	2.0	236.1
17A	14	5.11×10^{14}	2.9	221.4
18A	12	2.61×10^{14}	2.0	279.0
18B	11	1.62×10^{14}	2.6	279.8
18C	10	1.26×10^{14}	1.7	280.7
19A	10	3.01×10^{15}	2.3	274.5
19D	10	2.61×10^{14}	1.4	274.1

Notes. The final best-fit models for CH_3OH are listed in Table B.2 (see Section 3.3.1 for more details).

Table B.2: Parameters of the best-fit model for all detected molecules and their abundances.

Source	Species, X	T (K)	N(X) (cm^{-2})	Δv_{FWHM} (km s^{-1})	v_{LSR} (km s^{-1})	$N(X)/N(H_2)^{\$}$	$n_{col}{}^{*}$ (cm^{-3})
1A	$CH_3OH^{\star}$	58	1.16×10^{14}	2.6	224.8	6.34×10^{-10}	4.9×10^{6}
	SO_2	35	8.40×10^{13}	2.8	224.5	4.59×10^{-10}	
	H_2CS	$58^{\dagger}$	3.55×10^{13}	3.8	224.5	1.94×10^{-10}	
	CS	"	1.06×10^{14}	4.0	225.4	5.79×10^{-10}	
	$HC^{15}N$	"	1.42×10^{12}	5.4	224.5	7.76×10^{-12}	
	SO	"	2.61×10^{14}	4.6	225.7	1.43×10^{-9}	
	$H^{13}CN$	"	2.02×10^{12}	6.3	224.0	1.10×10^{-11}	
	$H^{13}CO^{+}$	"	1.37×10^{12}	4.0	225.5	7.48×10^{-12}	
	SiO	"	2.07×10^{12}	3.7	226.5	1.13×10^{-11}	
2A	$CH_3OH^{\star}$	23	2.09×10^{13}	1.3	269.1	3.10×10^{-11}	2.0×10^{6}
	SO_2	$23^{\dagger}$	3.12×10^{13}	3.5	268.8	4.63×10^{-11}	
	CS	"	1.30×10^{13}	3.4	269.6	1.93×10^{-11}	
	SO	"	4.65×10^{13}	2.5	269.4	6.90×10^{-11}	
2B	$CH_3OH^{\star}$	22	1.70×10^{14}	1.8	268.7	4.33×10^{-10}	3.7×10^{6}
	SO_2	23	7.33×10^{13}	2.2	269.0	1.87×10^{-10}	
	H_2CS	$22^{\dagger}$	1.63×10^{13}	3.7	270.0	4.15×10^{-11}	
	CS	"	5.96×10^{13}	3.5	269.8	1.52×10^{-10}	
	$HC^{15}N$	"	5.13×10^{11}	4.7	271.5	1.31×10^{-12}	
	SO	"	2.88×10^{14}	3.3	270.0	7.34×10^{-10}	
	$H^{13}CN$	"	2.08×10^{12}	4.1	268.6	5.30×10^{-12}	
	$H^{13}CO^{+}$	"	4.41×10^{11}	3.1	270.3	1.12×10^{-12}	
	SiO	"	1.25×10^{12}	6.8	268.3	3.18×10^{-12}	
2C	$CH_3OH^{\star}$	67	5.56×10^{13}	2.1	267.8	6.87×10^{-10}	6.2×10^{5}
	H_2CS	$67^{\dagger}$	4.11×10^{13}	5.2	266.9	5.08×10^{-10}	
	CS	"	4.52×10^{13}	3.5	268.4	5.59×10^{-10}	
	SO	"	3.10×10^{13}	3.5	268.6	3.83×10^{-10}	
	$H^{13}CN$	"	1.35×10^{12}	9.6	271.9	1.67×10^{-11}	
2D	$CH_3OH^{\star}$	55	1.91×10^{13}	1.4	269.3	2.81×10^{-10}	2.0×10^{6}
	CS	$55^{\dagger}$	2.82×10^{13}	3.3	270.4	4.15×10^{-10}	
	SO	"	1.69×10^{13}	4.0	271.4	2.49×10^{-10}	
2E	$CH_3OH^{\star}$	11	7.80×10^{13}	1.8	268.4	2.07×10^{-10}	2.0×10^{6}
	CS	$11^{\dagger}$	3.14×10^{13}	2.8	270.1	8.33×10^{-11}	
	SO	"	1.54×10^{14}	2.9	271.2	4.08×10^{-10}	
2F	$CH_3OH^{\star}$	$27^{\ddagger}$	$< 8.28 \times 10^{12}$	$2.8^{\equiv}$	$270.9^{\equiv}$	$< 1.11 \times 10^{-10}$	

Continued ...

Table B.2: Parameters of the best-fit model for all detected molecules and their abundances.

Source	Species, X	T (K)	N(X) (cm^{-2})	Δv_{FWHM} (km s^{-1})	v_{LSR} (km s^{-1})	$N(X)/N(H_2)^{\$}$	$n_{col}{}^{*}$ (cm^{-3})
	CS	"	3.31×10^{12}	2.8	270.9	4.46×10^{-11}	
	$H^{13}CN$	"	2.68×10^{12}	13.1	276.0	3.61×10^{-11}	
3A	$CH_3OH^{\star}$	35	2.46×10^{14}	3.9	285.2	1.83×10^{-10}	9.0×10^{6}
	SO_2	43	1.06×10^{14}	4.7	285.0	7.89×10^{-11}	
	H_2CS	$35^{\dagger}$	2.59×10^{13}	4.3	285.5	1.93×10^{-11}	
	CS	"	8.60×10^{13}	4.8	285.8	6.40×10^{-11}	
	CH_3CN	"	2.97×10^{12}	2.9	284.1	2.21×10^{-12}	
	$HC^{15}N$	"	6.82×10^{11}	4.0	286.4	5.08×10^{-13}	
	SO	"	3.66×10^{14}	4.5	286.3	2.73×10^{-10}	
	$H^{13}CN$	"	1.00×10^{12}	3.8	284.3	7.45×10^{-13}	
	$H^{13}CO^{+}$	"	8.83×10^{11}	4.0	286.5	6.57×10^{-13}	
	SiO	"	1.79×10^{12}	8.9	288.7	1.33×10^{-12}	
3B	$CH_3OH^{\star}$	13	6.50×10^{13}	1.7	284.6	8.08×10^{-11}	4.9×10^{6}
	CS	$13^{\dagger}$	4.29×10^{13}	4.0	285.9	5.33×10^{-11}	
	SO	"	2.79×10^{14}	3.7	286.2	3.47×10^{-10}	
	$H^{13}CO^{+}$	"	2.60×10^{11}	3.4	285.5	3.23×10^{-13}	
3C	$CH_3OH^{\star}$	51	2.38×10^{13}	1.8	286.2	3.77×10^{-10}	2.0×10^{6}
	CS	$51^{\dagger}$	1.45×10^{13}	3.4	287.4	2.30×10^{-10}	
	SO	"	1.48×10^{13}	3.2	287.2	2.34×10^{-10}	
	$H^{13}CO^{+}$	"	1.74×10^{11}	3.0	288.3	2.76×10^{-12}	
3D	$CH_3OH^{\star}$	37	3.25×10^{13}	1.5	286.3	4.48×10^{-10}	1.3×10^{6}
	CS	$37^{\dagger}$	1.28×10^{13}	3.5	287.1	1.77×10^{-10}	
	SO	"	1.22×10^{13}	3.2	287.4	1.68×10^{-10}	
4A	CH_3OH	151	1.29×10^{15}	3.2	264.3	3.55×10^{-9}	
	$CH_3OH^{\star}$	26	1.25×10^{14}	4.5	264.3	4.86×10^{-11}	4.6×10^{7}
	SO_2	249	4.47×10^{15}	7.1	265.5	2.06×10^{-8}	
		42	8.07×10^{14}	5.0	264.3	5.57×10^{-10}	
	$^{33}SO_2$	249	3.73×10^{14}	7.1	265.5	1.72×10^{-9}	
		42	6.72×10^{13}	5.0	264.3	4.63×10^{-11}	
	$^{34}SO_2$	249	5.05×10^{14}	7.1	265.5	2.33×10^{-9}	
		42	9.10×10^{13}	5.0	264.3	6.28×10^{-11}	
	SO	$151^{\dagger}$	2.01×10^{15}	6.0	265.7	5.55×10^{-9}	
	^{33}SO	"	1.68×10^{14}	6.0	265.7	4.62×10^{-10}	
	CH_3CN	88	1.02×10^{13}	3.9	265.3	1.57×10^{-11}	
	CS	$151^{\dagger}$	2.60×10^{14}	5.0	265.1	7.15×10^{-10}	
	H_2CS	"	8.29×10^{13}	3.6	264.0	2.28×10^{-10}	

Continued ...

Table B.2: Parameters of the best-fit model for all detected molecules and their abundances.

Source	Species, X	T (K)	N(X) (cm^{-2})	Δv_{FWHM} (km s^{-1})	v_{LSR} (km s^{-1})	$N(X)/N(H_2)^{\$}$	$n_{col}{}^{*}$ (cm^{-3})
	$H^{13}CO^+$	"	1.20×10^{13}	5.1	265.6	3.30×10^{-11}	
	SiO	"	1.88×10^{13}	5.8	265.7	5.16×10^{-11}	
	$H^{13}CN$	"	1.20×10^{13}	6.0	264.0	3.31×10^{-11}	
	$HC^{15}N$	"	6.48×10^{12}	5.7	264.8	1.79×10^{-11}	
	HNCO	"	2.71×10^{13}	2.6	264.1	7.47×10^{-11}	
	HC_3N	"	6.62×10^{12}	8.0	264.9	1.82×10^{-11}	
	HDCO	"	$< 4.17 \times 10^{9}$	$3.2^{\equiv}$	$264.3^{\equiv}$	$< 1.15 \times 10^{-14}$	
	NH_2CHO	"	$< 5.60 \times 10^{10}$	"	"	$< 1.54 \times 10^{-13}$	
	H_2CCO	"	$< 5.23 \times 10^{12}$	"	"	$< 1.44 \times 10^{-11}$	
	CH_3CHO	"	$< 1.20 \times 10^{12}$	"	"	$< 3.31 \times 10^{-12}$	
	CH_3OCHO	"	$< 5.35 \times 10^{13}$	"	"	$< 1.47 \times 10^{-10}$	
	CH_3OCH_3	"	$< 5.07 \times 10^{8}$	"	"	$< 1.40 \times 10^{-15}$	
5A	$CH_3OH^{\star}$	15	3.16×10^{13}	2.7	246.0	2.12×10^{-11}	1.1×10^{6}
	CS	$15^{\dagger}$	2.91×10^{13}	4.2	246.6	1.95×10^{-11}	
	SO	"	9.08×10^{13}	3.9	246.3	6.08×10^{-11}	
	$H^{13}CN$	"	1.07×10^{12}	10.0	248.4	7.17×10^{-13}	
	$H^{13}CO^+$	"	3.84×10^{11}	3.9	246.0	2.57×10^{-13}	
	SiO	"	5.64×10^{12}	20.0	245.3	3.78×10^{-12}	
5B	$CH_3OH^{\star}$	19	9.76×10^{13}	2.1	242.2	1.53×10^{-10}	5.4×10^{6}
	SO_2	38	7.48×10^{13}	3.0	242.0	1.17×10^{-10}	
	H_2CS	$19^{\dagger}$	3.94×10^{13}	3.8	242.3	6.18×10^{-11}	
	CS	"	1.27×10^{14}	3.7	243.3	1.99×10^{-10}	
	$HC^{15}N$	"	9.31×10^{11}	7.1	241.9	1.46×10^{-12}	
	SO	"	3.92×10^{14}	3.7	243.3	6.15×10^{-10}	
	$H^{13}CN$	"	1.76×10^{12}	10.0	239.2	2.76×10^{-12}	
	$H^{13}CO^+$	"	6.35×10^{11}	3.5	243.4	9.96×10^{-13}	
6A	CH_3OH	149	1.46×10^{15}	5.7	242.4	3.60×10^{-9}	
	$CH_3OH^{\star}$	36	2.62×10^{14}	3.7	242.9	1.38×10^{-10}	1.3×10^{7}
	SO_2	161	5.28×10^{15}	12.5	245.5	1.42×10^{-8}	
		44	9.75×10^{14}	7.1	243.7	6.50×10^{-10}	
	$^{33}SO_2$	161	2.55×10^{14}	12.5	245.5	6.88×10^{-10}	
		44	4.74×10^{13}	7.1	243.7	3.16×10^{-11}	
	$^{34}SO_2$	161	2.80×10^{14}	12.5	245.5	7.55×10^{-10}	
		44	5.19×10^{13}	7.1	243.7	3.46×10^{-11}	
	SO	$149^{\dagger}$	4.58×10^{15}	9.5	244.9	1.13×10^{-8}	
	^{33}SO	"	2.23×10^{14}	9.5	244.9	5.50×10^{-10}	
	CH_3CN	77	2.46×10^{13}	6.8	243.7	3.04×10^{-11}	
	CS	$149^{\dagger}$	4.99×10^{14}	5.5	243.6	1.23×10^{-9}	

Continued ...

Table B.2: Parameters of the best-fit model for all detected molecules and their abundances.

Source	Species, X	T (K)	N(X) (cm^{-2})	Δv_{FWHM} (km s^{-1})	v_{LSR} (km s^{-1})	$N(X)/N(H_2)^{\$}$	$n_{col}{}^{*}$ (cm^{-3})
	H_2CS	"	2.05×10^{14}	5.3	242.8	5.07×10^{-10}	
	$H^{13}CO^+$	"	1.32×10^{13}	4.9	244.3	3.25×10^{-11}	
	SiO	"	8.80×10^{13}	11.5	246.0	2.17×10^{-10}	
	$H^{13}CN$	"	2.13×10^{13}	9.8	243.6	5.27×10^{-11}	
	$HC^{15}N$	"	1.31×10^{13}	7.5	244.7	3.25×10^{-11}	
	HNCO	"	8.35×10^{13}	5.8	242.8	2.06×10^{-10}	
	HC_3N	"	1.24×10^{13}	4.7	245.1	3.07×10^{-11}	
	NH_2CHO	"	4.09×10^{13}	4.8	241.5	1.01×10^{-10}	
	HDCO	"	$< 6.74 \times 10^{12}$	$5.7^{\equiv}$	$242.4^{\equiv}$	$< 1.66 \times 10^{-11}$	
	H_2CCO	"	$< 5.00 \times 10^{8}$	"	"	$< 1.23 \times 10^{-15}$	
	CH_3CHO	"	$< 5.02 \times 10^{8}$	"	"	$< 1.24 \times 10^{-15}$	
	CH_3OCHO	"	$< 5.03 \times 10^{8}$	"	"	$< 1.24 \times 10^{-15}$	
	CH_3OCH_3	"	$< 8.51 \times 10^{8}$	"	"	$< 2.10 \times 10^{-15}$	
6B	CH_3OH	181	1.60×10^{15}	2.9	243.1	5.50×10^{-9}	
	$CH_3OH^{\star}$	50	3.25×10^{14}	4.4	241.6	2.83×10^{-10}	2.8×10^{7}
	SO_2	175	1.53×10^{15}	6.0	243.0	5.03×10^{-9}	
		34	2.68×10^{14}	3.3	241.7	1.49×10^{-10}	
	$^{34}SO_2$	175	1.30×10^{14}	6.0	243.0	4.28×10^{-10}	
		34	2.28×10^{13}	3.3	241.7	1.27×10^{-11}	
	SO	$181^{\dagger}$	1.39×10^{15}	5.2	243.2	4.75×10^{-9}	
	^{33}SO	"	7.48×10^{13}	5.2	243.2	2.56×10^{-10}	
	CH_3CN	132	4.86×10^{13}	8.7	243.4	1.19×10^{-10}	
	CS	$181^{\dagger}$	3.85×10^{14}	5.0	242.4	1.32×10^{-9}	
	H_2CS	"	4.10×10^{14}	5.2	241.5	1.41×10^{-9}	
	$H^{13}CO^+$	"	1.08×10^{13}	4.0	242.9	3.72×10^{-11}	
	SiO	"	1.51×10^{13}	5.8	243.5	5.19×10^{-11}	
	$H^{13}CN$	"	2.65×10^{13}	5.6	242.1	9.08×10^{-11}	
	$HC^{15}N$	"	1.46×10^{13}	4.3	243.7	4.99×10^{-11}	
	HNCO	"	3.64×10^{13}	2.5	242.3	1.25×10^{-10}	
	HC_3N	"	1.41×10^{13}	4.5	243.9	4.83×10^{-11}	
	HDCO	"	$< 1.64 \times 10^{10}$	$2.9^{\equiv}$	$243.1^{\equiv}$	$< 5.61 \times 10^{-14}$	
	NH_2CHO	"	$< 2.77 \times 10^{9}$	"	"	$< 9.49 \times 10^{-15}$	
	H_2CCO	"	$< 3.45 \times 10^{13}$	"	"	$< 1.18 \times 10^{-10}$	
	CH_3CHO	"	$< 4.60 \times 10^{13}$	"	"	$< 1.58 \times 10^{-10}$	
	CH_3OCHO	"	$< 1.67 \times 10^{14}$	"	"	$< 5.71 \times 10^{-10}$	
	CH_3OCH_3	"	$< 2.39 \times 10^{14}$	"	"	$< 8.19 \times 10^{-10}$	
6C	$CH_3OH^{\star}$	30	2.38×10^{14}	3.6	241.9	3.23×10^{-10}	5.3×10^{6}
	SO_2	$30^{\dagger}$	4.90×10^{13}	2.2	241.3	6.66×10^{-11}	
	H_2CS	"	7.05×10^{13}	3.6	241.7	9.58×10^{-11}	

Continued ...

Table B.2: Parameters of the best-fit model for all detected molecules and their abundances.

Source	Species, X	T (K)	N(X) (cm^{-2})	Δv_{FWHM} (km s^{-1})	v_{LSR} (km s^{-1})	$N(X)/N(H_2)^{\$}$	$n_{col}{}^{*}$ (cm^{-3})
	CS	"	2.34×10^{14}	4.1	242.5	3.18×10^{-10}	
	SO	"	2.56×10^{14}	4.2	242.7	3.48×10^{-10}	
	$H^{13}CN$	"	1.25×10^{12}	2.3	242.6	1.70×10^{-12}	
	$H^{13}CO^{+}$	"	9.47×10^{11}	3.8	243.0	1.29×10^{-12}	
	SiO	"	8.50×10^{12}	18.9	238.2	1.16×10^{-11}	
6D	$CH_3OH^{\star}$	46	5.08×10^{14}	3.4	242.1	1.54×10^{-9}	2.1×10^{6}
	H_2CS	$46^{\dagger}$	8.41×10^{13}	3.9	242.7	2.55×10^{-10}	
	CS	"	1.88×10^{14}	5.2	243.0	5.69×10^{-10}	
	SO	"	2.47×10^{14}	5.5	242.8	7.48×10^{-10}	
	$H^{13}CO^{+}$	"	8.91×10^{11}	4.0	241.8	2.70×10^{-12}	
	SiO	"	$< 7.51 \times 10^{12}$	15.6	246.3	2.27×10^{-11}	
6E	$CH_3OH^{\star}$	38	5.19×10^{14}	2.6	243.0	1.28×10^{-9}	3.3×10^{6}
	H_2CS	$38^{\dagger}$	7.75×10^{13}	4.2	243.0	1.91×10^{-10}	
	CS	"	1.82×10^{14}	4.2	243.7	4.48×10^{-10}	
	SO	"	1.92×10^{14}	3.8	244.0	4.73×10^{-10}	
	$H^{13}CN$	"	1.78×10^{12}	4.6	242.4	4.38×10^{-12}	
	$H^{13}CO^{+}$	"	5.54×10^{11}	3.4	244.5	1.36×10^{-12}	
	SiO	"	8.59×10^{11}	4.9	238.1	2.12×10^{-12}	
6F	$CH_3OH^{\star}$	27	5.82×10^{13}	1.9	241.2	1.33×10^{-10}	1.0×10^{6}
	SO_2	$27^{\dagger}$	3.54×10^{13}	2.9	240.9	8.08×10^{-11}	
	CS	"	4.22×10^{13}	3.4	241.9	9.63×10^{-11}	
	SO	"	1.08×10^{14}	3.3	242.1	2.47×10^{-10}	
	$H^{13}CO^{+}$	"	6.01×10^{11}	3.1	242.1	1.37×10^{-12}	
7A	$CH_3OH^{\star}$	29	9.92×10^{13}	1.8	252.8	3.05×10^{-10}	2.4×10^{6}
	SO_2	22	3.25×10^{13}	1.6	253.1	9.98×10^{-11}	
	H_2CS	$29^{\dagger}$	1.40×10^{13}	3.3	253.3	4.30×10^{-11}	
	CS	"	4.91×10^{13}	3.4	253.8	1.51×10^{-10}	
	SO	"	1.36×10^{14}	3.1	254.1	4.18×10^{-10}	
	$H^{13}CN$	"	8.42×10^{11}	7.2	255.4	2.59×10^{-12}	
	$H^{13}CO^{+}$	"	8.17×10^{11}	3.6	254.2	2.51×10^{-12}	
7B	CH_3OH	$27^{\ddagger}$	$< 1.00 \times 10^{10}$	$2.8^{\equiv}$	$252.4^{\equiv}$	$< 8.11 \times 10^{-14}$	
	CS	"	5.83×10^{12}	2.8	252.4	4.73×10^{-11}	
7C	CH_3OH	$27^{\ddagger}$	$< 2.20 \times 10^{13}$	$2.9^{\equiv}$	$255.0^{\equiv}$	$< 1.74 \times 10^{-10}$	
	CS	$27^{\dagger}$	9.13×10^{12}	2.9	255.0	7.24×10^{-11}	
	$H^{13}CO^{+}$	"	2.19×10^{11}	3.2	255.3	1.74×10^{-12}	

Continued ...

Table B.2: Parameters of the best-fit model for all detected molecules and their abundances.

Source	Species, X	T (K)	N(X) (cm^{-2})	Δv_{FWHM} (km s^{-1})	v_{LSR} (km s^{-1})	$N(X)/N(H_2)^{\$}$	$n_{col}{}^{*}$ (cm^{-3})
8A	$CH_3OH^{\star}$	25	2.14×10^{14}	2.0	238.0	6.30×10^{-10}	7.3×10^{6}
	SO_2	36	4.00×10^{13}	3.1	237.9	1.18×10^{-10}	
	H_2CS	$25^{\dagger}$	1.68×10^{13}	4.0	237.4	4.94×10^{-11}	
	CS	"	5.23×10^{13}	3.8	238.6	1.54×10^{-10}	
	SO	"	2.33×10^{14}	3.6	239.0	6.86×10^{-10}	
	$H^{13}CN$	"	5.13×10^{11}	3.1	237.5	1.51×10^{-12}	
	$H^{13}CO^{+}$	"	1.55×10^{11}	5.3	238.2	4.56×10^{-13}	
8B[§]							
8C	$CH_3OH^{\star}$	27	2.08×10^{14}	2.8	239.9	1.13×10^{-9}	2.0×10^{6}
	CS	$27^{\dagger}$	5.67×10^{13}	4.2	240.8	3.09×10^{-10}	
	SO	"	1.21×10^{14}	3.7	240.8	6.59×10^{-10}	
9A	$CH_3OH^{\star}$	50	1.53×10^{14}	1.8	241.6	1.16×10^{-9}	1.9×10^{6}
	H_2CS	$50^{\dagger}$	2.08×10^{13}	3.4	241.3	1.57×10^{-10}	
	CS	"	7.34×10^{13}	3.7	242.4	5.55×10^{-10}	
	SO	"	6.96×10^{13}	3.4	242.6	5.26×10^{-10}	
	$H^{13}CN$	"	8.95×10^{11}	2.5	241.2	6.77×10^{-12}	
	$H^{13}CO^{+}$	"	4.01×10^{11}	3.1	242.5	3.03×10^{-12}	
10A	$CH_3OH^{\star}$	26	1.20×10^{14}	2.9	239.0	3.48×10^{-10}	2.5×10^{6}
	SO_2	30	2.19×10^{13}	2.3	239.4	6.36×10^{-11}	
	H_2CS	$26^{\dagger}$	9.92×10^{12}	3.4	239.3	2.88×10^{-11}	
	CS	"	4.20×10^{13}	4.0	240.4	1.22×10^{-10}	
	$HC^{15}N$	"	2.97×10^{11}	4.5	239.0	8.62×10^{-13}	
	SO	"	1.01×10^{14}	4.1	240.5	2.93×10^{-10}	
	$H^{13}CN$	"	8.44×10^{11}	7.2	241.2	2.45×10^{-12}	
	$H^{13}CO^{+}$	"	5.35×10^{11}	3.4	240.6	1.55×10^{-12}	
	SiO	"	1.13×10^{12}	4.7	240.7	3.28×10^{-12}	
10B	CH_3OH	$27^{\ddagger}$	$< 6.25 \times 10^{13}$	$3.6^{\equiv}$	$240.7^{\equiv}$	$< 3.43 \times 10^{-10}$	
	CS	"	2.21×10^{13}	3.6	240.7	1.21×10^{-10}	
	$H^{13}CO^{+}$	"	5.72×10^{11}	5.1	241.7	3.14×10^{-12}	
	SiO	"	2.01×10^{12}	4.7	241.5	1.10×10^{-11}	
10C	$CH_3OH^{\star}$	39	3.35×10^{13}	1.5	238.9	5.54×10^{-10}	2.5×10^{6}
	CS	$39^{\dagger}$	1.96×10^{13}	3.4	240.0	3.24×10^{-10}	
	$H^{13}CO^{+}$	"	1.88×10^{11}	2.4	240.4	3.11×10^{-12}	

Continued ...

Table B.2: Parameters of the best-fit model for all detected molecules and their abundances.

Source	Species, X	T (K)	N(X) (cm^{-2})	Δv_{FWHM} (km s^{-1})	v_{LSR} (km s^{-1})	$N(X)/N(H_2)^{\$}$	$n_{col}{}^{*}$ (cm^{-3})
10D	$CH_3OH^{\star}$	22	4.59×10^{13}	5.9	240.7	3.99×10^{-10}	2.0×10^{6}
	CS	$22^{\dagger}$	1.55×10^{13}	3.1	240.7	1.35×10^{-10}	
11A							
11B	$CH_3OH^{\star}$	24	6.28×10^{14}	2.0	236.0	1.87×10^{-9}	2.0×10^{7}
	H_2CS	$24^{\dagger}$	4.05×10^{13}	3.9	236.3	1.21×10^{-10}	
	CS	"	8.37×10^{13}	3.3	236.7	2.49×10^{-10}	
	SO	"	2.56×10^{14}	3.8	237.1	7.63×10^{-10}	
	$H^{13}CN$	"	5.41×10^{11}	2.6	236.1	1.61×10^{-12}	
	$H^{13}CO^{+}$	"	2.19×10^{11}	5.4	237.1	6.52×10^{-13}	
11C	$CH_3OH^{\star}$	10	1.21×10^{14}	1.5	235.6	2.11×10^{-10}	4.9×10^{6}
	CS	$10^{\dagger}$	6.58×10^{13}	3.3	236.5	1.15×10^{-10}	
	SO	"	3.48×10^{14}	3.5	236.8	6.06×10^{-10}	
	$H^{13}CO^{+}$	"	4.70×10^{11}	3.6	236.4	8.18×10^{-13}	
11D	$CH_3OH^{\star}$	22	3.74×10^{14}	2.2	235.6	2.97×10^{-9}	3.9×10^{6}
	H_2CS	$22^{\dagger}$	2.42×10^{13}	4.8	235.5	1.92×10^{-10}	
	CS	"	1.06×10^{14}	4.4	236.1	8.41×10^{-10}	
	SO	"	1.40×10^{14}	3.6	236.6	1.11×10^{-9}	
12A	$CH_3OH^{\star}$	19	7.88×10^{13}	1.6	267.9	1.91×10^{-10}	7.5×10^{6}
	H_2CS	$19^{\dagger}$	2.35×10^{13}	2.7	268.2	5.70×10^{-11}	
	CS	"	4.35×10^{13}	3.5	268.9	1.06×10^{-10}	
	SO	"	1.08×10^{14}	3.4	269.1	2.62×10^{-10}	
	$H^{13}CN$	"	1.44×10^{12}	10.0	269.4	3.49×10^{-12}	
	$H^{13}CO^{+}$	"	3.04×10^{11}	4.2	269.4	7.38×10^{-13}	
12B	CH_3OH	$27^{\ddagger}$	$< 7.99 \times 10^{12}$	$2.4^{\equiv}$	$271.4^{\equiv}$	$< 5.84 \times 10^{-11}$	
	CS	"	3.73×10^{12}	2.4	271.4	2.73×10^{-11}	
12C	CH_3OH	$27^{\ddagger}$	$< 3.33 \times 10^{12}$	2.8	270.7	$< 2.85 \times 10^{-11}$	
	CS	"	9.99×10^{12}	2.8	270.7	8.55×10^{-11}	
	SO	"	2.61×10^{13}	3.4	271.0	2.23×10^{-10}	
12D	$CH_3OH^{\star}$	38	1.85×10^{13}	1.3	270.2	3.06×10^{-10}	2.0×10^{6}
	CS	$38^{\dagger}$	1.02×10^{13}	3.1	271.0	1.69×10^{-10}	
13A	$CH_3OH^{\star}$	49	1.71×10^{14}	1.8	227.0	9.63×10^{-10}	2.6×10^{6}
	SO_2	$49^{\dagger}$	2.32×10^{13}	1.2	227.0	1.31×10^{-10}	

Continued ...

Table B.2: Parameters of the best-fit model for all detected molecules and their abundances.

Source	Species, X	T (K)	N(X) (cm^{-2})	Δv_{FWHM} (km s^{-1})	v_{LSR} (km s^{-1})	N(X)/N(H_2)[$]	n_{col}[*] (cm^{-3})
	H_2CS	"	1.75×10^{13}	3.8	227.5	9.86×10^{-11}	
	CS	"	7.01×10^{13}	3.4	227.9	3.95×10^{-10}	
	SO	"	7.19×10^{13}	2.5	227.9	4.05×10^{-10}	
	$H^{13}CN$	"	4.80×10^{11}	2.7	227.5	2.70×10^{-12}	
	$H^{13}CO^+$	"	3.49×10^{11}	3.0	228.0	1.97×10^{-12}	
	SiO	"	7.28×10^{11}	4.9	226.7	4.10×10^{-12}	
13B[§]							
13C	$CH_3OH^\star$	27	3.91×10^{14}	3.0	227.3	1.26×10^{-9}	1.4×10^6
	SO_2	27[†]	2.86×10^{13}	2.3	227.1	9.18×10^{-11}	
	H_2CS	"	2.61×10^{13}	5.3	227.2	8.38×10^{-11}	
	CS	"	1.03×10^{14}	4.1	228.2	3.31×10^{-10}	
	SO	"	1.50×10^{14}	4.0	228.1	4.82×10^{-10}	
	$H^{13}CN$	"	1.01×10^{12}	4.8	228.5	3.24×10^{-12}	
	$H^{13}CO^+$	"	3.18×10^{11}	4.5	229.1	1.02×10^{-12}	
	SiO	"	3.92×10^{12}	20.0	216.8	1.26×10^{-11}	
13D	CH_3OH	27[‡]	$< 8.62 \times 10^{13}$	4.3[≡]	230.7[≡]	$< 3.04 \times 10^{-10}$	
	SO_2	"	9.27×10^{13}	3.8	229.8	3.27×10^{-10}	
	H_2CS	"	1.94×10^{13}	4.0	229.6	6.85×10^{-11}	
	CS	"	4.98×10^{13}	4.3	230.7	1.76×10^{-10}	
	SO	"	2.68×10^{14}	4.5	230.2	9.46×10^{-10}	
13E	$CH_3OH^\star$	19	2.06×10^{13}	1.6	225.6	8.11×10^{-11}	2.0×10^6
	CS	19[†]	2.41×10^{13}	3.6	226.5	9.49×10^{-11}	
	SO	"	1.64×10^{13}	3.5	227.3	6.46×10^{-11}	
13F	$CH_3OH^\star$	42	2.09×10^{14}	2.1	227.6	2.51×10^{-9}	1.9×10^6
	SO_2	42[†]	2.23×10^{13}	1.7	227.3	2.68×10^{-10}	
	H_2CS	"	1.06×10^{13}	3.2	227.2	1.27×10^{-10}	
	CS	"	6.38×10^{13}	3.7	228.5	7.65×10^{-10}	
	SO	"	7.82×10^{13}	3.5	228.6	9.38×10^{-10}	
	$H^{13}CO^+$	"	1.45×10^{11}	2.5	228.9	1.74×10^{-12}	
13G	$CH_3OH^\star$	19	1.22×10^{14}	1.7	226.0	6.38×10^{-10}	6.4×10^6
	CS	19[†]	3.00×10^{13}	3.4	226.9	1.57×10^{-10}	
	SO	"	8.09×10^{13}	3.4	227.1	4.23×10^{-10}	
	$H^{13}CO^+$	"	2.51×10^{11}	4.3	227.7	1.31×10^{-12}	
13H	$CH_3OH^\star$	40	3.41×10^{13}	1.5	227.2	4.75×10^{-10}	2.0×10^6

Continued ...

Table B.2: Parameters of the best-fit model for all detected molecules and their abundances.

Source	Species, X	T (K)	N(X) (cm^{-2})	Δv_{FWHM} (km s^{-1})	v_{LSR} (km s^{-1})	$N(X)/N(H_2)^{\$}$	$n_{col}{}^{*}$ (cm^{-3})
	CS	40†	1.82×10^{13}	3.5	228.1	2.54×10^{-10}	
13K	CH_3OH	27‡	$< 1.27 \times 10^{13}$	3.3$^{\equiv}$	227.4$^{\equiv}$	$< 1.68 \times 10^{-10}$	
	CS	"	8.86×10^{12}	3.3	227.4	1.17×10^{-10}	
14A	CH_3OH	163	1.79×10^{15}	4.9	249.8	1.06×10^{-8}	
	$CH_3OH^{\star}$	50	2.63×10^{14}	3.1	248.1	4.38×10^{-10}	1.6×10^{7}
	SO_2	138	1.48×10^{15}	8.0	250.6	7.36×10^{-9}	
		19	1.32×10^{14}	2.8	248.8	6.77×10^{-11}	
	SO	163	1.40×10^{15}	7.3	250.1	8.26×10^{-9}	
	CH_3CN	42	1.78×10^{13}	4.2	249.9	2.42×10^{-11}	
	CS	163†	3.70×10^{14}	5.4	249.2	2.18×10^{-9}	
	H_2CS	"	1.19×10^{14}	4.0	248.2	7.04×10^{-10}	
	$H^{13}CO^{+}$	"	5.46×10^{12}	4.2	249.6	3.23×10^{-11}	
	SiO	"	6.57×10^{13}	34.9	256.4	3.88×10^{-10}	
	HDCO	"	2.54×10^{13}	4.0	247.5	1.50×10^{-10}	
	$H^{13}CN$	"	1.77×10^{13}	6.8	249.4	1.04×10^{-10}	
	$HC^{15}N$	"	1.01×10^{13}	5.8	250.8	5.97×10^{-11}	
	HNCO	"	7.35×10^{13}	4.6	249.5	4.34×10^{-10}	
	NH_2CHO	"	$< 5.09 \times 10^{8}$	4.9$^{\equiv}$	249.8$^{\equiv}$	$< 3.00 \times 10^{-15}$	
	H_2CCO	"	$< 5.10 \times 10^{8}$	"	"	$< 3.01 \times 10^{-15}$	
	CH_3CHO	"	$< 5.09 \times 10^{8}$	"	"	$< 3.00 \times 10^{-15}$	
	CH_3OCHO	"	$< 9.43 \times 10^{13}$	"	"	$< 5.57 \times 10^{-10}$	
	CH_3OCH_3	"	$< 1.18 \times 10^{14}$	"	"	$< 6.97 \times 10^{-10}$	
14B§							
15A	$CH_3OH^{\star}$	38	1.47×10^{14}	6.0	235.5	2.77×10^{-10}	2.0×10^{6}
	SO_2	38†	1.11×10^{14}	2.4	236.0	2.09×10^{-10}	
	CS	"	1.10×10^{14}	4.2	236.7	2.08×10^{-10}	
	SO	"	2.99×10^{14}	4.5	237.1	5.64×10^{-10}	
	$H^{13}CO^{+}$	"	1.42×10^{12}	3.5	236.4	2.68×10^{-12}	
	SiO	"	1.49×10^{13}	19.3	229.3	2.81×10^{-11}	
15B	$CH_3OH^{\star}$	33	1.42×10^{14}	2.2	238.5	7.48×10^{-10}	1.7×10^{6}
	SO_2	33†	9.49×10^{12}	1.6	238.0	5.00×10^{-11}	
	H_2CS	"	1.33×10^{13}	3.4	238.7	7.00×10^{-11}	
	CS	"	5.30×10^{13}	4.0	239.4	2.79×10^{-10}	
	SO	"	6.85×10^{13}	3.8	239.4	3.61×10^{-10}	
	$H^{13}CO^{+}$	"	3.39×10^{11}	3.8	239.8	1.79×10^{-12}	
	SiO	"	3.25×10^{12}	20.0	234.9	1.71×10^{-11}	

Continued ...

Table B.2: Parameters of the best-fit model for all detected molecules and their abundances.

Source	Species, X	T (K)	N(X) (cm^{-2})	Δv_{FWHM} (km s^{-1})	v_{LSR} (km s^{-1})	$N(X)/N(H_2)^{\$}$	$n_{col}{}^{*}$ (cm^{-3})
15C	CH_3OH	27‡	$< 1.29 \times 10^{13}$	3.1≡	238.6≡	$< 1.02 \times 10^{-10}$	
	CS	"	1.78×10^{13}	3.1	238.6	1.41×10^{-10}	
	$H^{13}CO^+$	"	1.58×10^{11}	2.3	239.0	1.25×10^{-12}	
	SiO	"	1.04×10^{12}	4.3	241.4	8.25×10^{-12}	
16A§							
16B	$CH_3OH^{\star}$	19	7.37×10^{13}	2.1	236.1	4.49×10^{-10}	3.7×10^6
	SO_2	19†	1.36×10^{13}	1.1	236.5	8.28×10^{-11}	
	CS	"	2.34×10^{13}	3.4	236.9	1.43×10^{-10}	
	SO	"	6.18×10^{13}	3.4	237.1	3.76×10^{-10}	
	$H^{13}CN$	"	8.00×10^{11}	4.4	243.1	4.87×10^{-12}	
	SiO	"	2.78×10^{12}	7.8	229.4	1.69×10^{-11}	
17A	$CH_3OH^{\star}$	31	2.76×10^{14}	2.8	221.3	4.93×10^{-10}	5.1×10^6
	SO_2	28	7.08×10^{13}	3.9	221.4	1.26×10^{-10}	
	H_2CS	31†	5.60×10^{13}	4.2	221.8	9.99×10^{-11}	
	CS	"	1.30×10^{14}	4.6	222.4	2.32×10^{-10}	
	SO	"	2.82×10^{14}	4.4	222.5	5.03×10^{-10}	
	$H^{13}CN$	"	4.49×10^{11}	2.3	221.8	8.01×10^{-13}	
	$H^{13}CO^+$	"	3.92×10^{11}	3.7	222.9	7.00×10^{-13}	
	SiO	"	2.48×10^{12}	18.1	221.6	4.43×10^{-12}	
17B§							
18A	$CH_3OH^{\star}$	26	1.21×10^{14}	2.0	278.9	3.05×10^{-10}	4.7×10^6
	SO_2	26†	1.46×10^{13}	2.2	278.6	3.67×10^{-11}	
	H_2CS	"	1.58×10^{13}	2.7	278.8	3.98×10^{-11}	
	CS	"	6.62×10^{13}	3.6	279.9	1.67×10^{-10}	
	SO	"	1.53×10^{14}	3.6	280.3	3.85×10^{-10}	
	$H^{13}CO^+$	"	4.66×10^{11}	3.2	280.1	1.17×10^{-12}	
18B	$CH_3OH^{\star}$	33	5.11×10^{13}	2.3	279.6	4.66×10^{-10}	2.1×10^6
	H_2CS	33†	2.36×10^{13}	10.0	275.6	2.15×10^{-10}	
	CS	"	4.99×10^{13}	3.7	280.4	4.55×10^{-10}	
	SO	"	2.65×10^{13}	3.2	281.0	2.42×10^{-10}	
	$H^{13}CO^+$	"	1.58×10^{11}	3.5	281.6	1.44×10^{-12}	
18C	$CH_3OH^{\star}$	23	3.80×10^{13}	1.6	280.6	3.96×10^{-10}	2.0×10^6
	H_2CS	23†	1.96×10^{13}	7.5	280.1	2.04×10^{-10}	

Continued ...

Table B.2: Parameters of the best-fit model for all detected molecules and their abundances.

Source	Species, X	T (K)	N(X) (cm^{-2})	Δv_{FWHM} (km s^{-1})	v_{LSR} (km s^{-1})	$N(X)/N(H_2)^{\$}$	$n_{col}{}^{*}$ (cm^{-3})
	CS	"	2.93×10^{13}	3.3	281.5	3.06×10^{-10}	
19A	$CH_3OH^{\star}$	25	6.73×10^{14}	2.7	274.4	1.89×10^{-9}	4.1×10^{6}
	SO_2	$25^{\dagger}$	6.59×10^{13}	2.2	274.6	1.85×10^{-10}	
	H_2CS	"	4.32×10^{13}	3.5	273.9	1.22×10^{-10}	
	CS	"	1.23×10^{14}	4.4	274.8	3.46×10^{-10}	
	SO	"	2.53×10^{14}	4.0	275.6	7.12×10^{-10}	
	SiO	"	1.67×10^{12}	5.2	277.1	4.70×10^{-12}	
19B[§]							
19C	CH_3OH	$27^{\ddagger}$	$< 3.07 \times 10^{12}$	$4.4^{\equiv}$	$274.1^{\equiv}$	$< 2.39 \times 10^{-11}$	
	CS	"	7.51×10^{12}	4.4	274.1	5.86×10^{-11}	
	SO	"	2.81×10^{13}	8.1	273.2	2.19×10^{-10}	
19D	$CH_3OH^{\star}$	42	6.23×10^{13}	1.4	274.0	8.66×10^{-10}	1.3×10^{6}
	SO_2	$42^{\dagger}$	1.75×10^{13}	3.1	274.1	2.43×10^{-10}	
	H_2CS	"	1.87×10^{13}	8.6	278.2	2.60×10^{-10}	
	CS	"	2.79×10^{13}	3.5	274.8	3.88×10^{-10}	
	SO	"	5.19×10^{13}	3.4	275.2	7.21×10^{-10}	
20A	CH_3OH	$27^{\ddagger}$	$< 5.32 \times 10^{12}$	$3.0^{\equiv}$	$284.5^{\equiv}$	$< 5.36 \times 10^{-11}$	
	CS	"	1.99×10^{12}	3.0	284.5	2.00×10^{-11}	

Notes.

[$] $N(H_2)$ was derived in Paper II with the temperatures derived in the current paper and assuming all of the 1.3 mm continuum emission originated in optically thin dust with an opacity of 1.04 cm^2 gr^{-1} and a gas-to-dust mass ratio of 320. We consider that the error values range from 40% to 60% for the temperatures, 20% to 40% for the column densities, and 10% to 30% for the line widths and velocity shifts.

[*] The collision partner number density.

[⋆] The fit parameters were derived with the non-LTE assumption.

[†] We adopted this value from the temperature for the CH_3OH. Where there were two components, the temperature we adopted was from the hot component.

[‡] The median value of the fit temperature for CH_3OH from all the sources, where we could fit.

[<] The upper limit estimations.

[≡] The upper limit on column density and abundance was estimated by fixing the line width and line shift. In the case of estimating the upper limits for CH_3OH, we used the best-fit parameters for CS, and for the other molecules, we used the best-fit parameters for CH_3OH.

[§] No emission line is detected.

Appendix C

Comparisons of molecular abundances in hot cores with chemical models

Section 3.4.2 discusses how the observed abundances of the hot cores in the LMC compare with the only hot core modeling for LMC's condition (Acharyya & Herbst, 2018). We present the comparisons for three molecules (CH_3OH, SO_2, and CH_3CN) in Section 3.4.2, and we expand this comparison in this appendix. Figures C.1 and C.2 show the comparisons of observed abundance for the seven hot cores in the LMC with the chemical models for the final hot core temperature of 100 and 200 K, respectively. It is evident from the plots that the solid curve representing the warm dust initial condition (T_d = 25 K) does not appear in any of the subplots. The only exception is SiO, for which a sharp increase in the model at a time of $\approx 1 \times 10^6$ yr could also reproduce the observed abundances. As the modelings do not include shocks, this increase in the SiO is not reliable. Moreover, the observed abundance of HNCO could not be reproduced by models; the peak abundance of the models is smaller by more than an order of magnitude. The underestimation of abundances is also apparent in the case of SO_2 and SO. These three species (HNCO, SO_2, and SO) are also commonly found to be associated with shocks in star-forming regions. The higher observed abundances could imply the presence of shocks in the hot cores of the LMC, which is not included in the modelings.

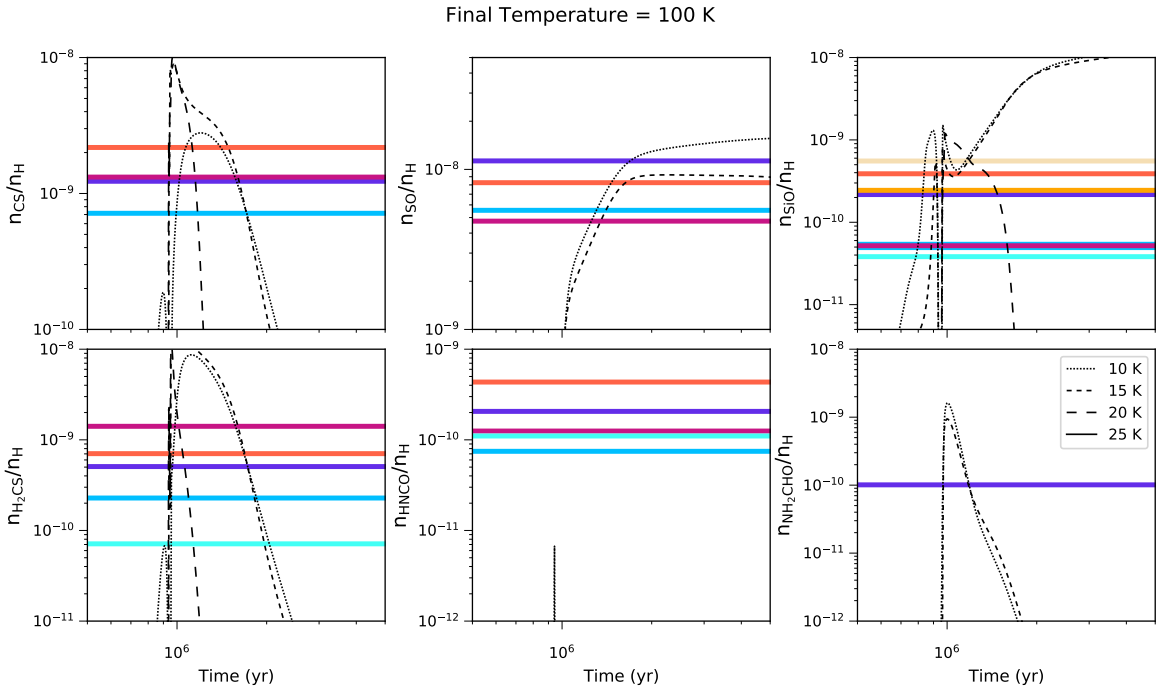


Figure C.1: Comparisons of abundances for CS, SO, SiO, H_2CS, HNCO, and NH_2CHO from observations of the seven hot cores detected in the LMC and the LMC hot core models for the final hot core temperature of 100 K. The black curves show abundances over time for initial dust temperatures of 10 (dotted line), 15 (dashed curve), 20 (larger dashed curve), and 25 K (solid curve; this curve does not necessarily appear in the range of abundances in the plot). The horizontal colored line shows the single abundance value for each hot core and follows the same color code as Fig. 3.13 (see the text for more details).

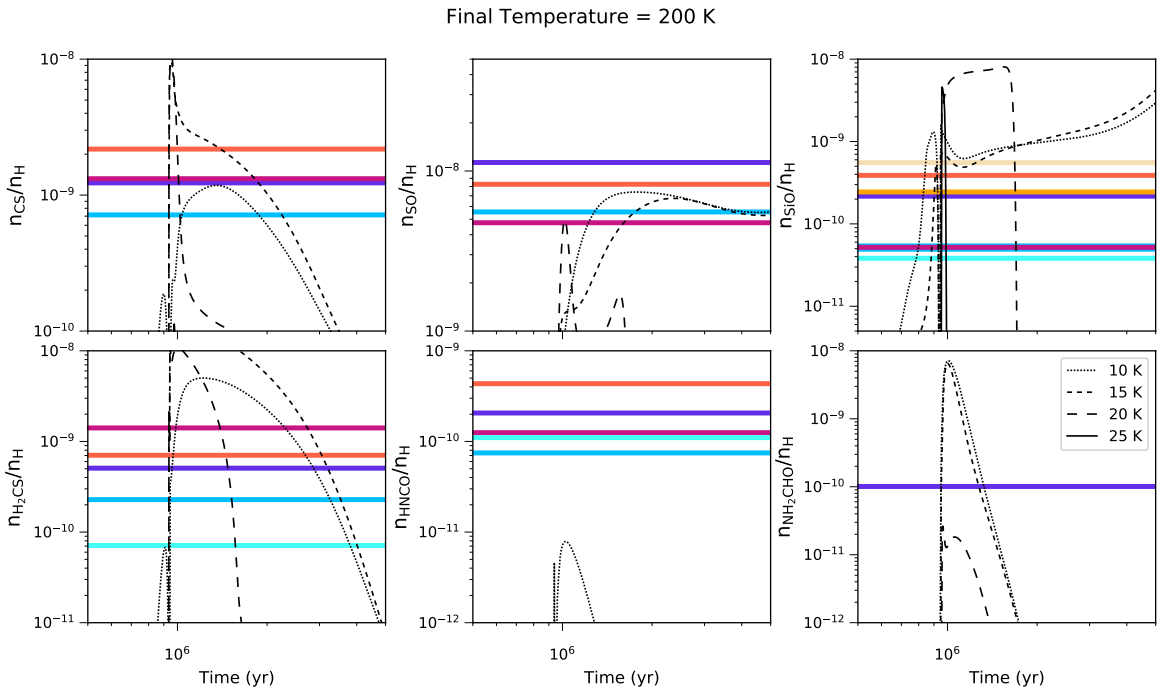


Figure C.2: Same as Fig. C.1 but for the LMC hot core models for the final hot core temperature of 200 K.

Appendix D

Filaments detected in the 20 star-forming regions

In Section 4.1, the filaments were identified using `Filfinder` applied to the CS peak intensity maps. The CS peak intensity maps overlaid with the identified filaments for Field 1 and Field 2 are presented in the same section. The corresponding maps for the remaining fields are included in this appendix.

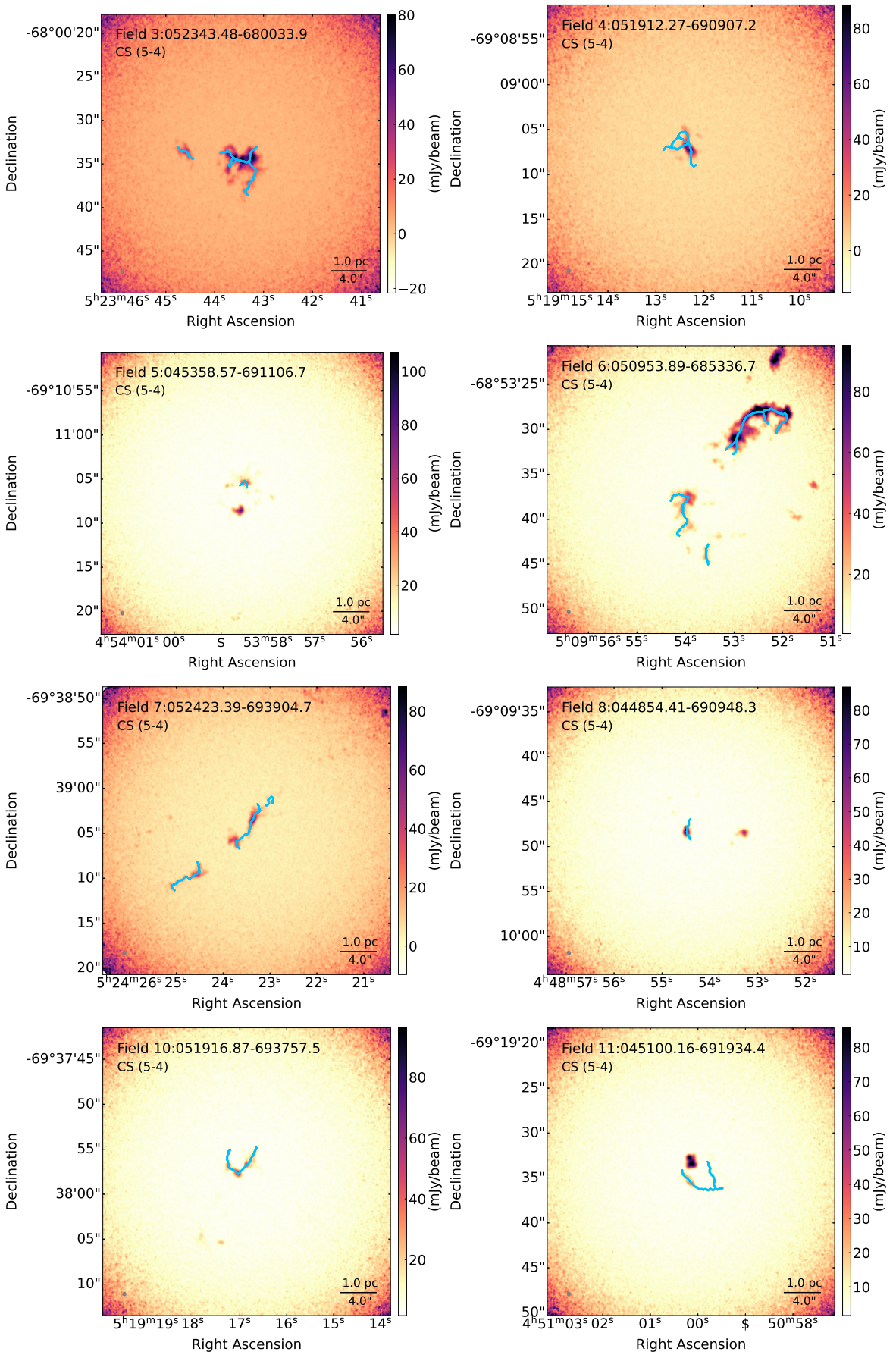


Figure D.1: Filaments detected in the CS peak-intensity maps for Fields 3 to 11.

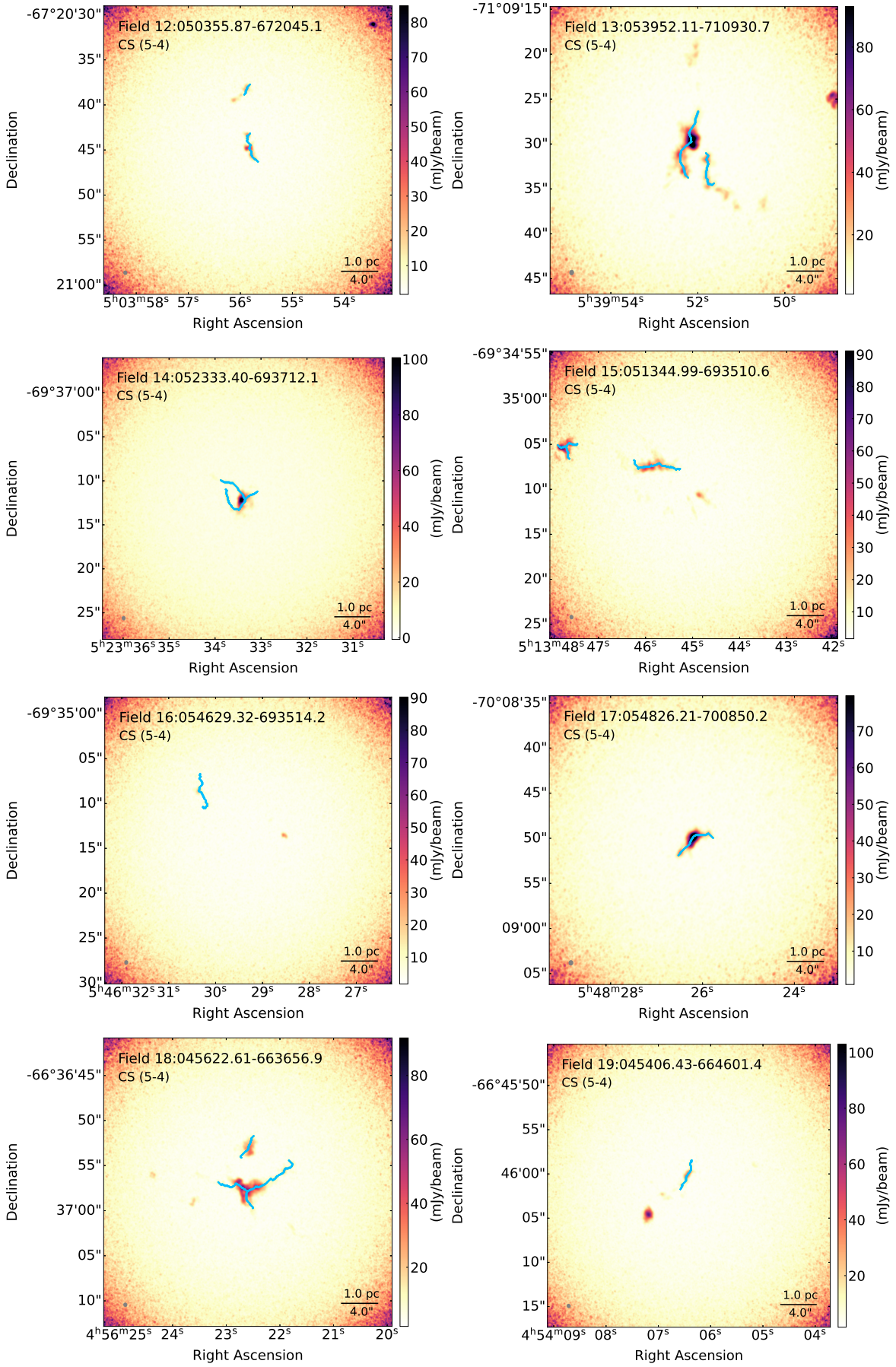


Figure D.2: Same as Fig. D.1 but for Fields 12 to 19.

Appendix E

HII regions

The HII regions were identified in 13 of the 20 regions in our sample using the ATCA 4 cm maps. The ATCA 4 cm emission maps for Fields 3 and 4 are presented in Section4.2, while the maps for the remaining fields are included in this Appendix. For reference, the ALMA 1.2 mm continuum contours are overlaid at 4, 8, 12 times the $\sigma_{\rm rms}$ on these maps.

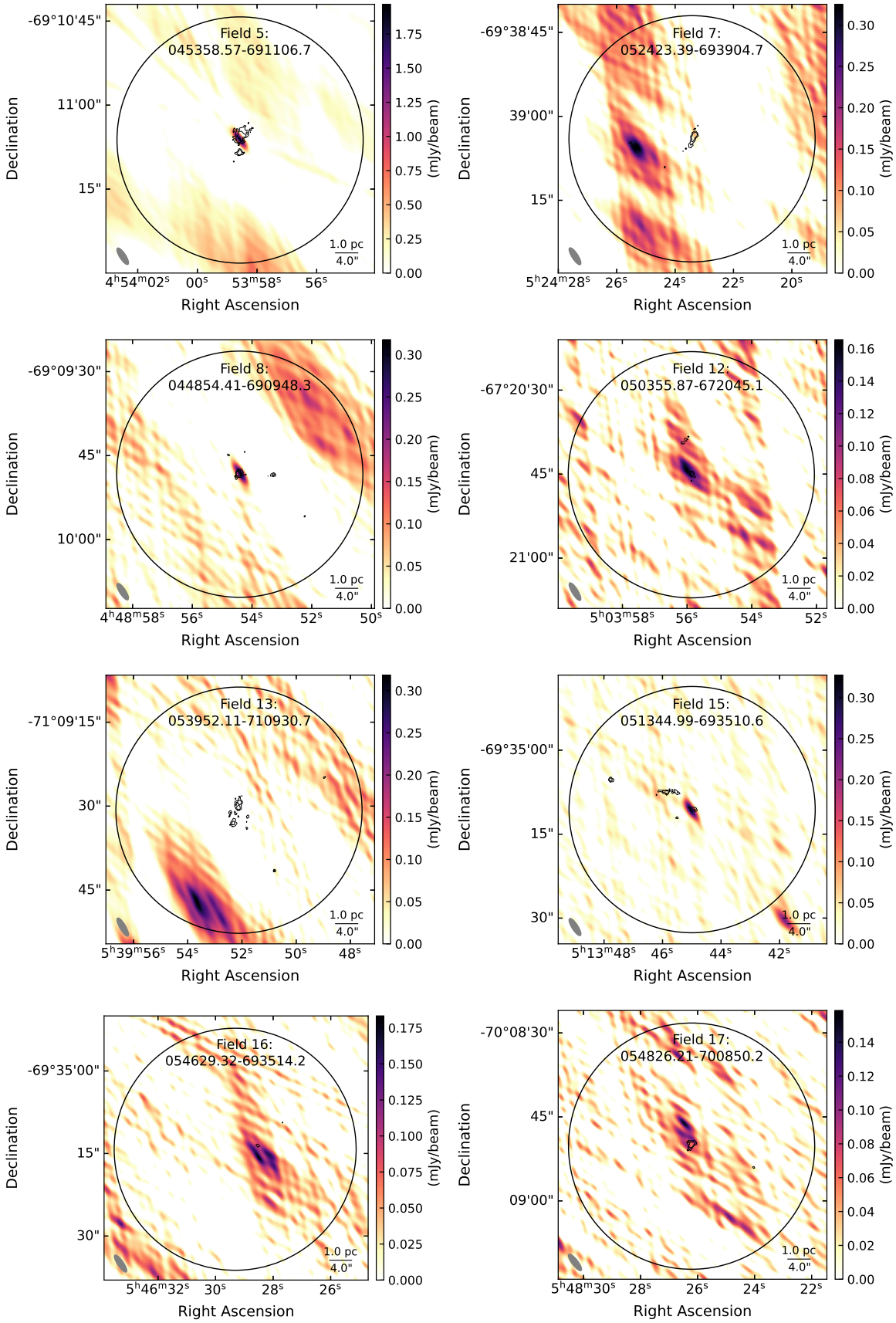


Figure E.1: ATCA 4 cm maps, tracing the free-free continuum emission for Fields 5, 7, 8, 12, 13, 15, 16 and 17. ALMA 1.2 mm continuum contours are overlaid at 4, 8, 12 times the $\sigma_{\rm rms}$.

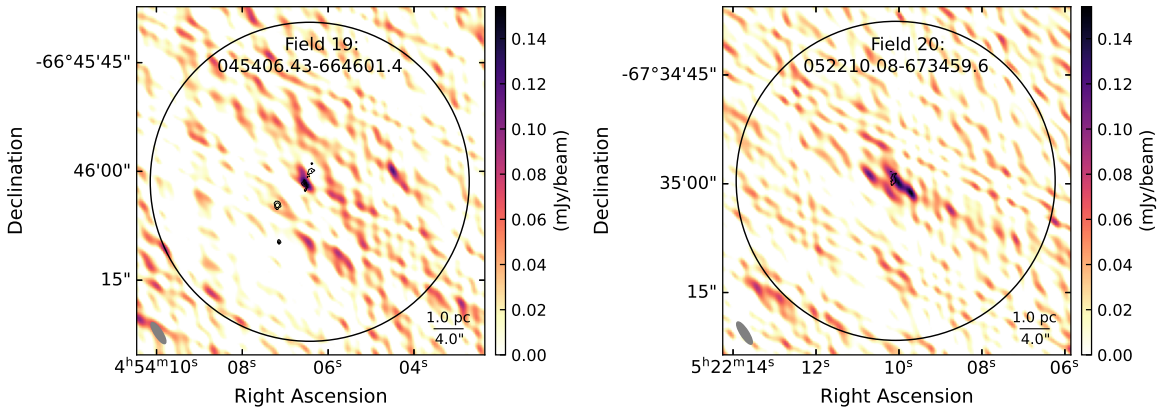


Figure E.2: Same as Fig. E.1 for Fields 19 and 20.

Appendix F

Multi-wavelength view of the target regions

A multi-wavelength perspective on the parent clouds of our 20 target fields, spanning scales from 150 pc down to 1 pc, is discussed in Chapter 5. This appendix presents the figures for Fields 2 to 20, while the figure for Field 1 is included in the main body of the chapter. Each figure specifies the bands included. In the larger-scale map (top panel), two circles are depicted: one representing the ALMA field and another representing an area 15 times the size of the ALMA field. The remaining four panels provide a closer view of the ALMA field, with its extent marked with the circle. The ALMA continuum contours are overlaid at 4, 8, 12 times the $\sigma_{\rm rms}$ for reference.

Figure caption: The larger-scale map (top panel) shows two circles: one representing the ALMA field and another encompassing an area 15 times the size of the ALMA field. The remaining four panels provide a closer view of the ALMA field, with its extent marked by a circle. ALMA continuum contours are overlaid at levels of 4, 8, and 12 times the $\sigma_{\rm rms}$ for reference.

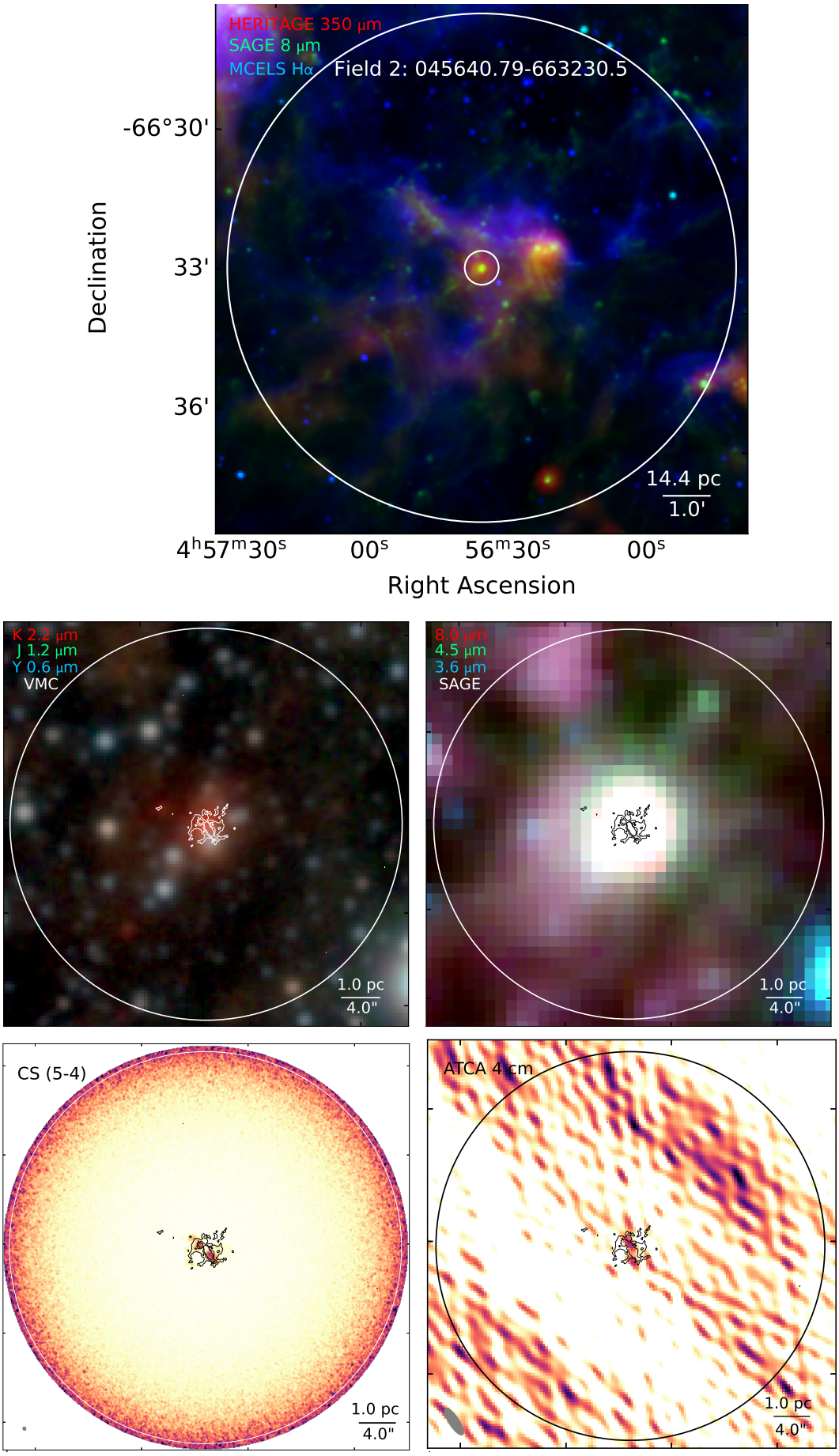


Figure F.1: Multi-wavelength view of Field 2. For caption details see the Appendix text.

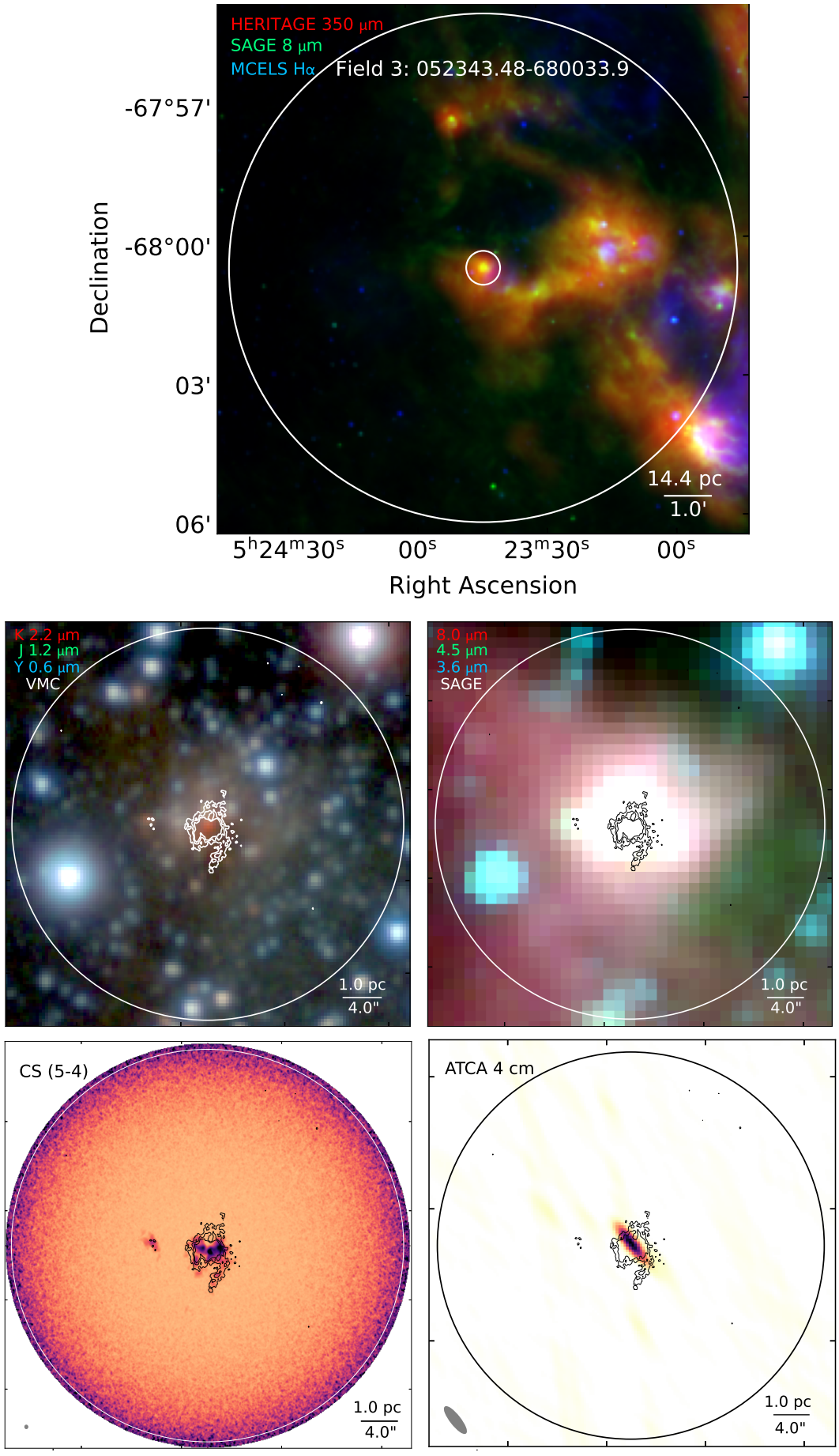


Figure F.2: Same as Fig F.1 but for Field 3.

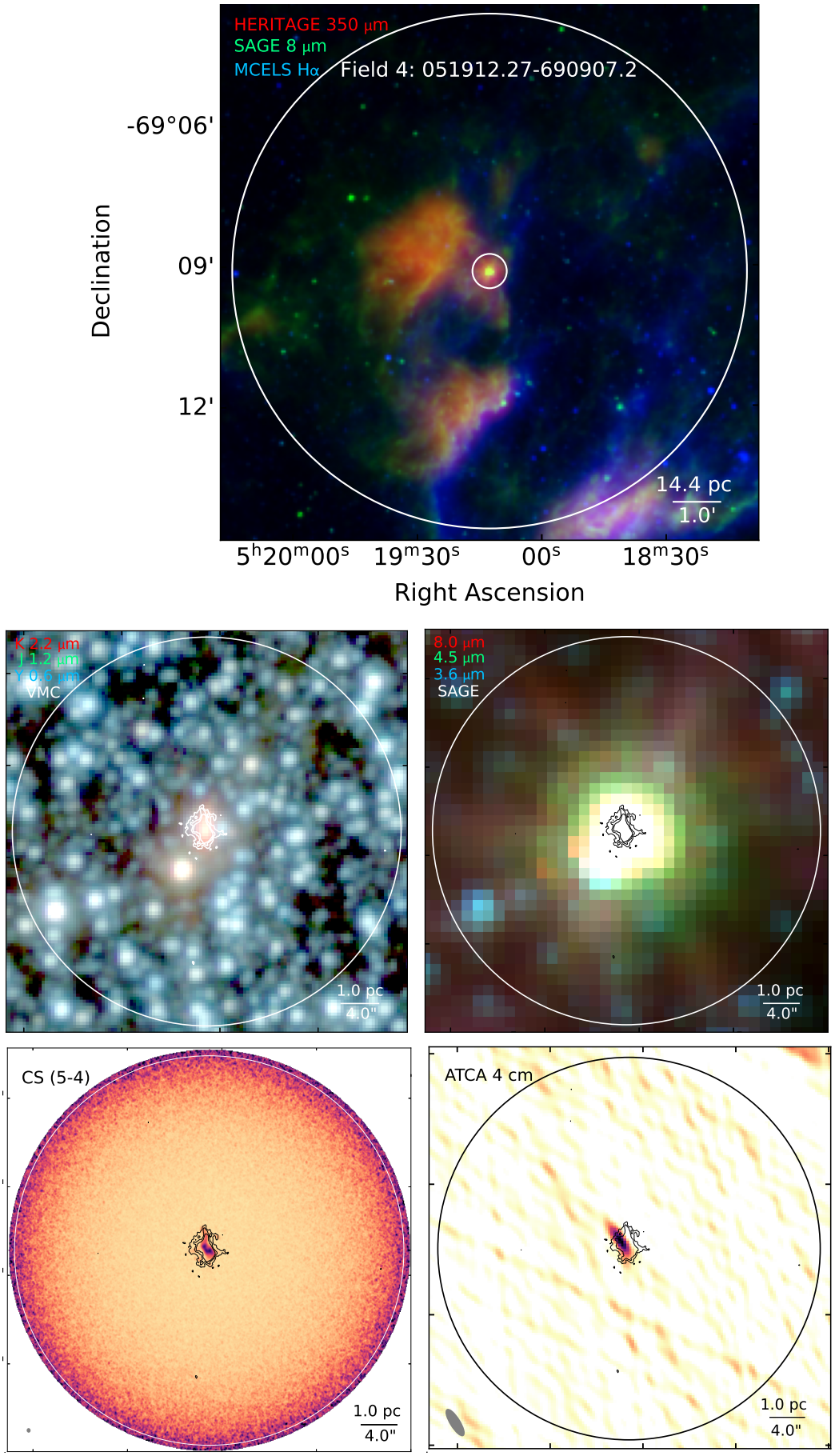


Figure F.3: Same as Fig F.1 but for Field 4.

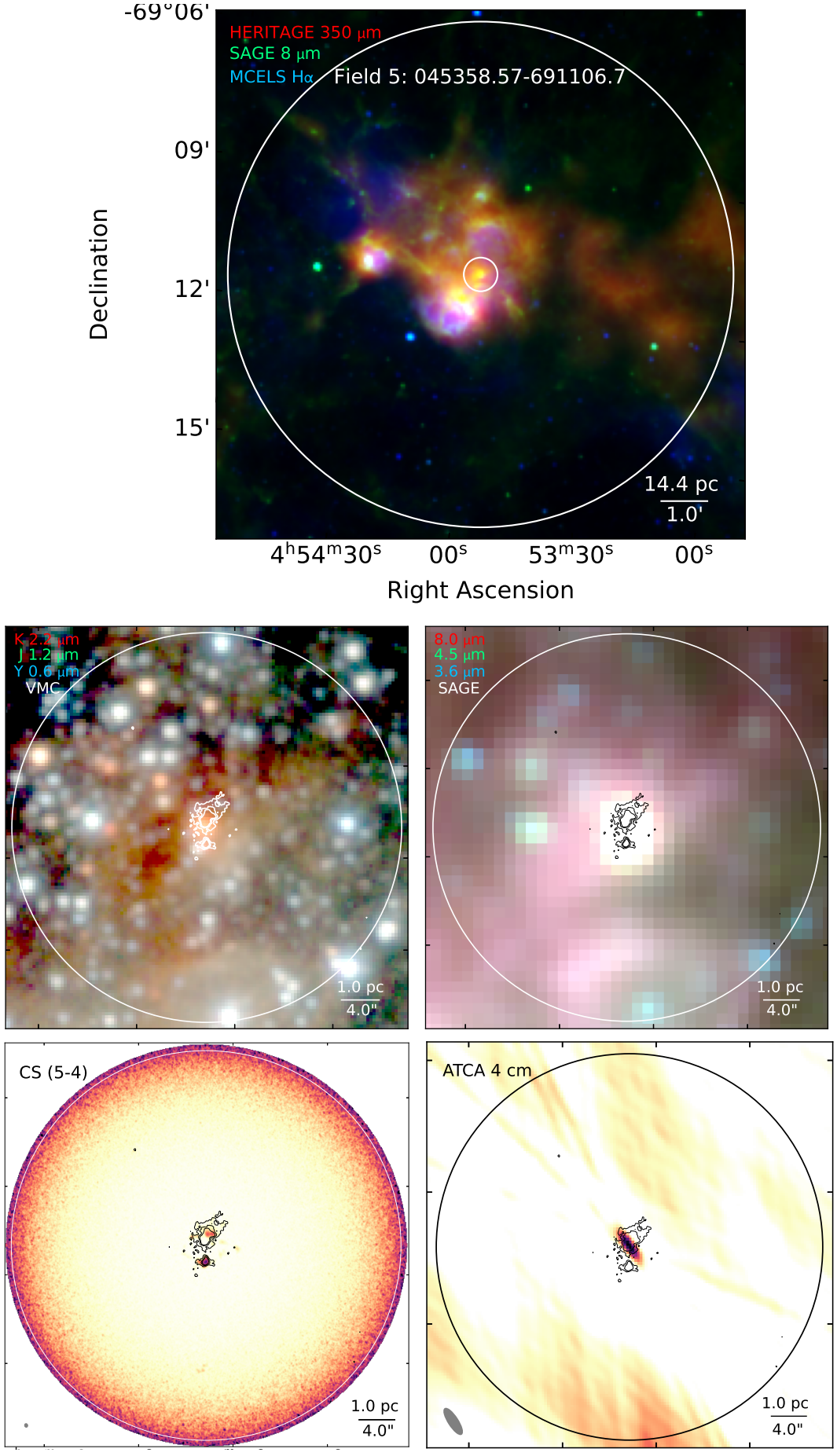


Figure F.4: Same as Fig F.1 but for Field 5.

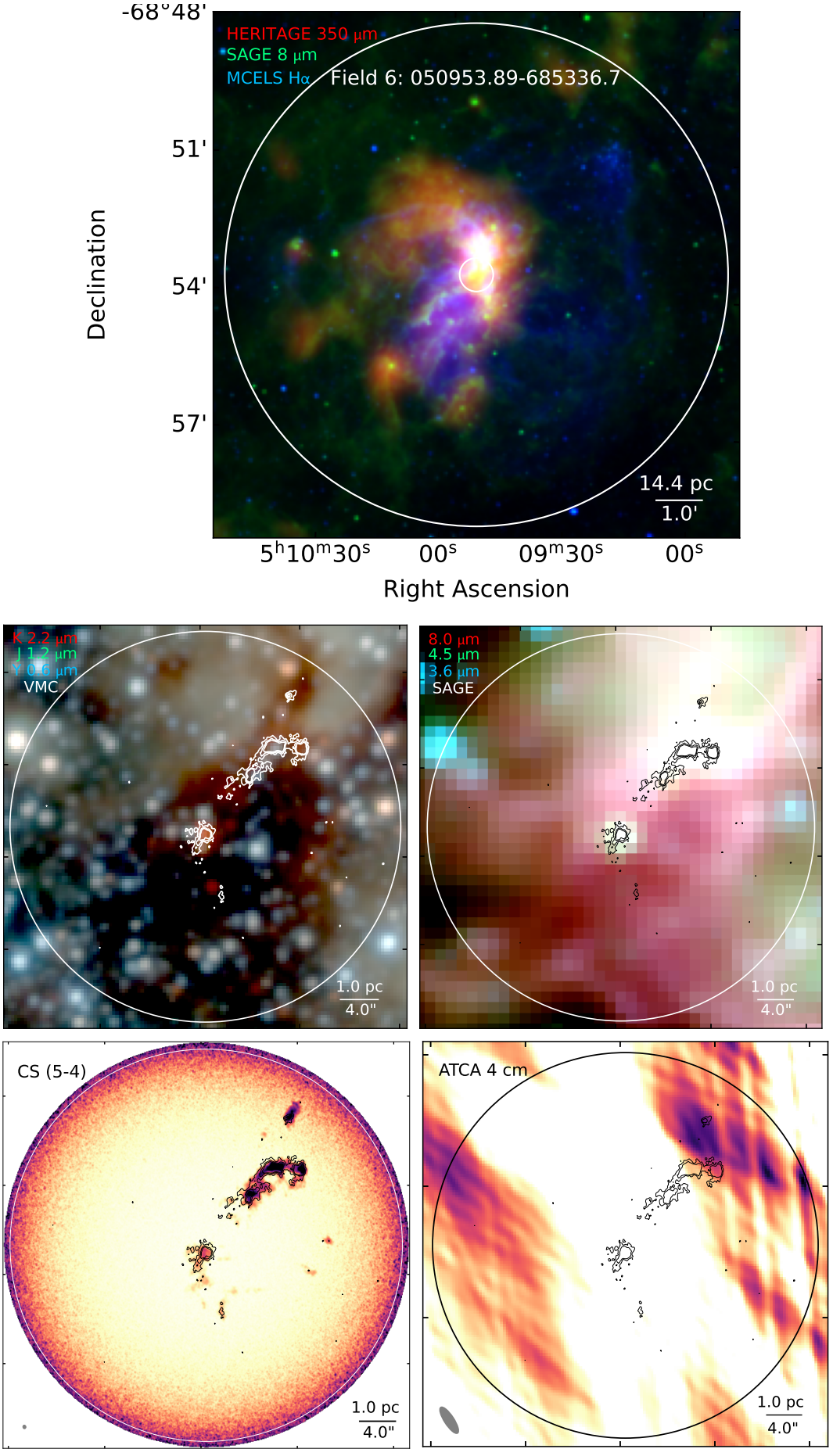


Figure F.5: Same as Fig F.1 but for Field 6.

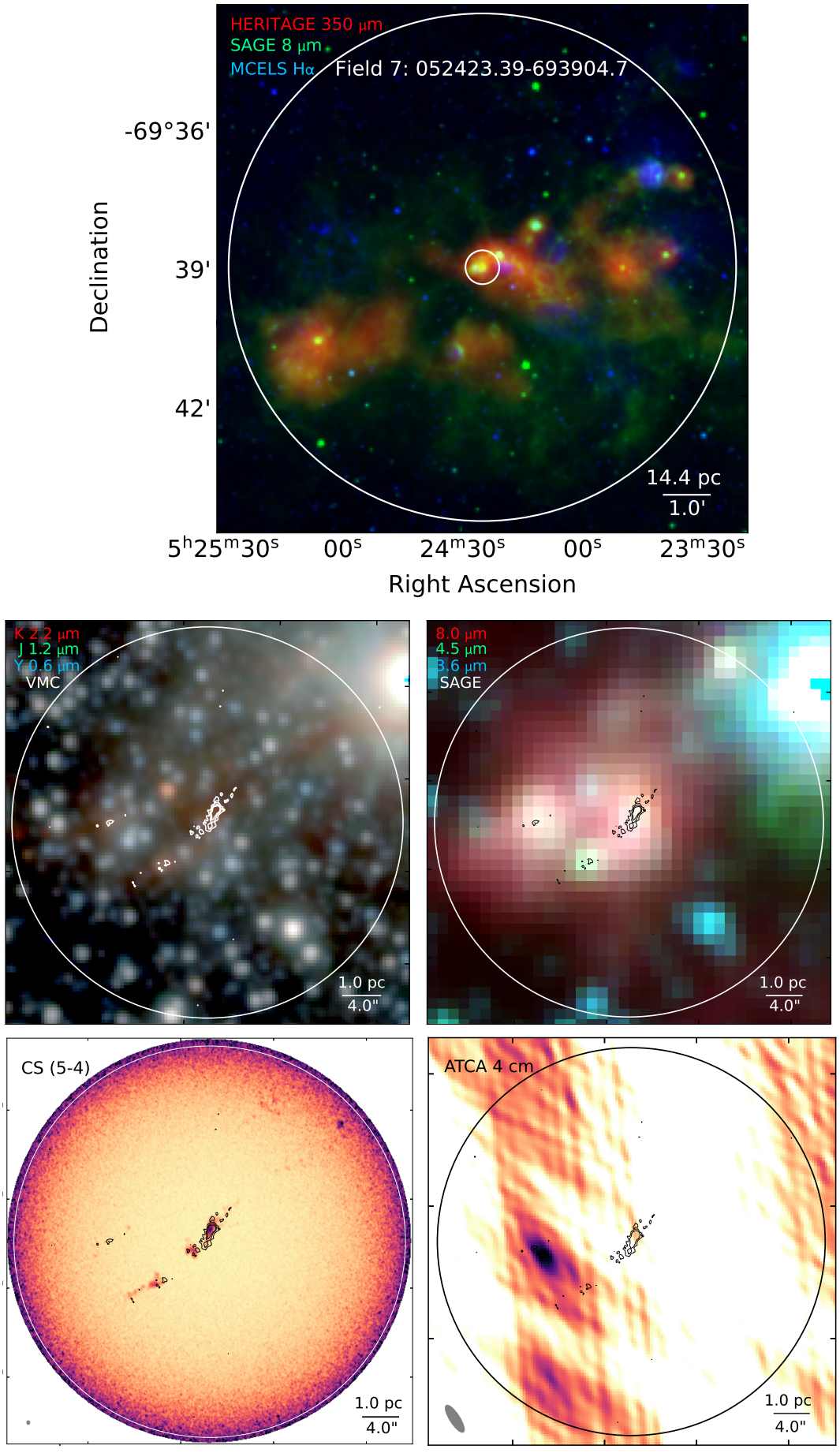


Figure F.6: Same as Fig F.1 but for Field 7.

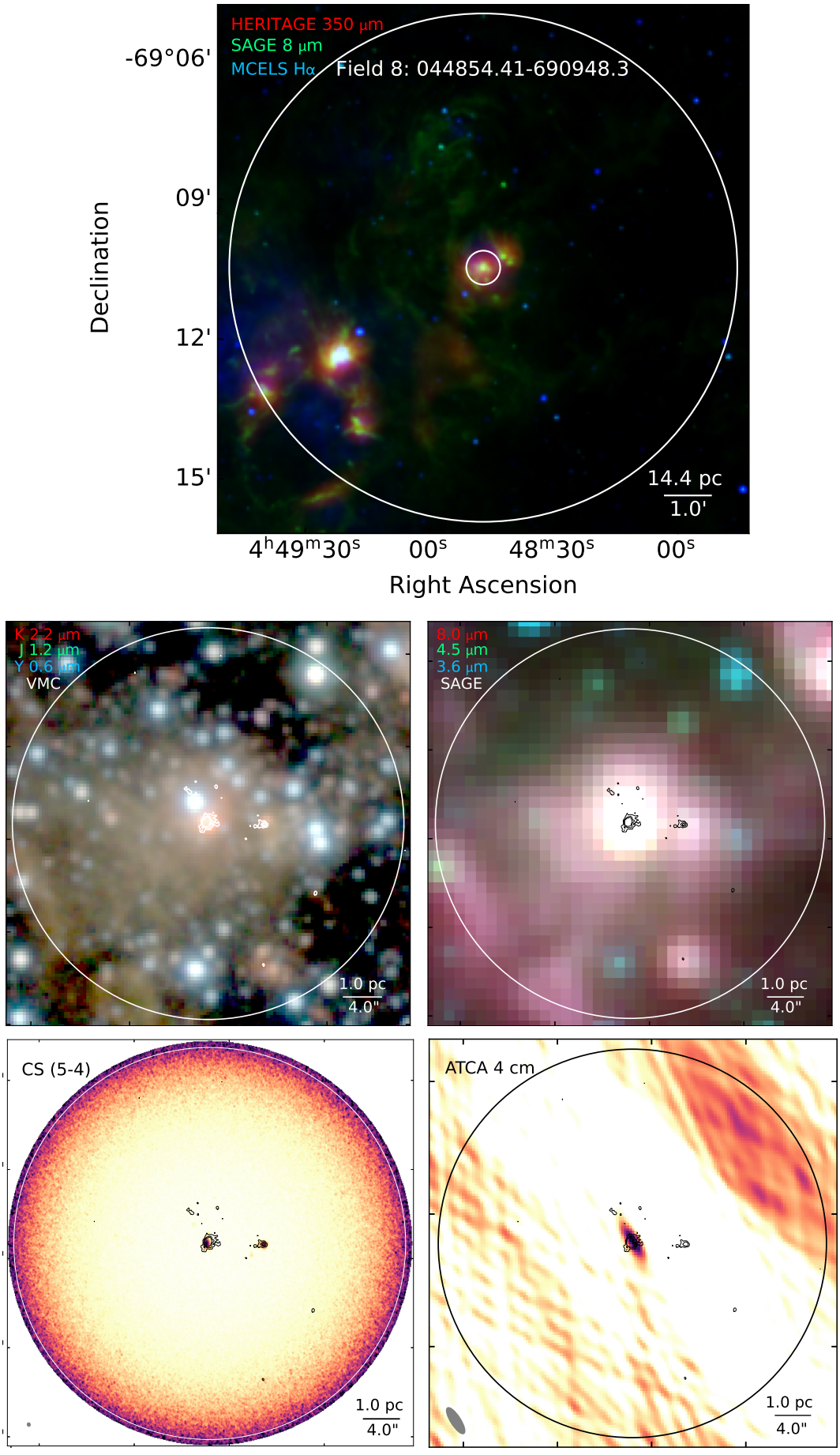


Figure F.7: Same as Fig F.1 but for Field 8.

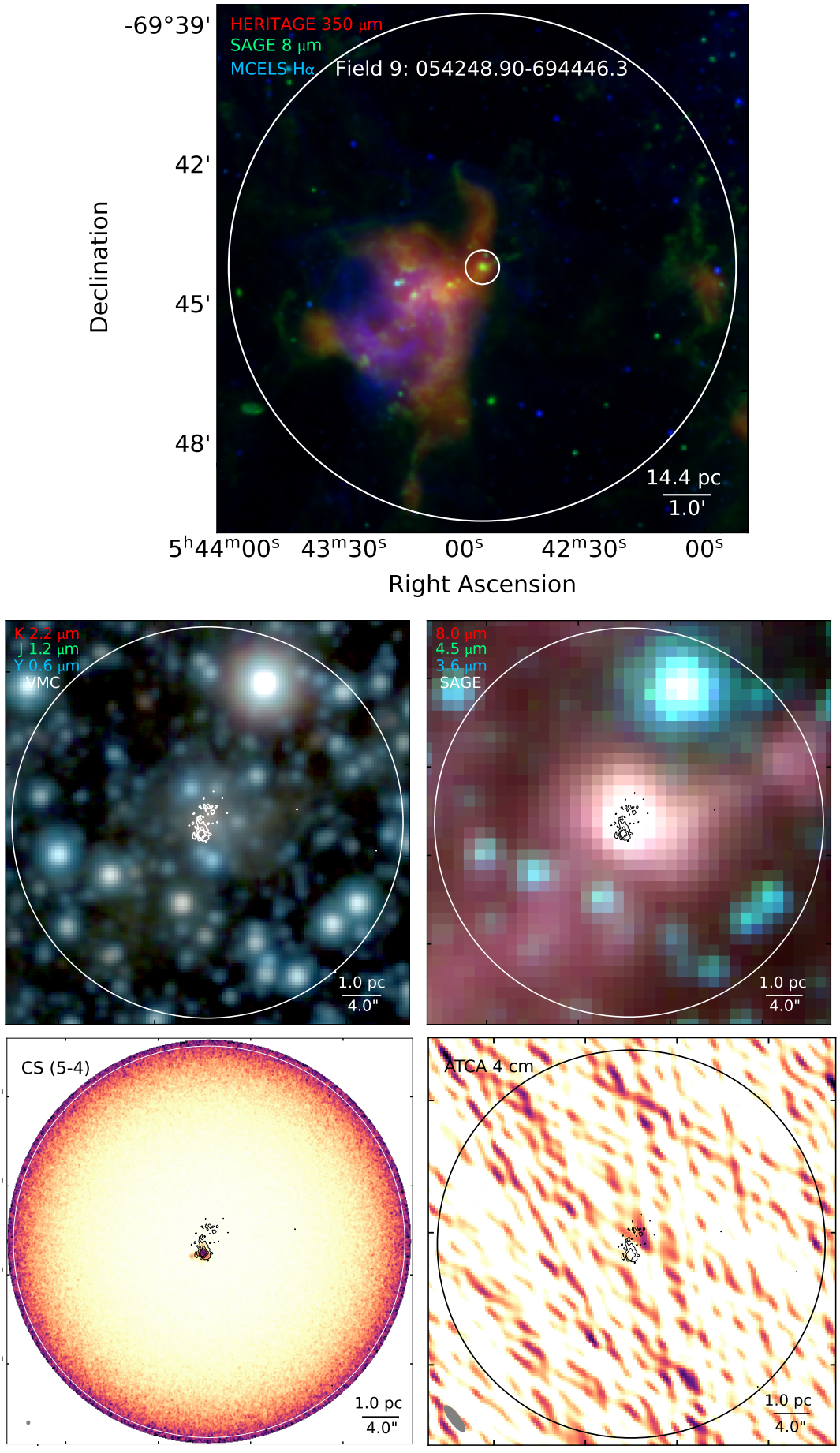


Figure F.8: Same as Fig F.1 but for Field 9.

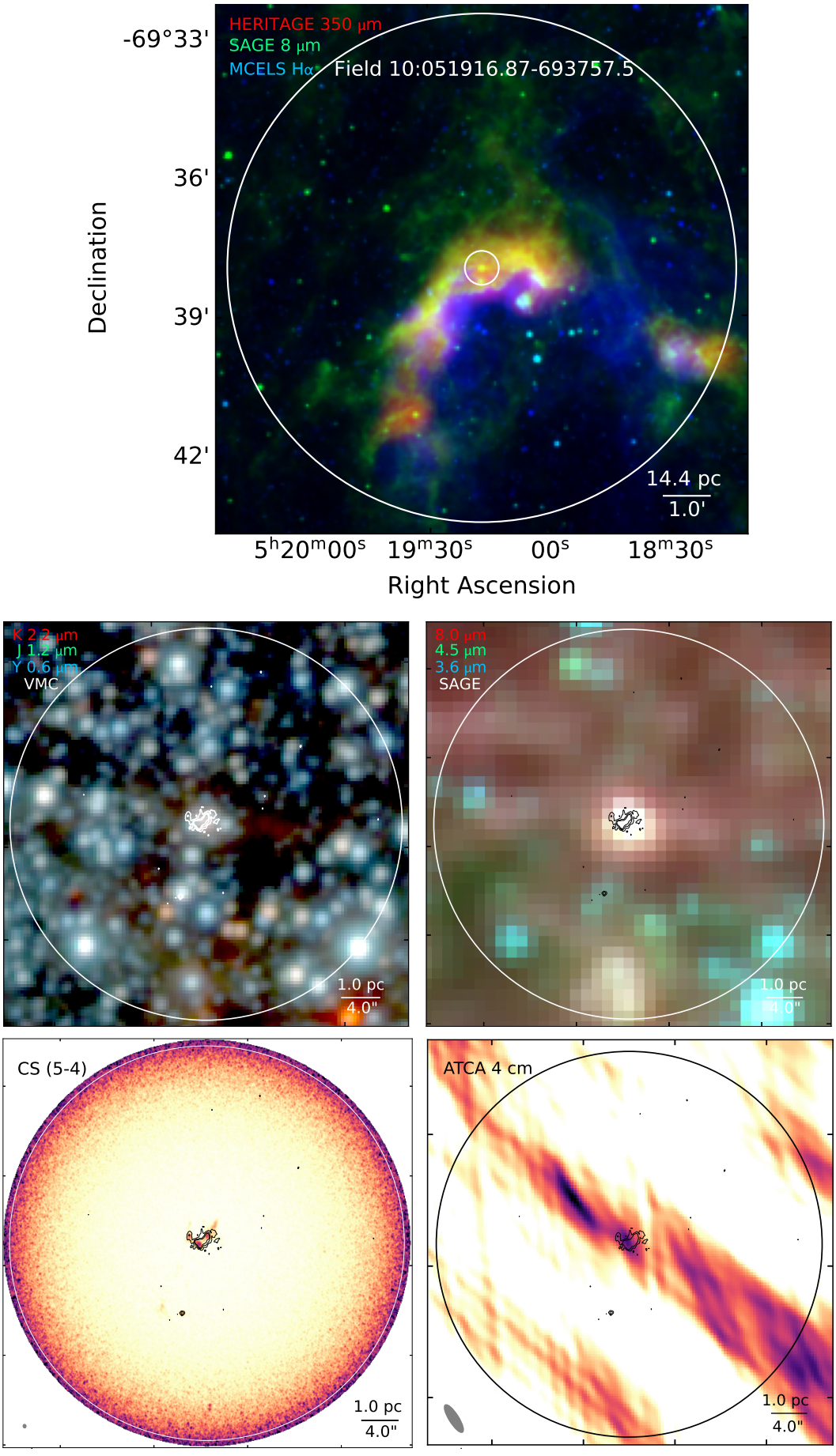


Figure F.9: Same as Fig F.1 but for Field 10.

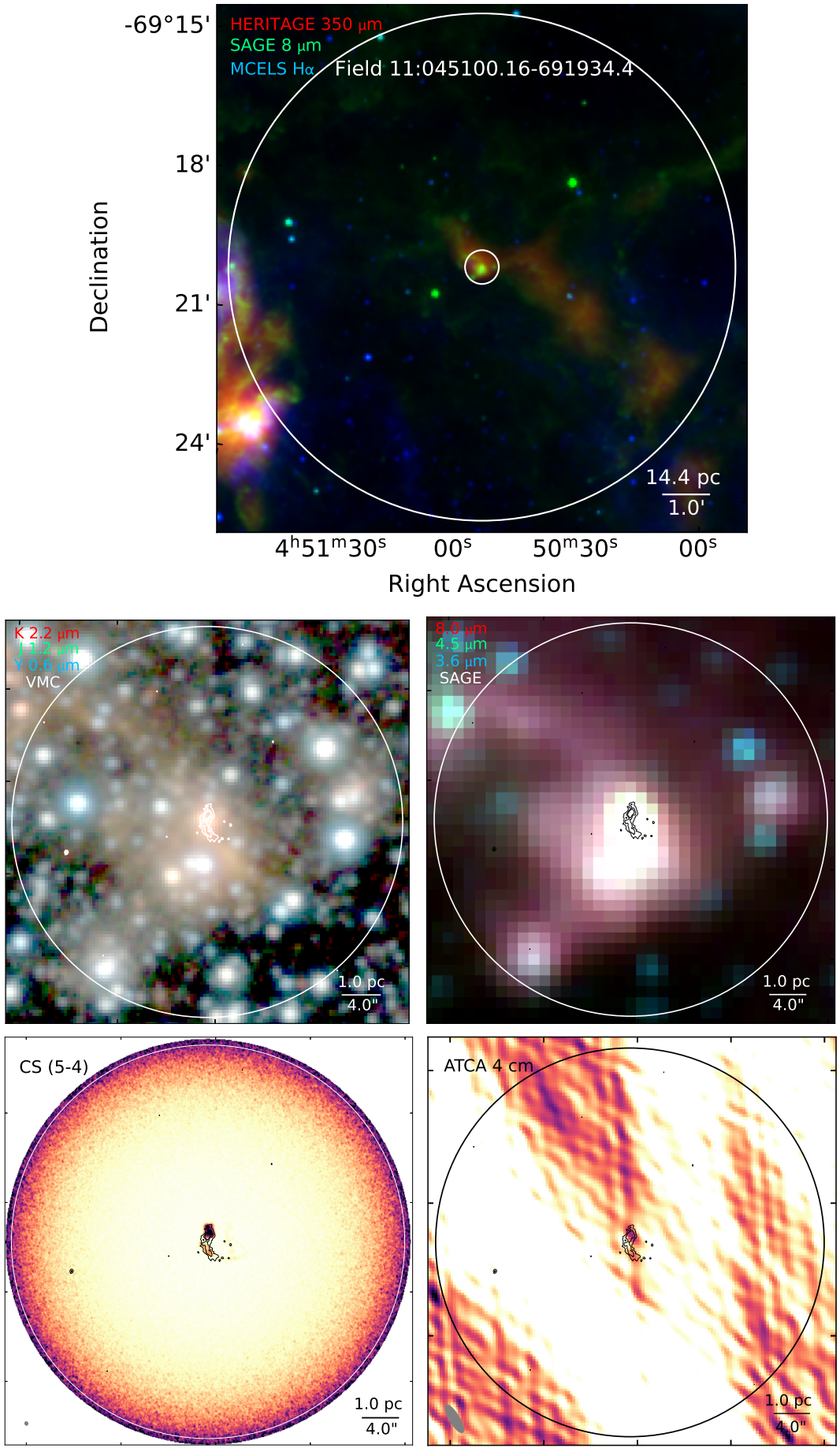


Figure F.10: Same as Fig F.1 but for Field 11.

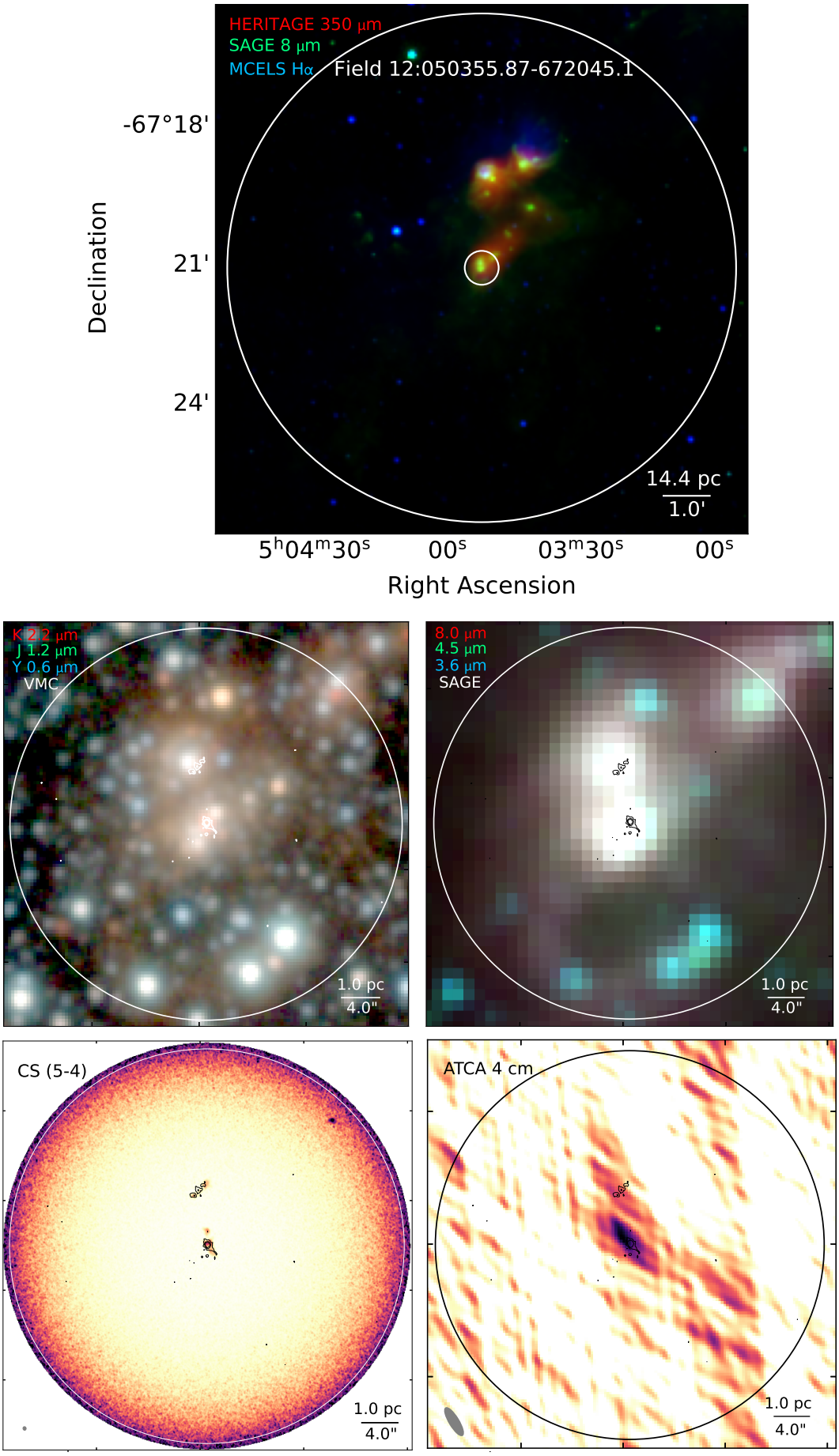


Figure F.11: Same as Fig F.1 but for Field 12.

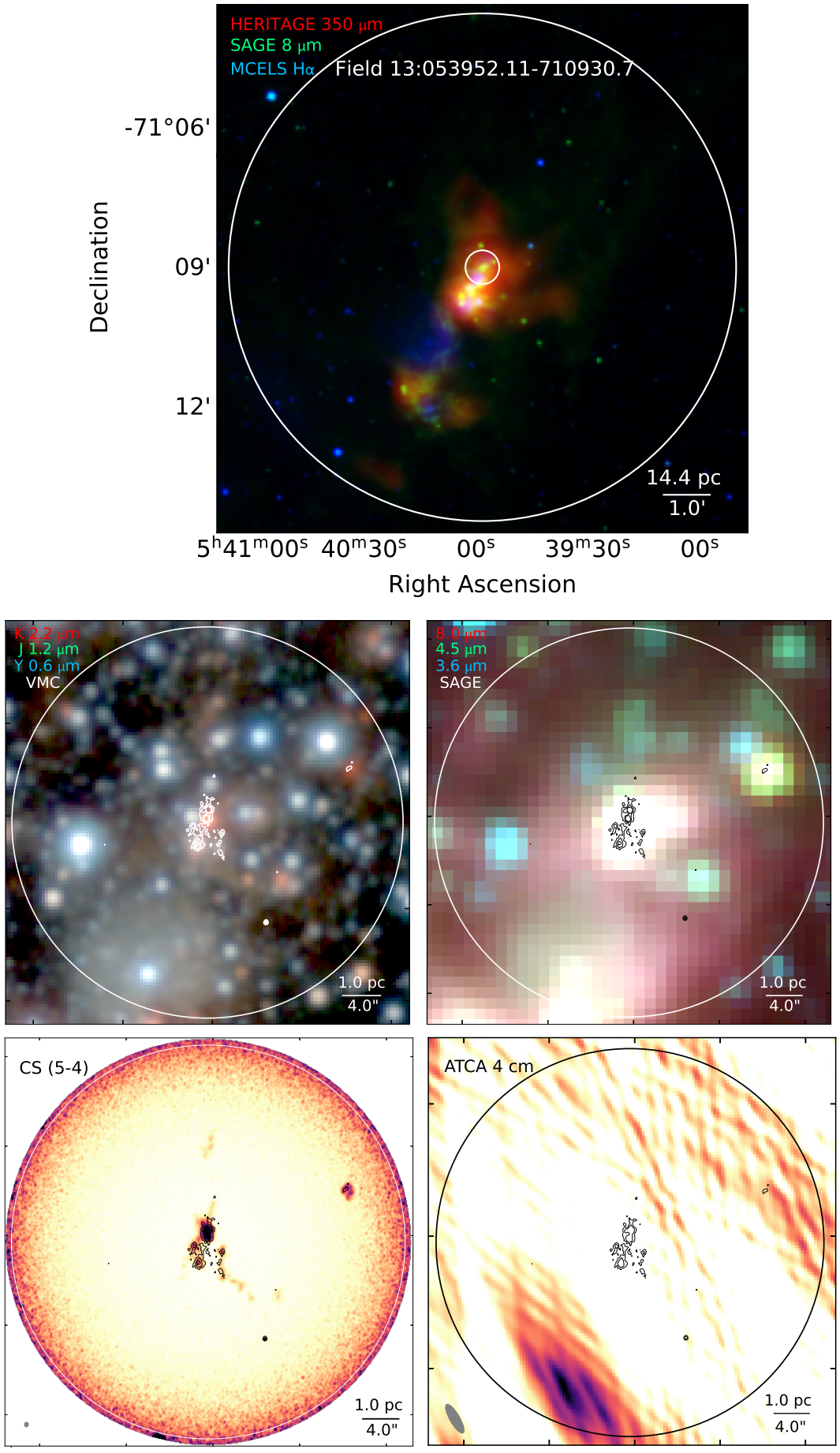


Figure F.12: Same as Fig F.1 but for Field 13.

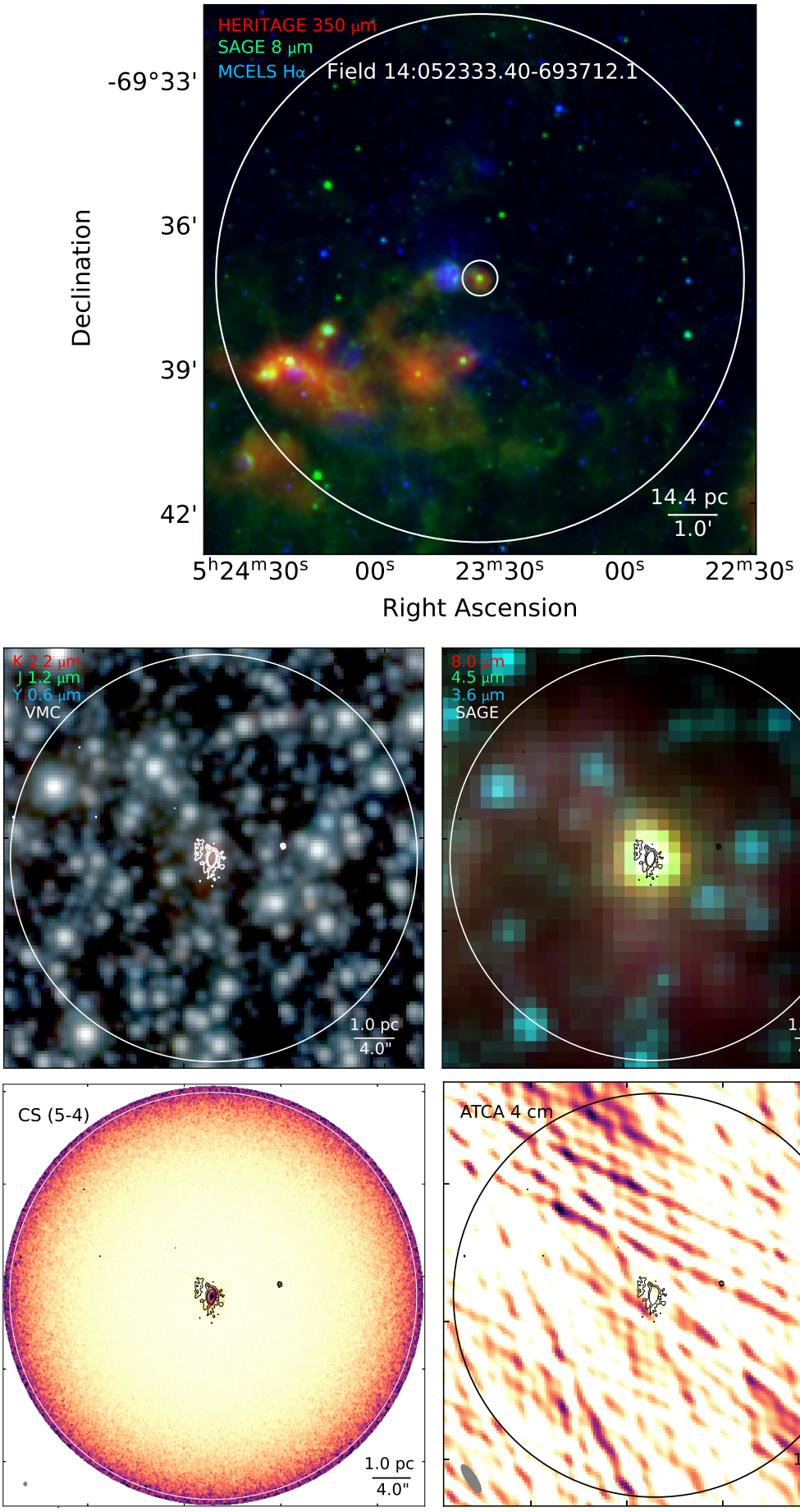


Figure F.13: Same as Fig F.1 but for Field 14.

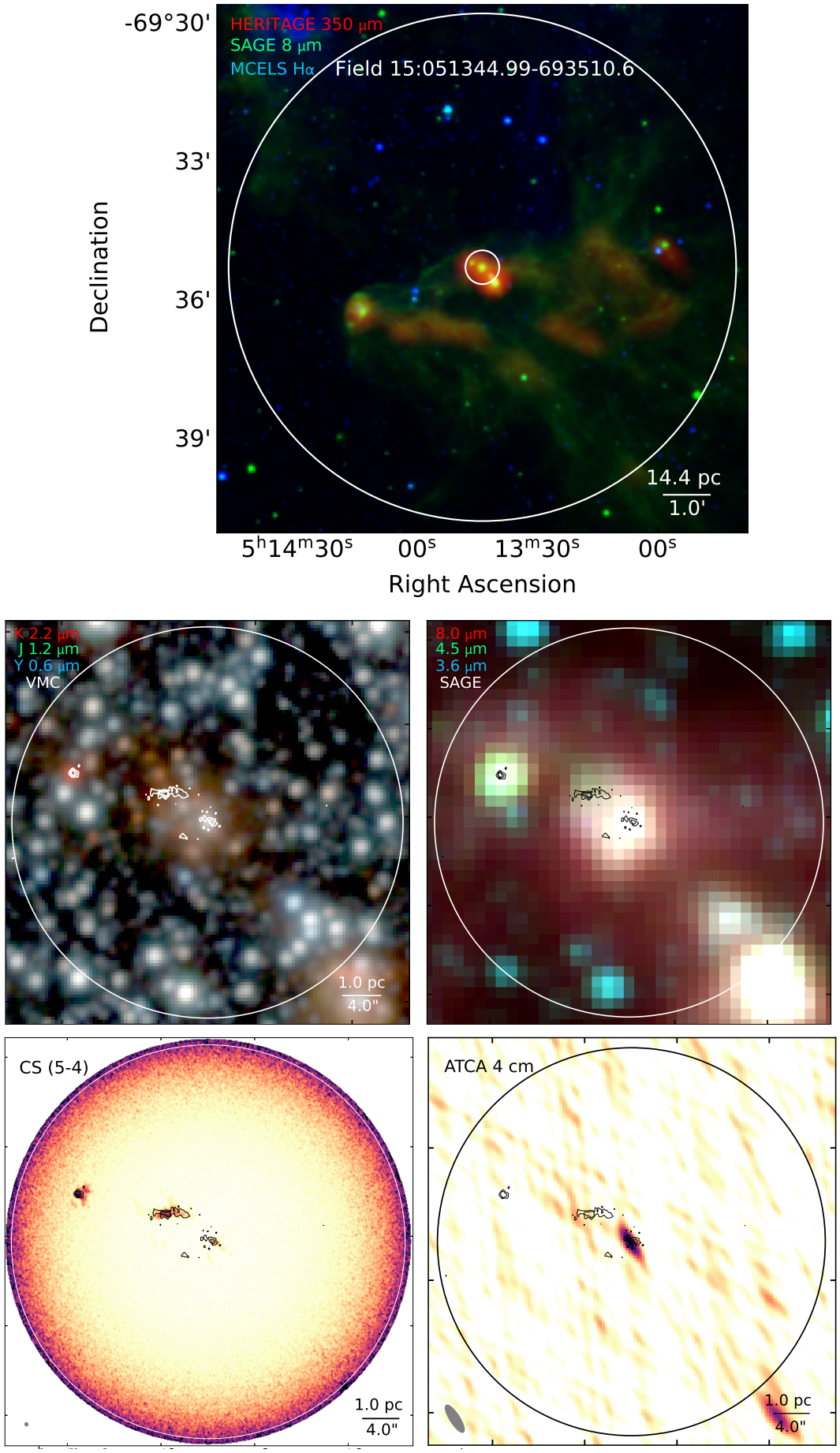


Figure F.14: Same as Fig F.1 but for Field 15.

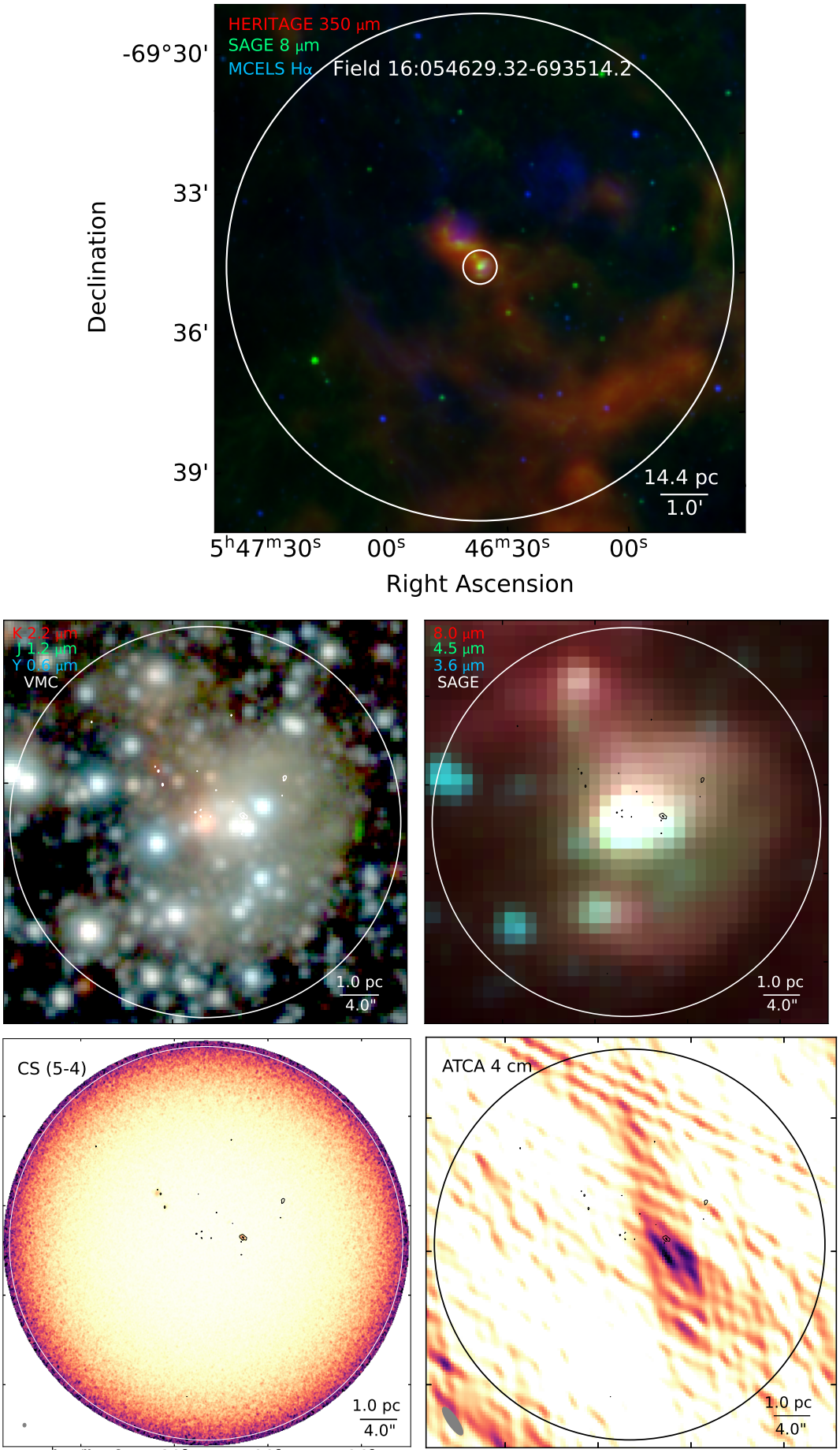


Figure F.15: Same as Fig F.1 but for Field 16.

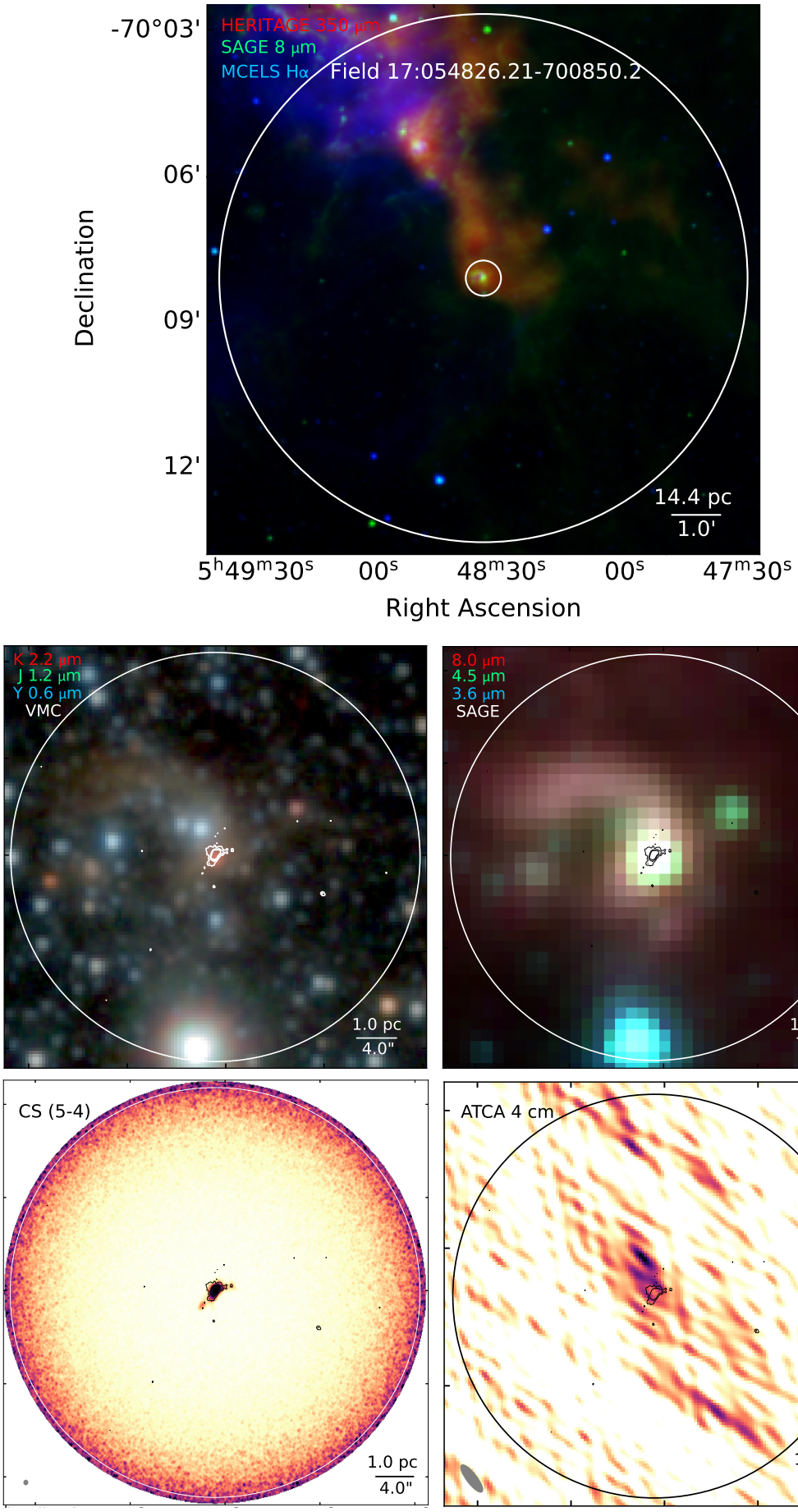


Figure F.16: Same as Fig F.1 but for Field 17.

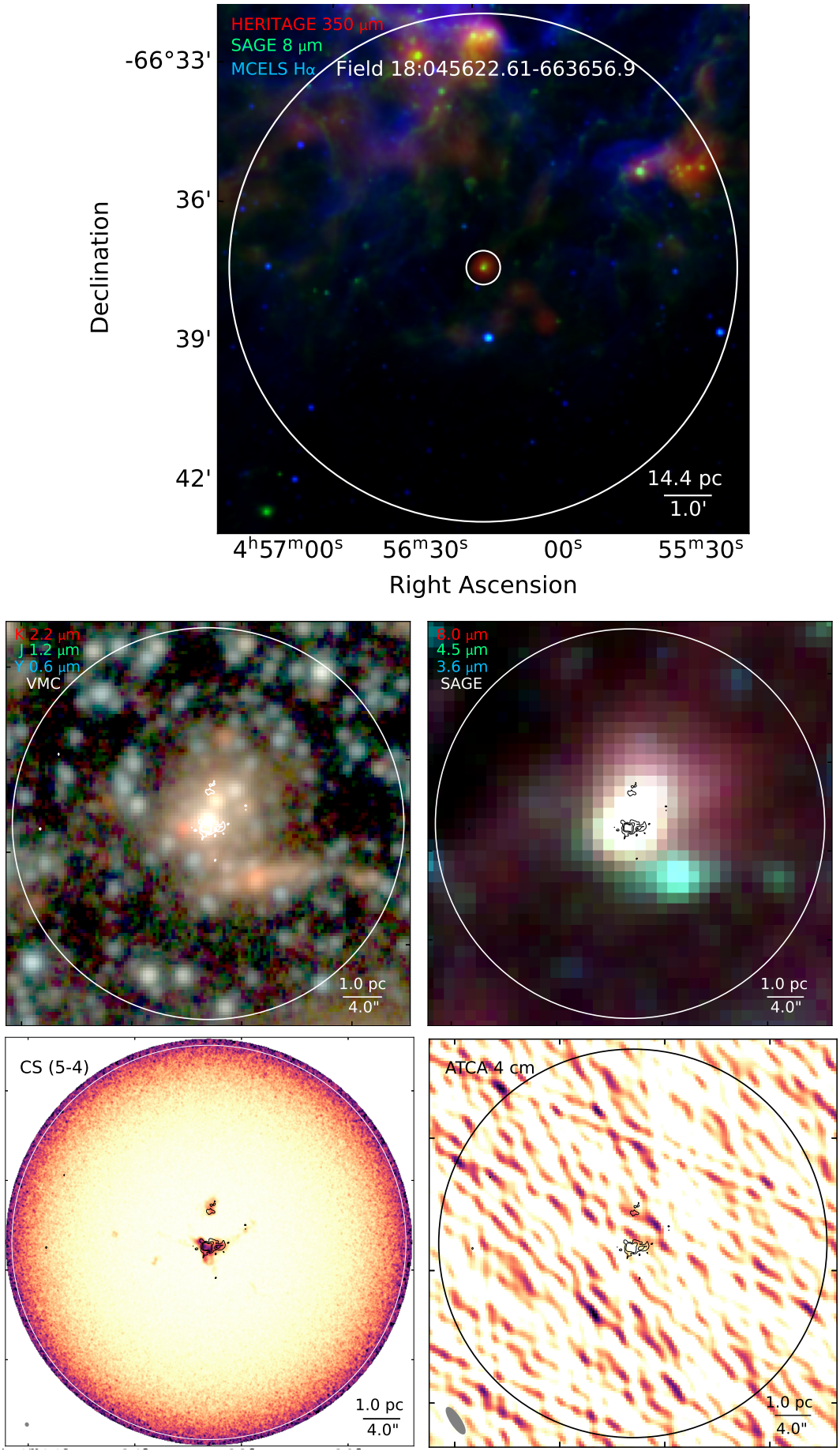


Figure F.17: Same as Fig F.1 but for Field 18.

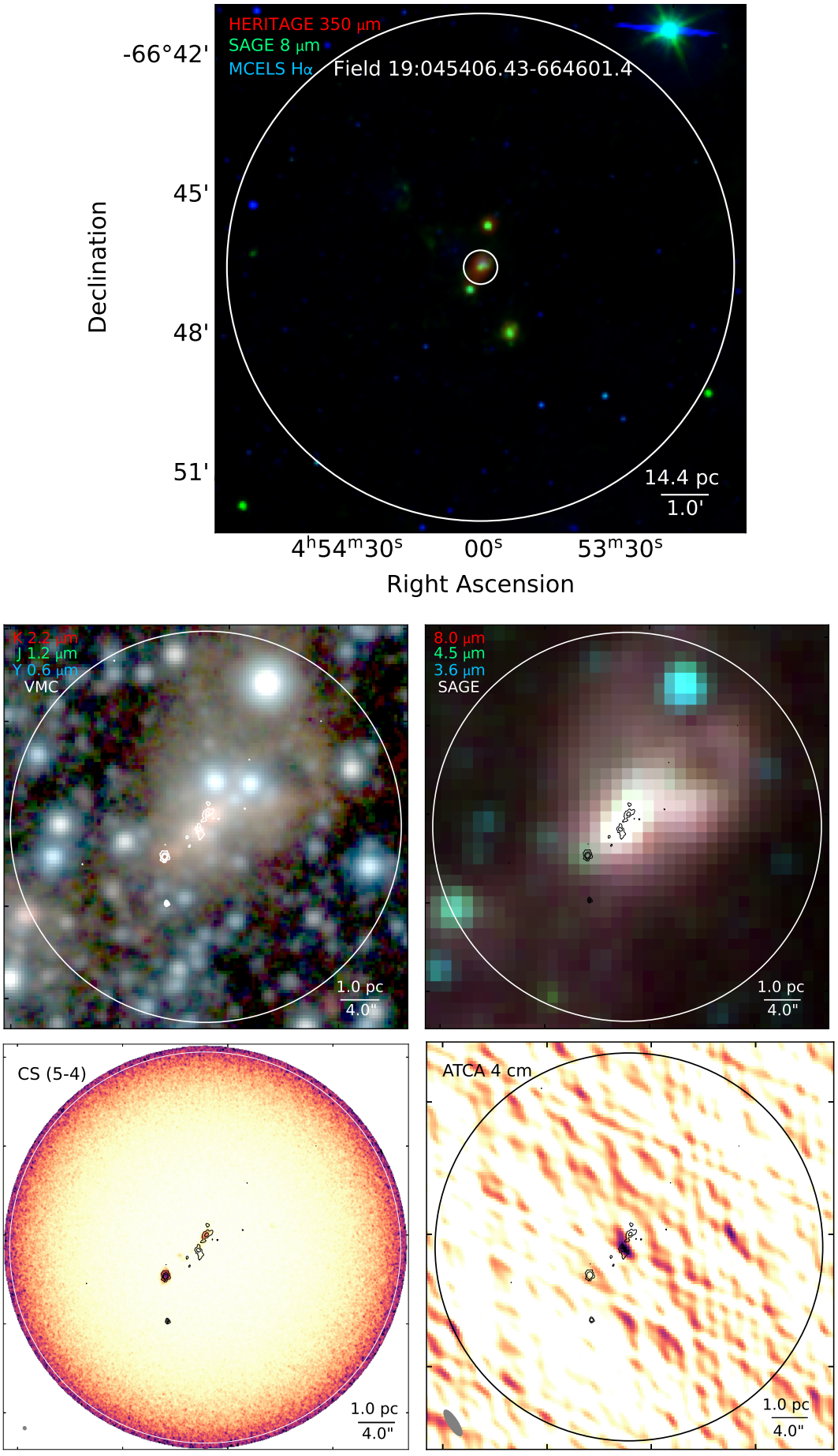


Figure F.18: Same as Fig F.1 but for Field 19.

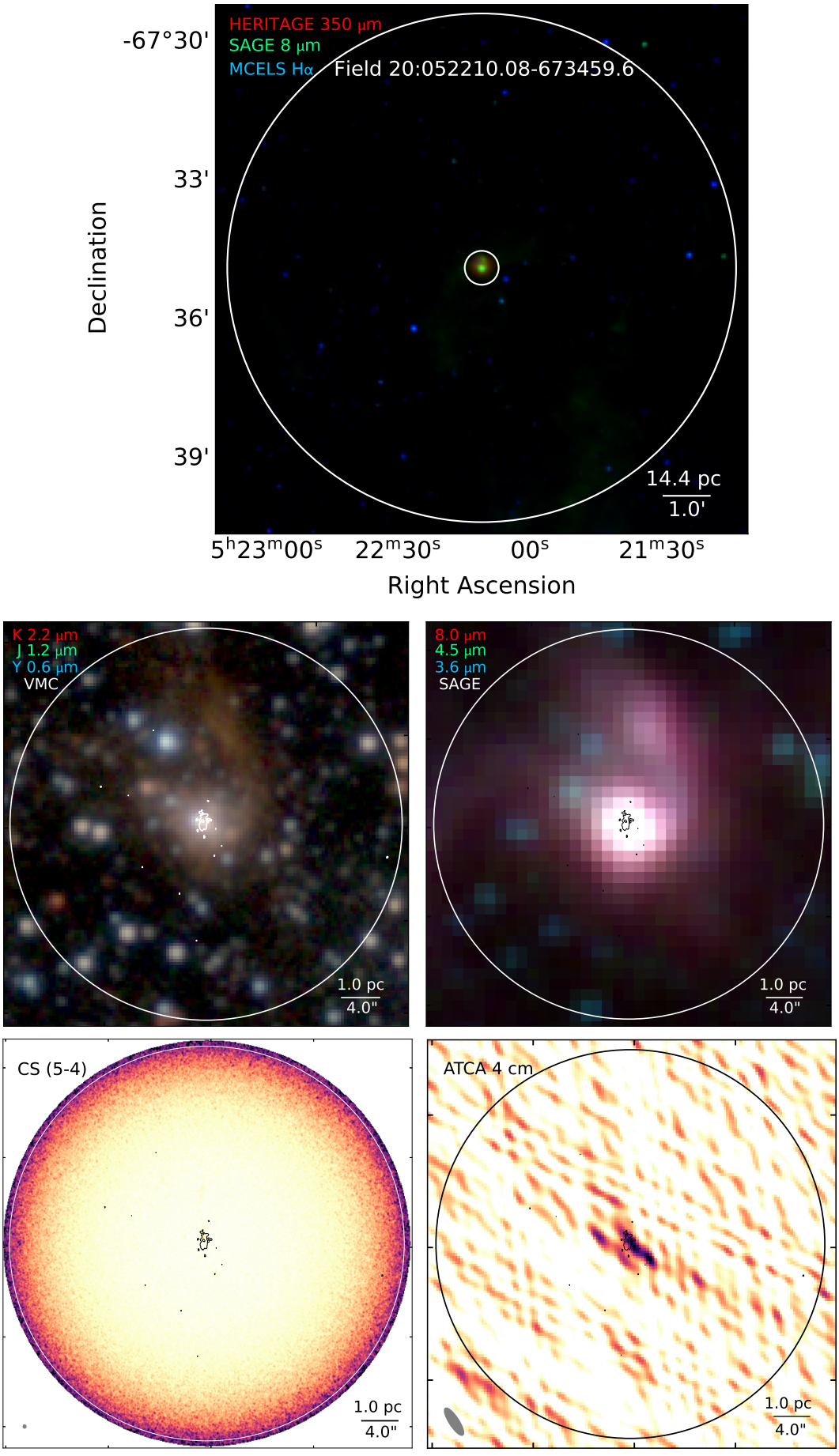


Figure F.19: Same as Fig F.1 but for Field 20.

Bibliography

Abdo, A. A., Ackermann, M., Ajello, M., et al. 2010, A&A, 512, A7

Acharyya, K. & Herbst, E. 2018, ApJ, 859, 51

Anderson, L. D., Zavagno, A., Barlow, M. J., García-Lario, P., & Noriega-Crespo, A. 2012, A&A, 537, A1

André, P., Arzoumanian, D., Könyves, V., Shimajiri, Y., & Palmeirim, P. 2019, A&A, 629, L4

André, P. J., Palmeirim, P., & Arzoumanian, D. 2022, A&A, 667, L1

Arzoumanian, D., André, P., Könyves, V., et al. 2019, A&A, 621, A42

Bekki, K. & Chiba, M. 2007a, PASA, 24, 21

Bekki, K. & Chiba, M. 2007b, MNRAS, 381, L16

Belloche, A., Müller, H. S. P., Menten, K. M., Schilke, P., & Comito, C. 2013, A&A, 559, A47

Besla, G., Kallivayalil, N., Hernquist, L., et al. 2012, MNRAS, 421, 2109

Bestenlehner, J. M., Crowther, P. A., Caballero-Nieves, S. M., et al. 2020, MNRAS, 499, 1918

Browning, M. K., Tumlinson, J., & Shull, J. M. 2003, ApJ, 582, 810

Brunetti, N. & Wilson, C. D. 2019, MNRAS, 483, 1624

Cesaroni, R., Sánchez-Monge, Á., Beltrán, M. T., et al. 2017, A&A, 602, A59

Cheng, Y., Lu, X., Sanhueza, P., et al. 2024, ApJ, 967, 56

Choudhury, S., de Grijs, R., Bekki, K., et al. 2021, MNRAS, 507, 4752

Choudhury, S., Subramaniam, A., & Cole, A. A. 2016, MNRAS, 455, 1855

Choudhury, S., Subramaniam, A., Cole, A. A., & Sohn, Y. J. 2018, MNRAS, 475, 4279

Cioni, M. R. L., Clementini, G., Girardi, L., et al. 2011, A&A, 527, A116

D'Onghia, E. & Fox, A. J. 2016, ARA&A, 54, 363

Fontani, F., Colzi, L., Bizzocchi, L., et al. 2022, A&A, 660, A76

Fontani, F., Palau, A., Caselli, P., et al. 2011, A&A, 529, L7

Fox, A., Krishnarao, D., D'Onghia, E., et al. 2023, in American Astronomical Society Meeting Abstracts, Vol. 241, American Astronomical Society Meeting Abstracts, 335.08

Fox, A. J., Frazer, E. M., Bland-Hawthorn, J., et al. 2020, ApJ, 897, 23

Fujii, M. S. & Portegies Zwart, S. 2015, MNRAS, 449, 726

Fukui, Y., Abe, R., Hara, A., et al. 1999, in New Views of the Magellanic Clouds, ed. Y. H. Chu, N. Suntzeff, J. Hesser, & D. Bohlender, Vol. 190, 61

Furuya, R. S., Cesaroni, R., Takahashi, S., et al. 2005, ApJ, 624, 827

Garrod, R. T., Widicus Weaver, S. L., & Herbst, E. 2008, ApJ, 682, 283

Gieser, C., Beuther, H., Semenov, D., et al. 2021, A&A, 648, A66

Gong, Y., Henkel, C., Menten, K. M., et al. 2023, A&A, 679, L6

Graczyk, D., Pietrzyński, G., Thompson, I. B., et al. 2014, ApJ, 780, 59

Grishunin, K., Weiss, A., Colombo, D., et al. 2024, A&A, 682, A137

Groves, B., Kreckel, K., Santoro, F., et al. 2023, MNRAS, 520, 4902

Gruendl, R. A. & Chu, Y.-H. 2009, ApJS, 184, 172

Hacar, A., Clark, S. E., Heitsch, F., et al. 2023, in Astronomical Society of the Pacific Conference Series, Vol. 534, Protostars and Planets VII, ed. S. Inutsuka, Y. Aikawa, T. Muto, K. Tomida, & M. Tamura, 153

Hamedani Golshan, R., Sánchez-Monge, Á., Schilke, P., et al. 2024, A&A, 688, A3

Helmich, F. P. & van Dishoeck, E. F. 1997, A&AS, 124, 205

Henize, K. G. 1956, ApJS, 2, 315

Herbst, E. & van Dishoeck, E. F. 2009, ARA&A, 47, 427

Indebetouw, R., Brogan, C., Chen, C. H. R., et al. 2013, ApJ, 774, 73

Jin, Y., Sutherland, R., Kewley, L. J., & Nicholls, D. C. 2023, ApJ, 958, 179

Jones, O. C., Woods, P. M., Kemper, F., et al. 2017, MNRAS, 470, 3250

Kim, S., Staveley-Smith, L., Dopita, M. A., et al. 1998, ApJ, 503, 674

Koch, E. W. & Rosolowsky, E. W. 2015, MNRAS, 452, 3435

Krishnarao, D., Fox, A. J., D'Onghia, E., et al. 2022, Nature, 609, 915

Kroupa, P. 2001, MNRAS, 322, 231

Krumholz, M. R., McKee, C. F., & Bland-Hawthorn, J. 2019, ARA&A, 57, 227

Kurtz, S., Cesaroni, R., Churchwell, E., Hofner, P., & Walmsley, C. M. 2000, in Protostars and Planets IV, ed. V. Mannings, A. P. Boss, & S. S. Russell, 299–326

Lah, P., Colless, M., D'Eugenio, F., Groves, B., & Gelfand, J. D. 2024, MNRAS, 529, 2611

Launhardt, R., Stutz, A. M., Schmiedeke, A., et al. 2013, A&A, 551, A98

Li, J., Liu, C., Zhang, Z.-Y., et al. 2023, Nature, 613, 460

Liu, M., Tan, J. C., Cheng, Y., & Kong, S. 2018, ApJ, 862, 105

Liu, T., Evans, N. J., Kim, K.-T., et al. 2020, MNRAS, 496, 2790

Lucchini, S., D'Onghia, E., & Fox, A. J. 2024, ApJ, 967, 16

Lucchini, S., D'Onghia, E., Fox, A. J., et al. 2020, Nature, 585, 203

Mangum, J. G. & Shirley, Y. L. 2015, PASP, 127, 266

Massey, P. 2003, ARA&A, 41, 15

McKee, C. F. & Ostriker, E. C. 2007, ARA&A, 45, 565

McLeod, A. F., Klaassen, P. D., Reiter, M., et al. 2024, Nature, 625, 55

McMullin, J. P., Waters, B., Schiebel, D., Young, W., & Golap, K. 2007, in Astronomical Society of the Pacific Conference Series, Vol. 376, Astronomical Data Analysis Software and Systems XVI, ed. R. A. Shaw, F. Hill, & D. J. Bell, 127

Meixner, M., Gordon, K. D., Indebetouw, R., et al. 2006, AJ, 132, 2268

Meixner, M., Panuzzo, P., Roman-Duval, J., et al. 2013, AJ, 146, 62

Minh, Y. C., Liu, H. B., & Galvań-Madrid, R. 2016, ApJ, 824, 99

Möller, T., Bernst, I., Panoglou, D., et al. 2013, A&A, 549, A21

Möller, T., Endres, C., & Schilke, P. 2017, A&A, 598, A7

Möller, T., Schilke, P., Sánchez-Monge, Á., Schmiedeke, A., & Meng, F. 2023, A&A, 676, A121

Motte, F., Bontemps, S., Csengeri, T., et al. 2022, A&A, 662, A8

Motte, F., Bontemps, S., & Louvet, F. 2018a, ARA&A, 56, 41

Motte, F., Nony, T., Louvet, F., et al. 2018b, Nature Astronomy, 2, 478

Müller, H. S. P., Schlöder, F., Stutzki, J., & Winnewisser, G. 2005, Journal of Molecular Structure, 742, 215

Nayak, O., Hirschauer, A. S., Kavanagh, P. J., et al. 2024, ApJ, 963, 94

Neralwar, K. R., Colombo, D., Duarte-Cabral, A., et al. 2022, A&A, 664, A84

Nummelin, A., Bergman, P., Hjalmarson, Å., et al. 2000, ApJS, 128, 213

Ossenkopf, V. & Henning, T. 1994, A&A, 291, 943

Panagia, N. 1973, AJ, 78, 929

Pelkonen, V. M., Padoan, P., Haugbølle, T., & Nordlund, Å. 2021, MNRAS, 504, 1219

Pietrzyński, G., Graczyk, D., Gallenne, A., et al. 2019, Nature, 567, 200

Pillai, T., Kauffmann, J., Wyrowski, F., et al. 2011, A&A, 530, A118

Qin, S.-L., Liu, T., Liu, X., et al. 2022, MNRAS, 511, 3463

Reid, M. A. & Wilson, C. D. 2006, ApJ, 650, 970

Robitaille, T., Ginsburg, A., Beaumont, C., Leroy, A., & Rosolowsky, E. 2016, spectral-cube: Read and analyze astrophysical spectral data cubes, Astrophysics Source Code Library, record ascl:1609.017

Rolleston, W. R. J., Smartt, S. J., Dufton, P. L., & Ryans, R. S. I. 2000, A&A, 363, 537

Roman-Duval, J., Jenkins, E. B., Tchernyshyov, K., et al. 2021, ApJ, 910, 95

Russeil, D., Schneider, N., Anderson, L. D., et al. 2013, A&A, 554, A42

Sadaghiani, M., Sánchez-Monge, Á., Schilke, P., et al. 2020, A&A, 635, A2

Salpeter, E. E. 1955, ApJ, 121, 161

Sánchez-Monge, Á., Beltrán, M. T., Cesaroni, R., et al. 2013a, A&A, 550, A21

Sánchez-Monge, Á., Kurtz, S., Palau, A., et al. 2013b, ApJ, 766, 114

Sánchez-Monge, Á., López-Sepulcre, A., Cesaroni, R., et al. 2013c, A&A, 557, A94

Sánchez-Monge, Á., Schilke, P., Schmiedeke, A., et al. 2017, A&A, 604, A6

Sanhueza, P., Contreras, Y., Wu, B., et al. 2019, ApJ, 886, 102

Sault, R. J., Teuben, P. J., & Wright, M. C. H. 1995, in Astronomical Society of the Pacific Conference Series, Vol. 77, Astronomical Data Analysis Software and Systems IV, ed. R. A. Shaw, H. E. Payne, & J. J. E. Hayes, 433

Schilke, P., Walmsley, C. M., Pineau des Forets, G., & Flower, D. R. 1997, A&A, 321, 293

Schöier, F. L., van der Tak, F. F. S., van Dishoeck, E. F., & Black, J. H. 2005, A&A, 432, 369

Seale, J. P., Looney, L. W., Chu, Y.-H., et al. 2009, ApJ, 699, 150

Seale, J. P., Meixner, M., Sewiło, M., et al. 2014, AJ, 148, 124

Selier, R. & Heydari-Malayeri, M. 2012, A&A, 545, A29

Sewiło, M., Cordiner, M., Charnley, S. B., et al. 2022, ApJ, 931, 102

Sewiło, M., Indebetouw, R., Charnley, S. B., et al. 2018, ApJ, 853, L19

Shetty, R., Kauffmann, J., Schnee, S., Goodman, A. A., & Ercolano, B. 2009, ApJ, 696, 2234

Shimonishi, T., Dartois, E., Onaka, T., & Boulanger, F. 2016a, A&A, 585, A107

Shimonishi, T., Das, A., Sakai, N., et al. 2020, ApJ, 891, 164

Shimonishi, T., Izumi, N., Furuya, K., & Yasui, C. 2021, ApJ, 922, 206

Shimonishi, T., Onaka, T., Kawamura, A., & Aikawa, Y. 2016b, ApJ, 827, 72

Shimonishi, T., Tanaka, K. E. I., Zhang, Y., & Furuya, K. 2023, ApJ, 946, L41

Shirley, Y. L. 2015, PASP, 127, 299

Smith, C., Leiton, R., & Pizarro, S. 2000, in Astronomical Society of the Pacific Conference Series, Vol. 221, Stars, Gas and Dust in Galaxies: Exploring the Links, ed. D. Alloin, K. Olsen, & G. Galaz, 83

Smith, R. J., Longmore, S., & Bonnell, I. 2009, MNRAS, 400, 1775

Staveley-Smith, L., Kim, S., Calabretta, M. R., Haynes, R. F., & Kesteven, M. J. 2003, MNRAS, 339, 87

Sutton, E. C., Peng, R., Danchi, W. C., et al. 1995, ApJS, 97, 455

Tang, X. D., Henkel, C., Chen, C. H. R., et al. 2017, A&A, 600, A16

Tanvir, T. S. & Krumholz, M. R. 2024, MNRAS, 527, 7306

Taquet, V., Wirström, E. S., & Charnley, S. B. 2016, ApJ, 821, 46

Tenorio-Tagle, G., Bodenheimer, P., Rozyczka, M., & Franco, J. 1986, A&A, 170, 107

Tokuda, K., Harada, N., Tanaka, K. E. I., et al. 2023, ApJ, 955, 52

Tokuda, K., Kunitoshi, Y., Zahorecz, S., et al. 2025, ALMA 0.1 pc View of Molecular Clouds Associated with High-Mass Protostellar Systems in the Small Magellanic Cloud: Are Low-Metallicity Clouds Filamentary or Not?

Traficante, A., Jones, B. M., Avison, A., et al. 2023, MNRAS, 520, 2306

Treviño-Morales, S. P., Fuente, A., Sánchez-Monge, Á., et al. 2019, A&A, 629, A81

Treviño-Morales, S. P., Pilleri, P., Fuente, A., et al. 2014, A&A, 569, A19

van der Marel, R. P. & Kallivayalil, N. 2014, ApJ, 781, 121

van der Tak, F. F. S., Black, J. H., Schöier, F. L., Jansen, D. J., & van Dishoeck, E. F. 2007, A&A, 468, 627

van Dishoeck, E. F. 2004, ARA&A, 42, 119

van Loon, J. T., Oliveira, J. M., Gordon, K. D., Sloan, G. C., & Engelbracht, C. W. 2010, AJ, 139, 1553

Vázquez-Semadeni, E., González-Samaniego, A., & Colín, P. 2017, MNRAS, 467, 1313

Wakelam, V., Bron, E., Cazaux, S., et al. 2017, Molecular Astrophysics, 9, 1

Welty, D. E., Federman, S. R., Gredel, R., Thorburn, J. A., & Lambert, D. L. 2006, ApJS, 165, 138

Wilner, D. J., De Pree, C. G., Welch, W. J., & Goss, W. M. 2001, ApJ, 550, L81

Wolfire, M. G., Vallini, L., & Chevance, M. 2022, ARA&A, 60, 247

Wong, T., Hughes, A., Tokuda, K., et al. 2019, ApJ, 885, 50

Xu, F., Wang, K., Liu, T., et al. 2024, Research in Astronomy and Astrophysics, 24, 065011

Zhang, Q., Wang, K., Lu, X., & Jiménez-Serra, I. 2015, ApJ, 804, 141

Zivick, P., Kallivayalil, N., Besla, G., et al. 2019, ApJ, 874, 78